Instytut Fizyki Molekularnej Polskiej Akademii Nauk

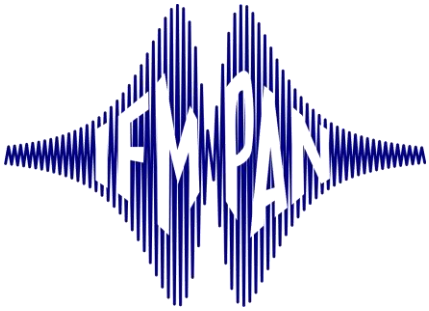

Rozprawa doktorska

DYNAMIKA NAMAGNESOWANIA CIENKICH WARSTW GRANATU ITROWO-ŻELAZOWEGO $Y_3Fe_5O_{12}$

Adam Krysztofik

Promotor: prof. dr hab. Janusz Dubowik

Promotor pomocniczy: prof. UAM dr hab. Emerson Coy

Poznań, 2022

Realizacja rozprawy doktorskiej była współfinansowana przez:

- Projekt „Nanoukłady elektroniki spinowej wykorzystujące transfer spinowego momentu pędu”, *NANOSPIN* PSPB- 045/2010
- Projekt “Magnonics, Interactions and Complexity: a multifunctional aspects of spin wave dynamics”, *MagIc* Horizon 2020 MSCA-RISE-2014 No 644348
- Program „Środowiskowe interdyscyplinarne studia doktoranckie w zakresie nanotechnologii”, *PO WER* 03.02.00-00-I032/16
- Projekt Preludium “Wytwarzanie i charakteryzacja cienkich warstw granatu itrowo-żelazowego na elektrodach przewodzących”, Narodowe Centrum Nauki 2018/31/N/ST5/03433

Streszczenie

Granat itrowo-żelazowy ($Y_3Fe_5O_{12}$, YIG) należy do intensywnie badanych związków ze względu na wielorakie zastosowania w urządzeniach mikrofalowych oraz, od niedawna, w urządzeniach magnonicznych. Materiał ten wyróżnia niskie tłumienie precesji namagnesowania umożliwiające dalekozasięgową propagację fal spinowych. Obecnie przewiduje się, że urządzenia przetwarzające informacje w oparciu o fale spinowe będą charakteryzować się znacząco niższym poborem energii w porównaniu do tych opartych wyłącznie o transport elektronowy. Główną motywacją podejmowanych badań są zatem potencjalne zastosowania.

W niniejszej rozprawie zaprezentowano wyniki badań właściwości strukturalnych i magnetycznych cienkich warstw granatu itrowo-żelazowego. Szczególną uwagę poświęcono zagadnieniu dynamiki namagnesowania oraz jej wzajemnej relacji ze strukturalnymi własnościami wytworzonych warstw. W pierwszych rozdziałach pracy przedstawiono wprowadzenie do rezonansu ferromagnetycznego, fal spinowych oraz podstaw teoretycznych wykorzystanych metod badawczych. W ramach rozprawy przedstawiono pięć publikacji, w których omówiono charakterystykę propagacji powierzchniowych fal spinowych oraz paczek falowych, wpływ naprężeń epitaksjalnych na dynamikę namagnesowania, a także właściwości epitaksjalnych, strukturyzowanych i nanokrystalicznych warstw YIG. W ostatnim rozdziale zawarto podsumowanie i sformułowano najistotniejsze wnioski płynące z uzyskanych rezultatów badań.

Abstract

Yttrium iron garnet ($Y_3Fe_5O_{12}$, YIG) is one of the compounds intensively investigated in terms of microwave and magnonic applications. This material is distinguished by its low damping of the magnetization precession enabling long-range propagation of spin waves. At the moment, it is predicted that information processing devices based on spin waves will have significantly lower energy consumption compared to those based solely on electronic transport. Potential applications are therefore the main motivation for the undertaken research.

This dissertation presents the results of research on structural and magnetic properties of thin yttrium iron garnet films. Particular attention was paid to the magnetization dynamics and its mutual relationship with the structural properties of the developed layers. The first chapters of this thesis present an introduction to ferromagnetic resonance, spin waves and theoretical basis of the employed research methods. The dissertation presents five publications that discuss the propagation characteristics of the surface spin waves and wave packets, the impact of epitaxial strain on the magnetization dynamics, as well as properties of epitaxial, structured and nanocrystalline YIG layers. The last chapter contains a summary and main conclusions from the obtained results.

Lista publikacji wliczona do rozprawy

1. *Characterization of spin wave propagation in (111) YIG thin films with large anisotropy*
   A. Krysztofik, H. Głowiński, P. Kuświk, S. Ziętek, L.E. Coy, J.N. Rychły, S. Jurga, T.W. Stobiecki, J. Dubowik
   Journal of Physics D: Applied Physics **50**, 235004 (2017)
   DOI: 10.1088/1361-6463/aa6df0

2. *Ultra-low damping in lift-off structured yttrium iron garnet thin films*
   A. Krysztofik, L. E. Coy, P. Kuświk, K. Załęski, H. Głowiński, J. Dubowik
   Applied Physics Letters **111**, 192404 (2017)
   DOI: 10.1063/1.5002004

3. *Magnetization damping in nanocrystalline yttrium iron garnet thin films grown on oxidized silicon*
   A. Krysztofik, S. Özoğlu, E. Coy
   IEEE Magnetics Letters **12**, 7101605 (2021)
   DOI: 10.1109/LMAG.2021.3086454

4. *Effect of strain-induced anisotropy on magnetization dynamics in $Y_3Fe_5O_{12}$ films recrystallized on a lattice-mismatched substrate*
   A. Krysztofik, S. Özoğlu, R.D. McMichael, E. Coy
   Scientific Reports **11**, 14011 (2021)
   DOI: 10.1038/s41598-021-93308-3

5. *Tuning of Magnetic Damping in $Y_3Fe_5O_{12}$ / metal bilayers for spin-wave conduit termination*
   A. Krysztofik, N. Kuznetsov, H. Qin, L. Flajšman, E. Coy, S. van Dijken
   Materials **15**, 2814 (2022)
   DOI: 10.3390/ma15082814

Lista publikacji nie wliczona do rozprawy

1. *CoFeB/MgO/CoFeB structures with orthogonal easy axes: perpendicular anisotropy and damping*
   H. Głowiński, A. Żywczak, J. Wrona, A. Krysztofik, I. Gościańska, T. Stobiecki, J. Dubowik
   Journal of Physics: Condensed Matter **29**, 485803 (2017)
   DOI: 10.1088/1361-648X/aa9530

2. *High-temperature magnetodielectric $Bi(Fe_{0.5}Mn_{0.5})O_3$ thin films with checkerboard-ordered oxygen vacancies and low magnetic damping*
   E. Coy, I. Fina, K. Załęski, A. Krysztofik, L. Yate, L. Rodriguez, P. Graczyk, H. Głowiński, C. Ferrater, J. Dubowik, M. Varela
   Physical Review Applied **10**, 054072 (2018)
   DOI: 10.1103/PhysRevApplied.10.054072

3. *Non-negligible imaginary part of the spin-mixing conductance and its impact on magnetization dynamics in heavy-metal–ferromagnet bilayers*
J. Dubowik, P. Graczyk, A. Krysztofik, H. Głowiński, E. Coy, K. Załęski, I. Gościańska
Physical Review Applied **13**, 054011 (2020)
DOI: 10.1103/PhysRevApplied.13.054011

Aktywność naukowa

Udział w konferencjach naukowych:

The European Conference PHYSICS OF MAGNETISM
Structural and magnetic properties of $Y_3Fe_5O_{12}$ thin films grown by pulsed laser deposition
A. Krysztofik, H. Głowiński, P. Kuświk, E. Coy, S. Jurga, and J. Dubowik
Poznań, 26-30.06.2017

The European Conference PHYSICS OF MAGNETISM
Influence of anisotropy on spin wave propagation characteristics in PLD-grown YIG thin films
A. Krysztofik, H. Głowiński, P. Kuświk, S. Ziętek, E. Coy, J. Rychły, S. Jurga, T. Stobiecki, and J. Dubowik
Poznań, 26-30.06.2017

MagIC – Magnetism, Interactions and Complexity: a multifunctional aspects of spin wave dynamics

Yttrium Iron Garnet structured thin films for magnonic applications

A. Krysztofik, P. Kuświk, E. Coy, H. Głowiński, J. Dubowik

Poznań, Trzebaw, 02-07.07.2017

NanoTech Poland

Spin pumping effects in Finemet|Pt and Finemet|Ta bilayers

A. Krysztofik, P. Graczyk, H. Głowiński, E. Coy, K. Załęski, I. Gościańska, J. Dubowik

Poznań, 05-08.06.2019

Soft Magnetic Materials Conference

Experimental Evidence of Non-Negligible Imaginary Part of Spin Mixing Conductance

A. Krysztofik, P. Graczyk, H. Głowiński, E. Coy, K. Załęski, I. Gościańska, J. Dubowik

Poznań, 04-07.09.2019

QUTECNOMM 2019 The Fifth Poznań Symposium on Quantum Technologies, Nonlinear Optics, Magnonics, and Metamaterials

Damping and Magnetic Anisotropy of YIG Thin Films Deposited on Different Substrates

A. Krysztofik, S. Özoğlu, E. Coy, J. Dubowik

Poznań, 14-18.11.2019

IV Konferencja Doktorantów Polskiej Akademii Nauk

Can electrical signals flow through an insulator?

A. Krysztofik

Konferencja *on-line,* 23.11.2020

NanoTech Poland

Coplanar waveguide design for spin-wave excitation

A. Krysztofik

Poznań, 09-11.06.2021

NanoTech Poland

Spin-wave and spin-wave packet propagation in yttrium-iron garnet thin films

A. Krysztofik, E. Coy

Poznań, 01-03.06.2022

Sol-SkyMag

Magnetization dynamics in yttrium iron garnet films recrystallized on a lattice-mismatched substrate

A. Krysztofik, S. Özoğlu, Robert D. McMichael, Emerson Coy

San Sebastian, Hiszpania, 27.06-01.07.2022

Joint European Magnetic Symposia

Effect of strain induced anisotropy on magnetization dynamics in $Y_3Fe_5O_{12}$ thin films grown on $Y_3Al_5O_{12}$

A. Krysztofik, S. Özoğlu, Robert D. McMichael, Emerson Coy

Warszawa, 24-29.07.2022

IEEE 12th International Conference Nanomaterials: Applications & Properties

Nonlinear FMR linewidth dependence on frequency in strained garnet films

A. Krysztofik, S. Özoğlu, Robert D. McMichael, Emerson Coy

Kraków, 11-16.09.2022

Udział w projektach naukowych:

- “Nanoscale spin torque devices for spin electronics”, NANOSPIN (PSPB-045/2010)
- “Magnonics, Interactions and Complexity: a multifunctional aspects of spin wave dynamics”, European Union Horizon 2020 research and innovation programme under the Marie Skłodowska- Curie grant agreement No 644348 (MagIC)
- “Wytwarzanie i charakteryzacja cienkich warstw granatu itrowo-żelazowego na elektrodach przewodzących”, Projekt Preludium Narodowego Centrum Nauki nr 2018/31/N/ST5/03433 (kierownik projektu)

Udział w stażach naukowych:

- 12.11-25.11.2018, Staż na na Uniwersytecie w Kassel, Niemcy
- 20.10-02.11.2019, Staż na na Uniwersytecie w Kassel, Niemcy
- 12.08-09.12.2021, Staż na na Uniwersytecie Aalto, Finlandia

Spis treści

1 Wstęp

Obecnie przewiduje się, że urządzenia, których zasada działania opiera się na falach spinowych, pozwolą w wydajny sposób przetwarzać informacje oraz rozwiązać problem miniaturyzacji. W stosunku do konwencjonalnych układów elektronicznych wykorzystujących technologię półprzewodnikową CMOS, prototypy urządzeń magnonicznych wykazują szereg zalet. Najważniejszą z nich jest obniżenie zużycia energii. Współczesne komputery wytwarzają znaczne ilości ciepła, ponieważ bazują na wykorzystaniu translacyjnego ruchu ładunków elektrycznych. W technologiach opartych o fale spinowe straty energii są ograniczone, bowiem do przenoszenia informacji wykorzystywany jest transfer magnetycznego momentu pędu. Inną, równie ważną zaletą urządzeń magnonicznych jest możliwość pracy w szerokim zakresie częstotliwości. Jak wynika ze związków dyspersyjnych fal spinowych, częstotliwości te mogą sięgać kilkudziesięciu, a nawet kilkuset gigaherców.

Fale spinowe, aby mogły być wykorzystane do przetwarzania informacji, wymagają odpowiedniego wzbudzenia, detekcji oraz sterowania w falowodach magnetycznych. Niezwykle ważnym parametrem jest zasięg propagacji fal, który określają straty magnetyczne danego materiału. Niemal idealnym ośrodkiem dla efektywnej propagacji fal spinowych jest granat itrowo-żelazowy ($Y_3Fe_5O_{12}$, YIG) w postaci monokrystalicznej. Jest on izolatorem i charakteryzuje się najmniejszymi znanymi do tej pory stratami magnetycznymi. Obie te właściwości czynią go atrakcyjnym z punktu widzenia przyszłych zastosowań.

Niniejsza rozprawa doktorska podejmuje tematykę wzbudzeń magnetycznych w cienkich warstwach granatu itrowo-żelazowego wytwarzanych

w celu uzyskania możliwie największego zasięgu propagacji fal spinowych. W związku z tym, zagadnienia prezentowane w tej rozprawie łączą ze sobą dwa aspekty: aspekt technologiczny (związany z technologią cienkich warstw YIG) oraz aspekt badań podstawowych związany ze wzajemną relacją dynamiki namagnesowania i strukturalnych własności wytworzonych warstw.

Pierwszym zagadnieniem badawczym postawionym w niniejszej pracy jest eksperymentalna weryfikacja propagacji powierzchniowych fal spinowych i odpowiedź na pytanie, czy uzyskane metodą ablacji laserowej epitaksjalne warstwy YIG wykazują dostatecznie niskie tłumienie precesji namagnesowania[1]. Należy podkreślić, że w tym przypadku proces osadzania warstw prowadzony był w wysokiej temperaturze (650°C), a warstwy te charakteryzuje tzw. anizotropia indukowana wzrostem, która związana jest z tetragonalną dystorsją komórki elementarnej. Skłoniło to do postawienia również pytań o wpływ pól anizotropii na zależność dyspersyjną, prędkość grupową fal oraz na doświadczalne określenie wartości wzbudzanych liczb falowych.

Problematyka strukturyzacji cienkich warstw stanowiła drugie omawiane w tej pracy zagadnienie[2]. Wcześniejsze doniesienia literaturowe wskazywały, że trawienie jonowe warstw ciągłych wprowadza defekty krystaliczne, modyfikuje powierzchnię otrzymywanych struktur oraz powoduje wzrost tłumienia precesji namagnesowania. Alternatywne podejście wykorzystujące technikę *lift-off* pozwala uniknąć tego problemu. Jednakże technika ta wymaga osadzania warstw YIG w temperaturze pokojowej oraz ich późniejszą krystalizację. Podjęte badania miały na celu określenie, czy i w jakim stopniu proponowana nowa procedura strukturyzacji oraz otrzymywania warstw YIG wpływa na ich właściwości magnetyczne.

Trzecie zagadnienie poruszone w rozprawie dotyczy prób zastąpienia standardowo stosowanych podłoży granatu gadolinowo-galowego ($Gd_3Ga_5O_{12}$, GGG) innym materiałem. Motywację podjęcia tego kierunku badań wyraża chęć integracji warstw YIG z technologiami opartymi na krzemie przy jednoczesnym

utrzymaniu wyjątkowych własności warstw. W związku z tym, w pierwszej kolejności postanowiono zbadać właściwości strukturalne i magnetyczne warstw YIG osadzanych na amorficznym tlenku krzemu[3]. Podobne badania były już wcześniej prowadzone, jednakże analiza literaturowa nie pozwoliła zawęzić mechanizmów i przyczyn poszerzania linii rezonansowych obserwowanych w przypadku wykorzystania tego podłoża.

Równocześnie uwagę poświęcono zastąpieniu monokryształu GGG granatem itrowo-glinowym ($Y_3Al_5O_{12}$, YAG) o innym parametrze sieciowym[4]. Niedopasowanie parametru sieciowego pomiędzy YIG a YAG wynosi około 3% i jest znacznie większe w porównaniu do niedopasowania YIG i GGG (≈0.1%). Pomiary dynamiki namagnesowania układu YIG/YAG doprowadziły do poczynienia zaskakującej obserwacji z punktu widzenia teorii rezonansu ferromagnetycznego. Szerokość linii rezonansowej w funkcji częstotliwości wykazuje nie tylko nieliniową zależność, ale również jej wartość maleje wraz ze wzrostem częstotliwości mikrofalowej. Zjawisko to wyjaśniono przy pomocy autorskiego modelu poszerzenia linii rezonansowej.

Prezentowane badania kończy analiza właściwości strukturalnych i magnetycznych warstw YIG osadzanych na polikrystalicznych warstwach metali[5]. Wybrano trzy kolejne w układzie okresowym metale przejściowe wykazujące odporność na utlenianie. Były nimi iryd, platyna oraz złoto. W szczególności zbadano wpływ grubości warstwy metalu na parametry opisujące tłumienie precesji namagnesowania. Uzyskane rezultaty pozwoliły na zaproponowanie wykorzystania dwuwarstw YIG/metal do zakończeń falowodów magnonicznych.

Podstawę rozprawy stanowi cykl pięciu artykułów opublikowanych w recenzowanych czasopismach naukowych. Są one poprzedzone krótkimi rozdziałami opisującymi podstawy teoretyczne, preparatykę warstw, zastosowane metody badawcze oraz metodykę analizy danych eksperymentalnych. Rozprawę kończy podsumowanie badań oraz sformułowane na ich podstawie wnioski.

2 Podstawy teoretyczne

2.1 Granat itrowo-żelazowy $Y_3Fe_5O_{12}$

Niniejsza rozprawa oparta jest o cienkie warstwy granatu itrowo-żelazowego $Y_3Fe_5O_{12}$ (YIG) o grubościach rzędu dziesiątek nanometrów. YIG krystalizuje w układzie regularnym i ma złożoną strukturę krystalograficzną (grupa przestrzenna $Ia\bar{3}d$, nr 230). Parametr sieci dla materiału objętościowego wynosi 1.2376 nm[6]. Pojedyncza komórka elementarna zawiera osiem jednostek chemicznych i składa się ze 160 jonów. W szczególności wyróżniamy[7]:

- 24 jony żelaza zajmujące położenia tetraedryczne; każdy jon Fe^{3+} otoczony jest przez 4 jony tlenu O^{2-};
- 16 jonów żelaza Fe^{3+} zajmujących położenia oktaedryczne; każdy jon Fe^{3+} otoczony jest przez 6 jonów tlenu O^{2-};
- 24 jony itru zajmujące położenia dodekaedryczne; każdy jon Y^{3+} otoczony jest przez 8 jonów tlenu O^{2-};

Ze względu na znaczne odległości pomiędzy jonami żelaza oddziaływanie pomiędzy nimi jest przenoszone przez pośredniczące elektrony tlenu (tzw. nadwymiana), a siła oddziaływań zależy od odległości oraz od kąta wiązania Fe-O-Fe[8]. Dla YIGu prowadzi to antyrównoległego uporządkowania spinów jonów żelaza. Momenty magnetyczne pochodzące od Fe^{3+} w położeniach tetraedrycznych są częściowo skompensowane przez momenty Fe^{3+} w pozycjach oktaedrycznych (ferrimagnetyzm). W temperaturze zera bezwzględnego wypadkowy moment magnetyczny jednostki chemicznej wynosi 5 μ_B. W temperaturze pokojowej własności magnetyczne YIGu charakteryzuje namagnesowanie

nasycenia $M_s = 140$ kA/m, stała wymiany $A_{\mathrm{ex}} = 3.7$ pJ/m[9]. Temperatura Curie wynosi $T_c = 559$ K.

Jony żelaza charakteryzuje sferyczny rozkład ładunku, przez co ich oddziaływanie z fononami czy deformacjami sieci jest słabe. Ponadto YIG jest izolatorem, dzięki czemu nie występuje sprzężenie typu magnon-elektron. W rezultacie, YIG wykazuje niskie tłumienie precesji namagnesowania, a co za tym idzie, wykazuje długie czasy relaksacji dla fal spinowych (rzędu setek nanosekund), które przekładają się na odległości propagacji fal sięgające setek mikrometrów[10].

Cienkie warstwy YIG otrzymuje się wykorzystując metodę epitaksji z fazy ciekłej (LPE)[11], ablację laserową (PLD)[12], rozpylanie jonowe[13], gdy wzrost warstwy jest prowadzony na podłożu $Gd_3Ga_5O_{12}$ (GGG). Parametr sieci GGG (1.2383 nm) jest bliski YIG, a małe niedopasowanie parametru sieci umożliwia wytworzenie epitaksjalnych warstw o wysokiej jakości i niskiej liczbie defektów strukturalnych.

2.2 Rezonans ferromagnetyczny

Spektroskopia rezonansu ferromagnetycznego jest techniką pozwalającą badać dynamiczne własności magnetycznych cienkich warstw. W modelu fenomenologicznym zaproponowanym przez Smita i Beljersa[14] warunek rezonansu oblicza się na podstawie równania:

$$\left(\frac{\omega}{\gamma}\right)^2 = \frac{1}{M_S^2 \sin^2\theta_M}\left(F_{\theta\theta}F_{\phi\phi} - F_{\theta\phi}^2\right), \qquad (2.2.1)$$

$$F_\theta = \frac{\partial F}{\partial \theta_M} \qquad F_{\theta\theta} = \frac{\partial^2 F}{\partial \theta_M^2}$$
$$F_\phi = \frac{\partial F}{\partial \phi_M} \qquad F_{\phi\phi} = \frac{\partial^2 F}{\partial \phi_M^2} \quad , \qquad (2.2.2)$$
$$F_{\theta\phi} = \frac{\partial^2 F}{\partial \theta_M \partial \phi_M}$$

gdzie $\omega = 2\pi f$ oznacza częstość kołową, γ współczynnik żyromagnetyczny, M_s namagnesowanie nasycenia, F_{ij} pochodne cząstkowe energii swobodnej, θ_M i ϕ_M kąt biegunowy i azymutalny wektora magnetyzacji $\vec{M}$. Należy podkreślić, że równanie 2.2.1 dla $\theta_M = 0°$ posiada osobliwość, która podczas wyprowadzania równań szczegółowych o postaci analitycznej powoduje niedogodności. Problem ten został rozwiązany w pracy[15] poprzez modyfikację równania 2.2.1 do postaci, która jednocześnie umożliwia obliczenia dla magnetyzacji leżącej w płaszczyźnie warstwy oraz w kierunku prostopadłym do płaszczyzny:

$$\left(\frac{\omega}{\gamma}\right)^2 = \frac{1}{M_S^2}\left[F_{\theta\theta}\left(\frac{F_{\phi\phi}}{\sin^2\theta_M} + \frac{\cos\theta_M}{\sin\theta_M}F_\theta\right) - \left(\frac{F_{\theta\phi}}{\sin\theta_M} - \frac{\cos\theta_M}{\sin\theta_M}\frac{F_\phi}{\sin\theta_M}\right)^2\right]. \quad (2.2.3)$$

Energia swobodna F zawiera szereg członów energetycznych. W ogólnym przypadku, do opisu warstw granatu itrowo-żelazowego rozważamy:

- energię Zeemana F_{Zee} opisującą oddziaływanie zewnętrznego pola magnetycznego $\vec{H}$ z magnetyzacją $\vec{M}$:

$$F_{\mathrm{Zee}} = -\mu_0 H M_s (\sin\theta_M \sin\theta_H \cos(\phi_H - \phi_M) + \cos\theta_M \cos\theta_H). \quad (2.2.4)$$

- energię magnetostatyczną F_d wynikającą z dalekozasięgowych oddziaływań dipolowych, która związana jest z kształtem ferromagnetyka. Dla cienkiej warstwy leżącej w płaszczyźnie XY przyjmuje ona postać:

$$F_d = \frac{1}{2}\mu_0 M_s^2 \cos^2\theta_M. \quad (2.2.5)$$

- energię anizotropii prostopadłej F_u. Dla warstw YIG, pośród źródeł tego członu energetycznego należy wymienić naprężenia epitaksjalne, luki tlenowe, czy proces porządkowania jonów w krysztale poprzez warunki wzrostu warstw (tzw.

anizotropia indukowana wzrostem)[16]. Człon związany z polem anizotropii prostopadłej H_u dla warstwy leżącej w płaszczyźnie XY wyrażamy jako:

$$F_u = -\frac{1}{2}\,\mu_0\,H_u\,M_s\cos^2\theta_M. \tag{2.2.6}$$

- energię anizotropii magnetokrystalicznej F_c, która zależy od kierunku namagnesowania względem kierunków krystalograficznych. Za oddziaływanie pomiędzy wektorem namagnesowania a siecią krystaliczną odpowiedzialne jest sprzężenie spin-orbita. Dla YIGu, oddziaływanie to jest bliskie zeru ze względu na zaniedbywalnie mały moment orbitalny jonów żelaza[17]. Stąd, pole anizotropii magnetokrystalicznej H_c dla YIGu jest o rząd wielkości mniejsze w porównaniu do metalicznych ferromagnetyków[18–22]. Energię anizotropii magneto-krystalicznej zapisujemy jako:

$$F_c = \frac{1}{2}\,\mu_0\,H_c\,M_s\left(\alpha_x^2\alpha_y^2 + \alpha_y^2\alpha_z^2 + \alpha_z^2\alpha_x^2\right), \tag{2.2.7}$$

gdzie α_x, α_y, α_z oznaczają kosinusy kierunkowe. Postać kosinusów kierunkowych dla warstw o orientacji krystalograficznej (001) przyjmuje postać:

$$\alpha_x = \sin\theta_M\cos\phi_M, \tag{2.2.8}$$

$$\alpha_y = \sin\theta_M\sin\phi_M, \tag{2.2.9}$$

$$\alpha_z = \cos\theta_M, \tag{2.2.10}$$

natomiast dla warstw o orientacji (111)[23]:

$$\alpha_x = \frac{1}{\sqrt{3}}\left(\cos\theta_M + \sqrt{2}\sin\theta_M\cos\phi_M\right), \tag{2.2.11}$$

$$\alpha_y = \frac{1}{\sqrt{3}}\left(\cos\theta_M + \sqrt{2}\sin\theta_M\cos\left(\phi_M - \frac{2}{3}\pi\right)\right), \tag{2.2.12}$$

$$\alpha_z = \frac{1}{\sqrt{3}}\left(\cos\theta_M + \sqrt{2}\sin\theta_M\cos\left(\phi_M - \frac{4}{3}\pi\right)\right). \tag{2.2.13}$$

Całkowita energia swobodna F jest zatem równa:

$$F = F_{\mathrm{Zee}} + F_d + F_u + F_c. \tag{2.2.14}$$

Na podstawie równań 2.2.2-2.2.14 można wyprowadzić równania Kittla opisujące warunek rezonansu. Postaci analityczne zależności częstotliwości od pola magnetycznego wyprowadzane są przy założeniu $\theta_M = \theta_H$ oraz $\phi_M = \phi_H$, a więc gdy $\vec{M} \parallel \vec{H}$.

Informacji na temat procesów relaksacji w pomiarach rezonansu ferromagnetycznego dostarcza analiza szerokości linii rezonansowej. Podstawowe równie opisujące zależność szerokości linii rezonansowej ΔH od częstotliwości f ma postać liniową[24,25]:

$$\mu_0 \Delta H = \frac{4\pi\,\alpha}{\gamma} f + \mu_0 \Delta H_0. \tag{2.2.15}$$

Równanie 2.2.15 dostarcza informacji na temat wewnętrznych procesów tłumienia precesji namagnesowania wyrażonych poprzez parametr Gilberta α oraz procesów zewnętrznych poprzez parametr ΔH_0 związany z niejednorodnościami magnetycznymi w badanych próbkach. Równanie 2.2.15 pozwala zatem na rozróżnienie pomiędzy dwoma mechanizmami relaksacji: związanym z właściwościami danego materiału oraz związanym z obecnością defektów. Zależność 2.2.15 bada się, gdy pomiary rezonansu ferromagnetycznego wykonywane są w tzw. trybie przemiatania polem. Przy ustalonej, stałej częstotliwości mikrofal zmienia się natężenie pola magnetycznego i w warunkach rezonansu rejestrowana jest linia rezonansowa, której szerokość wyrażona jest w jednostkach pola.

Innym sposobem pomiarów rezonansu jest tryb przemiatania częstotliwością. Wtedy to, szerokość połówkowa linii rezonansowej Δf mierzona jest w jednostkach częstotliwości. Zaletą tego podejścia jest możliwość oszacowania efektywnego parametru tłumienia α_{eff}, który bezpośrednio wiąże się z czasem relaksacji τ badanego materiału:

$$\alpha_{\mathrm{eff}} = \frac{\Delta f}{2f} = \frac{1}{2\pi\, f\, \tau}. \tag{2.2.16}$$

Dla warstw YIGu, czasy relaksacji sięgają setek nanosekund, co umożliwia znaczący zasięg propagacji fal spinowych[10]. Zaniedbując przyczynek od pola anizotropii magnetokrystalicznej, można wykazać związek pomiędzy efektywnym parametrem tłumienia α_{eff} a czynnikami α oraz ΔH_0. Dla warstw namagnesowanych w płaszczyźnie α_{eff} przyjmuje postać:

$$\alpha_{\mathrm{eff}}^{\mathrm{IP}} \approx \left(\alpha + \frac{\gamma\mu_0\Delta H_0}{4\pi f}\right)\sqrt{1+\left(\frac{\gamma\mu_0 M_{\mathrm{eff}}}{4\pi f}\right)^2}, \tag{2.2.17}$$

gdzie $M_{\mathrm{eff}} = M_s - H_u$, zaś dla warstw namagesowanych w kierunku prostopadłym do płaszczyzny:

$$\alpha_{\mathrm{eff}}^{\mathrm{OP}} \approx \alpha + \frac{\gamma\mu_0\Delta H_0}{4\pi f}. \tag{2.2.18}$$

Równania 2.2.17 i 2.2.18 pokazują istotne znaczenie parametru ΔH_0 na efektywne tłumienie precesji namagnesowania oraz, jak zostanie to przedstawione w kolejnym rozdziale, na zasięg propagacji koherentnych fal spinowych.

2.3 Fale spinowe

Fale spinowe są kolektywnymi wzbudzeniami układu spinów, które mogą propagować w uporządkowanych magnetycznie materiałach. Ich częstotliwości mieszczą się w zakresie od kilkuset megaherców do teraherzów, a odpowiadające tym częstotliwościom długości fal sięgają dziesiątek nanometrów. Zależność pomiędzy częstotliwością a długością fal spinowych określają tzw. relacje dyspersji, które znacząco różnią się od dobrze znanej dyspersji światła czy fali dźwiękowej w ośrodkach jednorodnych. Związki dyspersyjne dla fal spinowych są silnie anizotropowe. Dzięki znacznie bogatszym i bardziej złożonym zależnościom dyspersyjnym fale spinowe propagujące w materiałach magnetycznych mogą zostać wykorzystane jako nośniki informacji w urządzeniach o rozmiarach mikro- i nanoskopowych.

Ze względu na wzajemną orientację wektora falowego $\vec{k}$ i wektora magnetyzacji $\vec{M}$, którego ułożenie wynika z kierunku przyłożonego pola magnetycznego, wyróżniamy trzy charakterystyczne mody propagacji fal spinowych[26,27]:

- fale powierzchniowe (z ang. *surface spin waves* lub *Damon-Eshbach modes*), gdy wektor magnetyzacji leży w płaszczyźnie warstwy oraz $\vec{k} \perp \vec{M}$:

$$f(k) = \frac{\gamma}{2\pi}\sqrt{(\mu_0 H + D_{\mathrm{ex}}k^2)(\mu_0 H + D_{\mathrm{ex}}k^2 + \mu_0 M_s) + \left(\frac{1}{2}\mu_0 M_s\right)^2 (1 - e^{-2kd})},$$

(2.3.1)

- fale typu *backward volume spin waves*, gdy wektor magnetyzacji leży w płaszczyźnie warstwy oraz $\vec{k} \parallel \vec{M}$:

$$f(k) = \frac{\gamma}{2\pi}\sqrt{(\mu_0 H + D_{\mathrm{ex}}k^2)\left(\mu_0 H + D_{\mathrm{ex}}k^2 + \mu_0 M_s \frac{1-e^{-kd}}{kd}\right)}, \qquad (2.3.2)$$

- fale typu *forward volume spin waves*, gdy kierunek wektora magnetyzacji jest prostopadły do płaszczyzny warstwy oraz $\vec{k} \perp \vec{M}$:

$$f(k) = \frac{\gamma}{2\pi}\sqrt{(\mu_0 H + D_{\mathrm{ex}}k^2 - \mu_0 M_s)\left(\mu_0 H + D_{\mathrm{ex}}k^2 - \mu_0 M_s \frac{1-e^{-kd}}{kd}\right)},$$

(2.3.3)

gdzie f oznacza częstotliwość, k liczbę falową, γ współczynnik żyromagnetyczny, H natężenie pola magnetycznego, M_s namagnesowanie nasycenia, D_{ex} stałą sztywności fal spinowych związaną ze stałą wymiany A_{ex} ($D_{\mathrm{ex}} = 2A_{\mathrm{ex}}/\, M_s$), oraz d grubość warstwy.

Równania 2.3.1-2.3.3 stanowią podstawowe zależności dyspersyjne charakteryzujące propagację fal spinowych. Należy zaznaczyć, że w powyżej

wymienionych związkach zaniedbano pole anizotropii prostopadłej i pole anizotropii magnetokrystalicznej[1,28]. Niemniej jednak, relacje te pozwalają przewidzieć zasięg propagacji fal odgrywający ważną rolę podczas projektowania eksperymentu fizycznego. Charakterystyczna droga L_d (z ang. *decay length*), po której amplituda fali zmniejsza się e-krotnie, dana jest przez:

$$L_d = v_g\,\tau = \frac{v_g}{2\pi f\;\alpha_{\mathrm{eff}}}, \tag{2.3.4}$$

gdzie $v_g = 2\pi\frac{\partial f}{\partial k}$ oznacza prędkość grupową fali, τ czas relaksacji i α_{eff} efektywny parametr tłumienia. Wykorzystanie falowodów koplanarnych czy pojedynczych linii mikrofalowych zintegrowanych z próbką pozwala na wzbudzenie i detekcję fal spinowych o $k =$ 0-10 rad/μm[10]. Spośród wymienionych wyżej modów propagacji, najwyższe prędkości grupowe w tym zakresie liczb falowych wykazują fale powierzchniowe. Stąd, w przedstawionej rozprawie badania objęły ten wybrany mod propagacji.

3 Otrzymywanie warstw i metodyka badawcza

3.1 Impulsowa ablacja laserowa (PLD)

Impulsowa ablacja laserowa (ang. *Pulsed Laser Deposition*) jest powszechnie stosowaną techniką wykorzystywaną do osadzania cienkich warstw tlenków. Pozwala ona odtwarzać stechiometrię chemicznie złożonych materiałów z dużą wiernością oczekiwanego składu[29]. W tej metodzie wiązka lasera skupiana jest na masywnej tarczy, z której każdy impuls lasera odparowuje niewielką ilość materiału. Rozproszone jony w postaci plazmy osiadają następnie na oddalonym o kilka centymetrów podłożu. W celu zapewnienia równomiernego usuwania odparowywanego materiału tarcza obraca się, podczas gdy wiązka lasera jest odchylana przez soczewkę skupiającą poruszającą się horyzontalnie. Proces nanoszenia warstw może być prowadzony w warunkach ultra wysokiej próżni ($\approx 10^{-8}$ mbar). Jednakże, w przypadku osadzania warstw tlenkowych najczęściej odbywa się on przy parcjalnym ciśnieniu tlenu rzędu 10^{-4} - 10^{-2} mbar.

Do osadzania cienkich warstw YIG posłużono się laserem Nd:YAG wybierając trzecią harmoniczną o długości fali $\lambda = 355$ nm. Odległość pomiędzy podłożem a tarczą wynosiła $\approx$ 5 cm, częstotliwość impulsów 5 Hz, a gęstość energii promieniowania około 3 J/cm^2. Przy parcjalnym ciśnieniu tlenu $2.4 \cdot 10^{-4}$ mbar warunki te pozwalają uzyskać prędkość osadzania warstw rzędu $\approx$ 1 nm/min.

3.2 Magnetronowe rozpylanie jonowe

Technika magnetronowego rozpylania jonowego została wykorzystana do osadzania warstw metali takich jak złoto, platyna oraz iryd. Proces nanoszenia prowadzony był w atmosferze argonu o ciśnieniu parcjalnym około 10^{-3} mbar i próżni bazowej poniżej 2×10^{-8} mbar. Technika magnetronowego rozpylania jonowego polega na rozpraszaniu atomów tarczy przy użyciu jonów argonu, które przyspieszane są w polu elektrycznym w kierunku tarczy, i w ten sposób rozpylany materiał osadzany jest na podłożu. Znaczne natężenie pola elektrycznego przyspiesza jony oraz elektrony powodując zderzenia z obojętnymi cząsteczkami gazu i ich jonizację. Liczba jonów może dzięki temu rosnąć lawinowo. Aby zwiększyć prawdopodobieństwo jonizacji przez elektrony wtórne, używa się dodatkowo magnesów trwałych. Pole magnetyczne umożliwia utrzymanie plazmy w pobliżu tarczy, zwiększenie prędkości nanoszenia, oraz utrzymanie niskiego ciśnienia argonu, a przez to obniżenie zanieczyszczenia warstw gazami resztkowymi[30]. Otrzymane warstwy, których wzrost prowadzony był w temperaturze pokojowej, są na ogół polikrystaliczne.

3.3 Bezmaskowa litografia optyczna

Technika bezmaskowej litografii optycznej została wykorzystana do planarnego strukturyzowania warstw YIG oraz warstw złota w celu wytworzenia zintegrowanych z próbką falowodów koplanarnych i anten mikrofalowych. W metodzie tej wykorzystuje się emulsją światłoczułą (rezyst) oraz układ optyczny umożliwiający selektywną zmianę jej własności fizyko-chemicznych poprzez naświetlanie wybranych obszarów.

Na etapy procesu strukturyzowania układów warstwowych składają się:

1) Przygotowanie powierzchni podłoża: czyszczenie próbki ze śladowych ilości związków organicznych i zanieczyszczeń nieorganicznych w myjce

ultradźwiękowej stosując np. aceton, trichloroetylen, izopropanol oraz wygrzewanie na płycie grzewczej w celu odparowania wody.

2) Nałożenie fotorezystu za pomocą techniki nazywanej z ang. *spin-coating*: nakropienie roztworu polimeru na powierzchnię podłoża i równomierne rozprowadzenie rezystu podczas wirowania z szybkościami sięgającymi kilku tysięcy obrotów na minutę. Dzięki siłom odśrodkowym nadmiar rezystu usuwany jest z powierzchni próbki. Otrzymywana grubość rezystu zależy od lepkości roztworu rezystu i szybkości wirowania.

3) Wygrzanie fotorezystu na płycie grzewczej w celu poprawienia jego przyczepności do podłoża, odparowania nadmiaru rozpuszczalnika i utwardzenia rezystu.

4) Naświetlenie struktur wiązką światła z lasera. Na tym etapie wykonuje się centrowanie powierzchni próbki i przygotowanego projektu wzoru. Naświetlenie rezystu powoduje zmianę jego struktury chemicznej, jak i jego rozpuszczalności w roztworach zasad.

5) Wywołanie rezystu – częściowe usunięcie rezystu w roztworze zasadowym. Dla rezystu pozytywowego następuje usunięcie poprzednio naświetlonych obszarów. W celu poprawy czystości odsłoniętych części podłoża można stosować dodatkowo czyszczenie powierzchni plazmą niskociśnieniową.

6) Naniesienie warstw

7) Usunięcie pozostałego fotorezystu z powierzchni próbki za pomocą rozpuszczalnika organicznego np. acetonu.

3.4 Dyfrakcja rentgenowska (XRD)

Metoda dyfrakcji rentgenowskiej (ang. *X-Ray Diffraction*) pozwala badać strukturę krystalograficzną[31]. Technika zasadza się na ugięciu i interferencji skolimowanej wiązki promieniowania o długości fali około 0.1 nm. Promieniowanie padające na próbkę ulega rozproszeniu na równoległych do siebie płaszczyznach atomowych oddalonych od siebie na odległość międzypłaszczyznową d_{hkl}. Wzmocnienie fal odbitych następuje, gdy różnica dróg, które pokonują, jest równa całkowitej wielokrotności długości fali. Nakładające się fale są wtedy zgodne w fazie. Warunek wzmocnienia fal opisuje równanie Bragga:

$$2d_{hkl}\sin\theta = n\lambda, \tag{3.4.1}$$

gdzie θ oznacza kąt, jaki tworzy wiązka padająca z płaszczyzną atomową, n rząd ugięcia, i λ długość fali promieniowania. Analiza zależności intensywności promieniowania od kąta θ umożliwia wyznaczenie odległości międzypłaszczyznowej d_{hkl} i wyznaczenie parametru sieci komórki elementarnej. Dla układu regularnego parametr sieci a dany jest:

$$a = d_{hkl}\sqrt{(h^2 + k^2 + l^2)}, \tag{3.4.2}$$

gdzie h, k, l to wskaźniki Millera płaszczyzn krystalograficznych.

Typowy dyfraktometr rentgenowski składa się z lampy rentgenowskiej, układu szczelin oraz szczelin Sollera kolimujących promieniowanie, stolika pomiarowego, na którym umieszczana jest próbka, detektora oraz komputera służącego do sterowania pracą dyfraktometru i akwizycji danych. Ponadto, wykorzystuje się monochromator grafitowy w celu obniżenia intensywności promieniowania charakterystycznego K_β lub monochromator Bartelsa (układ czterech płytek germanowych), który umożliwia zarejestrowanie dyfraktogramu o wysokiej rozdzielczości poprzez zredukowanie intensywności promieniowania K_β

oraz $K_{\alpha 2}$. W niniejszej pracy jako źródło rentgenowskie wykorzystano lampę z anodą miedzianą o mocy 2 kW generującą promieniowanie o długości fali $\lambda_{K\alpha 1} =$ 0.15418 nm.

3.5 Reflektometria rentgenowska (XRR)

Reflektometria rentgenowska (ang. *X-Ray Reflectometry*) pozwala scharakteryzować grubość, gęstość oraz szorstkość układów cienkowarstwowych. Pomiary przy użyciu tej techniki prowadzone są w konfiguracji θ-2θ w zakresie niskokątowym ($2\theta =$ 0-10°). Poniżej kąta krytycznego θ_c, wiązka promieniowania rentgenowskiego ulega całkowitemu odbiciu od powierzchni badanej próbki. Kąt krytyczny przyjmuje zazwyczaj wartości poniżej 0.5° ze względu na bliski jedności współczynnik załamania $n = 1 - \delta$, gdzie δ jest tzw. dekrymentem współczynnika załamania o wartościach rzędu 10^{-5} [32]. Dla kątów większych od θ_c, promieniowanie rentgenowskie wnika w strukturę materiału, a intensywność promieniowania odbitego maleje wraz ze wzrostem kąta padania. Ponadto, na granicy ośrodków o różnej gęstości, np. międzywierzchni podłoże-warstwa, promieniowanie ulega załamaniu oraz odbiciu. Dochodzi wtedy do interferencji promieniowania odbitego od podłoża z tym bezpośrednio rozproszonym na powierzchni warstwy. Badając zależność intensywności od kąta padania, interferencję obserwuje się w postaci oscylacji intensywności. Analiza uzyskanych wyników eksperymentalnych prowadzona jest przy użyciu oprogramowania pozwalającego określić wyżej wymienione parametry charakteryzujące cienkie warstwy. W niniejszej pracy korzystano z oprogramowania *Reflectivity* (firmy *Malvern Panalytical*), a także programu *Relfex*[33].

3.6 Dyfrakcja rentgenowska pod kątem ślizgowym (GIXRD)

Dyfrakcja rentgenowska pod kątem ślizgowym (ang. *Grazing Incidence X-ray Diffraction*) jest techniką pokrewną konwencjonalnej dyfrakcji wykonywanej w geometrii θ-2θ. Zaletą metody GIXRD jest ograniczenie intensywnego sygnału od podłoża i jednoczesne uzyskanie silniejszego sygnału pochodzącego od cienkiej warstwy[34]. Pomiary wykonywane są pod stałym kątem padania wiązki promieniowania, tzw. kątem ślizgowym. Kąt ślizgowy jest zwykle dobierany tak, aby był nieco wyższy od kąta krytycznego θ_c dla całkowitego zewnętrznego odbicia. Dzięki temu głębokość wnikania promieniowania rentgenowskiego utrzymywana jest na poziomie kilku-, kilkunastu nanometrów. Pozwala to na badanie struktury krystalicznej cienkich warstw w obszarze przypowierzchniowym.

3.7 Skaningowa mikroskopia elektronowa (SEM)

Skaningowa mikroskopia elektronowa (ang. *Scanning Electron Microscopy*) jest narzędziem dostarczającym informacji o topografii powierzchni i składzie próbki[35]. Podobnie jak w każdym mikroskopie, podstawową funkcją skaningowego mikroskopu elektronowego jest powiększanie obiektów niewidocznych dla ludzkiego wzroku. Duże powiększenia (sięgające setek tysięcy razy) oraz wysoką zdolność rozdzielczą (teoretycznie aż 0.0037 nm przy napięciu przyspieszającym 100 kV) umożliwia wykorzystanie wiązki elektronów do obrazowania. Zgodnie z teorią de Broglie'a, elektrony traktujemy jako fale o określonej długości i stosujemy dla niej prawa optyki. Ze względu na mniejszą długość fali de Broglie'a elektronów możliwe jest uzyskanie wyższej zdolności rozdzielczej w porównaniu z mikroskopią optyczną.

Źródłem elektronów w skaningowej mikroskopii elektronowej są katody. Wyróżniamy trzy rodzaje katod: gorące, w których przepływający prąd wywołuje emisję termiczną elektronów oraz zimne, w których przyłożone pole elektryczne powoduje emisję polową elektronów. Trzecim typem katody jest tzw. źródło Schottkiego wykorzystujące zarówno emisję termiczną, jak i polową. Wytworzona w ten sposób pierwotna wiązka elektronów jest następnie w kolejnych częściach mikroskopu kolimowana, skupiana i odchylana podczas skanowania. Pośród parametrów wiązki elektronów należy wymienić: średnicę wiązki na próbce, prąd elektronowy docierający do próbki, kąt konwergencji wiązki i napięcie przyspieszające.

Zasada działania soczewek elektromagnetycznych kształtujących wiązkę opiera się o wykorzystanie siły Lorentza działającej na elektrony. Na elektrony poruszające się w niejednorodnym polu magnetycznym działają dwie składowe indukcji pola magnetycznego. Jedynie dla elektronów poruszających się wzdłuż osi radialnej odchylanie jest zerowe. Tory pozostałych elektronów pod wpływem pola magnetycznego wykazują malejące oscylacje względem osi układu. Soczewki elektromagnetyczne wykazują podobne wady jak te znane z układów optycznych. Wyróżniamy tutaj:

- aberrację chromatyczną – elektrony o różnych energiach są ogniskowane w różnych położeniach; jej przyczyną są niestabilności napięcia przyspieszającego;
- aberrację sferyczną – elektrony bliżej brzegów soczewki są odchylane silniej niż te w pobliżu centrum; przyczyną jest niejednorodny rozkład pola magnetycznego;
- astygmatyzm – soczewka nie ma idealnej symetrii osiowej i w dwóch prostopadłych kierunkach ma różną ogniskową;

Padająca na próbkę pierwotna wiązka elektronów jest rozpraszana na próbce. Wynikiem tego rozpraszania jest katodoluminescencja (promieniowanie światła), promieniowanie rentgenowskie, elektrony Augera, elektrony wstecznie

rozproszone oraz elektrony wtórne. Dwa ostatnie typy elektronów są wykorzystywane do obrazowania w technice SEM. Elektrony wtórne charakteryzują się niską energią, a uzyskiwany w mikroskopii kontrast przy ich obserwacji odzwierciedla topografię powierzchni. Natomiast elektrony wstecznie rozproszone, pozwalają na uzyskanie kontrastu atomowego.

3.8 Mikroskopia sił atomowych (AFM)

Mikroskopia sił atomowych (ang. *Atomic Force Microscopy*) jest techniką pozwalającą na obrazowanie topografii powierzchni z rozdzielczością sięgającą ułamków nanometra[36]. W przeciwieństwie do skaningowej mikroskopii tunelowej, w której wielkością mierzoną jest prąd tunelowania, mikroskop AFM znajduje zastosowanie w pomiarach powierzchni próbek izolatorów i półprzewodników. Wielkością mierzoną jest bowiem siła oddziaływania pomiędzy próbką a końcówką sondy w postaci ostro zakończonej igły. Detekcję sygnału umożliwia wiązka lasera, która docierając do czterosekcyjnej fotodiody, ulega odchyleniu w zależności od położenia sondy. Ze względu na odległość ostrze-próbka wyróżniamy trzy tryby pracy mikroskopu:

- tryb bezkontaktowy – kiedy ostrze znajduje się stosunkowo blisko powierzchni (≈ 1-10 nm) dominują siły przyciągające, w szczególności siła wynikająca z oddziaływań van der Waalsa, jak również siły elektrostatyczne.
- tryb kontaktowy – przy bardzo małych odległościach między ostrzem a próbką występuje silna siła odpychająca związana z przykrywaniem się rozkładów ładunków.
- tryb kontaktu przerywanego – belka, na której umieszczona jest igła wprowadzana w drgania blisko swojej częstotliwości rezonansowej w pobliżu powierzchni próbki. W trybie tym unika się uszkodzeń związanych z tarciem powierzchni. Poza dalekozasięgowymi siłami przyciągającymi znaczenie mają również krótkozasięgowe siły odpychające. Gdy ostrze zbliża się do powierzchni,

interakcja między nim a próbką zmienia częstotliwość rezonansową belki oraz amplitudę drgań. Zmiany w amplitudzie mogą z kolei być następnie wykorzystane jako sygnał zwrotny do regulacji odległości ostrze-próbka. Tryb kontaktu przerywanego umożliwia ponadto uzyskanie obrazu fazowego. Gdy ostrze napotyka obszar o istotnie innym składzie chemicznym, zmiana siły oddziaływania prowadzi także do zmiany fazy rejestrowanego sygnału.

W przypadku pomiaru cienkich warstw obrazowanie AFM pozwala na określenie szorstkości powierzchni, lateralnego rozmiaru ziaren dla warstw polikrystalicznych, czy szerokości tarasów, gdy obrazowane są warstwy epitaksjalne.

3.9 Magnetometria VSM i SQUID

Magnetometr z wibrującą próbką (ang. *Vibrating Sample Magnetometer*) oraz magnetometr SQUID (ang. *Superconducting Quantum Interference Device*) pozwalają badać proces przemagnesowania. W przypadku pomiarów ferromagnetyków obie metody dostarczają informacji o wartości momentu magnetycznego, polu koercji, namagnesowaniu remanencji czy polu anizotropii magnetokrystalicznej (gdy pole magnetyczne przyłożone jest w płaszczyźnie warstwy w tzw. trudnym kierunku magnesowania badanego monokryształu).

Zasada działania magnetometru VSM opiera się na prawie Faradaya[37,38]. Drgająca w jednorodnym polu magnetycznym próbka wytwarza zmienny w czasie strumień magnetyczny, który indukuje siłę elektromotoryczną w cewkach odbiorczych. Wartość indukowanej siły elektromotorycznej ϵ jest proporcjonalna do momentu magnetycznego $\vec{m}$ zgodnie z zależnością:

$$\epsilon = \mu_0 \delta\omega \, \vec{m} \cdot \vec{g} \cos(\omega t) \tag{3.9.1}$$

gdzie μ_0 oznacza przenikalność magnetyczną próżni, δ amplitudę drgań, ω częstość drgań, $\vec{g}$ wektorowy czynnik geometryczny charakteryzujący zależność

indukowanego sygnału od geometrii cewek odbiorczych, t oznacza czas. Częstotliwość drgań wynosi zazwyczaj kilka-, kilkadziesiąt herców, a amplituda drgań jest rzędu kilku-, kilkunastu milimetrów. Przekłada się to na czułość magnetometru pozwalającą na detekcję momentów rzędu 10^{-8}-10^{-9} A·m^2. Aby wyznaczyć moment badanej próbki wykorzystuje się próbkę wzorcową o znanym momencie magnetycznym oraz zbliżonym kształcie. W celu oszacowania namagnesowania nasycenia wymagana jest dodatkowo informacja o objętości ferromagnetyka, która stanowi znaczny przyczynek do niepewności pomiarowej.

Istotnie wyższą czułość pomiarową uzyskuje się w magnetometrze SQUID[39,40]. Magnetometr ten złożony jest z trzech zasadniczych elementów: cewki detekcyjnej nawiniętej w konfiguracji gradiometru drugiego rzędu, urządzenia SQUID oraz magnesu nadprzewodzącego będącego źródłem pola magnetycznego. Podobnie jak w magnetometrii VSM, poruszająca się wewnątrz cewek detekcyjnych próbka jest źródłem strumienia indukcji magnetycznej wytwarzającego prąd. Budowa cewek detekcyjnych jest jednak odmienna w porównaniu do VSM. Składają się na nie dwie cewki boczne oraz cewka środkowa, która ma dwa razy więcej zwojów i jest nawinięta w kierunku przeciwnym aniżeli cewki boczne. W tym przypadku, generowana siła elektromotoryczna równa jest drugiej pochodnej przestrzennej strumienia indukcji w funkcji czasu. Wartość siły elektromotorycznej zależy zatem od położenia próbki. Otrzymany sygnał przekazywany jest dalej do urządzenia SQUID, dzięki któremu magnetometr zawdzięcza wysoką czułość. Urządzenie SQUID umieszczone jest w specjalnej osłonie izolującej od pól magnetycznych i składa się z pary złączy Josephsona umieszczonych w nadprzewodzącej pętli. Następuje w nim konwersja strumienia pola magnetycznego (wyindukowanego przez zmienny prąd z cewek detekcyjnych) na napięcie. Otrzymana w wyniku pomiarów zależność położenie próbki – napięcie wykorzystywana jest do wyznaczenia momentu magnetycznego badanego materiału.

3.10 Szerokopasmowy rezonans ferromagnetyczny (VNA-FMR)

Spektroskopia szerokopasmowego rezonansu ferromagnetycznego pozwala badać dynamiczne własności magnetyczne cienkich warstw. Jak przedstawiono w rozdziale drugim, umożliwia ona wyznaczenie szeregu parametrów, np. namagnesowania efektywnego, pola anizotropii magnetokrystalicznej, współczynnika żyromagnetycznego czy współczynnika tłumienia Gilberta.

Głównym komponentem układu pomiarowego jest wektorowy analizator obwodów (ang. *Vector Network Analyzer*). Pełni on jednocześnie rolę źródła i detektora prądu mikrofalowego w szerokim zakresie częstotliwości od 10 MHz do 40 GHz z rozdzielczością 1 Hz. Rejestrowane wielkości wyraża w postaci tzw. parametrów S macierzy rozproszenia. W przypadku analizatora od dwóch portach jest to macierz 2x2. Elementy S_{11} oraz S_{22}, nazywane również parametrami odbicia, określają stosunek sygnału powracającego do sygnału wychodzącego odpowiednio dla portu 1 oraz 2. Natomiast elementy S_{12} oraz S_{21} wyrażają transmisję sygnału mikrofalowego pomiędzy portami. Ze względu na symetrię typowego układu eksperymentalnego, parametr S_{11} równy jest S_{22}, jak i S_{12} równy jest S_{21}. Elementy macierzy rozproszenia są wielkościami zespolonymi, a zatem wyrażają amplitudę oraz fazę prądu mikrofalowego.

W warunkach rezonansu dochodzi do absorpcji części promieniowania mikrofalowego przez warstwę ferromagnetyczną, co prowadzi do obniżonej transmisji sygnału mikrofalowego. W szerokopasmowych pomiarach rezonansu badaną próbkę umieszcza się na falowodzie koplanarnym, który podłączony do portów VNA przy pomocy kabli koncentrycznych pełni rolę czujnika. Falowód koplanarny składa się z centralnej linii sygnałowej oraz dwóch półpłaszczyzn uziemiających umieszczonych na dielektrycznym laminacie. Dodatkowo posiada płaszczyznę uziemiającą pod laminatem, jak i metalizowane otwory wzdłuż linii sygnałowej w celu ograniczenia strat przypadających na jednostkę długości linii

sygnałowej. Rozmiary geometryczne falowodu koplanarnego, tj. szerokość linii sygnałowej (około 500 μm), odległość pomiędzy linią sygnałową a półpłaszczyznami uziemiającymi i grubość metalizacji, są w ścisły sposób dobrane tak, by impedancja falowodu była bliska 50 Ω. Ma to na celu zredukowanie odbić sygnału na połączeniach z kablami koncentrycznymi.

Przepływający przez falowód koplanarny prąd mikrofalowy indukuje zmienne pole magnetyczne wokół linii sygnałowej zgodnie z prawem Biota-Savarta. Falowód koplanarny wraz z próbką umieszczony jest pomiędzy nabiegunnikami elektromagnesu w taki sposób, aby składowa zmiennego pola magnetycznego wzbudzającego precesję namagnesowania była ortogonalna do kierunku zewnętrznego pola magnetycznego. Przedstawione w niniejszej pracy pomiary rezonansu prowadzone były przede wszystkim w trybie przemiatania polem, tzn. przy stałej częstotliwości prądu mikrofalowego zmianie ulegało natężenie zewnętrznego pola magnetycznego.

3.11 Spektroskopia fal spinowych z wykorzystaniem wektorowego analizatora obwodów

Do wzbudzenia i detekcji koherentnych fal spinowych wykorzystuje się pary falowodów koplanarnych lub anten mikrofalowych w postaci pojedynczej linii sygnałowej. Układy te są zintegrowane z próbką i wykonuje się je przy pomocy technik litografii oraz osadzania warstw. Podłączenie do wektorowego analizatora obwodów odbywa się przy pomocy sond mikrofalowych. Takie rozwiązanie pozwala badać szereg układów mikrofalowych wytworzonych w ramach jednej próbki. Szerokość linii sygnałowej jest znacząco mniejsza w porównaniu do falowodów używanych w pomiarach rezonansu ferromagnetycznego. Wynika to z faktu, że zakres liczb falowych możliwych do wzbudzenia jest odwrotnie proporcjonalny do szerokości linii sygnałowej. Wynosi ona

zazwyczaj kilka-, kilkanaście mikrometrów i pozwala badać fale spinowe o liczbach falowych sięgających nawet 10 rad/μm.

Szczegółowe widmo wzbudzeń wykorzystywanych układów mikrofalowych obliczamy wykonując transformatę Fouriera rozkładu pola magnetycznego indukowanego przez prąd mikrofalowy. Rozkład pola magnetycznego można otrzymać na różne sposoby. Jednym z nich są symulacje w module *RF Module* pakietu *COMSOL Multiphysics*. Oprogramowanie to pozwala na rozwiązywanie równań Maxwella metodą elementów skończonych. Definiowane konfiguracje przestrzenne uwzględniają właściwości materiałowe, położenie źródeł wzbudzających prąd mikrofalowy, a także warunki brzegowe. Implementacja modelowanej geometrii jest w znacznej mierze zautomatyzowana. W tym programie rozkład pola magnetycznego jest bezpośrednio otrzymywany z symulacji.

Pomiary spektroskopowe propagacji fal spinowych z wykorzystaniem wektorowego analizatora obwodów prowadzone są zwykle w trybie przemiatania częstotliwością. Podczas pomiaru rejestrowany jest parametr S_{21} lub S_{12} macierzy rozpraszania w funkcji częstotliwości, podczas gdy natężenie zewnętrznego pola magnetycznego utrzymywane jest na stałym poziomie. Procedura jest powtarzana dla szeregu wartości pola magnetycznego. Aby poprawić stosunek sygnału do szumu, wykonuje się pomiar referencyjny w polu magnetycznym o dostatecznie dużym natężeniu. Sygnał referencyjny jest następnie odejmowany od sygnału transmisji zmierzonego dla poszczególnych wartości pola magnetycznego.

3.12 Symulacje mikromagnetyczne w oprogramowaniu *Mumax3*

Obliczenia mikromagnetyczne w *MuMax3* pozwalają na teoretyczne badanie dynamiki namagnesowania z przestrzenną i czasową rozdzielczością[41]. Program umożliwia symulacje układów o rozmiarach nano- i mikrometrowych wykorzystując metodę różnic skończonych do rozwiązywania równania Landau-Lifshitza-Gilberta. W podejściu mikromagnetycznym przyjmuje się, że namagnesowanie reprezentuje wartość uśrednioną z pewnej objętości elementarnej, w której uporządkowanie momentów magnetycznych jest jednorodne i kolinearne[42]. Pomija się zatem szczegóły struktury atomowej materiałów. Badana geometria dzielona jest na układ komórek prostopadłościennych. Dla każdej komórki można określić parametry magnetyczne takie jak namagnesowanie nasycenia czy stałe anizotropii. Sprzężenie wymienne jest natomiast definiowane na granicy między dwiema komórkami. Rozmiar komórek nie powinien zatem przekraczać długości wymiany Néela $L_{\mathrm{ex}} = \sqrt{2A_{\mathrm{ex}}/(\mu_0 M_s^2)}$, dla której oddziaływania wymienne dominują nad oddziaływaniami dipolowymi. Dla granatu itrowo-żelazowego L_{ex} wynosi około 17 nm. W ramach symulacji przedstawionych w tej pracy rozmiar komórek wynosił 10 nm × 10 nm × d, gdzie d jest grubością badanej warstwy.

Wzbudzenie dynamiki namagnesowania w programie *MuMax3* odbywa się poprzez wprowadzenie zmiennego w czasie pola magnetycznego, które jest ortogonalne do kierunku zewnętrznego pola magnetycznego. Zmienne pole może być zadane dowolną funkcją czasu oraz zdefiniowane w wybranych komórkach lub w całej modelowanej strukturze. Pozwala to symulować wzbudzenia zależne od czasu i przestrzeni. Dla każdej komórki trzy składowe namagnesowania $(m_x(t),\ m_y(t),\ m_z(t))$ są rozwiązywane numerycznie i ich wartości są zapisywane w plikach wyjściowych.

3.13 Obliczenia i analiza danych w oprogramowaniu *Mathematica*

Oprogramowanie Mathematica to wszechstronne środowisko realizacji obliczeń symbolicznych i numerycznych cechujące się wysoką wydajnością oraz szerokimi możliwościami wizualizacji. W ramach prowadzonych badań stanowiło ono niezwykle ważne narzędzie do analizy wyników eksperymentalnych (w tym np. XRD, VNA-FMR, VSM), wyników symulacji mikromagnetycznych, rachunków teoretycznych oraz prezentacji uzyskanych rezultatów zarówno w postaci wykresów, jak i wideo. Wraz z upowszechnieniem procesorów wielordzeniowych obliczenia równoległe pozwoliły na przetwarzanie danych o znacznej objętości. W przypadku symulacji mikromagnetycznych objętości te sięgały nawet kilku gigabajtów. Liczne pomiary rezonansu ferromagnetycznego wymagały również opracowania autorskiego kodu umożliwiającego analizę linii rezonansowych w sposób w znacznej mierze zautomatyzowany. Przygotowane programy pozwalały na analizę wyników VNA-FMR uzyskanych zarówno w trybie przemiatania polem, jak i częstotliwością z możliwością symultanicznego dopasowania do części rzeczywistej i urojonej rejestrowanego sygnału, korekty fazy sygnału oraz późniejsze dopasowania wyznaczonych wielkości do równań Kittla czy zależności szerokości linii rezonansowych.

4 Wyniki badań

4.1 *Characterization of Spin Wave Propagation in (111) YIG Thin Films with Large Anisotropy*

Publikacja przedstawia wyniki badań propagacji powierzchniowych fal spinowych przy użyciu wektorowego analizatora obwodów. Szczegółowej analizie poddane jest eksperymentalne określenie liczb falowych wzbudzanych przez falowód koplanarny i porównanie wyznaczonych wartości z przewidywaniami teoretycznymi. W zaproponowanej geometrii doświadczalnej zaobserwowano propagację fal spinowych na odległość 150 μm w warstwie granatu itrowo-żelazowego o grubości 82 nm. Uzyskane rezultaty pozwoliły wskazać na konieczność uwzględnienia pól anizotropii w zależności dyspersyjnej (w szczególności indukowanej wzrostem anizotropii prostopadłej) w celu poprawnej interpretacji wyników eksperymentalnych.

Indywidualny wkład autora w powstanie tej publikacji obejmuje: napisanie pierwszej wersji manuskryptu, analizę danych eksperymentalnych i teoretycznych, analizę literaturową, naniesienie warstw metodą PLD, wykonanie pomiarów VNA-FMR, VSM, pomiarów kątowych rezonansu ferromagnetycznego, spektroskopii fal spinowych z wykorzystaniem VNA, oraz części symulacji w programie *Comsol Multiphysics* (rys. 7), wizualizację uzyskanych rezultatów i przygotowanie odpowiedzi na pytania recenzentów.

IOP Publishing Journal of Physics D: Applied Physics

J. Phys. D: Appl. Phys. **50** (2017) 235004 (7pp) https://doi.org/10.1088/1361-6463/aa6df0

Characterization of spin wave propagation in (1 1 1) YIG thin films with large anisotropy

A Krysztofik[1], H Głowiński[1], P Kuświk[1,2], S Ziętek[3], L E Coy[4], J N Rychły[5], S Jurga[4], T W Stobiecki[3,6] and J Dubowik[1]

[1] Institute of Molecular Physics, Polish Academy of Sciences, M. Smoluchowskiego 17, PL-60-179 Poznań, Poland
[2] Centre for Advanced Technology, Adam Mickiewicz University, Umultowska 89c, PL-61-614 Poznań, Poland
[3] Department of Electronics, AGH University of Science and Technology, Al. Mickiewicza 30, PL-30-059 Kraków, Poland
[4] NanoBioMedical Centre, Adam Mickiewicz University, Umultowska 85, PL-61-614 Poznań, Poland
[5] Faculty of Physics, Adam Mickiewicz University, Umultowska 85, PL-61-614 Poznań, Poland
[6] Faculty of Physics and Applied Computer Science, AGH University of Science and Technology, Al. Mickiewicza 30, PL-30-059 Kraków, Poland

E-mail: hubert.glowinski@ifmpan.poznan.pl and adam.krysztofik@ifmpan.poznan.pl

Received 6 February 2017, revised 27 March 2017
Accepted for publication 19 April 2017
Published 22 May 2017

Abstract

We report on long-range spin wave (SW) propagation in nanometer-thick yttrium iron garnet (YIG) film with an ultralow Gilbert damping. The knowledge of a wavenumber value $\left|\vec{k}\right|$ is essential for designing SW devices. Although determining the wavenumber $\left|\vec{k}\right|$ in experiments like Brillouin light scattering spectroscopy is straightforward, quantifying the wavenumber in all-electrical experiments has not been widely commented upon so far. We analyze magnetostatic spin wave (SW) propagation in YIG films in order to determine the SW wavenumber $\left|\vec{k}\right|$ excited by the coplanar waveguide. We show that it is crucial to consider the influence of magnetic anisotropy fields present in YIG thin films for precise determination of SW wavenumber. With the proposed methods we find that experimentally derived values of $\left|\vec{k}\right|$ are in perfect agreement with that obtained from electromagnetic simulation only if anisotropy fields are included.

Keywords: spin waves, ferromagnetic resonance, low damping materials

(Some figures may appear in colour only in the online journal)

1. Introduction

Spin wave (SW) propagation in magnetic thin film structures has become an intensively investigated topic in recent years, due to promising applications in modern electronics [1–4]. The wavenumber (or equivalently—the wavelength $\lambda = 2\pi/\left|\vec{k}\right|$) is an important parameter to account for propagation characteristics. For example, it is essential to choose a SW wavenumber and correlate it to a certain device dimension in order to ensure observation of the expected phenomena in SW devices e.g. in magnonic crystals [5, 6] or devices based on wave interference, such as SW transistors [2], SW logic gates [2] and Mach–Zehnder type interferometers [7]. The knowledge of the SW wavenumber is also very important in the assessment of the effective magnitude of the Dzyaloshinskii–Moriya interaction using collective spin-wave dynamics [8].

In propagating SW spectroscopy experiments, two shorted coplanar waveguides (CPWs) are commonly used as a transmitter and a receiver [9]. Each CPW, integrated within the film, consists of a signal line and two ground lines connected at one end. When an rf-current flows through the transmitter, it induces an oscillating magnetic field around the lines that exerts a torque and causes spin precession in the magnetic material beneath. The inverse effect is then used for SW detection by the receiver. Since the generated magnetic field is not homogenous with reference to the film plane and solely

depends on CPW geometry, it determines the distribution of the SW wavenumber that can be excited.

It is assumed that the transmitter excites a broad spectrum of SW wavevectors of wavenumber k extending to $k_{max} \approx \pi/W$ (W is a width of CPW line) with a maximum of excitation amplitude approximately around $k_{maxAmp} \approx \pi/2W$ [10]. The question now is: what is the actual wavenumber of the SW with the largest amplitude detected by the receiver situated at a certain distance from the transmitter. While in Brillouin light scattering spectroscopy k is easily accessible, in all electrical spin wave spectroscopic experiments the determination of the SW wavenumber is rather challenging [11].

We aim to answer this question by analyzing our experimental results of SW propagation in yttrium iron garnet ($Y_3Fe_5O_{12}$, YIG) thin films. YIG films are known for possessing the lowest Gilbert damping parameter, enabling the SW transmission over distances of several hundred micrometers [2, 12]. However, YIG films synthesized by pulsed laser deposition (PLD) exhibit substantially disparate values of anisotropy fields and saturation magnetization, depending on the growth process parameters and, consequently, the stoichiometry of the obtained film [13–15]. It has already been theoretically predicted that anisotropy may significantly affect SW propagation and the transmission characteristics [16, 17]. Therefore, for such YIG films, SW spectra analysis requires careful consideration of the anisotropic properties of a given film.

Here, we compare two methods of experimental determination of the SW wavenumber which include anisotropy fields. The experimental results are then compared with the electromagnetic simulations.

2. Results and discussion

YIG film was grown on a monocrystalline, 1 1 1-oriented gadolinium gallium garnet substrate ($Gd_3Ga_5O_{12}$, GGG) by means of the PLD technique. The substrate temperature was set to 650 °C and under the 1.2×10^{-4} mbar oxygen pressure (8×10^{-8} mbar base pressure) the thin film was deposited at the 0.8 nm min^{-1} growth rate using the third harmonic of a Nd:YAG laser ($\lambda = 355$ nm). After the growth, the sample was additionally annealed *ex situ* at 800 °C for 5 min. X-ray diffraction and reflection measurements showed that the YIG film was single-phase epitaxial with the GGG substrate with the thickness of 82 nm and RMS roughness of 0.8 nm. The XRD θ–2θ scan, presented in figure 1, clearly shows the high crystallinity of the YIG film, displaying well defined Laue oscillations, typical for highly epitaxial films, which clearly points to the high quality and well textured YIG (1 1 1) film [18]. Subsequently, a system of two CPWs made of 100 nm thick aluminum was integrated onto the YIG film (figure 2) using a maskless photolithography technique. The width W of the signal and ground lines was equal to 9.8 μm and the gaps between them were 4 μm wide. The distance between the centers of the signal lines was 150 μm.

To investigate SW propagation, we followed the approach presented in [9] and [12]. Using a vector network analyzer, the transmission signal S_{21} was measured for Damon-Eshbach surface modes with wavevector $\vec{k}$ perpendicular to the magnetization for magnetic fields ranging from −310 Oe to +310 Oe (figure 3(a)). Exemplary S_{21} signals (imaginary part), which are shown in figures 3(b) and (c), reveal a series of oscillations as a function of frequency with a Gaussian-like envelope corresponding to the excited SW wavenumber distribution. Figure 3(c) shows that the frequency separation Δf between the two oscillation maxima differs noticeably in value depending on the magnetic field. The decrease in signal amplitude is also observed since SW decay length is inversely proportional to the frequency, so that the low-frequency SWs propagate further away [12, 19].

For the frequencies of the highest signal amplitude, the wavenumber k_{maxAmp} can be determined according to the

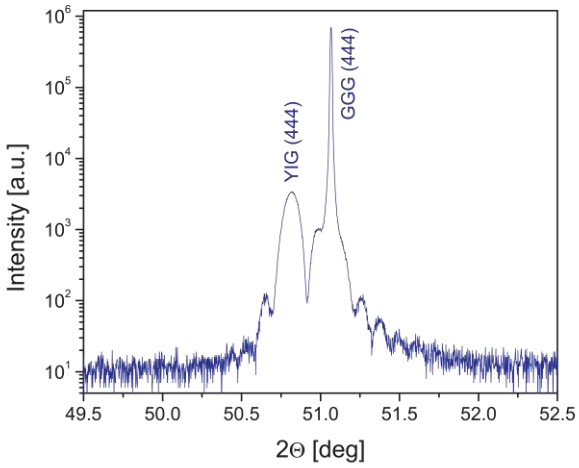

Figure 1. A θ–2θ XRD scan of epitaxial YIG film on GGG (1 1 1) substrate near the GGG (4 4 4) reflection.

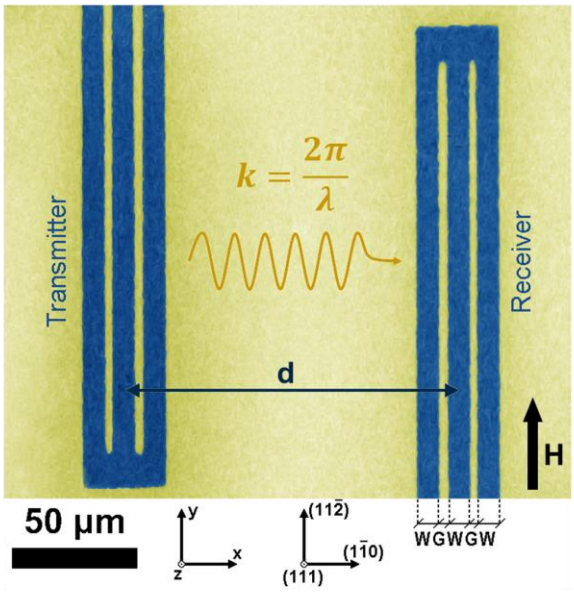

Figure 2. SEM image of the integrated CPWs on the YIG film. The distance d between the transmitter and the receiver is equal to 150 μm. The depicted Cartesian and crystallographic coordinate system is used throughout this paper. The widths of the signal and ground lines are marked with W. G denoting the gap width between the lines.

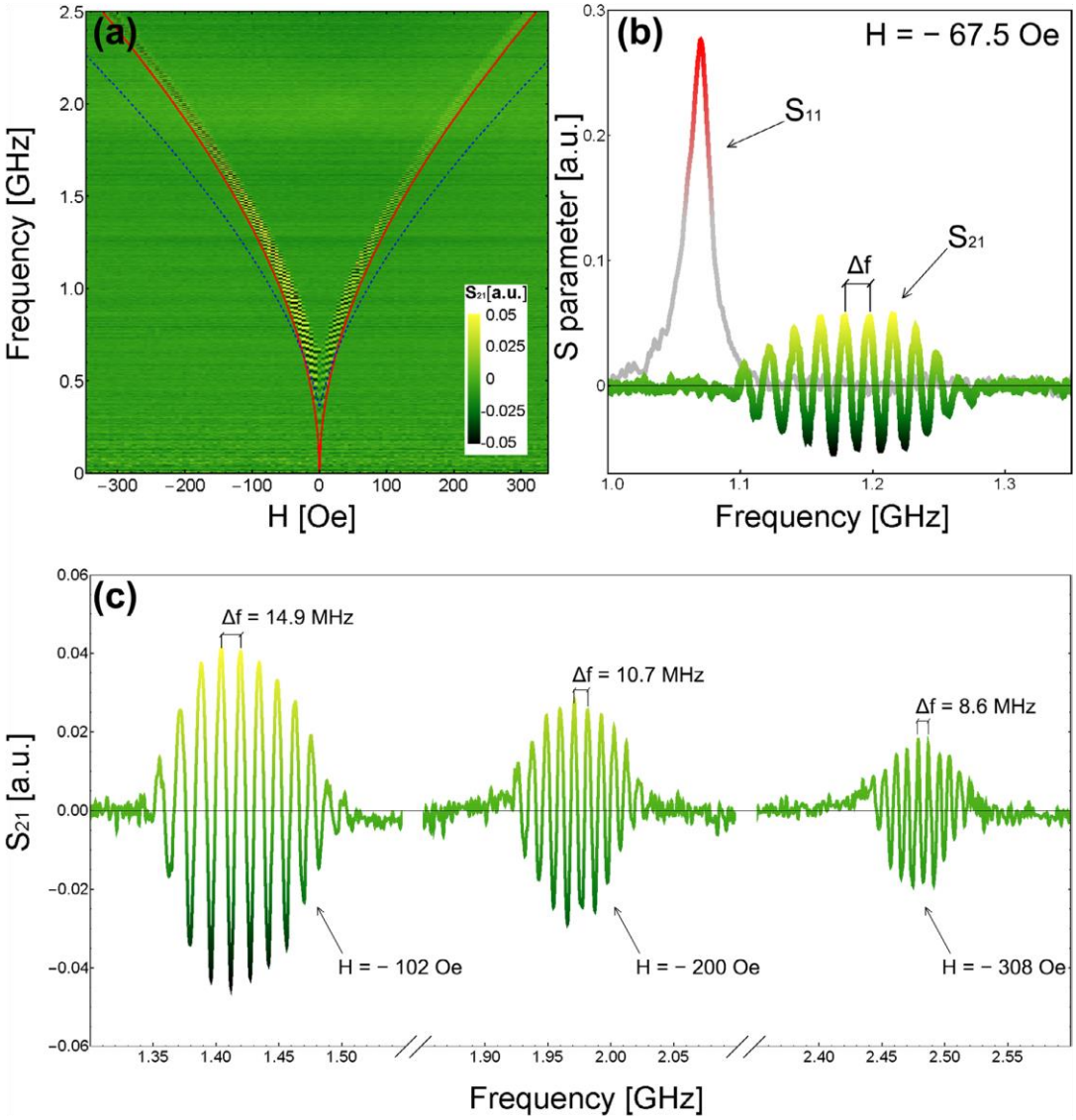

Figure 3. (a) Color-coded SW propagation data S_{21} measured at different magnetic fields. With a red line, the $f(H)$ dependence of the uniform excitation ($k = 0$) is depicted. The red line corresponds to the maximum in the S_{11} signal in (b). The blue dashed line represents a dispersion relation with $H_a = H_u = 0$. (b) Reflection (S_{11}, $k = 0$) and transmission (S_{21}, $k \neq 0$) signals. The plot illustrates a magnified cross-section of (a) at $H = -67.5$ Oe. (c) SW spectra measured at different magnetic fields. Color-coding in (b) and (c) corresponds to the one defined in (a).

dispersion relation derived for the (1 1 1) crystalline orientation of the YIG film [16, 17]:

$$f = \frac{\mu_B}{2\pi\hbar} g \sqrt{(H + 2\pi M_s tk)\left(H - \frac{1}{2}H_a - H_u + 4\pi M_s - 2\pi M_s tk\right), - \frac{1}{2}(H_a \sin(3\phi))^2} \quad (1)$$

where f is the microwave frequency, μ_B—the Bohr magneton constant, $\hbar$—the reduced Planck constant, g—the spectroscopic splitting factor, H—the external magnetic field, M_s—the saturation magnetization, t—the film thickness, k—the wavenumber, H_a—the cubic anisotropy field and H_u—the out-of-plane uniaxial anisotropy field. $H_a = \frac{2K_a}{M_s}$ and $H_u = \frac{2K_u}{M_s}$, where K_a and K_u are anisotropy constants. It should be highlighted that when $H_a = H_u = 0$, equation (1) becomes equivalent to the one originally obtained by Damon and Eshbach [20]. The azimuthal angle ϕ defines the in-plane orientation of the magnetization direction with respect to the (1 1 $\bar{2}$) axis of the YIG film. In our study, the term $-\frac{1}{2}(H_a \sin(3\phi))^2$ in equation (1) vanishes since the magnetic field H is parallel to the (1 1 $\bar{2}$) axis and $\phi = 0\,°$.

As can be seen from equation (1), in order to determine wavenumber k one needs to evaluate many material constants,

namely g, M_s, t, H_a, H_u in the first instance. This problem can be partially solved with a broadband ferromagnetic resonance measurement of the film. For $k = 0$ equation (1) simplifies to the formula, which allows for the determination of the spectroscopic factor g and the effective magnetization $4\pi M^*_{\text{eff}} = -\frac{1}{2}H_a - H_u + 4\pi M_s$:

$$f_{k=0} = \frac{\mu_B}{2\pi\hbar} g \sqrt{H(H + 4\pi M^*_{\text{eff}})}. \quad (2)$$

Therefore, within this approach, the film thickness and the saturation magnetization should be determined using other experimental methods.

To investigate the ferromagnetic resonance of the YIG film, the reflection signal S_{11} was measured. In order to avoid an extrinsic contribution to the resonance linewidth caused by non-monochromatic excitation of the CPW ($2\pi\Delta f_{\text{extr}} = v_g \Delta k$) [21] and, consequently, possible ambiguities in the interpretation of resonance peak position, it is recommended to perform this measurement with the use of a wide CPW. Note that the full width at half maximum of a CPW excitation spectra $\Delta k \approx k_{\text{maxAmp}}$ [21]. In our study we used a CPW with signal and ground lines of the width equal to 450 μm and with the 20 μm wide gaps between them. For such a CPW, the simulated value of k_{maxAmp} is equal to 49 cm^{-1} and, therefore, yields negligible broadening that is of the order of a few MHz.

The measured S_{11} signal (imaginary part) is depicted in figure 3(a) with the red line. It appears to lie just below the S_{21} signal. Fitting to the experimental data with equation (2) gave following value of the spectroscopic factor $g = 2.010 \pm 0.001$ and the effective magnetization $M^*_{\text{eff}} = 169 \pm 7$ emu cm^{-3}. A comparison of $4\pi M^*_{\text{eff}}$ with $4\pi M_s$ ($M_s = 120 \pm 19$ emu cm^{-3} was measured using vibrating sample magnetometry) gives $-\frac{1}{2}H_a - H_u$ of 616 Oe, showing the substantial difference between the obtained values of M^*_{eff} and M_s. The determined value of $-\frac{1}{2}H_a - H_u$ remains in the midst of the range reported for PLD-grown YIG thin films, from 229 Oe up to 999 Oe [14, 22]. It is worth mentioning that for fully stoichiometric, micrometer-thick YIG films made by means of liquid phase epitaxy (LPE) technique $-\frac{1}{2}H_a - H_u = 101$ Oe [14].

Substitution of the g, M^*_{eff}, M_s and t values into equation (1) enabled the determination of wavenumber $k_{\text{maxAmp}} = 1980 \pm 102$ cm^{-1}. It should be noted that if anisotropy fields were neglected in the equation (1) ($H_a = H_u = 0$), yet only saturation magnetization was taken into account, a fitting to the experimental data would not converge. The calculated dispersion relation with the derived value of k_{maxAmp}, assuming $H_a = H_u = 0$ is depicted with a blue dashed line in figure 3(a). Omission of anisotropy fields in magnetization dynamic measurements may therefore lead to the significant misinterpretation of the experimental results for the YIG thin films.

Typical values of the cubic magnetocrystalline anisotropy field H_a range from -18 Oe to -64 Oe for PLD grown YIG films [14, 15, 22], which indicates that resonance measurements, as well as spin wave propagation, are governed by

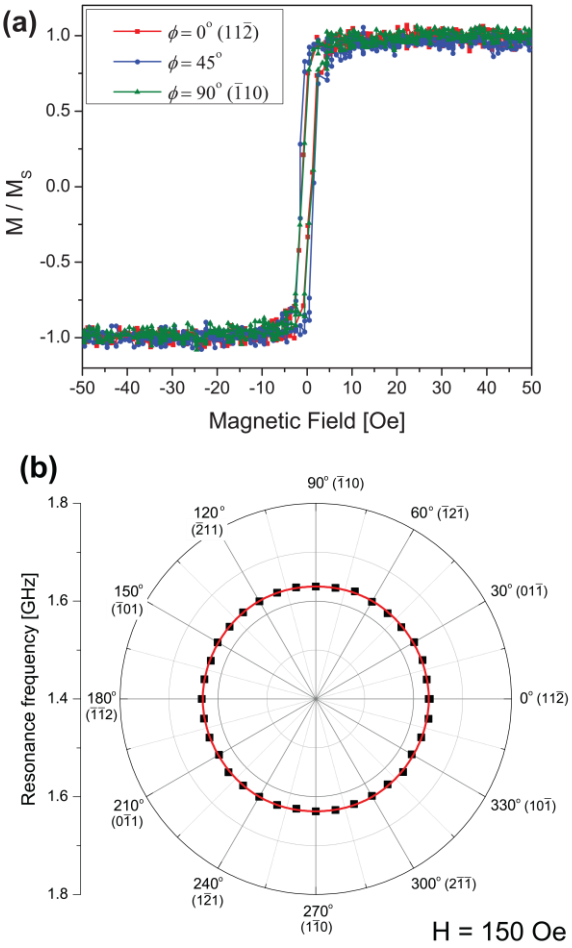

Figure 4. (a) VSM hysteresis loops measured in the film plane for three different crystallographic directions. The magnetization is normalized to the saturation magnetization $M_s = 120 \pm 19$ emu cm^{-3}. A paramagnetic contribution of the GGG substrate was subtracted for each loop. (b) Resonance frequency as a function of azimuthal angle ϕ taken at $H = 150$ Oe. The red line depicts the calculated values of resonance frequency according to equation (1) for $k = 0$, $H_a = -30$ Oe and $H_u = -600$ Oe.

the out-of-plane uniaxial anisotropy. For the film employed in our study, the H_u value is of about -600 Oe, in agreement with previous reports [14, 15, 22]. For any more complex architecture of magnonic waveguides and circuits, it is likewise imperative to investigate the in-plane anisotropy properties [24]. As can be seen from equation (1), one would expect a six fold anisotropy in the plane of (1 1 1)-oriented single crystals, which is common among rare-earth substituted YIG garnets and LPE-YIG films [18, 25–27]. To examine this issue, we performed VSM and angular resolved ferromagnetic resonance measurements. Hysteresis loops for all measured in-plane directions exhibit no substantial differences regarding the coercive field (≈ 1.2 Oe), saturation field and saturation magnetization (figure 4(a)). The angular resolved resonance measurements confirm this result and show that the (1 1 1) YIG film is isotropic in the film plane (figure 4(b)). The main reason for this behavior is the low

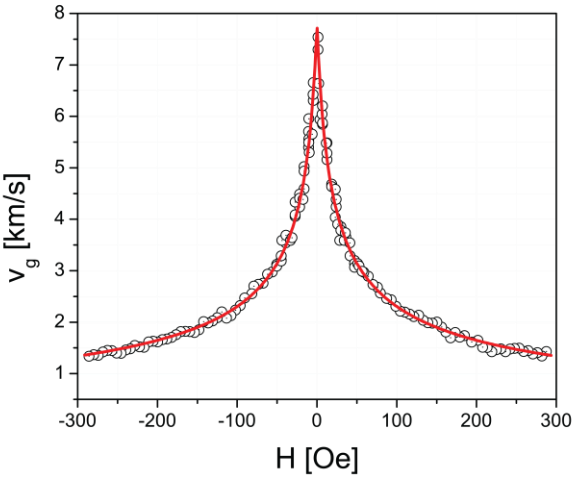

Figure 5. Spin wave group velocity as a function of the external magnetic field. The red line represents a fit according to equation (4).

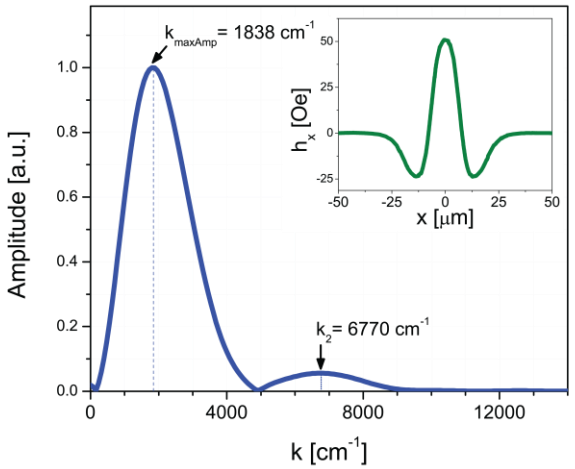

Figure 6. Excitation spectrum of the CPW with 9.8 μm wide signal lines and 4 μm gaps. The inset shows in-plane component of the dynamic magnetic field excited by the CPW.

value of cubic anisotropy field, which causes the resonance frequency modulation by a value of the fraction of MHz. Such small differences do not surpass the experimental error, nor would they significantly affect the coherent SW propagation. It is expected that the SW propagation characteristics, measured for any other crystallographic orientation, would therefore remain unaltered.

Another method of extracting the SW wavenumber involves the analysis of the SW group velocity v_g. Following [21], v_g can be determined from the frequency difference Δf between two oscillation maxima in a S_{21} signal according to the relation:

$$v_g = d\Delta f, \tag{3}$$

where d is the distance between two CPWs. To determine Δf we chose two neighboring oscillation maxima of the highest S_{21} signal amplitude, as shown in figures 3(b) and (c).

In figure 5 the derived values of group velocity are shown as a function of the magnetic field. It is found that v_g reaches the value of 7.6 km s^{-1} for the field of 1.3 Oe (preferable in magnonic information processing devices of high efficiency) and 1.4 km s^{-1} for the field of 285 Oe. It should be highlighted that such big differences in v_g values can be further utilized to design tunable, impulse-response delay lines, as v_g changes up to five times with the magnetic field. At a distance of 150 μm between CPWs, it would allow us to achieve 20–110 ns delay times of an impulse.

With the red line in figure 5 a fitting is depicted according to:

$$v_g = 2\pi\frac{\partial f}{\partial k} = \frac{\mu_B}{\hbar}g\frac{2\pi M_s t\left(-\frac{1}{2}H_a - H_u + 4\pi M_s - 4\pi M_s tk\right)}{2\sqrt{(H + 2\pi M_s tk)\left(H - \frac{1}{2}H_a - H_u + 4\pi M_s - 2\pi M_s tk\right)}}. \tag{4}$$

The main advantage of extracting the SW wavenumber from $v_g(H)$ dependence is that it does not require additional measurement of M_s, which is often notably influenced by an error in the estimated film volume. Since the saturation magnetization M_s can be treated as a fitting parameter in equation (4), the derivation of the SW wavenumber involves only S_{11}, S_{21} and thickness measurements. The determined values of $k_{maxAmp} = 1690 \pm 53$ cm^{-1} and $M_s = 116 \pm 2$ emu cm^{-3} remain in a good agreement with that obtained above—($k_{maxAmp} = 1980 \pm 102$ cm^{-1}, $M_s = 120 \pm 19$ emu cm^{-3}).

As can be seen from figure 5, SW group velocity attains the maximum value as the magnetic field approaches $H = 0$. The maximum value of v_g is given by:

$$v_g^{(H=0)} \cong \frac{\mu_B}{\hbar}g\sqrt{\frac{\pi M_s t}{2k}\left(-\frac{1}{2}H_a - H_u + 4\pi M_s[1 - tk]\right)}. \tag{5}$$

The zero-field region may therefore become the subject of interest for magnonic applications. Moreover, equation (5) shows that the maximum value of v_g depends on the anisotropy fields. PLD-grown YIG films possessing a high anisotropy would allow for faster information processing in SW circuits than LPE films for which the value of $-\frac{1}{2}H_a - H_u$ is smaller (as was pointed out above).

To confront our experimental results with the expected, theoretical value of k_{maxAmp}, we performed electromagnetic simulations in *Comsol Multiphysics*. Here, CPW was modeled according to the geometry of the performed CPW (figure 2), assuming lossless conductor metallization, relative permittivity of the substrate $\varepsilon_r = 12$ and 50 Ω port impedance. From the simulated in-plane distribution of the dynamic magnetic field h_x (inset of figure 6), an excitation spectra of CPW was obtained using a discrete Fourier transformation of $h_x(x)$. The highest excitation strength is observed for $k_{maxAmp} = 1838$ cm^{-1}, which corresponds well to the experimentally obtained values within 7% accuracy. The second observed maxima is at $k_2 = 6770$ cm^{-1}. However, as its

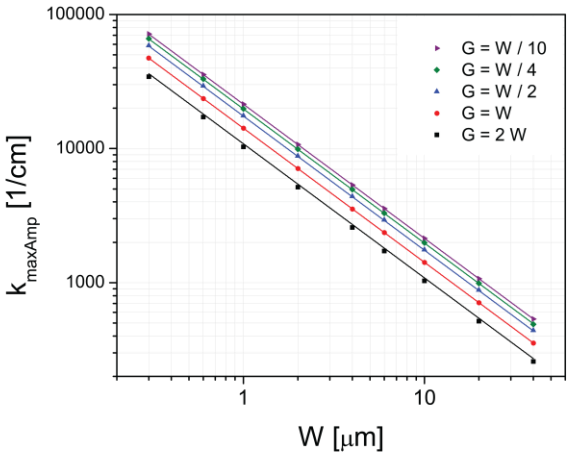

Figure 7. Wavenumber of the highest amplitude as a function of the CPW signal line width. The solid lines represent a fit according to equation (6).

amplitude is 20 times lower with respect to the amplitude of k_{maxAmp}, it is not observed in the measured S_{21} signal.

To extend our study, we performed a series of further simulations for the CPW dimensions, which are achievable with electron- and photolithography. We assumed equal widths of signal and ground lines (W), as well as equal widths of gaps between them (G). The results are presented in figure 7. It is found that for the widths W ranging from 300 nm to 40 μm, the wavenumber k_{maxAmp} vary between 70 000 cm^{-1} and 250 cm^{-1}, respectively, revealing the CPW wavenumber probing limits. We also note that the gap width significantly affects k_{maxAmp}. In order to accurately extrapolate its contribution to k_{maxAmp}, we developed empirical formula which incorporates width G:

$$k_{\mathrm{maxAmp}} = \frac{2.27}{W + 0.6\,G}. \qquad (6)$$

The fittings, according to the equation (6), are depicted in figure 7 with solid lines. We found that equation (6) is valid for gap width $0.1\,W < G < 2\,W$. For $G = 0.74\,W$ this formula is equivalent to the one previously proposed in [10] ($k_{\mathrm{maxAmp}} \approx \pi/2W$).

3. Conclusion

To conclude, we reported on long-range spin wave propagation in a 82 nm thick YIG film over a distance as large as 150 μm. In order to precisely determine the excited wavenumber by the coplanar antenna, it is essential to take into account anisotropy fields present in YIG films. We showed that anisotropy significantly affects SW propagation characteristics; namely it causes an increase in the SW frequency as well as in the SW group velocity. The main contribution comes from the out-of-plane uniaxial anisotropy field. The cubic anisotropy field is negligibly small in the YIG (1 1 1) film and it does not affect magnetization dynamics in the film plane. We explained that the wavenumber determination from group velocity versus magnetic field dependence requires only two types of measurement, which are broadband SW spectroscopy and the measurement of the film thickness.

Acknowledgments

This work was carried out within the Project NANOSPIN PSPB-045/2010 supported by a grant from Switzerland through the Swiss Contribution to the enlarged European Union. J Rychły and J Dubowik would like to acknowledge support from the European Union's Horizon 2020 MSCA-RISE-2014: Marie Skłodowska-Curie Research and Innovation Staff Exchange (RISE) Grant Agreement No. 644348 (MagIC). The authors would like to thank Professor Maciej Krawczyk for thoughtful suggestions. We also acknowledge valuable comments from Dr Piotr Graczyk and Paweł Gruszecki.

References

[1] Jamali M, Kwon J H, Seo S-M, Lee K-J and Yang H 2016 Spin wave nonreciprocity for logic device applications *Sci. Rep.* **3** 3160
[2] Chumak A V, Serga A A and Hillebrands B 2014 Magnon transistor for all-magnon data processing *Nat. Commun.* **5** 4700
[3] Vogt K, Fradin F Y, Pearson J E, Sebastian T, Bader S D, Hillebrands B, Hoffmann A and Schultheiss H 2014 Realization of a spin-wave multiplexer *Nat. Commun.* **5** 3727
[4] Gertz F, Kozhevnikov A V, Filimonov Y A, Nikonov D E and Khitun A 2015 Magnonic holographic memory: from proposal to device *IEEE J. Explor. Solid-State Comput. Devices Circuits* **1** 67–75
[5] Serga A A, Chumak A V and Hillebrands B 2010 YIG magnonics *J. Phys. D: Appl. Phys.* **43** 264002
[6] Bessonov V D, Mruczkiewicz M, Gieniusz G, Guzowska U, Maziewski A, Stognij A I and Krawczyk M 2015 Magnonic band gaps in YIG-based one-dimensional magnonic crystals: an array of grooves versus an array of metallic stripes *Phys. Rev.* B **91** 104421
[7] Kostylev M P, Serga A A, Schneider T, Leven B and Hillebrands B 2005 Spin-wave logical gates *Appl. Phys. Lett.* **87** 153501
[8] Lee J M, Jang C, Min B C, Lee S W, Lee K J and Chang J 2016 All-electrical measurement of interfacial Dzyaloshinskii–Moriya interaction using collective spin-wave dynamics *Nano Lett.* **16** 62–7
[9] Bailleul M, Olligs D and Fermon C 2003 Propagating spin wave spectroscopy in a permalloy film: a quantitative analysis *Appl. Phys. Lett.* **83** 972
[10] Neusser S, Duerr G, Bauer H G, Tacchi S, Madami M, Woltersdorf G, Gubbiotti G, Back C H and Grundler D 2010 Anisotropic propagation and damping of spinwaves in a nanopatterned antidot lattice *Phys. Rev. Lett.* **105** 067208
[11] Kwon J H, Mukherjee S S, Deorani P, Hayashi M and Yang H 2013 Characterization of magnetostatic surface spin waves in magnetic thin films: evaluation for microelectronic applications *Appl. Phys.* A **111** 369–78
[12] Yu H, Helly O, Cros V, Bernard R, Bartolotti P, Anane A, Brandl F, Huber R, Stasinopoulos I and Grundler D 2014 Magnetic thin-film insulator with ultra-low spin wave damping for coherent nanomagnonics *Sci. Rep.* **4** 6848
[13] Wang H L, Du C H, Pu Y, Adur R, Hammel P C and Yang F Y 2013 Large spin pumping from epitaxial $Y_3Fe_5O_{12}$ thin films to Pt and W layers *Phys. Rev.* B **88** 100406

[14] Manuilov S A, Khartsev S I and Grishin A M 2009 Pulsed laser deposited Y3Fe5O12 films: nature of magnetic anisotropy *J. Appl. Phys.* **106** 123917
[15] Chiang W-C, Chern M Y, Lin J G and Huang C Y 2002 FMR studies of $Y_3Fe_5O_{12}$/$Gd_3Ga_5O_{12}$ (YIG/GGG) superlattices and YIG thin films *J. Magn. Magn. Mater.* **239** 332
[16] Kalinikos B A, Kostylev M P, Kozhus N V and Slavin A N 1990 The dipole-exchange spin wave spectrum for anisotropic ferromagnetic films with mixed exchange boundary conditions *J. Phys.: Condens. Matter* **2** 9861–77
[17] Gubbiotti G, Carlotti G and Hillebrands B 1998 Spin waves and magnetic anisotropy in ultrathin (1 1 1)-oriented cubic films *J. Phys.: Condens. Matter* **10** 2171
[18] Kehlberger A *et al* 2015 Enhanced magneto-optic Kerr effect and magnetic properties of $CeY_2Fe_5O_{12}$ epitaxial thin films *Phys. Rev. Appl.* **4** 014008
[19] Vlaminck V and Bailleul M 2010 Spin-wave transduction at the submicrometer scale: experiment and modeling *Phys. Rev.* B **81** 014425
[20] Eshbach J R and Damon R W 1960 Surface magnetostatic modes and surface spin waves *Phys. Rev.* B **118** 1208
[21] Schwarze T 2013 Spin waves in 2D and 3D magnonic crystals: from nanostructured ferromagnetic materials to chiral helimagnets *PhD Thesis* Technische Universität München
[22] Manuilov S A and Grishin A M 2010 Pulsed laser deposited $Y_3Fe_5O_{12}$ films: nature of magnetic anisotropy II *J. Appl. Phys.* **108** 013902
[23] Onbasli M C, Kehlberger A, Kim D H, Jakob G, Kläui M, Chumak A V, Hillebrands B and Ross C A 2014 Pulsed laser deposition of epitaxial yttrium iron garnet films with low Gilbert damping and bulk-like magnetization *APL Mater.* **2** 106102
[24] Collet M *et al* 2017 Spin-wave propagation in ultra-thin YIG based waveguides *Appl. Phys. Lett.* **110** 092408
[25] Onbasli M C, Beran L, Zahradník M, Kučera M, Antoš R, Mistrík J, Dionne G F, Veis M and Ross C A 2016 Optical and magneto-optical behavior of cerium yttrium iron garnet thin films at wavelengths of 200–1770 nm *Sci. Rep.* **6** 23640
[26] Bonda A, Uba S and Uba L 2012 Ultrafast magneto-optical and magnetization-induced second harmonic generation techniques for studies of magnetic nanostructures *Acta Phys. Polon.* A **121** 1225
[27] Dubs C, Surzhenko O, Linke R, Danilewsky A, Brückner U and Dellith J 2017 Sub-micrometer yttrium iron garnet LPE films with low ferromagnetic resonance losses *J. Phys. D: Appl. Phys.* **50** 204005
[28] Perzlmaier K, Woltersdorf G and Back C H 2008 Observation of the propagation and interference of spin waves in ferromagnetic thin films *Phys. Rev.* B **77** 054425

4.2 *Ultra-low Damping in Lift-off Structured Yttrium Iron Garnet Thin Films*

Publikacja opisuje własności warstw granatu itrowo-żelazowego, które były strukturyzowane metodą bezmaskowej litografii optycznej. Wykorzystując ciągłą warstwę referencyjną, pokazano, że proces strukturyzowania nie wpływa istotnie na właściwości strukturalne i magnetyczne warstw. Wykazują one niskie tłumienie precesji namagnesowania, niską szorstkość powierzchni, namagnesowanie efektywne bliskie wartościom objętościowego granatu YIG, a także dobrze określone, ostre krawędzie struktur.

Indywidualny wkład autora w powstanie tej publikacji obejmuje: napisanie pierwszej wersji manuskryptu, analizę danych eksperymentalnych i teoretycznych, analizę literaturową, naniesienie warstw metodą PLD, wykonanie pomiarów VNA-FMR oraz pomiarów kątowych rezonansu ferromagnetycznego, wizualizację uzyskanych rezultatów i przygotowanie odpowiedzi na pytania recenzentów.

APPLIED PHYSICS LETTERS **111**, 192404 (2017)

Ultra-low damping in lift-off structured yttrium iron garnet thin films

A. Krysztofik,[1,a)] L. E. Coy,[2] P. Kuświk,[1,3] K. Załęski,[2] H. Głowiński,[1,a)] and J. Dubowik[1]
[1]*Institute of Molecular Physics, Polish Academy of Sciences, PL-60-179 Poznań, Poland*
[2]*NanoBioMedical Centre, Adam Mickiewicz University, PL-61-614 Poznań, Poland*
[3]*Centre for Advanced Technology, Adam Mickiewicz University, PL-61-614 Poznań, Poland*

(Received 29 August 2017; accepted 25 October 2017; published online 6 November 2017)

We show that using maskless photolithography and the lift-off technique, patterned yttrium iron garnet thin films possessing ultra-low Gilbert damping can be accomplished. The films of 70 nm thickness were grown on (001)-oriented gadolinium gallium garnet by means of pulsed laser deposition, and they exhibit high crystalline quality, low surface roughness, and the effective magnetization of 127 emu/cm^3. The Gilbert damping parameter is as low as 5×10^{-4}. The obtained structures have well-defined sharp edges which along with good structural and magnetic film properties pave a path in the fabrication of high-quality magnonic circuits and oxide-based spintronic devices. *Published by AIP Publishing.* https://doi.org/10.1063/1.5002004

Yttrium iron garnet ($Y_3Fe_5O_{12}$, YIG) has become an intensively studied material in recent years due to exceptionally low damping of magnetization precession and electrical insulation, enabling its applications in research on spin-wave propagation,[1–3] spin-wave based logic devices,[4–6] spin pumping,[7] and thermally driven spin caloritronics.[8] These applications inevitably entail film structurization in order to construct complex integrated devices. However, the fabrication of high-quality thin YIG films requires deposition temperatures over 500 °C (Refs. 6 and 9–18), leading to a top-down lithographical approach that is ion-beam etching of a previously deposited plain film, whereas a patterned resist layer serves as a mask. Consequently, this method introduces crystallographic defects and imperfections to the surface structure, and in the case of YIG films, it causes a significant increase in the damping parameter.[19–21] Moreover, it does not ensure well-defined structure edges for insulators, which play a crucial role in devices utilizing edge spin waves,[22] Goos-Hänchen spin wave shifts,[23,24] or standing spin waves modes.[25] On the contrary, the bottom-up structurization deals with these issues since it allows for the film growth in the selected, patterned areas followed by a removal of the resist layer along with redundant films during the lift-off process. Additionally, it reduces the patterning procedure by one step, that is, ion etching, and imposes room-temperature deposition, both of which are particularly important whenever low fabrication budget is required.

In this letter, we report on ultra-low damping in the bottom-up structured YIG film by means of a direct writing photolithography technique. In our case, the method allows for structure patterning with 0.6 μm resolution across the full writing area. In order to not preclude the lift-off process, the pulsed laser deposition (PLD) was conducted at room temperature, and since such as-deposited films are amorphous,[19,27] the *ex-situ* annealing was performed for recrystallization. Note that post-deposition, annealing of YIG films is commonly carried out regardless the substrate temperature during film deposition.[6,12,13,28,29] As a reference, we investigated a plain film which was grown in the same deposition process and underwent the same fabrication procedure except for patterning. Henceforth, we will refer to the structured and the plain film as sample 1 and sample 2, respectively. We anticipate that such a procedure may be of potential for fabrication of other magnetic oxide structures useful in spintronics.

Structural characterization of both samples was performed by means of X-Ray Diffraction (XRD). Atomic force microscopy (AFM) was applied to investigate the surface morphology and the quality of structure edges. SQUID magnetometry provided information on the saturation magnetization and magnetocrystalline anisotropy field. Using a coplanar waveguide connected to a vector network analyzer, broadband ferromagnetic resonance (VNA-FMR) was performed to determine the Gilbert damping parameter and anisotropy fields. All the experiments were conducted at room temperature.

The procedure for sample preparation was as follows: The (001)-oriented gadolinium gallium garnet substrates were ultrasonicated in acetone, trichloroethylene, and isopropanol to remove surface impurities. After a 1 min of hot plate baking for water evaporation, a positive photoresist was spin-coated onto the substrate (sample 1). Using maskless photolithography, an array of 500 μm × 500 μm squares separated over 500 μm was patterned and the exposed areas were developed. Detailed parameters of the photolithography process can be found in Ref. 26. We chose rather large size of the squares to provide a high signal-to-noise ratio in the latter measurements. Thereafter, plasma etching was performed to remove a residual resist. We would like to emphasize the importance of this step in the fabrication procedure as the resist residues may locally affect the crystalline structure of a YIG film, causing an undesirable increase in overall magnetization damping. Both substrates were then placed in a high vacuum chamber of 9×10^{-8} mbar base pressure, and a film was deposited from a stoichiometric ceramic YIG target under 2×10^{-4} mbar partial pressure of oxygen. We used a Nd:YAG laser ($\lambda = 355$ nm) for the ablation with a pulse rate of 2 Hz, which yielded 1 nm/min growth rate. The

a)Electronic addresses: adam.krysztofik@ifmpan.poznan.pl and hubert.glowinski@ifmpan.poznan.pl

target-to-substrate distance was approximately 50 mm. After the deposition, the lift-off process for sample 1 was performed using sonication in acetone to obtain the expected structures. Subsequently, both samples were annealed in a tube furnace under an oxygen atmosphere ($p \approx 1$ bar) for 30 min at 850 °C. The heating and cooling rates were about 50 °C/min and 10 °C/min, respectively.

The structure of YIG films was determined by X-ray diffraction. Although the as-deposited films were amorphous, with the annealing treatment, they inherited the lattice orientation of the GGG substrate and recrystallized along the [001] direction. Figure 1(a) presents diffraction curves taken in the vicinity of (004) Bragg reflection. The (004) reflection position of structured YIG well coincides with the reflection of the plain film. The $2\theta = 28.709°$ corresponds to the cubic lattice constant of 12.428 Å. A comparison of this value with the lattice parameter of a bulk YIG (12.376 Å) suggests distortion of unit cells due to slight nonstoichiometry.[16,30] Both samples exhibit distinct Laue oscillations depicted by the blue arrows, indicating film uniformity and high crystalline order, although the structured film showed lower intensity due to the lower mass of the film. From the oscillation period, we estimated a film thickness of 73 nm, in agreement with the nominal thickness and the value determined using AFM for sample 1 [Fig. 1(b)]. By measuring the diffraction in the expanded angle range, we also confirmed that no additional phases such as Y_2O_3 or Fe_2O_3 appeared.

The surface morphology of the structured film was investigated by means of AFM. In Fig. 1(b), the profile of a square's edge is shown. It should be highlighted that no edge irregularities have formed during the lift-off process. The horizontal distance between the GGG substrate and the surface of the YIG film is equal to 170 nm as marked in Fig. 1(b) by the shaded area. A fitting with a Gaussian function to the derivative of the height profile yields the full width at half maximum of 61 nm. This points to the well-defined structure edges achieved with bottom-up structurization. Both samples have smooth and uniform surfaces. The comparable values of root mean square (RMS) roughness (0.306 nm for sample 1 and 0.310 nm for sample 2) indicate that the bottom-up structurization process did not leave any resist residues. Note that a roughness of a bare GGG substrate before deposition was 0.281 nm, and therefore, the surface roughness of YIG is increased merely by 10%.

Figure 2 shows magnetization reversal curves measured along the [100] direction. For each hysteresis loop, a paramagnetic contribution arising for the GGG substrates was subtracted. The saturation magnetization M_s was equal to 117 emu/cm^3 and 118.5 emu/cm^3 for samples 1 and 2, respectively. Both hysteresis loops demonstrate in-plane anisotropy. For the (001)-oriented YIG, the [100] direction is a "hard" in-plane axis and the magnetization saturates at $H_a = 65$ Oe. This value we identify as the magnetocrystalline anisotropy field. The VNA-FMR measurements shown in Fig. 3(a) confirm these results. Using the Kittel dispersion relation, i.e., the frequency f dependence of the resonance magnetic field H

$$f = \frac{\gamma}{2\pi}\sqrt{(H + H_a\cos 4\varphi)\left(H + \frac{1}{4}H_a(3 + \cos 4\varphi) + 4\pi M_{eff}\right)}, \quad (1)$$

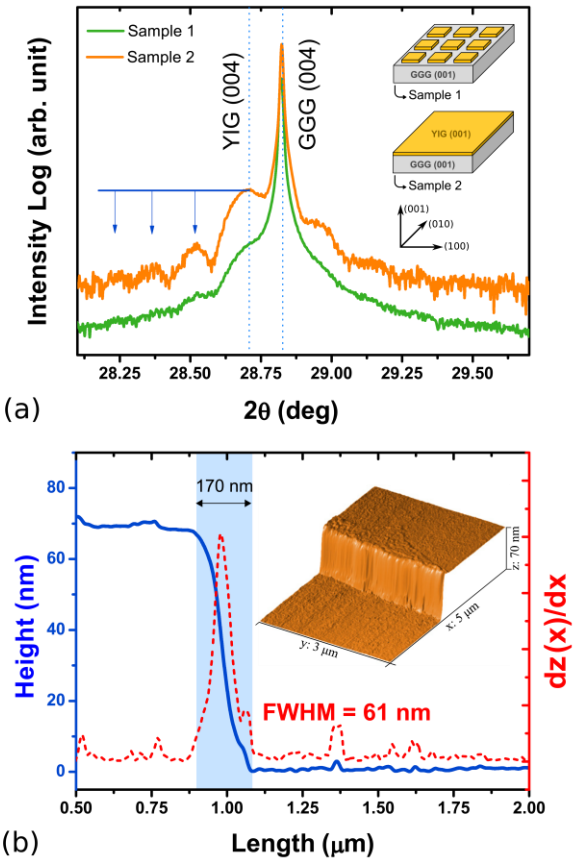

FIG. 1. (a) XRD $\theta - 2\theta$ plot near the (004) reflection of structured (sample 1) and plain (sample 2) YIG films. Blue arrows show clear Laue reflections of the plain film. Insets show a schematic illustration of the structured and plain films used in this study. (b) Height profile [z(x)] taken from the structured sample (left axis), and the right shows the differential of the profile, clearly showing the slope change. The inset shows the 3D map of the structure's edge.

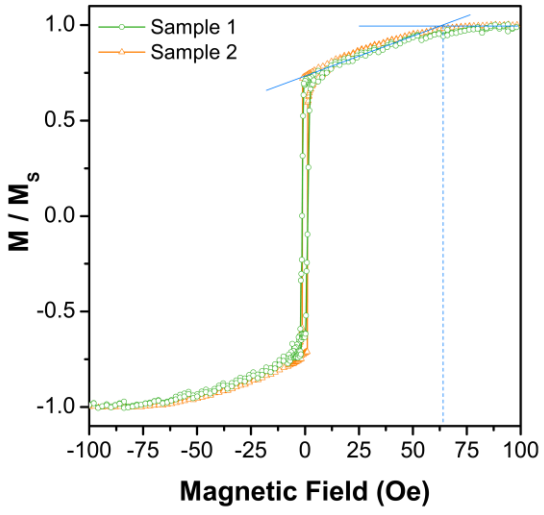

FIG. 2. Hysteresis loops of structured (sample 1) and plain (sample 2) YIG films measured by SQUID magnetometry along the [100] direction at room temperature.

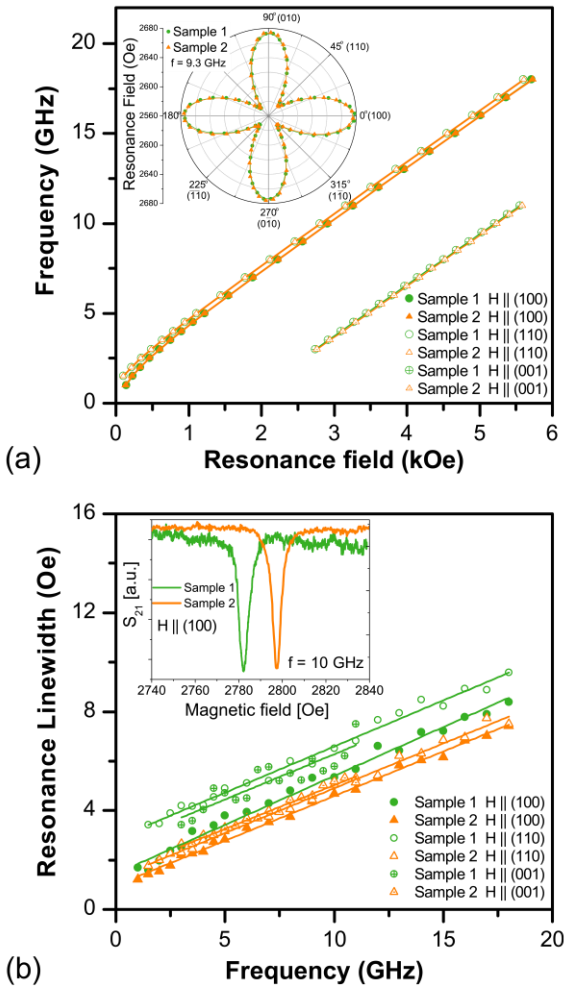

FIG. 3. (a) Kittel dispersion relations of the structured (sample 1) and plain (sample 2) YIG films. The inset shows the angular dependence of the resonance field, revealing perfect fourfold anisotropy for both samples. (b) Linewidth dependence on frequency fitted with Eq. (3). The inset shows resonance absorption peaks with very similar widths (5.3 Oe for sample 1 and 4.7 Oe for sample 2 at 10 GHz). Small differences of the resonance field originate from different values of $4\pi M_{eff}$.

$$4\pi M_{eff} = 4\pi M_s - H_u, \tag{2}$$

we derived H_a and the effective magnetization M_{eff}, both comparable to the values determined using SQUID and close to the values of a bulk YIG (see Table I). Here, the azimuthal angle φ defines the in-plane orientation of the magnetization direction with respect to the [100] axis of YIG and γ is the gyromagnetic ratio ($1.77 \times 10^7\ \mathrm{G^{-1}\,s^{-1}}$). To better compare the values of H_a between samples and to determine if the results are influenced by additional anisotropic contribution arising from the squares' shape in the structured film, we performed angular resolved resonance measurements [inset in Fig. 3(a)]. The fitting according to Eq. (1) gives $|H_a|$ equal to 69.5 ± 0.6 for sample 1 and 69.74 ± 0.28 for sample 2, in agreement with the values derived from the $f(H)$ dependence and better accuracy. Hence, we conclude that the structurization did not affect the in-plane anisotropy. The deviations of the derived M_s and H_a from bulk values can be explained in the framework of the Fe vacancy model developed for YIG films as a result of nonstoichiometry.[13,30] For the experimentally determined M_s and H_a, the model yields the chemical unit $Y_3Fe_{4.6}O_{11.4}$, which closely approximates to the composition of stoichiometric YIG $Y_3Fe_5O_{12}$.

Although the saturation magnetization of the films is decreased by 15% with respect to the bulk value, we can expect similar spin wave dynamics since magnon propagation does not solely depend on M_s but on the effective magnetization or equivalently on the uniaxial anisotropy field H_u.[12] Substitution of M_s into Eq. (2) gives average values of H_u equal to -122 Oe and -111 Oe for samples 1 and 2, respectively (to determine H_u from the out-of-plane FMR measurements when H || [001], we used the $f = \frac{\gamma}{2\pi}(H + H_a - 4\pi M_{eff})$ dependence[13] to fit the data and assumed the value of H_a from angular measurements). As $M_{eff}^{Sample\,1,2} \approx M_{eff}^{bulk}$, it follows that the low value of M_s in room-temperature deposited thin films is "compensated" by the uniaxial anisotropy field. Note that for bulk YIG saturation, magnetization is diminished by $H_u/4\pi$, giving a lower value of M_{eff}, while for samples 1 and 2, M_s is augmented by $H_u/4\pi$, giving a higher value of M_{eff} (Table I). The negative sign of the uniaxial anisotropy field is typical for PLD-grown YIG films and originates from the preferential distribution of Fe vacancies between different sites of the YIG octahedral sublattice.[30] This points to the growth-induced anisotropy mechanism, while the stress-induced contribution is of ≈10 Oe (Ref. 29), and as it can be estimated according to Ref. 32, the transition layer at the substrate-film interface due to Gd, Ga, and Y ion diffusion is ca. 1.5 nm thick for the 30 min of annealing treatment. We argue that the growth-induced anisotropy due to ordering of the magnetic

TABLE I. Key parameters reported for PLD and LPE YIG films.

		AFM	SQUID		VNA-FMR					
	Film thickness	RMS roughness (nm)	M_s (emu/cm^3)	H_a (Oe)	Field orientation	M_{eff} (emu/cm^3)	$\lvert H_a \rvert$ (Oe)	H_u (Oe)	α ($\times 10^{-4}$)	ΔH_0 (Oe)
Sample 1	70 nm	0.306	117 ± 1	65 ± 5	(100):	125 ± 1	64 ± 1	-101 ± 18	5.53 ± 0.13	1.45 ± 0.09
					(110):	126 ± 1	63 ± 1	-113 ± 18	5.24 ± 0.12	2.86 ± 0.09
					(001):	129 ± 2	…	-151 ± 28	5.19 ± 0.64	2.61 ± 0.34
Sample 2	70 nm	0.310	118.5 ± 2	65 ± 5	(100):	124 ± 1	62 ± 1	-69 ± 28	5.05 ± 0.07	0.97 ± 0.05
					(110):	127 ± 1	65 ± 1	-107 ± 28	5.09 ± 0.09	1.28 ± 0.06
					(001):	131 ± 2	…	-157 ± 36	5.02 ± 0.18	1.48 ± 0.09
LPE-YIG[31]	106 nm	0.3	143	…	(112):	…	…	…	1.2	0.75
LPE-YIG[30]	120 μm	…	139 ± 2	…	(111):	133 ± 2	85 ± 6	76 ± 1	0.3	…

ions is related to the growth condition, which in our study is specific. Namely, it is crystallization of an amorphous material.

Gilbert damping parameter α was obtained by fitting the dependence of the linewidth ΔH (full width at half maximum) on frequency f as shown in Fig. 3(b)

$$\Delta H = \frac{4\pi\alpha}{\gamma} f + \Delta H_0, \tag{3}$$

where ΔH_0 is a zero-frequency linewidth broadening. The α parameter of both samples is nearly the same, 5.32×10^{-4} for sample 1 and 5.05×10^{-4} for sample 2 on average (see Table I). It proves that bottom-up patterning does not compromise magnetization damping. The value of ΔH_0 contribution is around 1.5 Oe although small variations of ΔH_0 on φ can be noticed. Additional comments on angular dependencies of ΔH can be found in the supplementary material. The derived values of α remain one order of magnitude smaller than for soft ferromagnets such as $Ni_{80}Fe_{20}$,[33] CoFeB,[34] or Finemet[35] and are comparable to values reported for YIG films deposited at high temperatures (from 1×10^{-4} up to 9×10^{-4}).[6,9,11,14,15,17,18] It should be also highlighted that the α constant is significantly increased in comparison to the bulk YIG made by means of Liquid Phase Epitaxy (LPE). However, recently reported LPE-YIG films of nanometer thickness suffer from the increased damping as well (Table I) due to impurity elements present in the high-temperature solutions used in the LPE technique.[31] As the PLD method allows for a good contamination control, we attribute the increase as a result of slight nonstoichiometry determined above with the Fe vacancy model.[30] Optimization of growth conditions, which further improve the film composition, may resolve this issue and allow us to cross the $\alpha = 1 \times 10^{-4}$ limit. We also report that additional annealing of the samples (for 2 h) did not influence damping nor it improved the value of H_a or M_{eff} (within 5% accuracy).

In conclusion, the lift-off patterned YIG films possessing low damping have been presented. Although the structurization procedure required deposition at room temperature, the α parameter does not diverge from those reported for YIG thin films grown at temperatures above 500 °C. Using the plain, reference film fabricated along with the structured one, we have shown that structurization does not significantly affect the structural nor magnetic properties of the films, i.e., out-of-plane lattice constant, surface roughness, saturation magnetization, anisotropy fields, and damping. The structures obtained with bottom-up structurization indeed possess sharp, well-defined edges. In particular, our findings will help in the development of magnonic and spintronic devices utilizing film boundary effects and low damping of magnetization precession.

See supplementary material for the angular dependence of resonance linewidth.

This research received funding from the European Union Horizon 2020 research and innovation programme under the Marie Skłodowska-Curie Grant Agreement No. 644348 (MagIC). We would like to thank Andrzej Musiał for the assistance during film annealing.

[1]H. Yu, O. d'Allivy Kelly, V. Cros, R. Bernard, P. Bortolotti, A. Anane, F. Brandl, R. Huber, I. Stasinopoulos, and D. Grundler, Sci. Rep. **4**, 6848 (2015).
[2]S. Maendl, I. Stasinopoulos, and D. Grundler, Appl. Phys. Lett. **111**, 12403 (2017).
[3]A. V. Sadovnikov, C. S. Davies, V. V. Kruglyak, D. V. Romanenko, S. V. Grishin, E. N. Beginin, Y. P. Sharaevskii, and S. A. Nikitov, Phys. Rev. B **96**, 60401 (2017).
[4]A. A. Nikitin, A. B. Ustinov, A. A. Semenov, A. V. Chumak, A. A. Serga, V. I. Vasyuchka, E. Lahderanta, B. A. Kalinikos, and B. Hillebrands, Appl. Phys. Lett. **106**, 102405 (2015).
[5]U. H. Hansen, V. E. Demidov, and S. O. Demokritov, Appl. Phys. Lett. **94**, 252502 (2009).
[6]M. C. Onbasli, A. Kehlberger, D. H. Kim, G. Jakob, M. Kläui, A. V. Chumak, B. Hillebrands, and C. A. Ross, APL Mater. **2**, 106102 (2014).
[7]Z. Fang, A. Mitra, A. L. Westerman, M. Ali, C. Ciccarelli, O. Cespedes, B. J. Hickey, and A. J. Ferguson, Appl. Phys. Lett. **110**, 92403 (2017).
[8]H. Yu, S. D. Brechet, P. Che, F. A. Vetro, M. Collet, S. Tu, Y. G. Zhang, Y. Zhang, T. Stueckler, L. Wang, H. Cui, D. Wang, C. Zhao, P. Bortolotti, A. Anane, J. P. Ansermet, and W. Zhao, Phys. Rev. B **95**, 104432 (2017).
[9]C. Tang, M. Aldosary, Z. Jiang, H. Chang, B. Madon, K. Chan, M. Wu, J. E. Garay, and J. Shi, Appl. Phys. Lett. **108**, 102403 (2016).
[10]J. Fu, M. Hua, X. Wen, M. Xue, S. Ding, M. Wang, P. Yu, S. Liu, J. Han, C. Wang, H. Du, Y. Yang, and J. Yang, Appl. Phys. Lett. **110**, 202403 (2017).
[11]H. Yu, O. d'Allivy Kelly, V. Cros, R. Bernard, P. Bortolotti, A. Anane, F. Brandl, F. Heimbach, and D. Grundler, Nat. Commun. **7**, 11255 (2016).
[12]A. Krysztofik, H. Głowiński, P. Kuświk, S. Ziętek, L. E. Coy, J. N. Rychły, S. Jurga, T. W. Stobiecki, and J. Dubowik, J. Phys. D: Appl. Phys. **50**, 235004 (2017).
[13]S. A. Manuilov and A. M. Grishin, J. Appl. Phys. **108**, 13902 (2010).
[14]J. C. Gallagher, A. S. Yang, J. T. Brangham, B. D. Esser, S. P. White, M. R. Page, K. Y. Meng, S. Yu, R. Adur, W. Ruane, S. R. Dunsiger, D. W. McComb, F. Yang, and P. C. Hammel, Appl. Phys. Lett. **109**, 72401 (2016).
[15]O. D'Allivy Kelly, A. Anane, R. Bernard, J. Ben Youssef, C. Hahn, A. H. Molpeceres, C. Carrétéro, E. Jacquet, C. Deranlot, P. Bortolotti, R. Lebourgeois, J. C. Mage, G. D. Loubens, O. Klein, V. Cros, and A. Fert, Appl. Phys. Lett. **103**, 82408 (2013).
[16]N. S. Sokolov, V. V. Fedorov, A. M. Korovin, S. M. Suturin, D. A. Baranov, S. V. Gastev, B. B. Krichevtsov, K. Y. Maksimova, A. I. Grunin, V. E. Bursian, L. V. Lutsev, and M. Tabuchi, J. Appl. Phys. **119**, 23903 (2016).
[17]L. V. Lutsev, A. M. Korovin, V. E. Bursian, S. V. Gastev, V. V. Fedorov, S. M. Suturin, and N. S. Sokolov, Appl. Phys. Lett. **108**, 182402 (2016).
[18]C. L. Jermain, S. V. Aradhya, N. D. Reynolds, R. A. Buhrman, J. T. Brangham, M. R. Page, P. C. Hammel, F. Y. Yang, and D. C. Ralph, Phys. Rev. B **95**, 174411 (2017).
[19]N. Zhu, H. Chang, A. Franson, T. Liu, X. Zhang, E. Johnston-Halperin, M. Wu, and H. X. Tang, Appl. Phys. Lett. **110**, 252401 (2017).
[20]M. B. Jungfleisch, W. Zhang, W. Jiang, H. Chang, J. Sklenar, S. M. Wu, J. E. Pearson, A. Bhattacharya, J. B. Ketterson, M. Wu, and A. Hoffmann, J. Appl. Phys. **117**, 17D128 (2015).
[21]Y. Okamura, M. Ishida, and S. Yamamoto, Appl. Opt. **23**, 124 (1984).
[22]A. Lara, J. R. Moreno, K. Y. Guslienko, and F. G. Aliev, Sci. Rep. **1**, 5597 (2017).
[23]P. Gruszecki, J. Romero-Vivas, Y. S. Dadoenkova, N. N. Dadoenkova, I. L. Lyubchanskii, and M. Krawczyk, Appl. Phys. Lett. **105**, 242406 (2014).
[24]P. Gruszecki, Y. S. Dadoenkova, N. N. Dadoenkova, I. L. Lyubchanskii, J. Romero-Vivas, K. Y. Guslienko, and M. Krawczyk, Phys. Rev. B **92**, 54427 (2015).
[25]N. Kanazawa, T. Goto, K. Sekiguchi, A. B. Granovsky, H. Takagi, Y. Nakamura, and M. Inoue, AIP Adv. **6**, 95204 (2016).
[26]W. Koczorowski, P. Kuświk, M. Przychodnia, K. Wiesner, S. El-Ahmar, M. Szybowicz, M. Nowicki, W. Strupiński, and R. Czajka, Mater. Sci. Semicond. Process. **67**, 92 (2017).

[27]C. Hauser, T. Richter, N. Homonnay, C. Eisenschmidt, M. Qaid, H. Deniz, D. Hesse, M. Sawicki, S. G. Ebbinghaus, and G. Schmidt, Sci. Rep. **6**, 20827 (2016).
[28]Y. Sun, Y. Y. Song, H. Chang, M. Kabatek, M. Jantz, W. Schneider, M. Wu, H. Schultheiss, and A. Hoffmann, Appl. Phys. Lett. **101**, 152405 (2012).
[29]S. A. Manuilov, R. Fors, S. I. Khartsev, and A. M. Grishin, J. Appl. Phys. **105**, 33917 (2009).
[30]S. A. Manuilov, S. I. Khartsev, and A. M. Grishin, J. Appl. Phys. **106**, 123917 (2009).
[31]C. Dubs, O. Surzhenko, R. Linke, A. Danilewsky, U. Brückner, and J. Dellith, J. Phys. D: Appl. Phys. **50**, 204005 (2017).
[32]A. Mitra, O. Cespedes, Q. Ramasse, M. Ali, S. Marmion, M. Ward, R. M. D. Brydson, C. J. Kinane, J. F. K. Cooper, S. Langridge, and B. J. Hickey, Sci. Rep. **7**, 11774 (2017).
[33]S. Ziętek, J. Chęciński, M. Frankowski, W. Skowroński, and T. Stobiecki, J. Magn. Magn. Mater. **428**, 64 (2017).
[34]P. Kuświk, H. Głowiński, E. Coy, J. Dubowik, and F. Stobiecki, J. Phys.: Condens. Matter **29**, 435803 (2017).
[35]H. Głowiński, I. Gościańska, A. Krysztofik, J. Barnaś, M. Cecot, P. Kuświk, and J. Dubowik, in 21st International Conference on Microwave, Radar Wireless Communications MIKON 2016 (2016).

Supplementary material on Ultra-low damping in lift-off structured yttrium iron garnet thin films

A. Krysztofik,[1] L. E. Coy,[2] P. Kuświk,[1,3] K. Załęski,[2] H. Głowiński,[1] and J. Dubowik[1]

[1]*Institute of Molecular Physics, Polish Academy of Sciences, PL-60-179 Poznań, Poland*

[2]*NanoBioMedical Centre, Adam Mickiewicz University, PL-61-614 Poznań, Poland*

[3]*Centre for Advanced Technology, Adam Mickiewicz University, PL-61-614 Poznań, Poland*

Electronic mail: hubert.glowinski@ifmpan.poznan.pl, adam.krysztofik@ifmpan.poznan.pl

Angular dependence of resonance linewidth

Following the observation of a small but noticeable ΔH_0 increase in [110] direction with respect to [100] of patterned and plain YIG film (see Table I. in the main text) we have investigated in-plane angular dependences of resonance linewidth $\Delta H(\varphi)$ at 9.3 GHz with additional measurements in a resonance cavity. φ is the azimuthal angle between the field direction and [100] direction. As can be seen in Fig. S1, both films exhibit a clear fourfold symmetry (symbols). The continuous lines are the result of simulations with $A_4 \cos 4\varphi$ as the leading term and serve as a guide to the eye. A_4 corresponds to the amplitude of variations in ΔH, which is of 0.5 Oe and 1 Oe for the plain and patterned film, respectively. The variation of ΔH for the plain film can be explained as resulted from the cubic magnetocrystalline anisotropy[1] of YIG, while the enhanced variation of ΔH for the patterned film might be tentatively related both to the magnetocrystalline anisotropy and effect of inhomogeneous magnetization orientation at the edges of the patterned square (quadratic in shape). Note that the edges of the patterned squares coincide with the [100], [010], [-100] and [0-10] crystallographic directions. A detailed, quantitative analysis is beyond the scope of the study and requires further investigations.

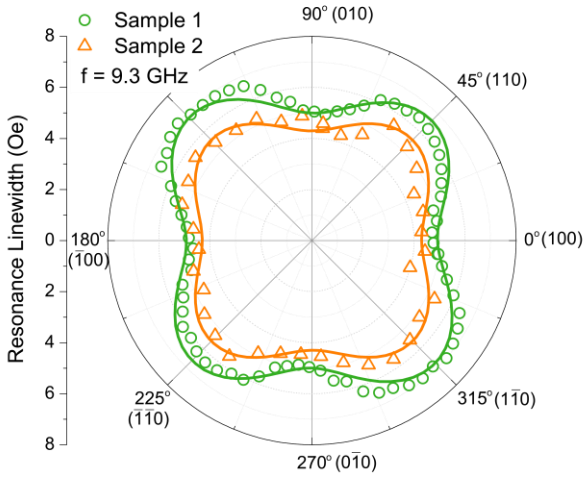

Figure S1. Angular dependence of resonance linewidth of patterned (Sample 1) and plain (Sample 2) film. The lines serve as a guide to the eye.

[1] Xinyu Liu and Jacek K Furdyna 2006 J. Phys.: Condens. Matter **18** R245

4.3 *Magnetization Damping in Nanocrystalline Yttrium Iron Garnet Thin Films Grown on Oxidized Silicon*

Publikacja dotyczy właściwości strukturalnych i magnetycznych cienkich warstw granatu itrowo-żelazowego osadzanych na amorficznym tlenku krzemu. Pomiary szerokopasmowego rezonansu ferromagnetycznego wykazały, że parametr tłumienia Gilberta dla tych warstw jest porównywalny do ferromagnetycznych warstw metali. Jednakże, ze względu na liczne defekty strukturalne parametr poszerzenia linii rezonansowej od niejednorodności magnetycznych $\mu_0 \Delta H_0$ przyjmuje wartości w przedziale 30-60 mT dla warstw o grubościach 25-125 nm. Ponadto zaobserwowano istotne obniżenie wartości namagnesowania efektywnego w wyniku indukowanych termicznie naprężeń.

Indywidualny wkład autora w powstanie tej publikacji obejmuje: napisanie pierwszej wersji manuskryptu, analizę danych eksperymentalnych, analizę literaturową, naniesienie warstw metodą PLD, wykonanie pomiarów XRD, SEM, VSM, VNA-FMR, wizualizację uzyskanych rezultatów, przygotowanie odpowiedzi na pytania recenzentów i korespondencję z wydawnictwem.

Soft Magnetic Materials

Magnetization Damping in Nanocrystalline Yttrium Iron Garnet Thin Films Grown on Oxidized Silicon

Adam Krysztofik[1], Sevgi Özoğlu[2,3], and Emerson Coy[4]

[1]Institute of Molecular Physics, Polish Academy of Sciences, 60-179 Poznan, Poland
[2]Faculty of Physics, Adam Mickiewicz University, 61-614 Poznan, Poland
[3]Department of Physics, Graduate School of Natural and Applied Sciences, Hakkari University, 30000 Hakkari, Turkey
[4]NanoBioMedical Centre, Adam Mickiewicz University, 61-614 Poznan, Poland

Received 5 May 2021, revised 28 May 2021, accepted 31 May 2021, published 4 Jun 2021, current version 1 Jul 2021.

Abstract—In this letter, we report on the magnetic and structural properties of $Y_3Fe_5O_{12}$ (YIG) thin films deposited on a thermally oxidized silicon substrate. Broadband ferromagnetic measurements allowed us to distinguish between intrinsic and extrinsic linewidth contributions, revealing relatively low values of the Gilbert damping parameter that is in the range of 10–20 $\times$ 10^{-4} for film thicknesses below 100 nm. However, the inhomogeneous linewidth broadening $\mu_0\Delta H_0$ remained larger than 30 mT as a result of structural defects. This could guide further development of YIG films integrated with silicon that exhibit low magnetic losses.

Index Terms—Soft magnetic materials, yttrium iron garnet films, pulsed laser deposition, ferromagnetic resonance, Gilbert damping.

I. INTRODUCTION

Yttrium iron garnet (**YIG**) thin films have been continuously studied in recent years due to potential applications in spintronic devices [Coll 2019, Yang 2021], data processing systems utilizing spin waves as an information carrier [Mohseni 2020, Sarker 2020, Träger 2020, Qin 2021], or microwave devices [Lutsev 2020, Zhao 2021]. The lowest magnetic losses have already been experimentally confirmed for the epitaxial films deposited on lattice-matched gadolinium gallium garnet (**GGG**) substrate that exhibit both low Gilbert damping parameter as well as small extrinsic contribution to the ferromagnetic resonance (**FMR**) linewidth [Dubs 2020, Schmidt 2020]. Utilization of the GGG substrates poses, however, attenuation of magnon and microwave excitations in the field of cavity spintronics, especially at cryogenic temperatures [Huebl 2013, Tabuchi 2014, 2015, Zhang 2014, Hou 2019, Li 2019, McKenzie-Sell 2019, Lachance-Quirion 2020].

Concurrently, it was recognized that the FMR linewidth is significantly increased for YIG films grown on CMOS-compatible silicon or silicon oxide substrates. By utilizing a variety of deposition techniques such as pulsed laser deposition (**PLD**) [Popova 2001, Kumar 2004, Che 2016, Saroha 2016, Capku 2020, Bhoi 2021], sputtering [Kang 2005], ion beam sputtering [Stognij 2015, 2017], sol-gel method [Delgado 2018], and co-precipitation with spin coating [Yamada 2020], films with a wide span of thicknesses (12–590 nm) were investigated. Although bulk saturation magnetization was achieved and the layers on Si or SiO_x exhibited a polycrystalline structure, the resonance linewidths in the range of 11–66 mT were considerably elevated in comparison to single-crystal YIG films (0.3–2 mT) [Schmidt 2020]. Since a majority of the FMR investigations reported the linewidth values at a specific frequency, it is not entirely clear whether the Gilbert damping parameter characterizing intrinsic properties of such films was sustained, and the observed broadening was a result of other accompanying effects contributing to the linewidth or rather broad resonance lines aroused from a combination of both factors.

From among few studies where the distinction between the Gilbert damping parameter α and the inhomogeneous linewidth broadening ΔH_0 was made, one should refer to the work of Yamada [2020], Bhoi [2021], and Che [2016], showing that the determined parameters can be substantially spread. For submicrometer-thick coatings obtained via chemical wet synthesis or PLD, strongly increased $\alpha = 270 \times 10^{-4}$ and $\alpha = 160 \times 10^{-4}$ were found, respectively [Yamada 2020, Bhoi 2021]. On the other hand, the films deposited using sputtering were characterized by $\alpha = 19 \times 10^{-4}$ and $\mu_0\Delta H_0$ =0.2 mT [Che 2016]. However, the estimation for the sputtered layers was based on the investigation of spin-wave reflection measurements utilizing highly selective meander-type coplanar waveguide exciting wavenumbers of 6.25 rad/μm. The authors also pointed out that the linewidth measured from an entire film is much higher than the linewidth measured via local means, although without providing the magnitudes [Che 2016].

Therefore, the main aim of this letter is to address this subject and investigate if the low Gilbert damping parameter can be maintained for layers deposited on thermally oxidized silicon. By using the PLD technique, we have grown YIG films with thicknesses ranging from 25 nm to 125 nm and show that it is achievable even in the nanocrystalline layers. The saturation magnetization is close to the bulk value, and the broadening of the FMR lines originates primarily from structural defects.

II. EXPERIMENTAL DETAILS

YIG films were deposited at room temperature using the third harmonic of the Nd:YAG laser (355 nm) with a pulse frequency of 2 Hz that yielded a growth rate of 0.65 nm/min. The target-to-substrate distance was 5 cm. The PLD parameters in our setup were optimized for achieving low-damping epitaxial films [Krysztofik 2017]. The base pressure was 8×10^{-6} Pa, and the partial oxygen pressure was 2.4×10^{-2} Pa (2.4×10^{-4} mbar). The films were *ex situ* annealed after the

Corresponding author: Adam Krysztofik (e-mail: adam.krysztofik@ifmpan.poznan.pl).
Digital Object Identifier 10.1109/LMAG.2021.3086454

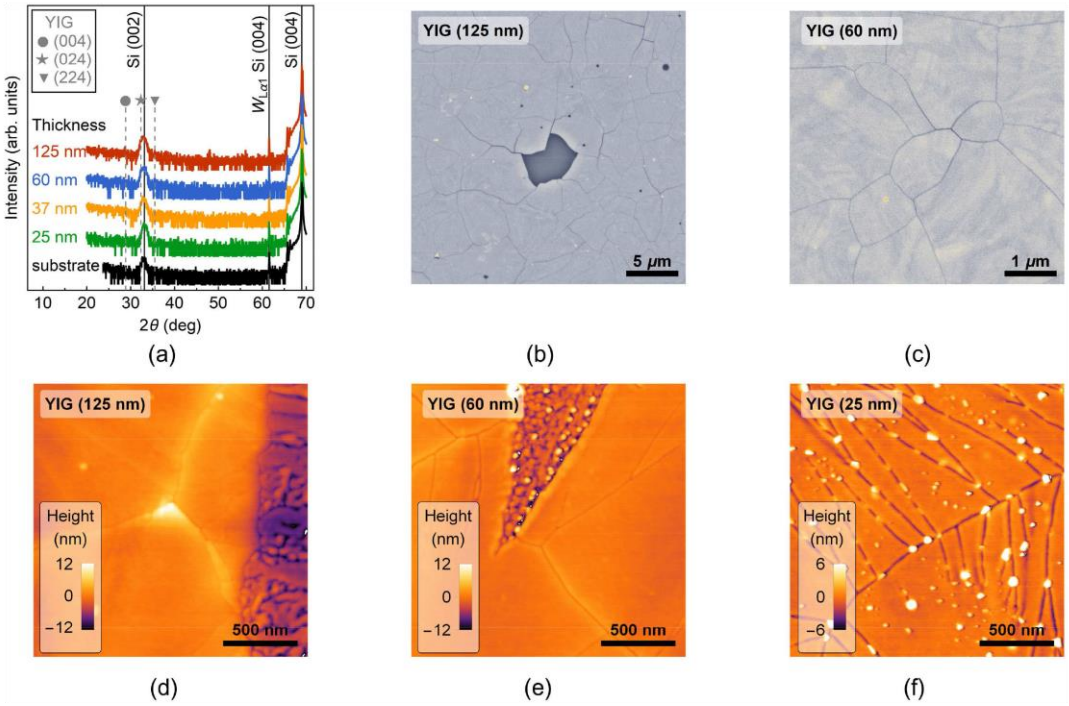

Fig. 1. (a) XRD patterns of the films with different thicknesses and a reference measurement of the silicon substrate. Gray symbols and dashed lines mark the expected position of YIG's highest intensity reflections. (b) and (c) SEM surface images. (d)–(f) AFM topography maps. It should be noted that the plain-film regions between crackings do not relate to grains with a particular crystallographic orientation.

deposition for 3 h in the air at 800 °C with a cooling/heating rate of 6.5 °C/min. The size of the thermally oxidized Si substrates was approximately 5 mm × 5 mm.

The structural properties were examined with Cu-K_α X-ray diffraction (**XRD**) in θ–2θ configuration (Seifert XRD system 3003TT). The surface morphology was investigated using scanning electron microscopy (FEI Nova NanoSEM 650) with a concentric back-scattered detector and atomic force microscopy (**AFM**) (Bruker ICON microscope). The film thicknesses were measured with a stylus profilometer (Bruker Dektak XT). The magnetic measurements were conducted with a vibrating sample magnetometer (**VSM**) and a broadband FMR technique VNA-FMR with a vector network analyzer (Agilent Technologies, PNA Network Analyser E8363C) utilizing a coplanar waveguide with a 500 µm wide signal line. The magnetic measurements were conducted with an in-plane applied external magnetic field unless otherwise noted. All experiments were performed at room temperature. The determined uncertainties are one standard deviation.

III. RESULTS AND DISCUSSION

The as-deposited films have not exhibited any ferromagnetic response during VSM or VNA-FMR experiments and, therefore, can be regarded as amorphous [Hauser 2016]. After annealing and recrystallization, a clear magnetic signal has been found; however, no substantive YIG reflections are visible in the XRD results, as shown in Fig. 1(a). This indicates that the films have a nanocrystalline structure where short-range lattice ordering gives rise to magnetic properties. The expected, highest intensity reflections for coarse, polycrystalline YIG are marked with gray symbols in Fig. 1(a). Although in the vicinity of the YIG (024) reflection position a rather broad peak appears, the reference measurement of the silicon substrate confirms that it can be identified as a basis-forbidden (002) Si reflection [Zaumseil 2015]. The intensities of Si (002) peak are in the range of 2–6 counts per second whereas the background noise is at the level of 1 count per second. The diffractograms reveal also a lack of $YFeO_3$, Fe_2O_3, or Y_2O_3 signatures.

Despite a slow cooling/heating rate, the postdeposition annealing resulted in the formation of film cracking due to different expansion coefficients of the film and the substrate [Fig. 1(b)–(f)]. Moreover, regions with granular structure of the film are observed for films with thicknesses of 125 nm and 60 nm, as shown in the right side of Fig. 1(d) and the top part of Fig. 1(e). However, surface images taken with SEM over the total area of 0.08 mm^2 showed that such regions comprise less than 1% of the films and, therefore, have a negligible impact on the magnetic film properties. Apart from thermal fracturing of the films, a brush-like pattern is visible in the SEM contrast, suggesting the occurrence of inhomogeneous stresses within continuous parts of YIG films [Fig. 1 (b) and (c)]. To conclude, the general morphology of the films suggests YIG crystallization and variations of surface topography signaling early stages of crystalline reconstruction, as observed in other complex stoichiometric oxides [Coy 2017].

The hysteresis loops presented in Fig. 2(a) display typically soft ferromagnetic characteristics. The coercive field of ≈4.5 mT is increased in comparison to epitaxial YIG films (0.018 mT) [Ding 2020]. No noticeable dependence of coercivity on film thickness is found. The saturation magnetization is comparable to the bulk YIG value

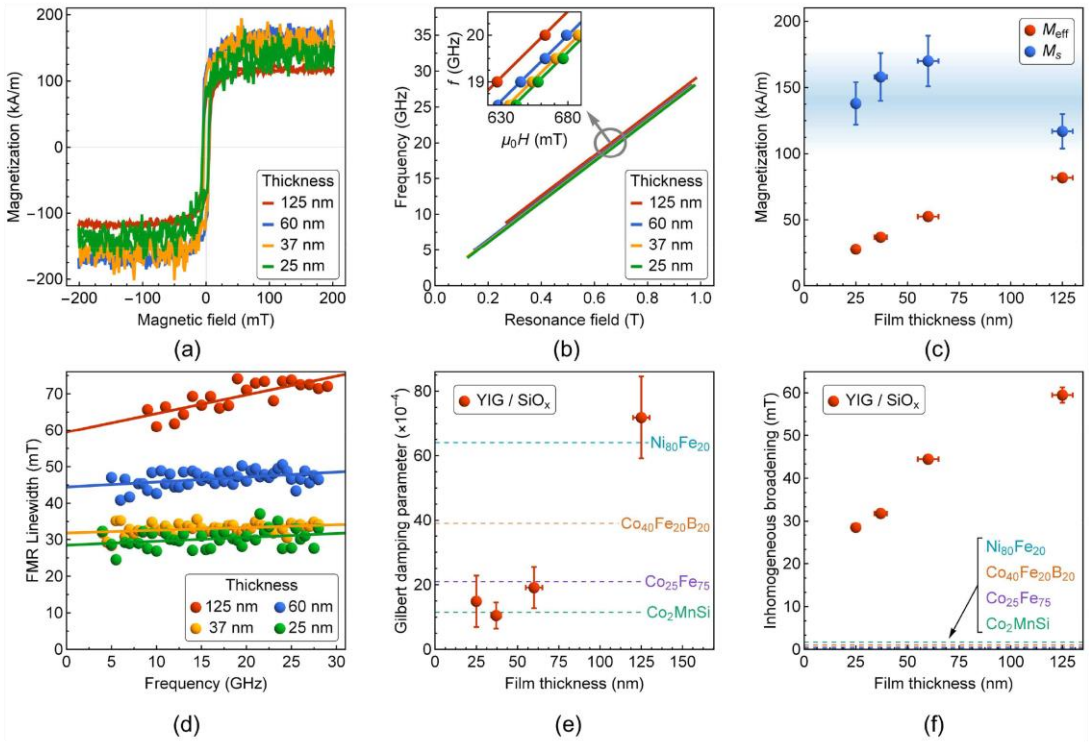

Fig. 2. (a) Magnetization reversal curves taken for the in-plane applied magnetic field. (b) Frequency dependence on the resonance magnetic field fitted with the Kittel equation for the in-plane applied magnetic field. The inset displays an enlarged region near f =20 GHz. (c) Effective magnetization M_{eff} and the saturation magnetization M_s as a function of film thickness. Resonance linewidth $\mu_0\Delta H$(full width at half-maximum) as a function of frequency. (e) and (f) Gilbert damping parameter α and inhomogeneous linewidth broadening $\mu_0\Delta H_0$ as a function of film thickness. For a perception of scale and a comparison with other low-damping polycrystalline materials compatible with silicon, the values corresponding to $Ni_{80}Fe_{20}$ [Zhao 2016], $Co_{40}Fe_{20}B_{20}$ [Conca 2014], $Co_{25}Fe_{75}$ [Schoen 2016], and Co_2MnSi [Guillemard 2019] are marked with dashed lines.

(140 kA/m) that also indicates a lack of the $YFeO_3$ phase for which M_s =8 kA/m [Kumar 2004]. The values of M_s (juxtaposed in Table 1) are determined with ≈11% error due to uncertainties in film volume estimation.

By using the Kittel equation describing the frequency f dependence on the resonance magnetic field H

$$f = \frac{\mu_0\gamma}{2\pi}\sqrt{H\,(H + M_{\text{eff}})} \tag{1}$$

where μ_0 is the vacuum permeability and γ is the gyromagnetic ratio, the effective magnetization M_{eff} has been evaluated [Fig. 2(b)]. The values significantly deviate from the saturation magnetization showing the impact of the perpendicular anisotropy field contribution $H_\perp$

$$M_{\text{eff}} = M_s - H_\perp. \tag{2}$$

Magnitudes of the $\mu_0 H_\perp$ are found in the range of 44–152 mT, in congruence with those reported previously for films deposited on amorphous quartz substrates, suggesting that $H_\perp$ originates from thermally induced stresses due to different thermal expansion coefficients between the substrate and the film [Popova 2001].

The full width at half-maximum FMR linewidth dependences on frequency are shown in Fig. 2(d). From fittings according to

$$\mu_0\Delta H = \alpha\frac{4\pi}{\gamma}f + \mu_0\Delta H_0 \tag{3}$$

the Gilbert damping parameter α and the inhomogeneous linewidth broadening ΔH_0 have been evaluated [Fig. 2 (e) and (f)]. Whereas the α parameter for the thickest studied sample is relatively large and close to the value of $Ni_{80}Fe_{20}$ [Zhao 2016], the films with thicknesses below 100 nm are characterized by the intrinsic damping similar to $Co_{25}Fe_{75}$ [Schoen 2016] or Co_2MnSi [Guillemard 2019]. In comparison to epitaxial YIG films on lattice-matched $Gd_3Ga_5O_{12}$ substrate, the α parameter is, however, increased by a factor of 1.3–30 depending on the deposition method, film stoichiometry, and growth conditions [Schmidt 2020].

Magnitudes of the inhomogeneous linewidth broadening parameter are significantly increased up to 60 mT, and a clear dependence on the film thickness is visible. Since the ΔH_0 parameter provides an insight into extrinsic linewidth contributions, one can consider an impact coming from boundary effects at the edges of cracking, dispersion of shape anisotropy (nonnegligible in-plane demagnetization factors), inhomogeneous stresses, magnetocrystalline anisotropy dispersion, or two-magnon scattering processes. The increasing ΔH_0 as a function of film thickness suggests, however, that the two-magnon scattering gives a minor contribution to ΔH_0 and other effects are dominating. To further strengthen this argument, we have additionally performed a linewidth analysis for FMR measurements taken with the out-of-plane applied magnetic field. As we have not observed a decrease in the FMR linewidth for this configuration, we conclude that the two-magnon scattering is negligible in our case.

The distinction between α and ΔH_0 allows us to conclude that the FMR linewidth in the YIG/SiO_x system is increased primarily due to structural and magnetic inhomogeneities. The range of $\mu_0\Delta H_0$, i.e.,

Table 1. Juxtaposed results of YIG magnetic properties for the films deposited on silicon or silicon oxide

Reference	Method	Substrate	t_{YIG} (nm)	M_s (kA/m)	M_{eff} (kA/m)	$\mu_0\Delta H$ (mT)	α ($\times 10^{-4}$)	$\mu_0\Delta H_0$ (mT)
[Yamada 2020]	Co-precipitation	Si/SiO_x	590	160	–	66 (at 6.5 GHz)	270	50
[Bhoi 2021]	PLD	SiO_2	430	129	127	7.8 (at 8 GHz)	160	3.3
[Kumar 2004]	PLD	Si	250	40	–	–	–	–
[Stognij 2017]	IBS	Si/SiO_2	200	138	–	36 (at 9.5 GHz)	–	–
[Kang 2005]	Sputtering	Si/SiO_x	150	138	–	6.8 (at 9.4 GHz)	–	–
[Delgado 2018]	Sol-gel	Si	134	–	–	11 (at 9.5 GHz)	–	–
[Che 2016]	PLD	Si/SiO_2	100	130	–	0.4 (at 2.8 GHz)	19[(a)]	0.2[(a)]
[Saroha 2016]	PLD	Si	73	–	–	–	–	–
[Stognij 2015]	IBS	Si/SiO_2	67	–	111	29 (at 9.4 GHz)	–	–
[Capku 2020]	PLD	Si	20	–	105	43 (at 9.1 GHz)	–	–
[Popova 2001]	PLD	SiO_2	12	75	–4	25 (at 9.2 GHz)	–	–
This study:	PLD	Si/SiO_x	125 ± 5	117 ± 13	81.7 ± 2.8	64 ± 3 (at 9.5 GHz)	72 ± 13	59.5 ± 1.8
			60 ± 5	170 ± 19	52.4 ± 0.9	46 ± 2 (at 9.5 GHz)	19 ± 6	44.4 ± 0.8
			37 ± 3	158 ± 18	36.9 ± 0.7	32 ± 2 (at 9.5 GHz)	10 ± 4	31.8 ± 0.5
			25 ± 2	138 ± 16	27.6 ± 0.9	29 ± 2 (at 9.5 GHz)	15 ± 8	28.5 ± 1.0

For the comparison, the values were converted to SI units, wherever necessary.
[(a)] Parameters estimated from spin-wave reflection measurements. The spin-wave wavenumber was $k = 6.25$ rad/μm.

29–60 mT, well corresponds to previously reported FMR linewidths $\mu_0\Delta H$(0.4–66 mT) evaluated at specific frequencies (Table 1). In comparison to the lowest reported value of $\mu_0\Delta H_0$ =0.2 mT [Che 2016], it should be noted that the measurements were conducted with a coplanar waveguide probing the YIG magnetic properties from an area of ≈27 μm^2, whereas in this letter, the FMR signal is collected from the area of ≈2.5 mm^2. In the context of spin-wave propagation, the effective damping or propagation distance in the YIG/SiO_x system, as studied here, may strongly depend on the spin-wave wavelength or a ratio of defect size to the wavelength.

In conclusion, relatively low values of the Gilbert damping parameter can be sustained even though nanocrystalline YIG films experience severe cracking and stress. The extrinsic effects are expressed giving the contribution to the inhomogeneous linewidth broadening. Further development of YIG processing may allow for the growth and engineering of films that are compatible with the silicon substrate and exhibit narrow FMR linewidths.

ACKNOWLEDGMENT

The work of Adam Krysztofik was supported in part by the National Science Centre Poland under PRELUDIUM Project 2018/31/N/ST5/03433 and in part by Program POWR.03.02.00-00-I032/16. Sevgi Özoğlu acknowledges the Erasmus+ program for her stay at Adam Mickiewicz University.

Authors' contributions: Adam Krysztofik deposited the films, analyzed the experimental results, wrote the original draft, and carried out the XRD, SEM, VSM, and FMR measurements. Sevgi Özoğlu carried out the AFM measurements under the supervision of Emerson Coy. Adam Krysztofik and Emerson Coy proposed the original idea. All authors revised the manuscript and approved its final version.

REFERENCES

Bhoi B, Diware M S (2021), "Preferred-oriented polycrystalline $Y_3Fe_5O_{12}$ films grown on quartz with low microwave loss," *J. Amer. Ceram. Soc.*, vol. 104, pp. 2423–2427, doi: 10.1111/jace.17675.

Capku Z, Deger C, Aksu P, Yildiz F (2020), "Origin of perpendicular magnetic anisotropy in yttrium iron garnet thin films grown on Si (100)," *IEEE Trans. Magn.*, vol. 56, 8400406, doi: 10.1109/TMAG.2020.3021646.

Che P, Zhang Y, Liu C, Tu S, Liao Z, Yu D, Vetro F A, Ansermet J P, Zhao W, Bi L, Yu H (2016), "Short-wavelength spin waves in yttrium iron garnet micro-channels on silicon," *IEEE Magn. Lett.*, vol. 7, 3508404, doi: 10.1109/LMAG.2016.2616105.

Coll M, Fontcuberta J, Althammer M, Bibes M, Boschker H, Calleja A, Cheng G, Cuoco M, Dittmann R, Dkhil B, El Baggari I, Fanciulli M, Fina I, Fortunato E, Frontera C, Fujita S, Garcia V, Goennenwein S T B, Granqvist C G, Grollier J, Gross R, Hagfeldt A, Herranz G, Hono K, Houwman E, Huijben M, Kalaboukhov A, Keeble D J, Koster G, Kourkoutis L F, Levy J, Lira-Cantu M, MacManus-Driscoll J L, Mannhart J, Martins R, Menzel S, Mikolajick T, Napari M, Nguyen M D, Niklasson G, Paillard C, Panigrahi S, Rijnders G, Sánchez F, Sanchis P, Sanna S, Schlom D G, Schroeder U, Shen K M, Siemon A, Spreitzer M, Sukegawa H, Tamayo R, van den Brink J, Pryds N, Granozio F M (2019), "Towards oxide electronics: A roadmap," *Appl. Surf. Sci.*, vol. 482, pp. 1–93, doi: 10.1016/j.apsusc.2019.03.312.

Conca A, Papaioannou E T, Klingler S, Greser J, Sebastian T, Leven B, Lösch J, Hillebrands B (2014), "Annealing influence on the Gilbert damping parameter and the exchange constant of CoFeB thin films," *Appl. Phys. Lett.*, vol. 104, 182407, doi: 10.1063/1.4875927.

Coy E, Graczyk P, Yate L, Załęski K, Gapiński J, Kuświk P, Mielcarek S, Stobiecki F, Mróz B, Ferrater C, Jurga S (2017), "Second harmonic generation response in thermally reconstructed multiferroic β'- $Gd_2(MoO_4)_3$ thin films," *Sci. Rep.*, vol. 7, 11800, doi: 10.1038/s41598-017-12370-y.

Delgado A, Guerra Y, Padron-Hernandez E, Pena-Garcia R (2018), "Combining the sol gel method and spin coating to obtain YIG films with low FMR linewidth on silicon (100) substrate," *Mater. Res. Exp.*, vol. 5, 026419, doi: 10.1088/2053-1591/aaaff8.

Ding J, Liu T, Chang H, Wu M (2020), "Sputtering growth of low-damping yttrium-iron-garnet thin films," *IEEE Magn. Lett.*, vol. 11, 5502305, doi: 10.1109/LMAG.2020.2989687.

Dubs C, Surzhenko O, Thomas R, Osten J, Schneider T, Lenz K, Grenzer J, Hübner R, Wendler E (2020), "Low damping and microstructural perfection of sub-40nm-thin yttrium iron garnet films grown by liquid phase epitaxy," *Phys. Rev. Mater.*, vol. 4, 024416, doi: 10.1103/PhysRevMaterials.4.024416.

Guillemard C, Petit-Watelot S, Rojas-Sánchez J C, Hohlfeld J, Ghanbaja J, Bataille A, Le Fèvre P, Bertran F, Andrieu S (2019), "Polycrystalline Co_2Mn-based Heusler thin films with high spin polarization and low magnetic damping," *Appl. Phys. Lett.*, vol. 115, 172401, doi: 10.1063/1.5121614.

Hauser C, Richter T, Homonnay N, Eisenschmidt C, Qaid M, Deniz H, Hesse D, Sawicki M, Ebbinghaus S G, Schmidt G (2016), "Yttrium iron garnet thin films with very low damping obtained by recrystallization of amorphous material," *Sci. Rep.*, vol. 6, 20827, doi: 10.1038/srep20827.

Hou J T, Liu L (2019), "Strong coupling between microwave photons and nanomagnet magnons," *Phys. Rev. Lett.*, vol. 123, 107702, doi: 10.1103/PhysRevLett.123.107702.

Huebl H, Zollitsch C W, Lotze J, Hocke F, Greifenstein M, Marx A, Gross R, Goennenwein S T B (2013), "High cooperativity in coupled microwave resonator ferrimagnetic insulator hybrids," *Phys. Rev. Lett.*, vol. 111, 127003, doi: 10.1103/PhysRevLett.111.127003.

Kang Y M, Wee S H, Baik S Il, Min S G, Yu S C, Moon S H, Kim Y W, Yoo S I (2005), "Magnetic properties of YIG($Y_3Fe_5O_{12}$) thin films prepared by the post annealing of amorphous films deposited by RF-magnetron sputtering," *J. Appl. Phys.*, vol. 97, 10A319, doi: 10.1063/1.1855460.

Krysztofik A, Coy L E, Kuswik P, Załęski K, Głowinski H, Dubowik J (2017), "Ultra-low damping in lift-off structured yttrium iron garnet thin films," *Appl. Phys. Lett.*, vol. 111, 192404, doi: 10.1063/1.5002004.

Kumar N, Misra D S, Venkataramani N, Prasad S, Krishnan R (2004), "Magnetic properties of pulsed laser ablated YIG thin films on different substrates," *J. Magn. Magn. Mater.*, vol. 272–276, pp. 899–900, doi: 10.1016/j.jmmm.2003.12.223.

Lachance-Quirion D, Wolski S P, Tabuchi Y, Kono S, Usami K, Nakamura Y (2020), "Entanglement-based single-shot detection of a single magnon with a superconducting qubit," *Science*, vol. 367, pp. 425–428, doi: 10.1126/science.aaz9236.

Li Y, Polakovic T, Wang Y L, Xu J, Lendinez S, Zhang Z, Ding J, Khaire T, Saglam H, Divan R, Pearson J, Kwok W K, Xiao Z, Novosad V, Hoffmann A, Zhang W (2019), "Strong coupling between magnons and microwave photons in on-chip ferromagnet-superconductor thin-film devices," *Phys. Rev. Lett.*, vol. 123, 107701, doi: 10.1103/PhysRevLett.123.107701.

Lutsev L V., Dubovoy V A, Stognij A I, Novitskii N N, Mozharov A M, Mukhin I S, Ketsko V A (2020), "Spin-wave filters based on thin $Y_3Fe_5O_{12}$ films on $Gd_3Ga_5O_{12}$ and Si substrates for microwave applications," *J. Appl. Phys.*, vol. 127, 183903, doi: 10.1063/5.0007338.

McKenzie-Sell L, Xie J, Lee C M, Robinson J W A, Ciccarelli C, Haigh J A (2019), "Low-impedance superconducting microwave resonators for strong coupling to small magnetic mode volumes," *Phys. Rev. B*, vol. 99, 140414, doi: 10.1103/PhysRevB.99.140414.

Mohseni M, Kewenig M, Verba R, Wang Q, Schneider M, Heinz B, Kohl F, Dubs C, Lägel B, Serga A A, Hillebrands B, Chumak A V., Pirro P (2020), "Parametric generation of propagating spin waves in ultrathin yttrium iron garnet waveguides," *Phys. Status Solidi - Rapid Res. Lett.*, vol. 14, 2000011, doi: 10.1002/pssr.202000011.

Popova E, Keller N, Gendron F, Thomas L, Brianso M-C, Guyot M, Tessier M, Parkin S S P (2001), "Perpendicular magnetic anisotropy in ultrathin yttrium iron garnet films prepared by pulsed laser deposition technique," *J. Vac. Sci. Technol. A Vacuum, Surfaces, Film.*, vol. 19, pp. 2567–2570, doi: 10.1116/1.1392395.

Qin H, Holländer R B, Flajšman L, Hermann F, Dreyer R, Woltersdorf G, van Dijken S (2021), "Nanoscale magnonic Fabry-Pérot resonator for low-loss spin-wave manipulation," *Nat. Commun.*, vol. 12, 2293, doi: 10.1038/s41467-021-22520-6.

Sarker M S, Yamahara H, Tabata H (2020), "Current-controlled magnon propagation in Pt/$Y_3Fe_5O_{12}$ heterostructure," *Appl. Phys. Lett.*, vol. 117, 152403, doi: 10.1063/5.0019024.

Saroha A, Dixit T, Ganapathi K L, Muralidhar M, Murakami M, Rao M S R (2016), "Nanoscale probing of magnetic and electrical properties of YIG/Si (100) thin films grown by pulsed laser deposition," *IEEE Magn. Lett.*, vol. 11, 7102305, doi: 10.1109/LMAG.2020.2985338.

Schmidt G, Hauser C, Trempler P, Paleschke M, Papaioannou E T (2020), "Ultra thin films of yttrium iron garnet with very low damping: A review," *Phys. Status Solidi*, vol. 257, 1900644, doi: 10.1002/pssb.201900644.

Schoen M A W, Thonig D, Schneider M L, Silva T J, Nembach H T, Eriksson O, Karis O, Shaw J M (2016), "Ultra-low magnetic damping of a metallic ferromagnet," *Nat. Phys.*, vol. 12, pp. 839–842, doi: 10.1038/nphys3770.

Stognij A I, Lutsev L V, Bursian V E, Novitskii N N (2015), "Growth and spin-wave properties of thin $Y_3Fe_5O_{12}$ films on Si substrates," *J. Appl. Phys.*, vol. 118, 023905, doi: 10.1063/1.4926475.

Stognij A I, Novitskii N N, Golikova O L, Bespalov A V., Gieniusz R, Maziewski A, Stupakiewicz A, Smirnova M N, Ketsko V A (2017), "Growth of $Y_3Fe_5O_{12}$ films on Si with AlO_x and SiO_2 buffer layers by ion beam sputtering," *Inorg. Mater.*, vol. 53, pp. 1069–1074, doi: 10.1134/S0020168517100156.

Tabuchi Y, Ishino S, Ishikawa T, Yamazaki R, Usami K, Nakamura Y (2014), "Hybridizing ferromagnetic magnons and microwave photons in the quantum limit," *Phys. Rev. Lett.*, vol. 113, 083603, doi: 10.1103/PhysRevLett.113.083603.

Tabuchi Y, Ishino S, Noguchi A, Ishikawa T, Yamazaki R, Usami K, Nakamura Y (2015), "Coherent coupling between a ferromagnetic magnon and a superconducting qubit," *Science*, vol. 349, pp. 405–408, doi: 10.1126/science.aaa3693.

Träger N, Groß F, Förster J, Baumgaertl K, Stoll H, Weigand M, Schütz G, Grundler D, Gräfe J (2020), "Single shot acquisition of spatially resolved spin wave dispersion relations using X-ray microscopy," *Sci. Rep.*, vol. 10, 18146, doi: 10.1038/s41598-020-74785-4.

Yamada K, Kogiso K, Shiota Y, Yamamoto M, Yamaguchi A, Moriyama T, Ono T, Shima M (2020), "Dependence of Gilbert damping constant on microstructure in nanocrystalline YIG coatings prepared by co-precipitation and spin-coating on a Si substrate," *J. Magn. Magn. Mater.*, vol. 513, 167253, doi: 10.1016/j.jmmm.2020.167253.

Yang Y, Liu T, Bi L, Deng L (2021), "Recent advances in development of magnetic garnet thin films for applications in spintronics and photonics," *J. Alloys Compd.*, vol. 860, 158235, doi: 10.1016/j.jallcom.2020.158235.

Zaumseil P (2015), "High-resolution characterization of the forbidden Si 200 and Si 222 reflections," *J. Appl. Crystallogr.*, vol. 48, pp. 528–532, doi: 10.1107/S1600576715004732.

Zhang X, Zou C L, Jiang L, Tang H X (2014), "Strongly coupled magnons and cavity microwave photons," *Phys. Rev. Lett.*, vol. 113, 156401, doi: 10.1103/PhysRevLett.113.156401.

Zhao Y, Li Y, Zhu S, Chen C, Yao M, Zhao Y, Hu Z, Peng B, Liu M, Ziyao Z (2021), "Voltage tunable low damping YIG/PMN-PT multiferroic heterostructure for low-power RF/microwave devices," *J. Phys. D Appl. Phys. Phys.*, vol. 54, 245002, doi: 10.1088/1361-6463/abce7c.

Zhao Y, Song Q, Yang S H, Su T, Yuan W, Parkin S S P, Shi J, Han W (2016), "Experimental investigation of temperature-dependent gilbert damping in permalloy thin films," *Sci. Rep.*, vol. 6, 22890, doi: 10.1038/srep22890.

4.4 *Effect of Strain-Induced Anisotropy on Magnetization Dynamics in $Y_3Fe_5O_{12}$ Films Recrystallized on a Lattice-Mismatched Substrate*

Publikacja przedstawia właściwości strukturalne i magnetyczne cienkich warstw granatu itrowo-żelazowego osadzanych na monokrystalicznym granacie itrowo-glinowym. Pokazano, że niedopasowanie parametru sieciowego pomiędzy warstwą a podłożem indukuje naprężenia epitaksjalne, które istotnie wpływają na dynamikę namagnesowania. W szczególności proces krystalizacji warstw z fazy amorficznej w badanym układzie powoduje pojawienie się naprężeń rozciągających w płaszczyźnie warstwy oraz zauważalne zmiany w namagnesowaniu efektywnym. Szerokość linii rezonansowej w funkcji częstotliwości wykazuje ponadto nieliniową zależność, która nie może być opisana równaniem Heinricha (wzór 2.2.15) ani wytłumaczona procesami rozpraszania dwumagnonowego. W celu wyjaśnienia tego zjawiska i zinterpretowania danych eksperymentalnych zaproponowano model teoretyczny wskazujący, że za poszerzenie linii rezonansowej odpowiedzialna jest dyspersja anizotropii indukowanej naprężeniami.

Indywidualny wkład autora w powstanie tej publikacji obejmuje: napisanie pierwszej wersji manuskryptu, analizę danych eksperymentalnych i teoretycznych, analizę literaturową, naniesienie warstw metodą PLD, wykonanie pomiarów VSM, VNA-FMR, pomiarów kątowych rezonansu ferromagnetycznego oraz obliczeń teoretycznych (rys. 3(e,f), rys. 4, rys. 5), wizualizację uzyskanych rezultatów, przygotowanie odpowiedzi na pytania recenzentów i korespondencję z wydawnictwem.

---

scientific reports

Check for updates

OPEN

Effect of strain-induced anisotropy on magnetization dynamics in $Y_3Fe_5O_{12}$ films recrystallized on a lattice-mismatched substrate

Adam Krysztofik[1✉], Sevgi Özoğlu[2,3], Robert D. McMichael[4] & Emerson Coy[5]

We report on the correlation of structural and magnetic properties of $Y_3Fe_5O_{12}$ (YIG) films deposited on $Y_3Al_5O_{12}$ substrates using pulsed laser deposition. The recrystallization process leads to an unexpected formation of interfacial tensile strain and consequently strain-induced anisotropy contributing to the perpendicular magnetic anisotropy. The ferromagnetic resonance linewidth of YIG is significantly increased in comparison to a film on a lattice-matched $Gd_3Ga_5O_{12}$ substrate. Notably, the linewidth dependency on frequency has a negative slope. The linewidth behavior is explained with the proposed anisotropy dispersion model.

In recent years, yttrium iron garnet (YIG) has been an intensively studied material for spintronic, photonic, and magnonic applications, mainly due to the low damping of magnetization precession[1–4]. Because of its potential applications in modern electronic devices, the research interest has been dominated by the development and processing of thin garnet films with perpendicular magnetic anisotropy[5]. Therefore, much scientific effort has been put into tuning the magnetic anisotropy of YIG films on the atomic level. Typical approaches include the tuning via yttrium sites substitution with other rare earth elements[6–11], inducing interfacial strain due to lattice parameter mismatch[12–17], ion implantation[18], or reducing shape anisotropy by film patterning[19,20].

The intended general effect of these approaches on anisotropic film properties is essentially realized and its impact on the magnetization dynamics is understood as well. For instance, in rare earth substituted or doped iron garnets one can expect an increase in Gilbert damping due to enhancement of spin–orbit coupling[7]. However, the mechanism of ferromagnetic resonance (FMR) linewidth broadening for YIG films is less understood. For the layers deposited on any substrate other than lattice-matched GGG, the FMR linewidth is significantly increased mainly due to strain, the polycrystalline structure of the films resulting in magnetocrystalline anisotropy field dispersion or extrinsic effects caused by surface crackings[21–25]. The joint effect of these contributions makes the linewidth analysis ambiguous and hinders further development of the material which is known for possessing the lowest magnetization losses[15,26]. Nonetheless, controlled growth of epitaxial and strained YIG films can provide an opportunity to investigate the linewidth contribution coming only from epitaxial strain.

In the FMR and spin pumping experiments of Wang et al.[12], YIG films deposited on YAG exhibited exceptional crystalline quality, small surface roughness, and high spin mixing conductance of the interface with Pt. Nevertheless, the FMR linewidth of a bare, 73 nm thick YIG film on YAG was increased up to 8.4 mT when compared with YIG/GGG system. The authors suggested that the increase was likely related to the strain-induced defects in the films, although without further discussion. It was also reported that the films underwent a compressive strain which resulted in the easy-plane anisotropy contribution. The studies of YIG deposited on $Sm_3Ga_5O_{12}$, $(Gd_{0.63}Y_{2.37})(Sc_2Ga_3)O_{12}$, $Gd_3(Sc_2Ga_3)O_{12}$ revealed, on the other hand, that tensile strain leads to the emergence of the perpendicular magnetic anisotropy (with easy out-of-plane axis), however, the magnetization damping of such strained films remained to be investigated and explained[13,14].

Another important question concerns the effect of YIG thermal reconstruction on a lattice-mismatched substrate and its influence on the film properties. The deposition of amorphous material and subsequent recrystallization via annealing can provide technological advantages in terms of applicability of the lift-off technique

[1]Institute of Molecular Physics, Polish Academy of Sciences, ul. Smoluchowskiego 17, 60-179 Poznan, Poland. [2]Faculty of Physics, Adam Mickiewicz University, Uniwersytetu Poznanskiego 2, 61-614 Poznan, Poland. [3]Department of Physics, Graduate School of Natural and Applied Sciences, Hakkari University, 30000 Hakkari, Turkey. [4]National Institute of Standards and Technology, Gaithersburg, MD 20899, USA. [5]NanoBioMedical Centre, Adam Mickiewicz University, ul. Wszechnicy Piastowskiej 3, 61-614 Poznan, Poland. ✉email: adam.krysztofik@ifmpan.poznan.pl

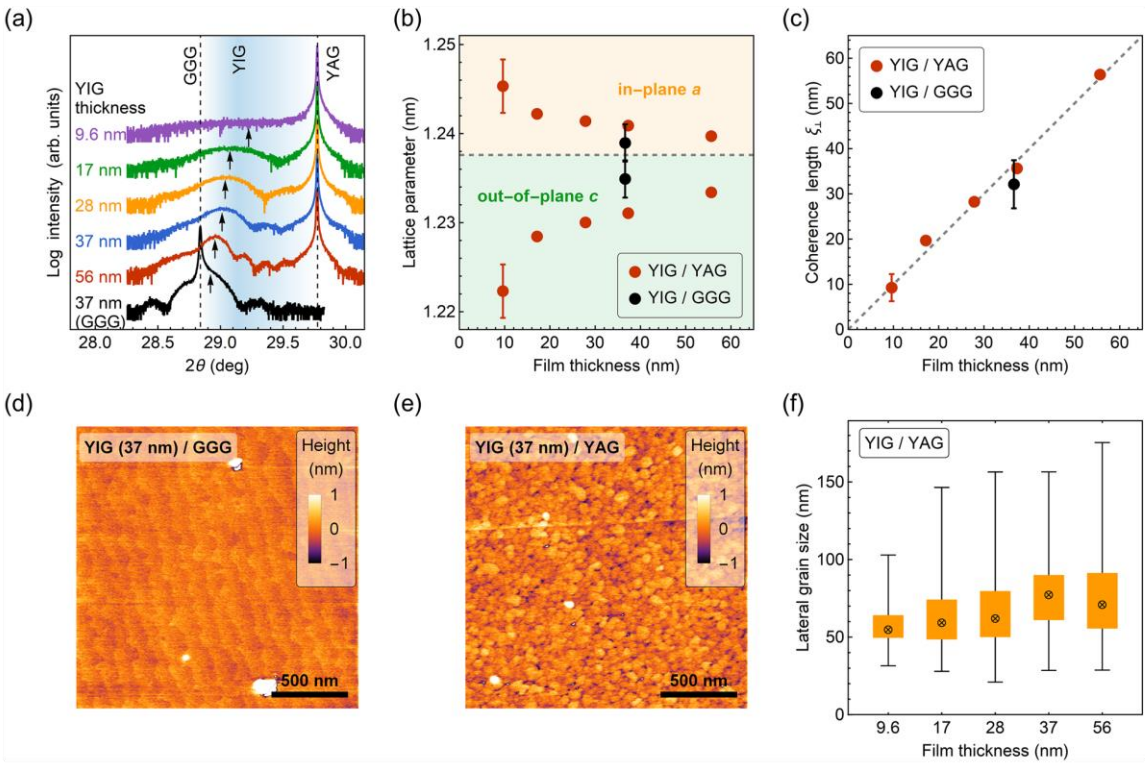

Figure 1. (**a**) X-ray ω-2θ diffraction patterns. (004) reflections of YIG are marked with arrows. The sharp peaks at 29.77° correspond to YAG (004) reflection, while the peak at 28.84° corresponds to GGG (004) reflection. (**b**) Thickness dependence of the determined out-of-plane lattice parameters *c* and calculated in-plane lattice parameters *a*. The dashed line corresponds to the value of a bulk, cubic YIG. Error bars represent one standard deviation uncertainty. (**c**) Thickness dependence of the x-ray coherence length determined via Scherrer equation. The dashed line serves as a guide to the eye showing a one-to-one correlation of the values. (**d**) and (**e**) display surface morphologies of YIG films grown on YAG and GGG substrate. (**f**) Box-whisker plot of the grain size distributions. For each film thickness, the statistics are based on at least 300 grain measurements. The ⊗ marker corresponds to the median value, the bottom and the top box edges to 25th and 75th percentile, respectively, and the black lines to the upper and lower fence, illustrating extreme values in the tails of the distributions.

for film patterning[19,27,28]. For YIG films deposited on GGG substrate using the pulsed laser deposition (PLD) technique, it was shown that the recrystallization does not significantly affect the structural or magnetic properties of the films, which can be the result of the rather low lattice mismatch of the YIG/GGG system[27]. It is however not clear if the same result can be accomplished for a strained YIG film on a lattice-mismatched substrate and if so, to which extent the functional properties of the films can be sustained.

Therefore, the aim of this study can be divided into two general objectives: to investigate the impact of the recrystallization process on structural properties of YIG deposited on YAG substrate and examine FMR linewidth broadening mechanisms for such a system. In this article, we will show that the recrystallization process of YIG films on YAG substrates is possible and that the lattice-mismatch of the substrates poses no impediment for its reconstruction. Moreover, we will show that the epitaxial strain follows unexpected tensile values, providing a unique opportunity for examining the perpendicular magnetic anisotropy. Finally, we provide a comprehensive interpretation for the linewidth broadening of the samples, based on the anisotropy dispersion model, with excellent agreement with our experimental results.

Results and discussion

Structural properties. X-ray diffraction results point to an occurrence of a tensile strain in the films. As shown in Fig. 1a, a gradual shift in the position of YIG (004) reflection is observed when the thickness of the layer changes. For the thickest YIG film (56 nm) on YAG, the (004) reflection nearly coincides with one of the reference film deposited on the GGG substrate. As the film thickness decreases, the films experience a strain and the YIG out-of-plane (OP) lattice parameter *c* approaches the lattice parameter of YAG substrate (1.2006 nm)[29]. Assuming that the volume of a unit cell is conserved, one can estimate in-plane (IP) lattice parameters according

t (nm)	RMS (nm)	c (nm)	a (nm)	$\frac{c-a}{a}$ (%)	M_s (kA/m)	$\mu_0 H_c$ (mT)	M_{eff} (kA/m)	$\mu_0 H_u$ (mT)	$\mu_0 \Gamma_4$ (mT)
9.6	0.4	1.2223	1.2453	− 1.85	–	–	–	–	–
17	1.0	1.2284	1.2422	− 1.11	127 ± 6	4.6 ± 0.3	68 ± 3	71.6 ± 3.8	0.27 ± 0.22
28	1.1	1.2300	1.2414	− 0.92	119 ± 8	5.1 ± 0.2	79 ± 1	57.8 ± 1.3	1.01 ± 0.08
37	0.3	1.2311	1.2409	− 0.79	123 ± 6	5.9 ± 0.3	95 ± 2	37.7 ± 2.5	1.33 ± 0.08
56	0.3	1.2334	1.2397	− 0.51	122 ± 6	5.7 ± 0.2	101 ± 1	30.2 ± 1.3	1.27 ± 0.04
37	*0.2*	*1.2349*	*1.2390*	*− 0.33*	*131 ± 5*	*9.5 ± 0.3*	*103 ± 1*	*27.6 ± 1.3*	*0.01 ± 0.03*

Table 1. Structural and magnetic properties of YIG films deposited on YAG and GGG (italic) substrate.

to $a = \sqrt{V_{\text{bulk}}/c}$, where $V_{\text{bulk}} = 1.2376^3$ nm^3 is a volume of a bulk, cubic YIG unit cell. The comparison of the determined IP and OP lattice parameters shown in Fig. 1b, indicates the IP stretching of a unit cell.

The observed dependence of OP lattice parameter versus film thickness is reversed in comparison to YIG films deposited on YAG at high temperatures[12,30]. The recrystallization process of YIG from an amorphous phase on a lattice-mismatched substrate may therefore result in different epitaxial relations which are subsequently reflected in the magnetic properties. The correlation with magnetic properties is discussed in the Magnetic properties section. The dynamical aspect of the crystal lattice formation during post-deposition annealing remains, however, an open question still to be addressed since one would expect a compressive strain based on a comparison of the lattice parameters of YIG and YAG ($a_{\text{YAG}} < a_{\text{YIG}}$). Nonetheless, the study of Popova et al. showed, that the strain relaxation for lattice-mismatched garnets can be realized via coexistence of the so-called Vernier of misfit and the tilted growth mechanisms[31]. The first type of relaxation occurs when the bond strength within the film or the substrate is larger than the bonding between them. Such a mechanism alone can result in a relatively small residual strain[31]. The second type, however, leads to a tensile strain which is accommodated via rotation (tilting) of the film unit cells with respect to the substrate as well as via dislocations in close vicinity to the interface[31].

Analysis of the Bragg reflection width for the investigated films indicates that the recrystallization occurred throughout the film thickness, although not many Laue oscillations are observed in the XRD spectra. The vertical size of a coherently scattering volume is evaluated by using Scherrer formula[32,33]:

$$\xi_{\perp} = \lambda/(\Gamma_{2\theta} \cos\theta), \tag{1}$$

where $\xi_{\perp}$ is the x-ray coherence length, $\lambda = 0.15406$ nm is the Cu K_{α} radiation wavelength, $\Gamma_{2\theta}$ is the full width at half maximum intensity in the 2θ direction. The determined values of $\xi_{\perp}$ are in exact correspondence with film thicknesses and point to a high crystallinity of the films (Fig. 1c).

AFM surface topography maps show a distinct difference between YIG films grown on YAG and GGG substrate (Fig. 1d, e). While the film deposited on GGG exhibits terraces of the length ≈ 120 nm and height ≈ 0.4 nm, for the films deposited on YAG the recrystallization resulted in the formation of grains of different lateral sizes. The area A of each distinguishable grain was measured and the grain diameter d was estimated ($d = 2\sqrt{A/\pi}$). The statistics of grain size distribution are presented in Fig. 1f with the use of a box-whisker plot. No significant dependence on film thickness is observed and the median value of the grain size is ≈ 60 nm. It should be concurrently noted that the root-mean-square surface roughness (RMS) of the films is around 1 nm or less (Table 1). One can tentatively interpret the observed grains as corresponding to regions characterized by different growth mechanisms (Vernier of misfit and/or the tilted growth).

Magnetic properties. The saturation magnetization M_s of the films has been found consistent across the set of samples (Table 1). The values at around 125 kA/m are congruent with previously reported 118 kA/m for the recrystallized YIG grown by us[27], although slightly decreased in comparison to a bulk YIG at 140 kA/m. The small deviation from the bulk value can be understood as a result of subtle oxygen and cation nonstoichiometry[34]. Contrary to the YIG/GGG sample exhibiting coercivity of $\mu_0 H = 0.4$ mT and rectangular hysteresis loop measured along IP easy axis [110], the hysteresis loop for YIG film deposited on YAG, reveals increased coercivity of $\mu_0 H = 4.5$ mT and remanent to saturation magnetization ratio of $M_r/M_s = 0.4$ (Fig. 2d). Additionally, a rounded saturation of the magnetization reversal curve for OP measurement is visible. The observed magnetostatic response has been found typical for the strained films[12–14,35,36].

Angle-resolved FMR measurements indicate that the YIG unit cells are well-ordered in-plane. The results displayed in Fig. 2e clearly show that the films possess magnetocrystalline anisotropy with IP fourfold symmetry. By using the Kittel equation (see derivation in the Supplementary Information)[37]:

$$f = \frac{\mu_0 \gamma}{2\pi} \sqrt{(H + H_c \cos 4\theta_H)\left(H + \frac{1}{4} H_c (3 + \cos 4\theta_H) + M_{\text{eff}}\right)}, \tag{2}$$

$$M_{\text{eff}} = M_s - H_u, \tag{3}$$

the magnetocrystalline anisotropy field H_c was evaluated from the dependence of resonance magnetic field H versus IP angle θ_H at a constant frequency $f = 20.000$ GHz. In Eq. (2), γ is the gyromagnetic ratio and H_u is the uniaxial, out-of-plane anisotropy field. The obtained values of $\mu_0 H_c$ (juxtaposed in Table 1), range from 4.6 to 9.5 mT, in agreement with the data reported for bulk and thin YIG films (1.2–8.7 mT)[12,27,34,38,39].

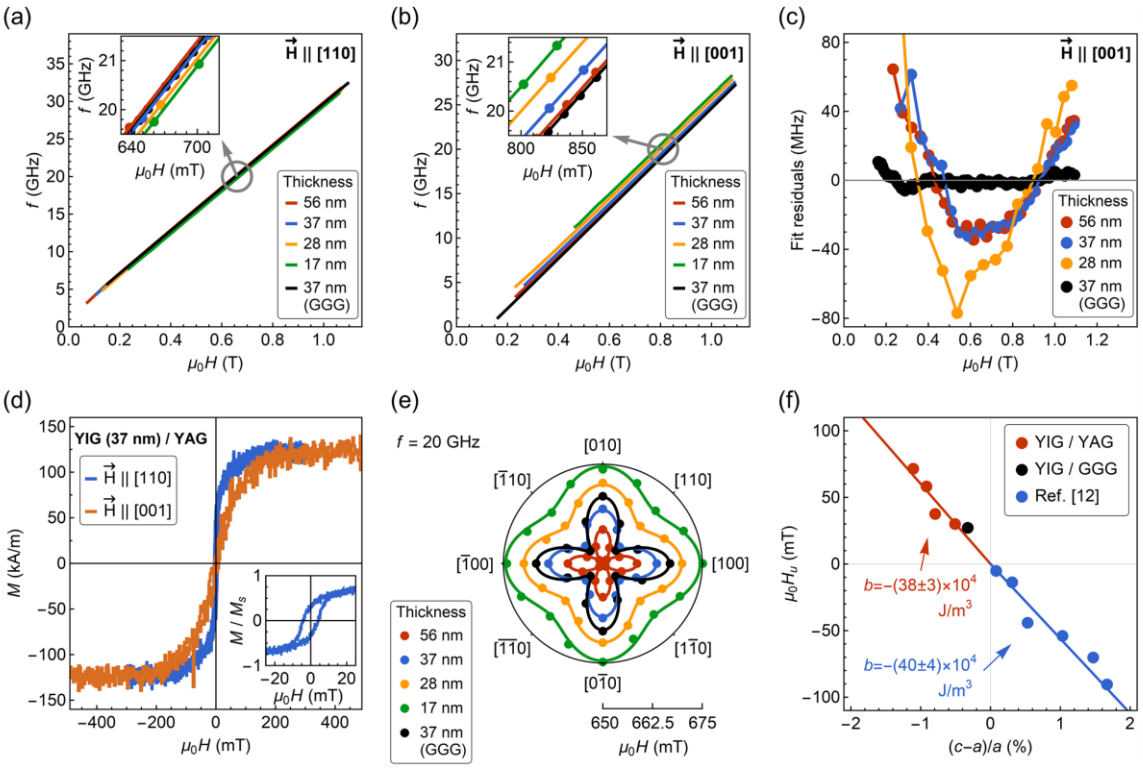

Figure 2. (**a**) and (**b**) show frequency versus resonance field dependencies for magnetic field applied along in-plane [110] and out-of-plane [001] directions, respectively. The insets display enlarged regions near $f = 20$ GHz. (**c**) Fit residuals obtained from a fitting with Eq. (4) for the out-of-plane measurement configuration. Due to larger linewidth and lower signal-to-noise ratio, the residuals for the 17 nm thick film varied randomly in the range of −45 to 60 MHz, and therefore, have been omitted. (**d**) Hysteresis loops of 37 nm thick film deposited on YAG. Diamagnetic contribution from the substrate was subtracted from the raw data. Inset shows the enlarged view at the low fields for $\vec{H} \parallel [110]$. (**e**) In-plane angular dependence of the resonance field recorded at a constant frequency $f = 20$ GHz. (**f**) Out-of-plane uniaxial anisotropy field as a function of the tetragonal distortion of YIG unit cell.

To investigate the influence of strain on magnetic anisotropy, we use broadband FMR measurements. Frequency versus resonance magnetic field dependence is analyzed for the data taken along easy IP direction [110] (Fig. 2a). The values of M_{eff} are determined from the fitting to Eq. (2) with $\theta_H = 45°$. Subsequently, by using Eq. (3), uniaxial OP anisotropy field H_u is calculated assuming constant $M_s = 125$ kA/m following the results obtained with VSM magnetometry.

The strain-induced anisotropy field H_u scales linearly with the tetragonal distortion of the YIG unit cell $(c - a)/a$, and the observed tensile strain results in positive values of the anisotropy field H_u (Fig. 2f). In comparison to YIG films deposited on YAG at high temperatures, which experienced a compressive strain, the negative values of H_u were reported, that corresponds to the easy-plane anisotropy contribution[12]. This shows that the strain tunability of the YIG anisotropy depends not only on the film thickness but also on the crystal growth conditions. From the slope of $\mu_0 H_u = b\frac{2}{M_s} \cdot \frac{c-a}{a}$ dependence[9,12], the magnetoelastic constant is evaluated $b = -(38 \pm 5) \times 10^4$ J/m^3, which is within the range $-(26$ to $47) \times 10^4$ J/m^3 reported for bulk and thin-film YIG[12,16]. Regardless of the exact type of the unit cell distortion, the anisotropy response due to strain engineering appears to be governed by the magnetoelastic constant as shown in Fig. 2f.

The frequency versus resonance field dependence for a perpendicularly applied magnetic field (Fig. 2b), yields the equivalent values of M_{eff} as for the IP applied field within 8% margin of error. However, the fitting according to the Kittel equation for the OP oriented magnetic field:

$$f = \frac{\mu_0 \gamma}{2\pi}(H + H_c - M_{\text{eff}}), \tag{4}$$

reveals an unexpected, U-shaped dependency in the fitting residuals provided by the high accuracy of the FMR technique (Fig. 2c). It should be highlighted that the measurements were carried out at the magnetic fields $H > M_{\text{eff}}$, which are sufficient enough to saturate the magnetization following Stoner-Wohlfarth free energy model and we estimate that the precision of the magnetic field alignment with the film normal is better than

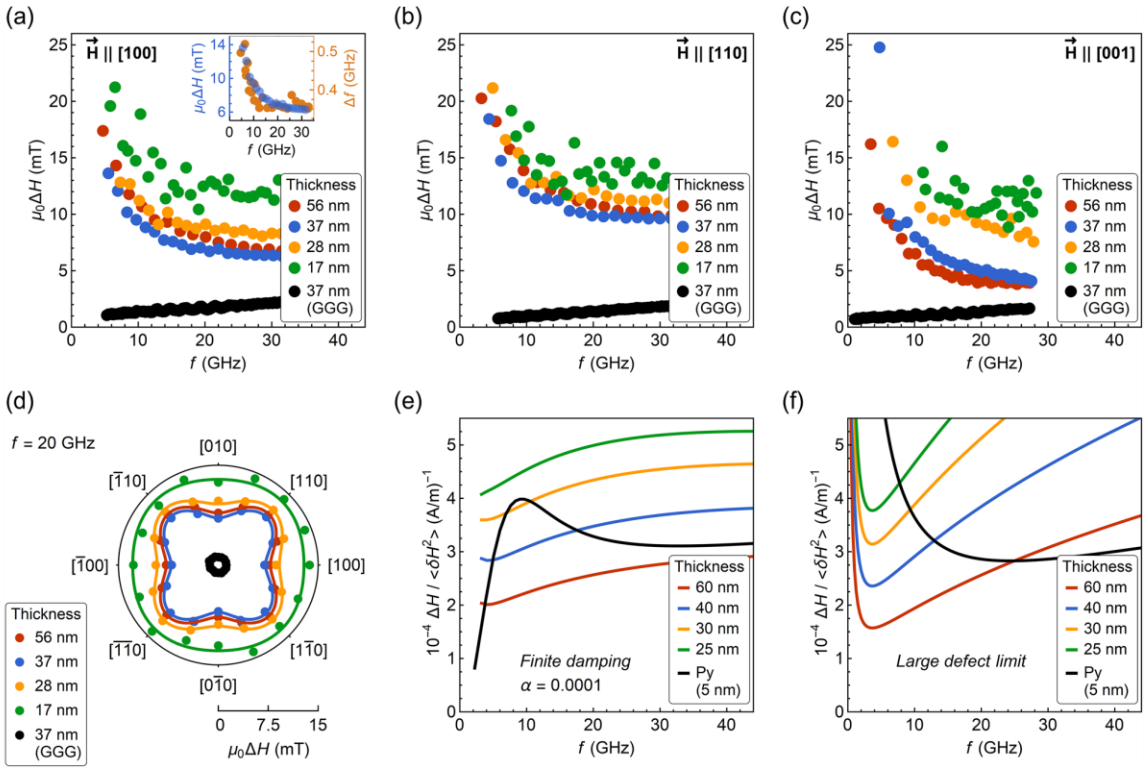

Figure 3. (**a**)-(**c**) Linewidth dependence on frequency for different orientations of the magnetic field with respect to crystallographic directions. The inset in (**a**) shows a comparison of linewidth changes for the field- and frequency-swept measurements of 37 nm thick film. (**d**) In-plane angular dependence of linewidth recorded at a constant frequency $f = 20$ GHz. (**e**) and (**f**) Two-magnon contribution to the linewidth as a function of frequency calculated for finite damping (**e**) and large defect limit (**f**). The color lines correspond to films with a saturation magnetization of $M_s = 120$ kA/m, while the black line denoted as "Py", corresponds to a film with $M_s = 800$ kA/m.

1°. The U-shaped dependency is not observed for the film deposited on GGG substrate, therefore, it might be ascribed as a resultant of a strain inhomogeneity.

The FMR linewidths (FWHM) for the films deposited on YAG are significantly increased compared to the reference film deposited on GGG, and the data vaguely suggests the two-magnon scattering (TMS) contribution. As shown in Fig. 3a-c, the linewidth ΔH noticeably reduces for OP measurement configuration ($\vec{H}||[001]$) with respect to the IP measurements carried out for $\vec{H}||[100]$ or $\vec{H}||[110]$. Although this can be seen for the two thickest films, it is however not observed for the 28 and 17 nm thick layers for which one can expect the effect to be more expressed[40,41]. Another indication of TMS presence (usually considered as a characteristic) are the apparent variations in the IP angular analysis of the linewidth exhibiting fourfold symmetry (Fig. 3d). The TMS contribution is given by:

$$\Delta H_{2mag} \propto \Gamma_4 \cos 4(\theta_H - \theta_4) \arcsin \frac{f}{\sqrt{f^2 + f_0^2} + f_0}, \tag{5}$$

where $f_0 = \mu_0 \gamma M_{\text{eff}}$ and $\theta_4 = 45°$ is the angle of the maximum scattering rate[42–44]. The TMS strength coefficients Γ_4 for YIG/YAG films are of the order of ≈ 1.0 mT and relatively low in comparison to the magnitude of the linewidths ≈ 10 mT (Table 1). No systematic dependence of Γ_4 on thickness is observed, yet the magnitude of Γ_4 for the thinnest film is the lowest, contrary to the expectations provided by the TMS model.

For YIG/YAG films we observe an increase in linewidth broadening at low magnetic fields for all measured crystallographic directions, i.e., [100], [110], and [001] (Fig. 3a-c). The $\Delta H(f)$ dependencies are not linear and the slope of $\Delta H(f)$ is negative even at the highest frequencies, although the measurements were carried out at magnetic fields $H > M_{\text{eff}}$. Evaluation of the Gilbert damping parameter α is therefore not feasible according to:

$$\mu_0 \Delta H = \alpha \frac{4\pi}{\gamma} f + \mu_0 \Delta H_0. \tag{6}$$

Clearly, an extrinsic contribution dominates over the intrinsic Gilbert term in Eq. (6) up to frequencies of 30 GHz. To investigate if this behavior can be attributed to the so-called field dragging effect[45], we have additionally performed frequency swept measurements. The result presented in the inset in Fig. 3a, shows that that frequency swept linewidth also increases at the low magnetic fields. Therefore, the broadening increase cannot be correlated with this kind of response, congruently with IP magnetization reversal curves from which we find magnetization saturation above 130 mT. For the reference film deposited on GGG, we determine $\alpha = (5.4 \pm 0.6) \times 10^{-4}$ and the inhomogeneous linewidth broadening $\mu_0 \Delta H_0 = 0.72 \pm 0.19$ mT.

The abovementioned TMS contribution may suggest that the increase in linewidth broadening at low magnetic fields is also a result of TMS processes. The classical model of extrinsic FMR linewidth predicts such an increase for a 5 nm thick film with the saturation magnetization of 800 kA/m, exchange length of 5 nm, and the defect size of 100 nm[41]. In Fig. 3e,f, the linewidth broadening for such a case is displayed with a black line for finite damping $\alpha = 1 \times 10^{-4}$ and large defect limit, respectively. The calculations were based on the Eq. 28 and 42 in Ref.[41]. However, for much smaller saturation magnetization (120 kA/m) and exchange length of 17 nm for YIG, the model predicts qualitatively opposite changes in linewidth for film thicknesses ranging from 25 to 60 nm (Fig. 3e,f). For magnetic parameters of YIG, the linewidth increases for frequencies above 3 GHz. This suggests that another extrinsic effect is responsible for the linewidth broadening at low magnetic fields. The modeling for such contribution is proposed in the following section.

Anisotropy dispersion model of FMR linewidth. We consider a thin film that is comprised of a set of non-interacting regions and assume that the inhomogeneous strain leads to the dispersion of uniaxial out-of-plane anisotropy, i.e., the magnitude of the anisotropy field vary in different regions and the anisotropy axis is tilted from the film normal. The cubic magnetocrystalline anisotropy is neglected to investigate the effect coming only from the uniaxial anisotropy. The analysis aims to examine resonant frequency distributions arising from the dispersion of uniaxial anisotropy for such sectioned thin film and to investigate if it can provide a qualitative agreement with the experiment.

For each region of the film, the total free energy F,

$$F = F_{\mathrm{Zee}} + F_d + F_u^*, \tag{7}$$

includes the Zeeman energy F_{Zee}, the demagnetizing energy F_d and the uniaxial anisotropy energy F_u^*, which axis orientation is defined by the angles θ_u and ϕ_u as shown in Fig. 4a. For certain values of H_u, θ_u and ϕ_u, the magnetization orientation (expressed by the angles θ_m and ϕ_m), is numerically calculated from the minimum of free energy: $\partial F/\partial \theta_M = 0$ and $\partial F/\partial \phi_M = 0$. An example illustrating a solution for these conditions is shown in Fig. 4b. Subsequently, a resonant frequency f_r for a single film region is derived from the Smit-Beljers equation (see Eq. S6 in the Supplementary Information).

The resonant frequency distribution $\mathrm{P}(f_r)$ with FWHM linewidth Δf_r, as shown in Fig. 4d, is obtained by taking into account the dispersion of uniaxial anisotropy:

1. H_u varying according to Gaussian distribution with a mean value of $\bar{H}_u = 50$ mT and standard deviation $\sigma_{H_u} = 10$ mT (inset in Fig. 4c);
2. tilting of uniaxial anisotropy axis that is described with Gaussian distribution of angle β with a mean value $\bar{\beta}$ and standard deviation σ_β (Fig. 4c), since experimental results have not indicated any induced in-plane anisotropy, other than magnetocrystalline, cubic anisotropy.

The angle β is related to θ_u and ϕ_u by $\cos\beta \equiv \sin\theta_u \sin\phi_u$. To probe the distributions of H_u and β, we use 10^5 sampling points and exclude the values that are larger or smaller than three standard deviations from the mean value. For the calculations, we have taken the magnetization saturation $M_s = 120$ kA/m.

A resonant line $\mathcal{L}(f)$ for a film comprised of non-interacting regions can be derived from:

$$\mathcal{L}(f) = \int \mathrm{P}(f_r)\, \mathrm{L}(f - f_r)\, df_r, \tag{8}$$

where

$$\mathrm{L}(f - f_r) \propto \frac{\left(\frac{1}{2}\Delta f\right)^2}{(f - f_r)^2 + \left(\frac{1}{2}\Delta f\right)^2} \tag{9}$$

is the Lorentz function, in which Δf is the FWHM linewidth related to the Gilbert damping parameter α:

$$\Delta f = \alpha \frac{4\pi}{\mu_0 \gamma} f \frac{\partial f}{\partial H}. \tag{10}$$

In the limiting case of $\Delta f \to 0$, the FWHM of $\mathcal{L}(f)$ tends to Δf_r, and vice versa, when $\Delta f_r \to 0$, the FWHM of $\mathcal{L}(f)$ tends to Δf. As we have not experimentally observed Gilbert damping contribution in resonance linewidth dependence on frequency for YIG/YAG films, we conclude that the FWHM linewidth is described primarily by Δf_r.

The Δf_r dependency on frequency obtained within this model agree well with our experimental results. For $\bar{\beta} = 20°$ and $\sigma_\beta > 0°$, the increase in linewidth at low magnetic fields is found for both in-plane and out-of-plane applied magnetic fields (Fig. 4e). This strongly suggests that the axis of the strain-induced anisotropy for

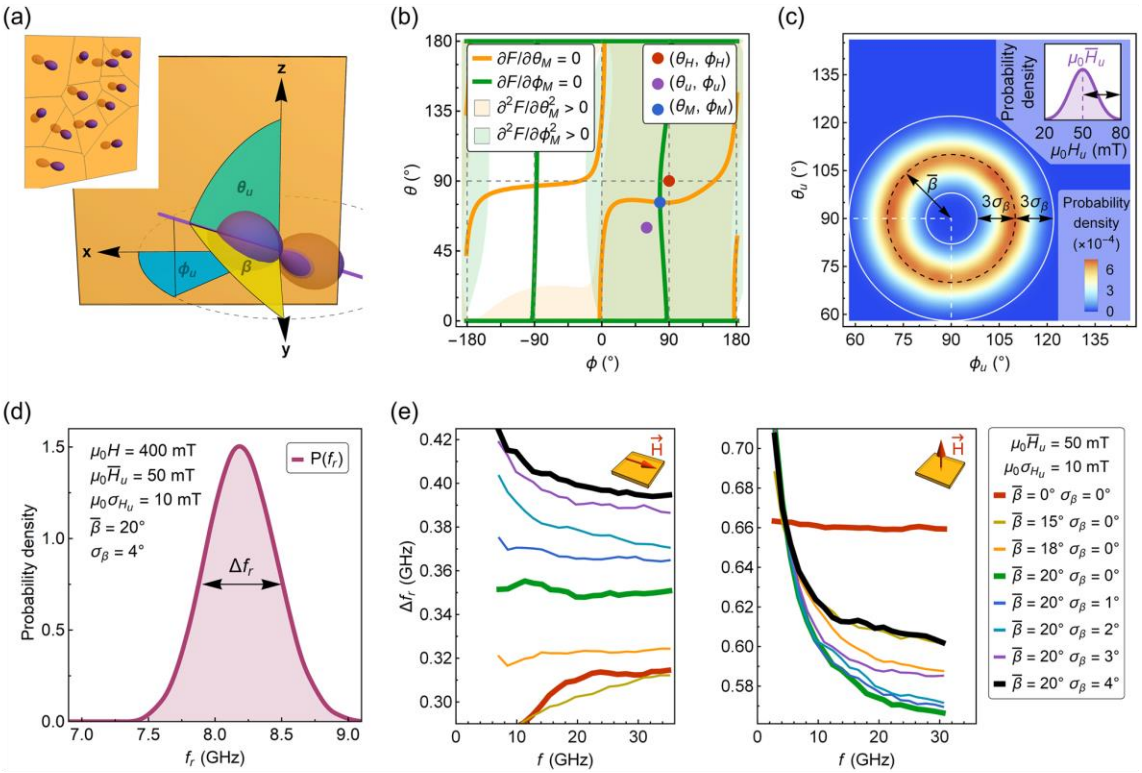

Figure 4. (**a**) Coordinate system used to describe the orientation of uniaxial anisotropy axis, the magnetization, and the applied field. Film lies in the x–z plane, normal to the film is along the y-direction. Inset schematically shows a film comprised of noninteracting regions with different orientations of uniaxial anisotropy axis. (**b**) Equilibrium orientation of magnetization determined from the condition of the free energy minimum with a tilted axis of uniaxial anisotropy. The example is given for the OP applied magnetic field $\mu_0 H = 200$ mT. (**c**) Gaussian distribution of the uniaxial anisotropy axis orientation. Inset shows the Gaussian distribution of the uniaxial anisotropy field and the arrows mark three standard deviations from the mean value ($3\,\sigma_{H_u}$). (**d**) Exemplary distribution of the calculated resonance frequencies for the out-of-plane magnetic field $\mu_0 H = 400$ mT. (**e**) FWHM linewidth Δf_r as a function of frequency for the in-plane applied magnetic field and the out-of-plane applied magnetic field (see the insets). All dependencies were calculated assuming $\bar{H}_u = 50$ mT and $\sigma_{H_u} = 10$ mT. The plot legend on the right side is valid for both IP and OP applied magnetic field. For $\bar{\beta} = 0°$ and $\sigma_\beta = 0°$ (red line), a constant broadening of the linewidth for OP magnetic field orientation and decreasing linewidth at low magnetic fields for IP orientation is observed. The tilting of the uniaxial anisotropy axis specified by $\bar{\beta} = 20°$ (green line) results in constant broadening and decreasing linewidth for IP and OP magnetic field, respectively. The decreasing linewidth as a function of frequency is found for both IP and OP magnetic field when $\sigma_\beta > 0°$.

YIG/YAG films is tilted from the perpendicular direction and dispersed. Moreover, the linewidth broadening due to the dispersion of the anisotropy has a semiquantitative agreement with the experiment. The values of $\Delta f_r \approx 0.3$–0.7 GHz are of the same range of magnitude as the determined linewidth for YIG/YAG samples ≈ 0.34–0.52 GHz (see inset in Fig. 3a). Furthermore, the model predicts a similar type of discrepancy between calculated $f(H)$ dependence and the Kittel equation for OP resonance measurements (Fig. 5a,b). The fit residuals obtained from a fitting with Eq. (4), exhibit a comparable U-shaped dependency as found experimentally (Fig. 2c). At the same time, the OP magnetization component M_y (mean over the film regions) displays only a minuscule decrease with decreasing magnetic field (Fig. 5c). This suggests that the tilting of magnetization can be hardly observed in the magnetization reversal curves at magnetic fields $H > M_{\text{eff}}$.

The main limitation of the proposed model comes from the assumption of non-interacting regions. Therefore, it does not provide accurate predictions at the magnetic fields close to the magnetization reversal, which in the FMR experiment, were not accessible due to large linewidth and consequently lack of FMR signal. Accordingly, the modeling was carried out at the field range from 0.2 to 1.2 T. Exchange and dipole interactions within and between the grains[46,47], the distribution of uniaxial anisotropy at a certain correlation length would be crucial for quantitative estimation of remanent magnetization M_r as well as for theoretical investigation of the magnetization reversal process. The proposed model can thus provide overestimated values of M_r and coercive

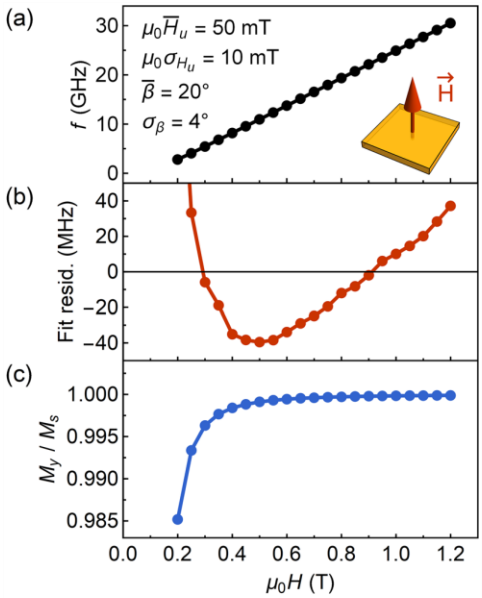

Figure 5. (**a**) Calculated Kittel relation for the out-of-plane magnetic field. Gaussian distributions of uniaxial anisotropy field H_u and angle β are specified inside the plot. (**b**) Fit residuals obtained from a fitting of dependency shown in (**a**) with Eq. (4). (**c**) Out-of-plane magnetization component as a function of the magnetic field.

field. Notwithstanding the foregoing, in hysteresis loops of YIG films deposited on YAG, we clearly observe the decreased remanence and increased coercivity.

Conclusions

In summary, the recrystallization of YIG on the lattice-mismatched substrate can result in different structural and magnetic properties when compared to the high-temperature deposition. As a consequence of the tensile strain, the positive values of the out-of-plane anisotropy field have been determined paving a path toward the attainment of the much-desired perpendicular anisotropy. We anticipate that, as shown here, the film growth conditions and strain control may play a significant role in the anisotropy tuning of other garnets as well. The mechanisms of the strain relaxation can lead to unexpected unit cell distortions, especially when inferred solely from a direct comparison of film and substrate lattice parameters. Moreover, the strain has a significant impact on FMR linewidth. For YIG/YAG films, the linewidth has been found noticeably increased, and the $\Delta H(f)$ dependency is characterized by an unusual negative slope across the entire frequency range from 5 to 30 GHz. The linewidth behavior was explained within the anisotropy dispersion model. Finally, good agreement of experimental findings with theoretical predictions suggests that the anisotropy axis is tilted from the film normal and dispersed. Therefore, we conclude that the strain homogeneity plays a crucial role in the attainment of narrow FMR linewidths reflecting low magnetization damping of the films.

Methods

YIG films with thicknesses ranging from 9.6 nm to 56 nm were deposited at room temperature onto (001)-oriented $Y_3Al_5O_{12}$ (YAG) substrates using the pulsed laser ablation technique (Nd:YAG laser, 355 nm). The pulse frequency of 2 Hz yielded a growth rate of ≈ 0.65 nm/min. The base pressure of the vacuum chamber was 8×10^{-6} Pa (8×10^{-8} mbar) and the partial pressure of oxygen was set to 2.4×10^{-2} Pa (2.4×10^{-4} mbar). After the deposition, the films were annealed *ex-situ* in air for 3 h at 800 °C. All samples were treated in a single annealing process for proper comparison. For reference, a 37 nm film was simultaneously deposited on a YAG substrate and a (001)-oriented $Gd_3Ga_5O_{12}$ (GGG) substrate and reconstructed in the same process.

The structural properties of the films were investigated using high-resolution X-ray diffraction (XRD) with a four-crystal Ge (220) monochromator. The 2Theta/Omega scans allowed for a direct determination of the out-of-plane lattice parameters. The nominal values of film thicknesses were confirmed with X-ray reflectivity measurements. The surface morphology was examined with atomic force microscopy (AFM). The magnetic properties were investigated with a vibrating sample magnetometer (VSM) and broadband ferromagnetic resonance (VNA-FMR). All measurements were performed at room temperature and all uncertainties are one standard deviation unless otherwise noted.

Received: 1 May 2021; Accepted: 23 June 2021
Published online: 07 July 2021

References

1. Coll, M. *et al.* Towards oxide electronics: A roadmap. *Appl. Surf. Sci.* **482**, 1–93 (2019).
2. Schmidt, G., Hauser, C., Trempler, P., Paleschke, M. & Papaioannou, E. T. Ultra thin films of yttrium iron garnet with very low damping: A review. *Phys. Status Solidi* **257**, 1900644 (2020).
3. Yang, Y., Liu, T., Bi, L. & Deng, L. Recent advances in development of magnetic garnet thin films for applications in spintronics and photonics. *J. Alloys Compd.* **860**, 158235 (2021).
4. Jin, L. *et al.* Pulsed laser deposition grown yttrium-iron-garnet thin films: Effect of composition and iron ion valences on microstructure and magnetic properties. *Appl. Surf. Sci.* **483**, 947–952 (2019).
5. Zanjani, S. M. & Onbasli, M. C. Predicting new iron garnet thin films with perpendicular magnetic anisotropy. *J. Magn. Magn. Mater.* **499**, 166108 (2020).
6. Soumah, L. *et al.* Ultra-low damping insulating magnetic thin films get perpendicular. *Nat. Commun.* **9**, 1–6 (2018).
7. Ciubotariu, O., Semisalova, A., Lenz, K. & Albrecht, M. Strain-induced perpendicular magnetic anisotropy and Gilbert damping of Tm3Fe5O12 thin films. *Sci. Rep.* **9**, 1–8 (2019).
8. Ortiz, V. H. *et al.* Systematic control of strain-induced perpendicular magnetic anisotropy in epitaxial europium and terbium iron garnet thin films. *APL Mater.* **6**, 121113 (2018).
9. Wang, C. T. *et al.* Controlling the magnetic anisotropy in epitaxial $Y_3Fe_5O_{12}$ films by manganese doping. *Phys. Rev. B* **96**, 224403 (2017).
10. Lin, Y. *et al.* Bi-YIG ferrimagnetic insulator nanometer films with large perpendicular magnetic anisotropy and narrow ferromagnetic resonance linewidth. *J. Magn. Magn. Mater.* **496**, 165886 (2020).
11. Jermain, C. L. *et al.* Low-damping sub-10-nm thin films of lutetium iron garnet grown by molecular-beam epitaxy. *Appl. Phys. Lett.* **109**, 192408 (2016).
12. Wang, H., Du, C., Hammel, P. C. & Yang, F. Strain-tunable magnetocrystalline anisotropy in epitaxial $Y_3Fe_5O_{12}$ thin films. *Phys. Rev. B - Condens. Matter Mater. Phys.* **89**, 134404 (2014).
13. Fu, J. *et al.* Epitaxial growth of $Y_3Fe_5O_{12}$ thin films with perpendicular magnetic anisotropy. *Appl. Phys. Lett.* **110**, 202403 (2017).
14. Li, G. *et al.* Tunable perpendicular magnetic anisotropy in epitaxial $Y_3Fe_5O_{12}$ films. *APL Mater.* **7**, 041104 (2019).
15. Kumar, R., Samantaray, B. & Hossain, Z. Ferromagnetic resonance studies of strain tuned Bi:YIG films. *J. Phys. Condens. Matter* **31**, 435802 (2019).
16. Vysotskii, S. L. *et al.* The Influence of strains on the ferromagnetic resonance spectrum of submicron yttrium iron garnet films obtained by ion beam sputtering. *J. Commun. Technol. Electron.* **64**, 1398–1406 (2019).
17. Gurjar, G., Sharma, V. & Patnaik, S. Control of magnetization dynamics by substrate orientation in YIG thin films. *Mater. Res. Express* **8**, 066401 (2021).
18. Guo, H. *et al.* Strain doping: Reversible single-axis control of a complex oxide lattice via helium implantation. *Phys. Rev. Lett.* **114**, 256801 (2015).
19. Zhu, N. *et al.* Patterned growth of crystalline $Y_3Fe_5O_{12}$ nanostructures with engineered magnetic shape anisotropy. *Appl. Phys. Lett.* **110**, 252401 (2017).
20. Sarker, M. S., Nakamura, S., Yamahara, H., Seki, M. & Tabata, H. Multifrequency spin-wave propagation for parallel data processing using microstructured yttrium iron garnet thin films. *IEEE Trans. Magn.* https://doi.org/10.1109/tmag.2021.3087812 (2021).
21. Capku, Z., Deger, C., Aksu, P. & Yildiz, F. Origin of perpendicular magnetic anisotropy in yttrium iron garnet thin films grown on Si (100). *IEEE Trans. Magn.* **56**, 2–7 (2020).
22. Yamada, K. *et al.* Dependence of Gilbert damping constant on microstructure in nanocrystalline YIG coatings prepared by co-precipitation and spin-coating on a Si substrate. *J. Magn. Magn. Mater.* **513**, 167253 (2020).
23. Delgado, A., Guerra, Y., Padron-Hernandez, E. & Pena-Garcia, R. Combining the sol gel method and spin coating to obtain YIG films with low FMR linewidth on silicon (100) substrate. *Mater. Res. Express* **5**, 026419 (2018).
24. Stognij, A. I. *et al.* Growth of $Y_3Fe_5O_{12}$ films on Si with AlO_x and SiO_2 buffer layers by ion beam sputtering. *Inorg. Mater.* **53**, 1069–1074 (2017).
25. Krysztofik, A., Özoglu, S. & Coy, E. Magnetization damping in nanocrystalline yttrium iron garnet thin films grown on oxidized silicon. *IEEE Magn. Lett.* https://doi.org/10.1109/LMAG.2021.3086454 (2021).
26. Coy, E. *et al.* High-temperature magnetodielectric $Bi(Fe_{0.5}Mn_{0.5})O_3$ thin films with checkerboard-ordered oxygen vacancies and low magnetic damping. *Phys. Rev. Appl.* **10**, 054072 (2018).
27. Krysztofik, A. *et al.* Ultra-low damping in lift-off structured yttrium iron garnet thin films. *Appl. Phys. Lett.* **111**, 192404 (2017).
28. Li, S. *et al.* Epitaxial patterning of nanometer-thick $Y_3Fe_5O_{12}$ films with low magnetic damping. *Nanoscale* **8**, 388–394 (2016).
29. Nakatsuka, A., Yoshiasa, A. & Yamanaka, T. Cation distribution and crystal chemistry of $Y_3Al_{5-x}Ga_xO_{12}$ ($0 \le x \le 5$) garnet solid solutions. *Acta Crystallogr. Sect. B Struct. Sci.* **55**, 266–272 (1999).
30. Wang, H. L. *et al.* Large spin pumping from epitaxial $Y_3Fe_5O_{12}$ thin films to Pt and W layers. *Phys. Rev. B Condens. Matter Mater. Phys.* **88**, 100406(R) (2013).
31. Popova, E. *et al.* Interplay between epitaxial strain and low dimensionality effects in a ferrimagnetic oxide. *J. Appl. Phys.* **121**, 115304 (2017).
32. Shin, C. S. *et al.* Growth, surface morphology, and electrical resistivity of fully strained substoichiometric epitaxial TiN_x ($0.67 \le x < 1.0$) layers on MgO(001). *J. Appl. Phys.* **95**, 356 (2004).
33. Willmann, H. *et al.* Epitaxial growth of Al-Cr-N thin films on MgO(111). *Thin Solid Films* **517**, 598–602 (2008).
34. Manuilov, S. A., Khartsev, S. I. & Grishin, A. M. Pulsed laser deposited $Y_3Fe_5O_{12}$ films: Nature of magnetic anisotropy I. *J. Appl. Phys.* **106**, 123917 (2009).
35. Zaki, A. M., Blythe, H. J., Heald, S. M., Fox, A. M. & Gehring, G. A. Growth of high quality yttrium iron garnet films using standard pulsed laser deposition technique. *J. Magn. Magn. Mater.* **453**, 254–257 (2018).
36. Zhou, X., Cheng, W., Lin, F., Ma, X. & Shi, W. Effect of post-annealing temperature on the microstructure and magnetic properties of Ce:YIG thin films deposited on Si substrates. *Appl. Surf. Sci.* **253**, 2108–2112 (2006).
37. Baselgia, L. *et al.* Derivation of the resonance frequency from the free energy of ferromagnets. *Phys. Rev. B* **38**, 2237–2242 (1988).
38. Manuilov, S. A. & Grishin, A. M. Pulsed laser deposited $Y_3Fe_5O_{12}$ films: Nature of magnetic anisotropy II. *J. Appl. Phys.* **108**, 013902 (2010).
39. Lee, S. *et al.* Ferromagnetic resonance of a YIG film in the low frequency regime. *J. Appl. Phys.* **120**, 033905 (2016).
40. Arias, R. & Mills, D. L. Extrinsic contributions to the ferromagnetic resonance response of ultrathin films. *Phys. Rev. B Condens. Matter Mater. Phys.* **60**, 7395–7409 (1999).
41. McMichael, R. D. & Krivosik, P. Classical Model of Extrinsic Ferromagnetic Resonance Linewidth in Ultrathin Films. *IEEE Trans. Magn.* **40**, 2–11 (2004).
42. Belmeguenai, M. *et al.* Co_2FeAl thin films grown on MgO substrates: Correlation between static, dynamic, and structural properties. *Phys. Rev. B* **87**, 184431 (2013).
43. Lee, H. K. *et al.* Magnetic anisotropy, damping, and interfacial spin transport in Pt/LSMO bilayers. *AIP Adv.* **6**, 055212 (2016).

44. Oliveira, A. B. *et al.* Filtering magnetic relaxation mechanisms of YIG(001) thin films using ferromagnetic resonance. *J. Magn. Magn. Mater.* **507**, 166851 (2020).
45. Zakeri, K. *et al.* Spin dynamics in ferromagnets: Gilbert damping and two-magnon scattering. *Phys. Rev. B Condens. Matter Mater. Phys.* **76**, 104416 (2007).
46. McMichael, R. D., Twisselmann, D. J. & Kunz, A. Localized ferromagnetic resonance in inhomogeneous thin films. *Phys. Rev. Lett.* **90**, 227601 (2003).
47. McMichael, R. D. A mean-field model of extrinsic line broadening in ferromagnetic resonance. *J. Appl. Phys.* **103**, 07B114 (2008).

Acknowledgements
A.K. acknowledges financial support from the National Science Centre Poland through the PRELUDIUM Project No. 2018/31/N/ST5/03433 and program POWR.03.02.00-00-I032/16. S.O. acknowledges the Erasmus+ program for her stay at Adam Mickiewicz University.

Author contributions
A.K. deposited the films, analyzed the experimental results, wrote the original draft, carried out the FMR and VSM measurements. S.O. carried out AFM, XRD, and XRR measurements under the supervision of E.C. A.K. and R.D.M. developed the linewidth model. A.K. and E.C. proposed the original idea. All authors revised the manuscript and approved its final version.

Competing interests
The authors declare no competing interests.

Additional information
Supplementary Information The online version contains supplementary material available at https://doi.org/10.1038/s41598-021-93308-3.

Correspondence and requests for materials should be addressed to A.K.

Reprints and permissions information is available at www.nature.com/reprints.

Publisher's note Springer Nature remains neutral with regard to jurisdictional claims in published maps and institutional affiliations.

Supplementary Information

Effect of strain-induced anisotropy on magnetization dynamics in $Y_3Fe_5O_{12}$ films recrystallized on a lattice-mismatched substrate

Adam Krysztofik[1]*, Sevgi Özoğlu[2,3], Robert D. McMichael[4], Emerson Coy[5]

[1] *Institute of Molecular Physics, Polish Academy of Sciences, ul. Smoluchowskiego 17, 60-179 Poznań, Poland*

[2] *Faculty of Physics, Adam Mickiewicz University, Uniwersytetu Poznanskiego 2, 61-614 Poznan, Poland*

[3] *Department of Physics, Graduate School of Natural and Applied Sciences, Hakkari University, Hakkari, Turkey*

[4] *National Institute of Standards and Technology, Gaithersburg, MD 20899, USA*

[5] *NanoBioMedical Centre, Adam Mickiewicz University, ul. Wszechnicy Piastowskiej 3, 61-614 Poznań, Poland*

* Corresponding author: adam.krysztofik@ifmpan.poznan.pl

- Derivation of Kittel equations
- X-ray diffraction pattern of 9.6 nm thick YIG film on YAG substrate
- Typical FMR spectra of YIG/YAG and YIG/GGG films

Derivation of Kittel equations

Free energy density for (001) oriented films with lattice distortion is defined as:

$$F = F_{\text{Zee}} + F_d + F_u + F_c, \tag{S1}$$

$$F_{\text{Zee}} = -\mu_0 H M_s \left(\sin\theta_M \sin\theta_H \cos(\phi_H - \phi_M) + \cos\theta_M \cos\theta_H\right), \tag{S2}$$

$$F_d = \frac{1}{2} \mu_0 M_s^2 \sin^2\theta_M \sin^2\phi_M, \tag{S3}$$

$$F_u = -\frac{1}{2} \mu_0 H_u M_s \sin^2\theta_M \sin^2\phi_M, \tag{S4}$$

$$F_c = \frac{1}{2} \mu_0 H_c M_s \left(\alpha_x^2\alpha_y^2 + \alpha_y^2\alpha_z^2 + \alpha_z^2\alpha_x^2\right), \tag{S5}$$

where F_{Zee} is Zeeman energy term, F_d is the demagnetization energy term, F_u is the uniaxial out-of-plane anisotropy term, F_c is the magnetocrystalline cubic anisotropy term and α_x, α_y, α_z are the direction cosines. Expressions of F_d and F_u are defined for a film placed in the x-z plane. To derive Kittel equations, one can use the Smit-Beljers equation:

$$\left(\frac{\omega}{\gamma}\right)^2 = \frac{1}{M_s^2 \sin^2\theta_M}\left(F_{\theta\theta}F_{\phi\phi} - F_{\theta\phi}^2\right), \tag{S6}$$

however, to avoid an angular-dependent mixing it is more convenient to use the expression with Baselgia correction [1]:

$$\left(\frac{\omega}{\gamma}\right)^2 = \frac{1}{M_s^2}\left[F_{\theta\theta}\left(\frac{F_{\phi\phi}}{\sin^2\theta_M} + \frac{\cos\theta_M}{\sin\theta_M}F_\theta\right) - \left(\frac{F_{\theta\phi}}{\sin\theta_M} - \frac{\cos\theta_M}{\sin\theta_M}\frac{F_\phi}{\sin\theta_M}\right)^2\right], \tag{S7}$$

where

$$\begin{aligned} F_\theta &= \frac{\partial F}{\partial \theta_M} \qquad F_{\theta\theta} = \frac{\partial^2 F}{\partial \theta_M^2} \\ F_\phi &= \frac{\partial F}{\partial \phi_M} \qquad F_{\phi\phi} = \frac{\partial^2 F}{\partial \phi_M^2} \\ & \qquad\quad F_{\theta\phi} = \frac{\partial^2 F}{\partial \theta_M \partial \phi_M} \end{aligned} \tag{S8}$$

and $\omega = 2\pi f$ is the angular frequency, γ is the gyromagnetic ratio.

For the in-plane applied magnetic field ($\phi_H = 0°$), Eq. S7 takes the form:

$$f = \frac{\mu_0 \gamma}{2\pi} \sqrt{(H + H_c \cos 4\theta_H)\left(H + \frac{1}{4} H_c (3 + \cos 4\theta_H) + M_{\text{eff}}\right)}, \tag{S9}$$

while for the out-of-plane applied magnetic field ($\theta_H = 90°, \phi_H = 90°$) it yields:

$$f = \frac{\mu_0 \gamma}{2\pi} (H + H_c - M_{\text{eff}}), \tag{S10}$$

where $M_{\text{eff}} = M_s - H_u$ is the effective magnetization.

References

1. Baselgia, L. *et al.* Derivation of the resonance frequency from the free energy of ferromagnets. *Phys. Rev. B* **38**, 2237–2242 (1988).

X-ray diffraction pattern of 9.6 nm thick YIG film on YAG substrate

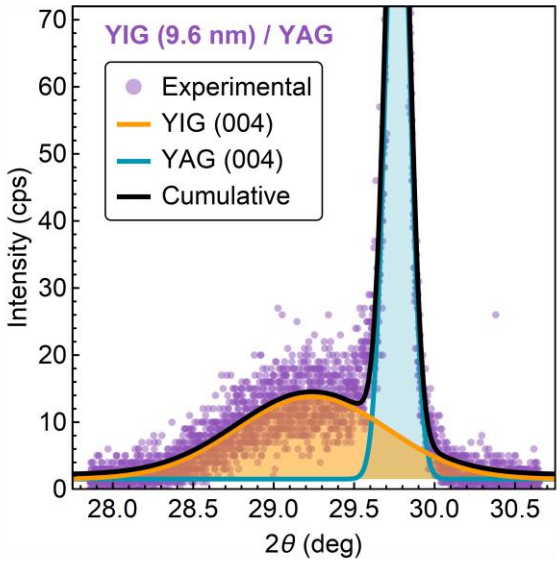

Fig. 1. X-ray diffraction pattern of 9.6 nm thick YIG film.

Typical FMR spectra of YIG/YAG and YIG/GGG films

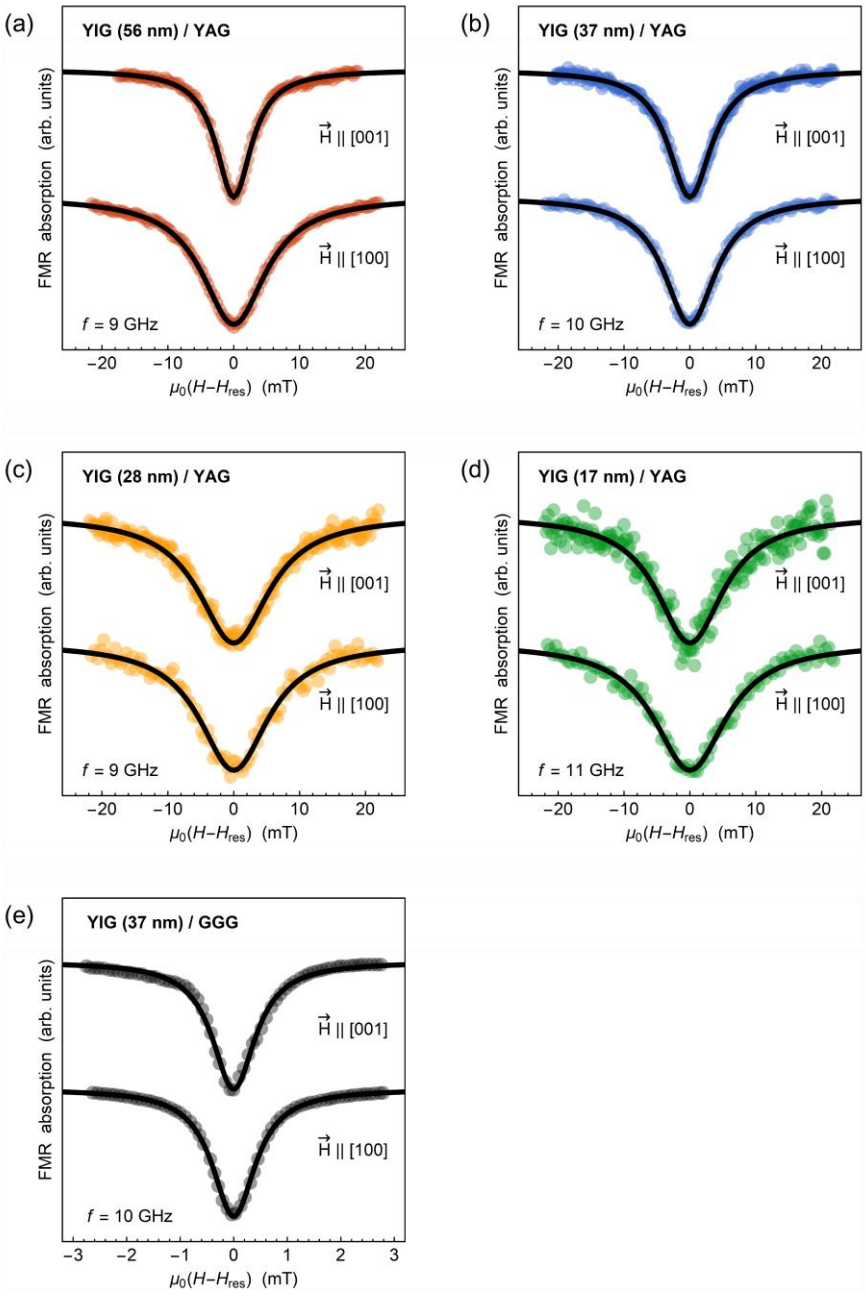

Fig. 2. (a)-(e) Typical FMR spectra taken at $f \approx 10$ GHz.

4.5 *Tuning of Magnetic Damping in $Y_3Fe_5O_{12}$ / Metal Bilayers for Spin-Wave Conduit Termination*

Publikacja przedstawia właściwości strukturalne i magnetyczne cienkich warstw granatu itrowo-żelazowego (YIG) osadzanych na klinowych warstwach irydu, platyny i złota o maksymalnej grubości 7 nm. Oddzielenie warstw YIG od podłoża $Gd_3Ga_5O_{12}$ warstwą metalu powoduje znaczący wzrost efektywnego tłumienia magnetyzacji. W przypadku warstw osadzanych na złocie, pomimo stosunkowo niskiej wartości parametru tłumienia Gilberta $\alpha \approx 8 \cdot 10^{-4}$, parametr poszerzenia linii rezonansowej $\mu_0 \Delta H_0$ mieści się w zakresie 8-15 mT. Pomiary propagacji fal spinowych pozwoliły pokazać, że w tym układzie fale spinowe są silnie tłumione i nie dochodzi do ich propagacji. Przeprowadzone symulacje mikromagnetyczne wskazują, że dwuwarstwy YIG/metal mogą być wykorzystane do skutecznego rozpraszania pakietów fal spinowych w falowodach magnonicznych.

Indywidualny wkład autora w powstanie tej publikacji obejmuje: napisanie pierwszej wersji manuskryptu, analizę danych eksperymentalnych i teoretycznych, analizę literaturową, naniesienie warstw metodą PLD, wykonanie pomiarów XRD, XRR, GIXRD, SEM, VNA-FMR, części pomiarów spektroskopii fal spinowych z wykorzystaniem VNA, obliczeń teoretycznych oraz symulacji mikromagnetycznych, wizualizację uzyskanych rezultatów, przygotowanie odpowiedzi na pytania recenzentów i korespondencję z wydawnictwem.

---

materials

MDPI

Article

Tuning of Magnetic Damping in $Y_3Fe_5O_{12}$/Metal Bilayers for Spin-Wave Conduit Termination

Adam Krysztofik [1,*], Nikolai Kuznetsov [2], Huajun Qin [2], Lukáš Flajšman [2], Emerson Coy [3] and Sebastiaan van Dijken [2]

[1] Institute of Molecular Physics, Polish Academy of Sciences, Smoluchowskiego 17, 60-179 Poznan, Poland
[2] NanoSpin, Department of Applied Physics, Aalto University School of Science, P.O. Box 15100, FI-00076 Aalto, Finland; nikolai.1.kuznetsov@aalto.fi (N.K.); huajun.qin@aalto.fi (H.Q.); lukas.flajsman@aalto.fi (L.F.); sebastiaan.van.dijken@aalto.fi (S.v.D.)
[3] NanoBioMedical Centre, Adam Mickiewicz University, Wszechnicy Piastowskiej 3, 61-614 Poznan, Poland; coyeme@amu.edu.pl
* Correspondence: adam.krysztofik@ifmpan.poznan.pl

Abstract: In this work, we investigate the structural and dynamic magnetic properties of yttrium iron garnet (YIG) films grown onto gadolinium gallium garnet (GGG) substrates with thin platinum, iridium, and gold spacer layers. Separation of the YIG film from the GGG substrate by a metal film strongly affects the crystalline structure of YIG and its magnetic damping. Despite the presence of structural defects, however, the YIG films exhibit a clear ferromagnetic resonance response. The ability to tune the magnetic damping without substantial changes to magnetization offers attractive prospects for the design of complex spin-wave conduits. We show that the insertion of a 1-nm-thick metal layer between YIG and GGG already increases the effective damping parameter enough to efficiently absorb spin waves. This bilayer structure can therefore be utilized for magnonic waveguide termination. Investigating the dispersionless propagation of spin-wave packets, we demonstrate that a damping unit consisting of the YIG/metal bilayers can dissipate incident spin-wave signals with reflection coefficient $R < 0.1$ at a distance comparable to the spatial width of the wave packet.

Keywords: yttrium iron garnet; YIG; ferromagnetic resonance; effective damping parameter; spin-waves; spin wave packet

Citation: Krysztofik, A.; Kuznetsov, N.; Qin, H.; Flajšman, L.; Coy, E.; van Dijken, S. Tuning of Magnetic Damping in $Y_3Fe_5O_{12}$/Metal Bilayers for Spin-Wave Conduit Termination. *Materials* **2022**, *15*, 2814. https://doi.org/10.3390/ma15082814

Academic Editors: Voicu Octavian Dolocan and Sylvain Bertaina

Received: 18 March 2022
Accepted: 8 April 2022
Published: 12 April 2022

1. Introduction

The employment of spin-waves (SW) for performing logic operations is considered to be an innovative concept competing with the standard CMOS paradigm [1–7]. A material of choice for complex SW conduits is yttrium iron garnet (YIG) in the single-crystal phase [8]. The growth of ultra-low damping YIG films has been optimized in the last decade [9–12] and the development of garnet layers is ongoing [13–26]. Hitherto, state-of-art YIG films provide high relaxation times of hundreds of nanoseconds corresponding to millimeter-scale SW decay length [27–29]. These long propagation distances pose questions on how to attenuate SWs when waveguides terminate without causing back reflection and signal interference. In micromagnetic simulations, this problem is solved by applying parabolic or exponential damping conditions near the edges of magnetic structures [30–34]. However, the experimental realization of this approach is not trivial. Up to now, the standard experimental approach has involved the use of elongated SW waveguides, usually with canted ends [27,28,35,36]. Moreover, a recent study showed that the SW intensity is well maintained in nanoscopic, tapered waveguides [37]. Following further miniaturization and an increased packing of SW devices, controlled SW damping will become important in limiting back reflection at open-ended or unused waveguide ports.

In the current paper, we propose the utilization of YIG/metal bilayers for SW conduit termination. We systematically investigate the magnetic properties of crystallized YIG

films on GGG substrates with wedge-shaped metal films. For this study, three consecutive metals in the periodic table were chosen, namely Ir, Pt, and Au, which are resistant to oxidation. This article is organized as follows. In Section 2, we describe the growth methods, sample preparation, and the used experimental apparatus. In Sections 3.1 and 3.2, we present the structural and magnetic properties of the YIG films. In Section 3.3, we analyze the propagation of SW packets in continuous YIG films. In Section 3.4, we investigate SW packet reflection from a damping unit using micromagnetic simulations. Section 4 summarizes the study.

2. Materials and Methods

We use the pulsed laser deposition (PLD) technique to grow 40-nm-thick YIG films (Nd:YAG laser, 355 nm) and magnetron sputtering to deposit thin metal layers. The growth processes were conducted at room temperature for both methods. The GGG substrates were ultrasonicated in acetone and isopropanol before loading into the deposition chamber. Wedge-shaped layers of Pt, Ir, and Au were deposited with a thickness increase of 0.5 nm per millimeter by moving a shutter plate at a constant speed over the sample surface (2 cm $\times$ 0.5 cm) during the deposition process. This resulted in 0–7 nm wedge films and an uncovered substrate area (6 mm in length), which we used as a reference. Subsequently, the samples were transferred to the PLD chamber without breaking the vacuum. The target-to-substrate distance was 5 cm. The pulse frequency of 2 Hz yielded a growth rate of $\approx$0.65 nm/min at the partial oxygen pressure of 2.4×10^{-2} Pa (2.4×10^{-4} mbar) [38]. After the deposition, the bilayers were annealed ex-situ in air for 5 min at 800 °C. For VNA spectroscopy measurements, 150-nm-thick Au microwave antennas with a width of 2 µm were fabricated using direct laser-writing lithography (Laserwriter LW 405), magnetron sputtering, and lift-off.

The structural properties of the films were investigated using X-ray diffraction and grazing incidence X-ray diffraction (Seifert system 3003TT) as well as high-resolution XRD utilizing a four-crystal Ge (220) monochromator (Malvern Panalytical, Malvern, UK, X'pert Pro3 system). The scans provided the out-of-plane lattice parameters. Nominal values of film thicknesses were confirmed with X-ray reflectivity (XRR) measurements (Seifert system 3003TT). The surface topography was investigated with atomic force microscopy (AFM) using a Bruker ICON microscope and scanning electron microscopy (SEM) using FEI Nova NanoSEM 650 with a concentric back-scattered (CBS) detector. From the contrast changes in SEM images, the height-height correlation function (HHCF) was evaluated to estimate the lateral correlation length of a defect [39]. The dynamic magnetic properties were studied with a broadband ferromagnetic resonance setup in field-sweep mode (VNA-FMR), with VNA spectroscopy in frequency-sweep mode utilizing a set of microwave antennas, as well as with super-Nyquist-sampling magneto-optical Kerr effect microscopy (SNS-MOKE) [40]. All measurements were performed at room temperature with an in-plane applied magnetic field. The determined uncertainties are one standard deviation unless noted otherwise. To investigate SW packet propagation, micromagnetic simulations were performed using open-source GPU-accelerated *MuMax3* software [41].

3. Results and Discussions

3.1. Structural Properties

X-ray diffraction patterns (Figure 1a) display a lack of YIG reflections if the YIG film is grown onto Pt, Ir, or Au. For coarse, polycrystalline YIG samples, XRD reflections are expected at 32.326° ((024), 100%), 35.510° ((224), 43%), or 28.835° ((004), 32%) [42].

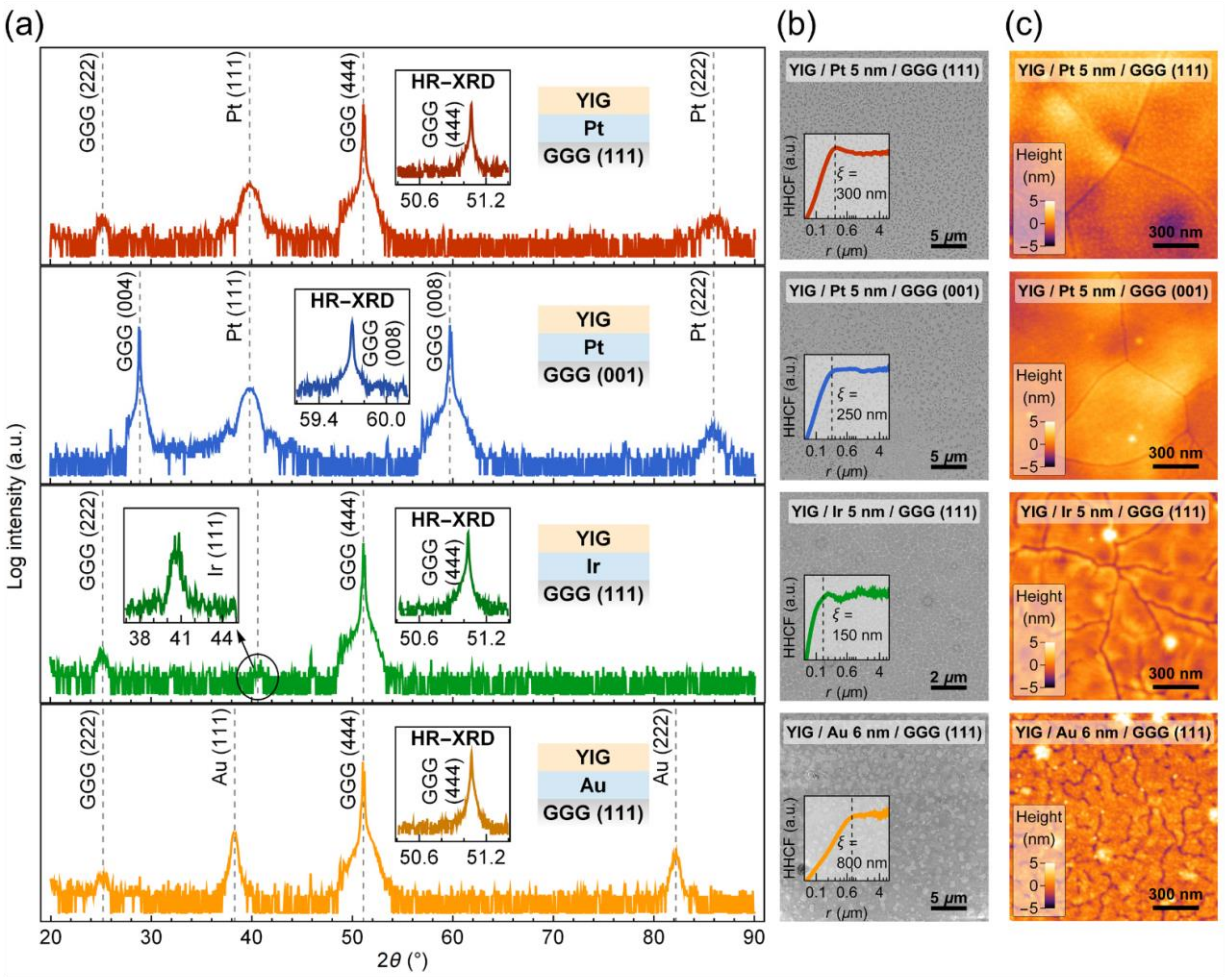

Figure 1. Structural properties of 40-nm-thick YIG films grown on GGG substrates with thin metal layers. (**a**) X-ray diffraction patterns recorded on samples with 5–7 nm metal underlayers. Note that the (222) peaks of the GGG substrate are so-called basis-forbidden reflections due to multiple diffraction [43]. Insets denoted as HR-XRD show high-resolution scans utilizing a four-crystal monochromator. The inset showing the Ir (111) reflection comes from a separate scan with a long statistical exposure. (**b**) SEM surface images. Insets show height-height correlation function (HHCF) as a function of lateral distance r calculated on the basis of SEM contrast changes to evaluate the defect correlation length ξ. (**c**) AFM topography maps.

High-resolution scans around the main reflection of the single-crystal GGG substrate (insets in Figure 1a) further show that the YIG films are not characterized by a strong texture. Similarly to YIG layers deposited on silicon [44], this suggests that the films are nanocrystalline. The large intensity of Pt (111) and Au (111) reflections for 5-nm-thick layers as well as the absence of peaks from other family planes indicate that these metal films are textured. The much smaller intensity of the Ir (111) reflection, being nearly at the level of the background noise, demonstrates polycrystalline film growth of this metal on the GGG substrate. The determined lattice parameters of 0.392 nm for Pt on both GGG (111) and GGG (001), 0.384 nm for Ir, and 0.407 nm for Au are in agreement with the bulk values within a 1% error [45]. To further investigate the structural properties of YIG, we performed GI-XRD scans (see supplementary materials). Despite the small peak-to-background ratio, YIG reflections are clearly measured. From this, we estimated a mean crystallite size of 16.9 $\pm$ 2.7 nm corresponding to $\approx$13 YIG lattice constants. Additionally, XRR results

confirm a nominal YIG film thickness of 40.2 ± 1.3 nm, point to a consistent film density in different samples, but with increased roughness.

SEM and AFM measurements show significant structural defects in the YIG films grown onto the metal layers. In SEM images of the samples (Figure 1b), clear variations are visible in mixed topographic and compositional contrast as recorded using a CBS detector. Differences in defect length scales and size dispersion are also noticeable as inferred by the height-height correlation function (insets in Figure 1b). More thorough information about the surface morphology of YIG is provided by AFM imaging (Figure 1c). For all samples, nanoscale cracking is present, which can be understood as resulting from different thermal expansion coefficients of the metals and the garnets. Interestingly, fracturing of the YIG film is more severe for the Au layer than for Ir or Pt layers of similar thickness. This can be attributed to the early stages of Au shrinking towards the formation of Au nanoparticles or nanorods during the 5 min thermal annealing step [46,47]. This interpretation is congruent with the island-like pattern seen in the SEM images, corresponding to a defect correlation length of 800 nm. The YIG films on Pt exhibit larger flat areas between cracks when compared to Ir or Au. However, we observe additional height variations of ≈5 nm that are most likely caused by inhomogeneous stress in the YIG/Pt system (see bright and dark contrast in Figure 1c). The origin of these deformations is tentatively attributed to the high ductility and malleability of Pt as well as a lower thermal expansion coefficient when compared to Au [48]. Both these factors play a role during the post-annealing of the YIG film for crystallization.

3.2. Magnetization Dynamics

The insertion of a metal layer between a YIG film and a GGG drastically impacts the magnetization dynamics as found by broadband ferromagnetic resonance measurements. First, we analyze the relation between frequency f and resonance magnetic field H using the Kittel equation:

$$f = \frac{\gamma \mu_0}{2\pi} \sqrt{H(H + M_{\text{eff}})}, \tag{1}$$

where M_{eff} is the effective magnetization, γ is the gyromagnetic ratio, and μ_0 is the vacuum permeability. Fitting experimental data to Equation (1) (see supplementary materials), we determine $M_{\text{eff}}^{\text{ref}}$ in the range of 115–190 kA/m for reference YIG films on GGG in agreement with the previous reports [8]. With an increasing metal layer thickness d_m, the value of M_{eff} decreases and it is reduced to 0.7 $M_{\text{eff}}^{\text{ref}}$ for d_m = 6–7 nm (Figure 2a). For very thin metal layers (d_m = 0.5–2.5 nm), however, no significant changes in M_{eff} are observed for Au, while for Pt/GGG (111) the decrease of M_{eff} is small (≈0.92 $M_{\text{eff}}^{\text{ref}}$). The M_{eff} of the YIG film deposited on Ir, on the other hand, diminishes rapidly at the onset of the metal wedge.

The parameters characterizing SW damping (Figure 2b,c), i.e., the Gilbert damping parameter α and the inhomogeneous linewidth broadening ΔH_0 of the YIG films, were evaluated by measuring the dependence of the FMR linewidth ΔH on frequency f:

$$\mu_0 \Delta H = \alpha \frac{4\pi}{\gamma} f + \mu_0 \Delta H_0. \tag{2}$$

At the onset of the Pt or Ir wedge layer, we observe a significant increase of the α parameter, which saturates for metal thicknesses $d_m > 2.5$ nm at $\alpha \approx (150\text{–}180)\cdot 10^{-4}$ for Pt and $\alpha \approx (50\text{–}70)\cdot 10^{-4}$ for Ir. Considering the spin pumping effect, typical values of the spin mixing conductance vary between $5\cdot 10^{17}$ m^{-2} and $7\cdot 10^{18}$ m^{-2}, which corresponds to an increase in the α parameter of $\Delta\alpha \approx (1\text{–}19)\cdot 10^{-4}$ for 40 nm thick YIG [49–51]. This shows that the damping-like torque arising from a nonequilibrium spin accumulation at the metal/YIG interface [52] contributes only weakly to the overall intrinsic damping in the samples [53,54].

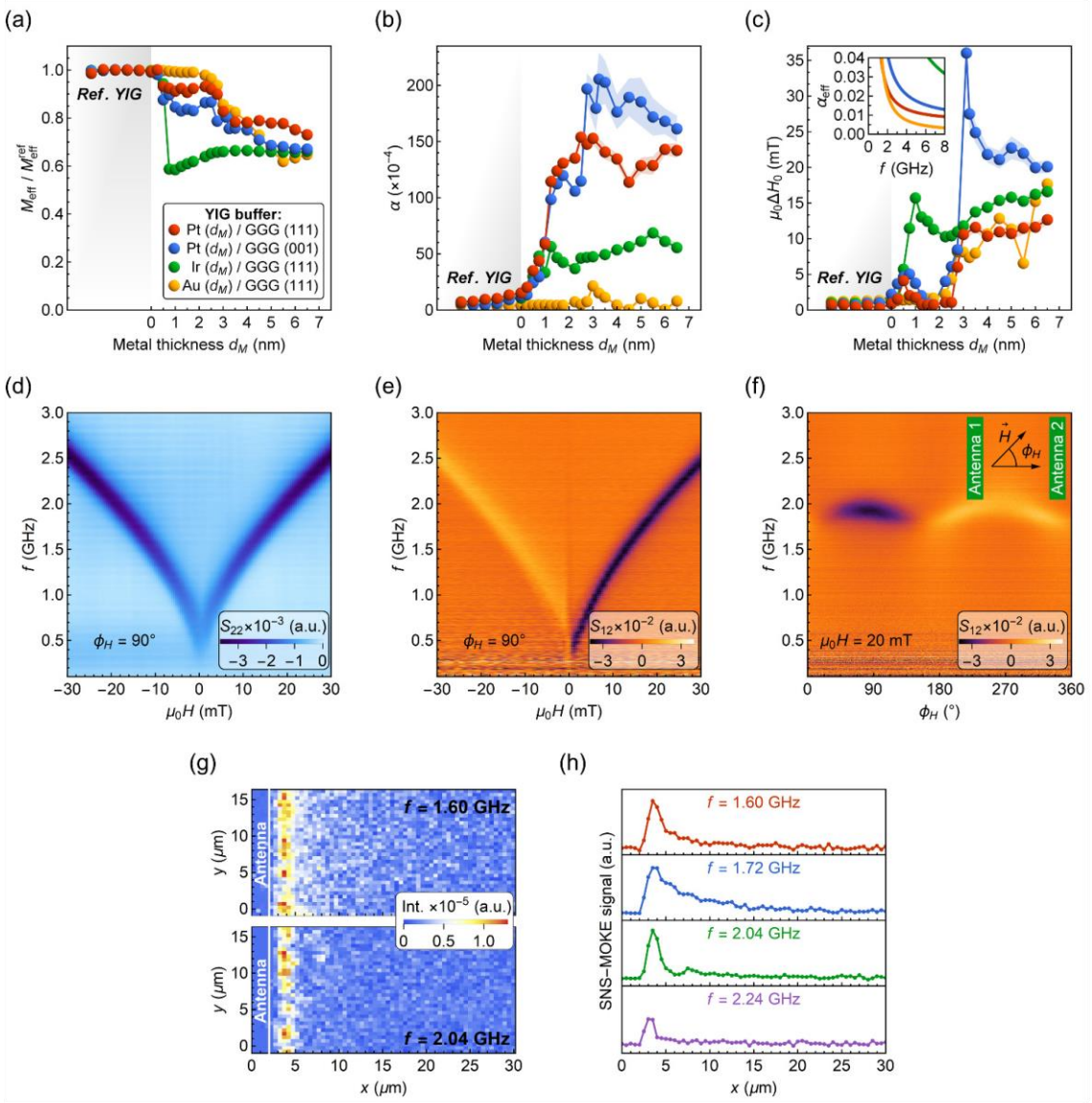

Figure 2. Broadband ferromagnetic resonance results for 40-nm-thick YIG films deposited on different metal underlayers with a nominal thickness d_m. (**a**) Effective magnetization M_{eff} normalized to $M_{\text{eff}}^{\text{ref}}$ of a reference YIG film. (**b**) Gilbert damping parameter α. (**c**) Inhomogeneous linewidth broadening $\mu_0\Delta H_0$. The inset shows calculated values of the effective damping parameter with Equation (3) for a 1-nm-thick metal layer. The color legend depicted in (**a**) also applies to (**b**,**c**). Values marked as reference YIG (shaded section) derive from measurements of the epitaxial film taken at the positions outside the metal wedge. (**d**–**f**) VNA spectroscopy results measured with lithographically patterned antennas for YIG (40 nm)/Au (3.0 nm)/GGG (111). (**d**) Color-coded reflection parameter S_{22} showing the FMR absorption. (**e**) Color-coded transmission parameter S_{12} for the magnetic field aligned parallel to the antennas ($\phi_H = 90°$). (**f**) Color-coded angular dependence of S_{12} spectrum. Inset depicts in-plane magnetic field orientation with respect to the antenna geometry ($\phi_H = 0°$ for the magnetic field aligned perpendicular to the antenna edge). In figures (**d**–**f**), the real part of the scattering parameter S_{pq} is plotted. (**g**,**h**) SNS-MOKE microscopy maps and line profiles recorded at $\mu_0 H = 20$ mT for YIG (40 nm)/Au (3.0 nm)/GGG (111).

Considering the excitation of microwave eddy currents in metal layers, we find this damping contribution to the α parameter to be less than $1{\cdot}10^{-4}$ for 5-nm-thick metal films, and thus negligible [53,55,56]. Therefore, we attribute the increase of α to a deterioration of the structural properties when YIG is grown onto Pt or Ir. Surprisingly, the Au layer does not deteriorate the α parameter ($\approx 8{\cdot}10^{-4}$) for the entire thickness range. Moreover, as shown in Figure 2c, the inhomogeneous linewidth broadening $\mu_0\Delta H_0$ of ≈8–15 mT for $d_{\mathrm{Au}} > 2.5$ nm is more than two times smaller when compared to recently reported values for YIG deposited on oxidized silicon ($\mu_0\Delta H_0 = 31.8$ mT) [44].

The obtained SW damping parameters for YIG/Au may enable coherent SW propagation in this system, which could be used to absorb SWs. To address this issue, we performed VNA spectroscopy measurements of SW transmission signals. Pairs of single-wire microwave antennas with a width of 2 µm were fabricated by photolithography and VNA spectroscopy measurements were conducted on YIG films with $d_{\mathrm{Au}} = 3$, 3.5, and 4 nm, corresponding to $\mu_0\Delta H_0 = 8.1$, 8.0, and 10.7 mT, respectively. The distance between the exciting and detecting antennae was 20 µm.

Figure 2e shows the spectra for YIG/Au (3 nm) bilayer taken in the Damon-Eshbach geometry. First, we observe an absence of phase oscillations in the S_{12} signal indicating no SW propagation between excitation and detection antennas [28,57,58]. Instead, we see broad FMR spectra, similar to the S_{22} absorption displayed in Figure 2d. The detected signal can be interpreted as a distant induction of FMR via long-range stray fields [59]. The r.f. currents inductively generated in the receiving antenna further interact with the bilayer and produce changes in the S_{12} transmission signal. The effect is reproducible for Au thicknesses $d_{\mathrm{Au}} = 3.5$ and 4 nm and correlates with the FMR intensity and linewidth (see additional data in the supplementary material). Angular dependence of the S_{12} spectra (Figure 2f) further points to the lack of SW propagation and additionally shows a small uniaxial anisotropy field of 2.0 ± 0.5 mT for the YIG/Au bilayer.

The S_{12} transmission spectra for YIG/Au bilayer allowed us to rule out the possibility of coherent SW propagation with large SW wavenumbers, i.e., corresponding to frequencies above the induced FMR signal. However, depending on the relative interplay between SW and inducted FMR signals, the oscillatory character of the SW phase on propagation may be hidden for long SWs [59]. To further verify this phenomenon, we have conducted SNS-MOKE measurements to investigate low-k excitations. As shown in Figure 2g, the intensity of SNS-MOKE signal quickly drops to zero over a distance of 2 µm. In addition, the line scans in Figure 2h show no oscillations for the out-of-plane magnetization component, proving that coherent SWs are not propagating in the bilayer. According to the measurements, we conclude that although the determined intrinsic damping for YIG/Au is relatively low ($\alpha \approx 8{\cdot}10^{-4}$), the SW decay length is very short. This can be better understood by considering the effective damping α_{eff} parameter encompassing both α and ΔH_0 parameters:

$$\alpha_{\mathrm{eff}} = \frac{\Delta f}{2f} \approx \left(\alpha + \frac{\gamma\mu_0\Delta H_0}{4\pi f}\right)\sqrt{1 + \left(\frac{\gamma\mu_0 M_{\mathrm{eff}}}{4\pi f}\right)^2}. \quad (3)$$

Equation (3) is derived for an in-plane applied magnetic field (see the supplementary material) and highlights the importance of the inhomogeneous linewidth broadening ΔH_0 on SW damping. For a 3-nm-thick Au layer, the YIG film exhibits $\mu_0\Delta H_0 \approx 8$ mT. This gives the effective damping parameter α_{eff} of 0.09 at 2 GHz, which is large and leads to strong SW damping. Furthermore, the insertion of a 1-nm-thick Pt or Au layer between YIG and GGG already increases the α_{eff} parameter to ≈0.02–0.03 at 2 GHz (see inset in Figure 2c). Based on these results, we infer that thin metal underlayers could be used to absorb SWs in YIG waveguides without detrimental back reflection.

3.3. SW Packet Propagation Characteristics

Before we discuss micromagnetic simulations, we introduce the basic properties of SW packet propagation. The envelope $|\psi(x,t)|$ of a SW packet can be described with:

$$|\psi(x,t)| \propto A(k,t)\, e^{-\frac{1}{4}\left(\frac{x-x_0-\omega'(k)\ t}{\sigma(t)}\right)^2}, \tag{4}$$

in which, the amplitude $A(k,t)$ is given by

$$A(k,t) = \sqrt{\frac{\sigma_x}{\sqrt{\sigma^2(t) + \alpha_{\text{eff}}\ \omega''(k)\ t}}}\, e^{-\alpha_{\text{eff}}\ \omega(k)\ t}, \tag{5}$$

and the SW packet broadening yields

$$\sigma^2(t) = \sigma_x^2 + \left(\frac{\omega''(k)}{2\sigma_x} t\right)^2. \tag{6}$$

Here, α_{eff} is the effective damping parameter, σ_x is the spatial width of the packet, $\omega(k)$ is the angular frequency depending on the wavenumber k, and $\omega'(k)$ and $\omega''(k)$ are the first and the second derivative of $\omega(k)$, respectively. The derivation of Equation (4) is presented in the supplementary material. From the exponent in Equation (4), we can see that the pulse peak travels at the group velocity $\omega'(k)$ and the packet broadens in time as described by $\sigma(t)$.

The decay length L_d of the propagating SW packet can thus be calculated from

$$A(k,\tau) = \frac{1}{e}, \tag{7}$$

with relaxation time $\tau = L_d/\omega'(k)$. In the limiting cases of Equation (7), when $\omega''(k) = 0$ or $\sigma_x \to \infty$, the amplitude $A(k,\tau) = e^{-\alpha_{\text{eff}}\ \omega(k)\ \tau}$, so that the attenuation length yields:

$$L_d^{\sigma_x \to \infty} = \frac{\omega'(k)}{\alpha_{\text{eff}}\ \omega(k)}. \tag{8}$$

If the spatial pulse width $\sigma_x \to 0$ and $\omega''(k) \neq 0$, the amplitude of the wave packet approaches zero. From an application point of view, it is, therefore, crucial to design SW devices so that the second derivative of the dispersion relation $\omega''(k)$ is minimized or, ideally, equal to zero to avoid amplitude loss and the SW packet broadening over time.

Analyzing the SW dispersion relations with an exchange term [60,61] for typical parameters of epitaxial YIG film (Figure 3a), we find that the condition $\omega''(k) = 0$ can be met for surface spin-waves (SSW, or Damon-Eshbach modes) as well as for forward volume spin-waves (FVSW). However, the condition is not met for the backward volume spin-waves (BVSW) propagating in a continuous film when the external magnetic field is greater than zero. Moreover, the wavenumber k for which $\omega''(k) = 0$ can be tuned by the external magnetic field for SSW and FVSW, as shown in Figure 3a. An increase of the magnetic field shifts the solution of $\omega''(k) = 0$ toward lower wavenumbers k.

Following Equation (7), the decay length of SW packets is significantly decreased when $\omega''(k) \neq 0$ (Figure 3b,c). To counteract this effect, one could consider the use of longer excitation pulses at the expense of a decreasing density of information that can be encoded and the speed of computation. Therefore, a careful choice of k (or equivalently, excitation frequency at a given bias field) is vital for the design of SW conduits to closely match the $\omega''(k) = 0$ condition.

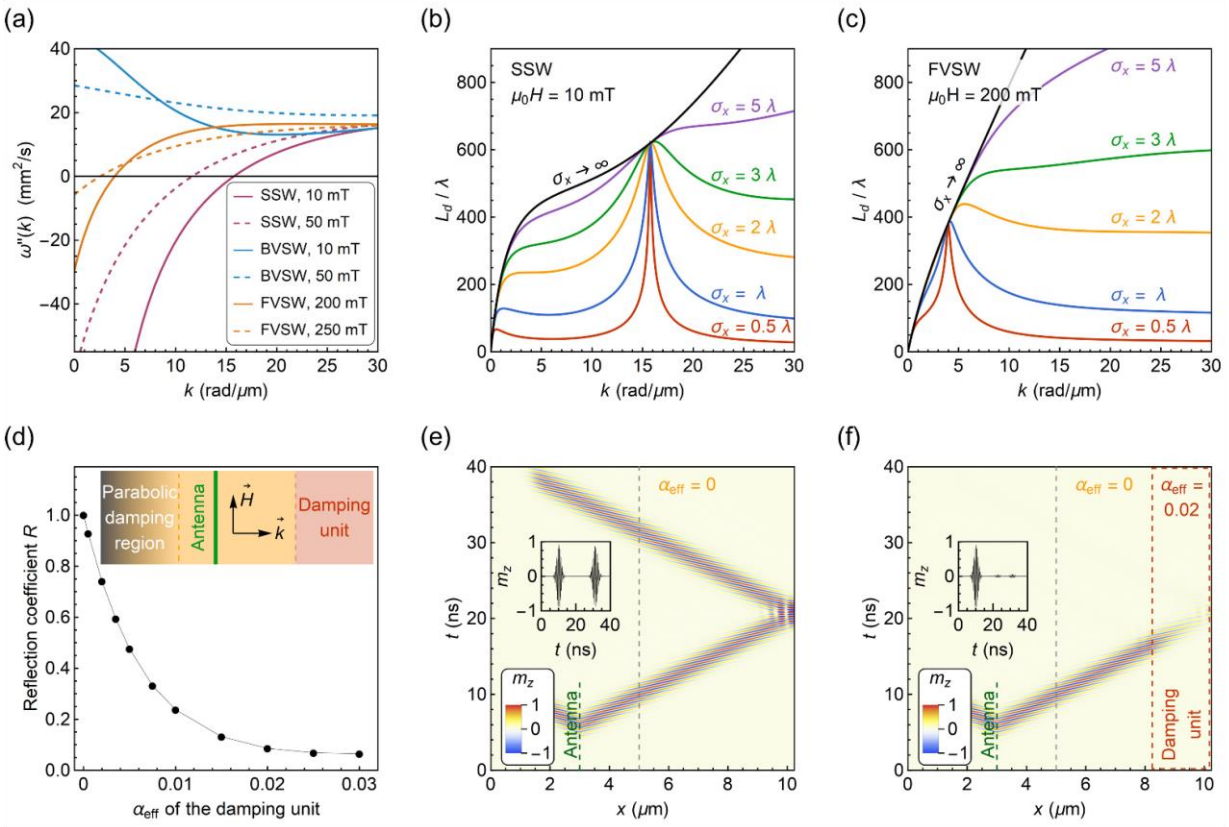

Figure 3. (**a**) Second derivative of the dispersion relation $\omega''(k)$ for the surface and backward volume, and the forward volume SWs. In (**b, c**), the ratio of the decay length L_d to the wavelength λ is shown for SSW and FVSW, respectively, for different values of the SW packet spatial width σ_x. In figures (**a**–**c**), the dependencies are calculated for typical parameters of a 50-nm-thick epitaxial YIG film with saturation magnetization $M_s = 140$ kA/m, exchange stiffness $D_{ex} = 5.3{\cdot}10^{-17}$ T·m^2, and effective damping $\alpha_{eff} = 1{\cdot}10^{-4}$. (**d**) Reflection coefficient as a function of the effective damping parameter α_{eff} in the damping unit. The inset illustrates the simulation geometry. In (**e**,**f**), the time evolution of SW packet is shown for a damping unit with $\alpha_{eff} = 0$ and $\alpha_{eff} = 0.02$, respectively. The insets show time dependences of the SW amplitude taken at $x = 5$ μm (marked with grey dashed lines). Figures (**e**,**f**) are also visualized in supplementary Videos S1 and S2.

3.4. SW Packet Reflection from a Damping Unit

To validate the application of the bilayers as an SW absorber, we performed micromagnetic simulations in *MuMax3* [41] to study the reflection of a SW packet from an area with different values of the effective damping parameter α_{eff}. For the modeling, we treat YIG/metal bilayer as an effective medium described with α_{eff}, and therefore, neglect the microstructural properties of the bilayer. The simulation geometry is schematically shown in the inset in Figure 3d. It consists of an antenna excitation region at $x = 3$ μm, an area with enhanced effective magnetic damping at 8 μm $< x <$ 10 μm, and an artificial damping region at 0 μm $< x <$ 2 μm, where parabolic damping conditions are defined to avoid SW reflection from the left edge. The YIG film is discretized into 1024 × 32 × 1 cells with a size of 10 × 10 × 10 nm^3 and one-dimensional periodic boundary conditions are applied along the *y*-axis to mimic a continuous film. The parameters for the YIG layer are: saturation magnetization $M_s = 140$ kA/m, exchange stiffness [62] $D_{ex} = 5.3{\cdot}10^{-17}$ T·m^2, and YIG film thickness $d_{YIG} = 10$ nm. The Gilbert damping parameter for 2 μm $< x <$ 8 μm is set to zero and α_{eff} is varied for the damping area. To excite the wave packet, we used a

Gaussian-enveloped sinusoidal magnetic pulse. A frequency of 1.7 GHz at the external bias field $\mu_0 H = 10$ mT was optimized in order to minimize wave packet dispersion for the surface waves, as discussed above. For these conditions, the spatial width of the pulse is $\sigma_x = 0.41$ µm, which is comparable to the SW wavelength $\lambda = 0.69$ µm and the width of the damping area. We recorded the time evolution of the out-of-plane component of magnetization m_z for 40 ns.

To evaluate the SW reflection, we compared the amplitude of the reflected wave packet to the incident one:

$$R = \frac{A_r}{A_i}, \tag{9}$$

where the amplitudes A_r and A_i are obtained by the Fourier transform of the reflected and incident signal at $x = 5$ µm. As shown in Figure 3e, when α_{eff} for the damping unit is equal to zero as for the rest of the film, the SW packet is fully reflected from the right edge so that $R = 1$. One can also clearly see that the propagating wave packet does not disperse in time, i.e., the SW packet broadening and the associated amplitude loss is not observed over time. For an increasing α_{eff} parameter, we find that R decreases gradually (Figure 3d). At $\alpha_{\text{eff}} = 0.02$ (also visualized in Figure 3f), the reflection coefficient yields $R = 0.086$, and for $\alpha_{\text{eff}} = 0.03$, $R = 0.065$. The decrease in amplitude of the reflected signal, which is more than an order of magnitude, substantiates the potential application of the YIG/metal bilayers as an efficient SW absorber. Moreover, $\alpha_{\text{eff}} \approx 0.02$–$0.03$ can already be met for a very thin metal underlayer of ≈1 nm for Pt or Au as calculated with Equation (3) (see inset in Figure 2c). Additionally, the insertion of such a thin metal layer does not deteriorate the effective magnetization significantly which further strongly supports the low reflection coefficients.

4. Summary

In conclusion, we investigated the structural and magnetic properties of YIG films grown onto GGG substrates with thin metal layers. The insertion of nanometer-thick platinum, iridium, or gold films at the YIG/GGG interface enables accurate tuning of the effective magnetic damping through material selection and variation of the metal underlayer thickness. Micromagnetic simulations based on parameters derived from experiments show that YIG/Au or YIG/Pt bilayers can be used as effective SW absorbers that can limit the reflection coefficient of SWs to $R < 0.1$. Applications of such absorbers are envisioned in integrated magnonic circuits.

Supplementary Materials: The following supporting information can be downloaded at: https://www.mdpi.com/article/10.3390/ma15082814/s1, X-ray reflectometry results; Gi-XRD measurements of YIG/Ir/GGG (111); AFM additional data; VNA-FMR basic data; VNA spectroscopy results for YIG/Au/GGG (111); Derivation of spin-wave packet evolution in a dispersive medium; Calculation of the effective damping parameter; Spin wave dispersion relations; Fourier transform of the magnetic pulse and the spin-wave packet; Basic material properties of bulk Ir, Pt, Au, YIG and GGG [48,63–66]; Video S1: Total spin-wave packet reflection from the film edge; Video S2: Spin-wave packet absorption by the damping unit.

Author Contributions: A.K. analyzed the experimental results, wrote the original draft, carried out the SEM, XRD, Gi-XRD, XRR and VNA-FMR measurements and performed PLD depositions, micromagnetic simulations, and analytical calculations. N.K. and A.K conducted VNA spectroscopy measurements. H.Q. designed and fabricated microwave antennas using optical lithography and magnetron sputtering. L.F. conducted SNS-MOKE measurements. E.C. carried out HR-XRD and AFM measurements. S.v.D. supervised the work. All authors revised the manuscript and approved its final version. All authors have read and agreed to the published version of the manuscript.

Funding: A.K. acknowledges financial support from the National Science Centre Poland through the PRELUDIUM Project No. 2018/31/N/ST5/03433 and program POWR.03.02.00-00-I032/16. This work was supported by the Academy of Finland (Grant No. 338748).

Institutional Review Board Statement: Not applicable.

Informed Consent Statement: Not applicable.

Data Availability Statement: The data presented in this study are available on request from the corresponding author.

Conflicts of Interest: The authors declare no conflict of interest.

References

1. Barman, A.; Gubbiotti, G.; Ladak, S.; Adeyeye, A.O.; Krawczyk, M.; Grafe, J.; Adelmann, C.; Cotofana, S.; Naeemi, A.; Vasyuchka, V.I.; et al. The 2021 Magnonics Roadmap. *J. Phys. Condens. Matter* **2021**, *33*, 413001. [CrossRef] [PubMed]
2. Mahmoud, A.; Ciubotaru, F.; Vanderveken, F.; Chumak, A.V.; Hamdioui, S.; Adelmann, C.; Cotofana, S. Introduction to Spin Wave Computing. *J. Appl. Phys.* **2020**, *128*, 161101. [CrossRef]
3. Barman, A.; Mondal, S.; Sahoo, S.; De, A. Magnetization Dynamics of Nanoscale Magnetic Materials: A Perspective. *J. Appl. Phys.* **2020**, *128*, 170901. [CrossRef]
4. Sheng, L.; Chen, J.; Wang, H.; Yu, H. Magnonics Based on Thin-Film Iron Garnets. *J. Phys. Soc. Jpn.* **2021**, *90*, 081005. [CrossRef]
5. Kruglyak, V.V. Chiral Magnonic Resonators: Rediscovering the Basic Magnetic Chirality in Magnonics. *Appl. Phys. Lett.* **2021**, *119*, 200502. [CrossRef]
6. Pirro, P.; Vasyuchka, V.I.; Serga, A.A.; Hillebrands, B. Advances in Coherent Magnonics. *Nat. Rev. Mater.* **2021**, *6*, 1114–1135. [CrossRef]
7. Yang, Y.; Liu, T.; Bi, L.; Deng, L. Recent Advances in Development of Magnetic Garnet Thin Films for Applications in Spintronics and Photonics. *J. Alloy. Compd.* **2021**, *860*, 158235. [CrossRef]
8. Schmidt, G.; Hauser, C.; Trempler, P.; Paleschke, M.; Papaioannou, E.T. Ultra Thin Films of Yttrium Iron Garnet with Very Low Damping: A Review. *Phys. Status Solidi* **2020**, *257*, 1900644. [CrossRef]
9. Hauser, C.; Richter, T.; Homonnay, N.; Eisenschmidt, C.; Qaid, M.; Deniz, H.; Hesse, D.; Sawicki, M.; Ebbinghaus, S.G.; Schmidt, G. Yttrium Iron Garnet Thin Films with Very Low Damping Obtained by Recrystallization of Amorphous Material. *Sci. Rep.* **2016**, *6*, 20827. [CrossRef]
10. Ding, J.; Liu, T.; Chang, H.; Wu, M. Sputtering Growth of Low-Damping Yttrium-Iron-Garnet Thin Films. *IEEE Magn. Lett.* **2020**, *11*, 5502305. [CrossRef]
11. Ding, J.; Liu, C.; Zhang, Y.; Erugu, U.; Quan, Z.; Yu, R.; Mccollum, E.; Mo, S.; Yang, S.; Ding, H.; et al. Nanometer-Thick Yttrium Iron Garnet Films with Perpendicular Anisotropy and Low Damping. *Phys. Rev. Appl.* **2020**, *14*, 014017. [CrossRef]
12. Krysztofik, A.; Coy, L.E.; Kuswik, P.; Załęski, K.; Głowinski, H.; Dubowik, J. Ultra-Low Damping in Lift-off Structured Yttrium Iron Garnet Thin Films. *Appl. Phys. Lett.* **2017**, *111*, 192404. [CrossRef]
13. Holzmann, C.; Ullrich, A.; Ciubotariu, O.T.; Albrecht, M. Stress-Induced Magnetic Properties of Gadolinium Iron Garnet Nanoscale-Thin Films: Implications for Spintronic Devices. *ACS Appl. Nano Mater.* **2022**, *5*, 1023–1033. [CrossRef]
14. Wu, G.; Wang, D.; Verma, N.; Rao, R.; Cheng, Y.; Guo, S.; Cao, G.; Watanabe, K.; Taniguchi, T.; Lau, C.N.; et al. Enhancing Perpendicular Magnetic Anisotropy in Garnet Ferrimagnet by Interfacing with Few-Layer WTe_2. *Nano Lett.* **2022**, *22*, 1115–1121. [CrossRef] [PubMed]
15. Böttcher, T.; Ruhwedel, M.; Levchenko, K.O.; Wang, Q.; Chumak, H.L.; Popov, M.A.; Zavislyak, I.V.; Dubs, C.; Surzhenko, O.; Hillebrands, B.; et al. Fast Long-Wavelength Exchange Spin Waves in Partially Compensated Ga:YIG. *Appl. Phys. Lett.* **2022**, *120*, 102401. [CrossRef]
16. Zhang, Y.; Yang, Q.; Liu, X.; Zhang, D.; Rao, Y.; Zhang, H. Comparison of the Magnetic Properties of Bismuth Substituted Thulium Iron Garnet and Yttrium Iron Garnet Films. *AIP Adv.* **2021**, *11*, 065113. [CrossRef]
17. Syvorotka, I.I.; Sugak, D.; Yakhnevych, U.; Buryy, O.; Włodarczyk, D.; Pieniążek, A.; Zhydachevskyy, Y.; Levintant-Zayonts, N.; Savytskyy, H.; Bonchyk, O.; et al. Investigation of the Interface of $Y_3Fe_5O_{12}/Gd_3Ga_5O_{12}$ Structure Obtained by the Liquid Phase Epitaxy. *Cryst. Res. Technol.* **2022**, 2100180. [CrossRef]
18. Rao, Y.; Zhang, D.; Jin, L.; Zhong, Z.; Yang, Q.; Li, M.; Li, J.; Yang, Y.; Wang, G.; Gan, G.; et al. Magnetic Properties of a $Y_3Fe_5O_{12}/(TmBi)_3(FeGa)_5O_{12}$ Heterostructure Related to Strain-Induced Magnetic Anisotropy. *J. Magn. Magn. Mater.* **2020**, *497*, 165817. [CrossRef]
19. Wu, Y.; Yang, Q.; Zhang, D.; Zhang, Y.; Rao, Y.; Wen, Q.; Syvorotka, I.I.; Zhang, H. The Submicron Garnet Film with Perpendicular Magnetic Anisotropy Prepared by Liquid Phase Epitaxy Method. *J. Magn. Magn. Mater.* **2020**, *506*, 166689. [CrossRef]
20. Capku, Z.; Yildiz, F. Spin Wave Modes Observation in YIG Thin Films with Perpendicular. *J. Magn. Magn. Mater.* **2021**, *538*, 168290. [CrossRef]
21. Zhao, Y.; Li, Y.; Zhu, S.; Chen, C.; Yao, M.; Zhao, Y.; Hu, Z.; Peng, B.; Liu, M.; Ziyao, Z. Voltage Tunable Low Damping YIG/PMN-PT Multiferroic Heterostructure for Low-Power RF/Microwave Devices. *J. Phys. D Appl. Phys. Phys.* **2021**, *54*, 245002. [CrossRef]
22. Gurjar, G.; Sharma, V.; Patnaik, S. Control of Magnetization Dynamics by Substrate Orientation in YIG Thin Films. *Mater. Res. Express* **2021**, *8*, 066401. [CrossRef]
23. Kim, H.; Jung, H.; Yang, J.; Jo, Y.; Yoo, J.; Park, A.M.; Jeong, J.; Kim, K. Deposition of Crystalline GdIG Samples Using Metal Organic Decomposition Method. *Magnetochemistry* **2022**, *8*, 28. [CrossRef]
24. Krichevsky, D.M.; Xia, S.; Mandrik, M.P.; Ignatyeva, D.O.; Bi, L.; Belotelov, V.I. Silicon-Based All-Dielectric Metasurface on an Iron Garnet Film for Efficient Magneto-Optical Light Modulation in near Ir Range. *Nanomaterials* **2021**, *11*, 2926. [CrossRef]

25. Hashimoto, R.; Itaya, T.; Uchida, H.; Funaki, Y.; Fukuchi, S. Properties of Magnetic Garnet Films for Flexible Magneto-Optical Indicators Fabricated by Spin-Coating Method. *Materials* **2022**, *15*, 1241. [CrossRef]
26. Wei, Z.; Yan, W.; Qin, J.; Deng, L.; Bi, L. Dysprosium Substituted Ce:YIG Thin Films for Temperature Insensitive Integrated Optical Isolator Applications. *Materials* **2022**, *15*, 1691. [CrossRef]
27. Yu, H.; d'Allivy Kelly, O.; Cros, V.; Bernard, R.; Bortolotti, P.; Anane, A.; Brandl, F.; Huber, R.; Stasinopoulos, I.; Grundler, D. Magnetic Thin-Film Insulator with Ultra-Low Spin Wave Damping for Coherent Nanomagnonics. *Sci. Rep.* **2015**, *4*, 6848. [CrossRef]
28. Qin, H.; Hämäläinen, S.J.; Arjas, K.; Witteveen, J.; Van Dijken, S. Propagating Spin Waves in Nanometer-Thick Yttrium Iron Garnet Films: Dependence on Wave Vector, Magnetic Field Strength, and Angle. *Phys. Rev. B* **2018**, *98*, 224422. [CrossRef]
29. Kanazawa, N.; Goto, T.; Sekiguchi, K.; Granovsky, A.B.; Ross, C.A.; Takagi, H.; Nakamura, Y.; Inoue, M. Demonstration of a Robust Magnonic Spin Wave Interferometer. *Sci. Rep.* **2016**, *6*, 30268. [CrossRef]
30. Venkat, G.; Fangohr, H.; Prabhakar, A. Absorbing Boundary Layers for Spin Wave Micromagnetics. *J. Magn. Magn. Mater.* **2018**, *450*, 34–39. [CrossRef]
31. Gołębiewski, M.; Gruszecki, P.; Krawczyk, M.; Serebryannikov, A.E. Spin-Wave Talbot Effect in a Thin Ferromagnetic Film. *Phys. Rev. B* **2020**, *102*, 134402. [CrossRef]
32. Martyshkin, A.A.; Beginin, E.N.; Sadovnikov, A.V. Spin Waves Transport in 3D Magnonic Waveguides. *AIP Adv.* **2021**, *11*, 035024. [CrossRef]
33. Álvarez-Prado, L.M. Control of Dynamics in Weak PMA Magnets. *Magnetochemistry* **2021**, *7*, 43. [CrossRef]
34. Yao, X.; Wang, Z.; Deng, M.; Li, Z.X.; Zhang, Z.; Cao, Y.; Yan, P. Magnetic Skyrmion Generation by Reflective Spin Wave Focusing. *Front. Phys.* **2021**, *9*, 729967. [CrossRef]
35. Collet, M.; Gladii, O.; Evelt, M.; Bessonov, V.; Soumah, L.; Bortolotti, P.; Demokritov, S.O.; Henry, Y.; Cros, V.; Bailleul, M.; et al. Spin-Wave Propagation in Ultra-Thin YIG Based Waveguides. *Appl. Phys. Lett.* **2017**, *110*, 092408. [CrossRef]
36. Stückler, T.; Liu, C.; Yu, H.; Heimbach, F.; Chen, J.; Hu, J.; Tu, S.; Alam, M.S.; Zhang, J.; Zhang, Y.; et al. Spin Wave Propagation Detected over 100 μm in Half-Metallic Heusler Alloy Co_2MnSi. *J. Magn. Magn. Mater.* **2018**, *450*, 13. [CrossRef]
37. Lake, S.R.; Divinskiy, B.; Schmidt, G.; Demokritov, S.O.; Demidov, V.E. Efficient Geometrical Control of Spin Waves in Microscopic YIG Waveguides. *Appl. Phys. Lett.* **2021**, *119*, 182401. [CrossRef]
38. Krysztofik, A.; Özoğlu, S.; McMichael, R.D.; Coy, E. Effect of Strain-Induced Anisotropy on Magnetization Dynamics in $Y_3Fe_5O_{12}$ Films Recrystallized on a Lattice-Mismatched Substrate. *Sci. Rep.* **2021**, *11*, 14011. [CrossRef]
39. Obaidulla, S.M.; Giri, P.K. Surface Roughening and Scaling Behavior of Vacuum-Deposited $SnCl_2Pc$ Organic Thin Films on Different Substrates. *Appl. Phys. Lett.* **2015**, *107*, 221910. [CrossRef]
40. Qin, H.; Holländer, R.B.; Flajšman, L.; Hermann, F.; Dreyer, R.; Woltersdorf, G.; van Dijken, S. Nanoscale Magnonic Fabry-Pérot Resonator for Low-Loss Spin-Wave Manipulation. *Nat. Commun.* **2021**, *12*, 2293. [CrossRef]
41. Vansteenkiste, A.; Leliaert, J.; Dvornik, M.; Helsen, M.; Garcia-Sanchez, F.; Van Waeyenberge, B. The Design and Verification of MuMax3. *AIP Adv.* **2014**, *4*, 107133. [CrossRef]
42. Nakatsuka, A.; Yoshiasa, A.; Takeno, S. Site Preference of Cations and Structural Variation in $Y_3Fe_{5-x}Ga_xO_{12}$ ($0 \leq x \leq 5$) Solid Solutions with Garnet Structure. *Acta Crystallogr. Sect. B* **1995**, *51*, 737–745. [CrossRef]
43. Zaumseil, P. High-Resolution Characterization of the Forbidden Si 200 and Si 222 Reflections. *J. Appl. Crystallogr.* **2015**, *48*, 528–532. [CrossRef] [PubMed]
44. Krysztofik, A.; Ozoglu, S.; Coy, E. Magnetization Damping in Nanocrystalline Yttrium Iron Garnet Thin Films Grown on Oxidized Silicon. *IEEE Magn. Lett.* **2021**, *12*, 7101605. [CrossRef]
45. Wyckoff, R.W. *Crystal Structures*, 2nd ed.; New York, NY, USA, 1963.
46. Li, Z.; Zhang, X.; Zhang, D.; Liu, B.; Meng, H.; Xu, J.; Zhong, Z.; Tang, X.; Zhang, H.; Jin, L. Magnetization Dynamics in the YIG/Au/YIG Magnon Valve. *APL Mater.* **2022**, *10*, 021101. [CrossRef]
47. Jin, L.; Zhang, D.; Zhang, H.; Yang, Q.; Tang, X.; Zhong, Z.; Xiao, J.Q. Tuning of the Spin Pumping in Yttrium Iron Garnet/Au Bilayer System by Fast Thermal Treatment. *J. Appl. Phys.* **2014**, *115*, 17C511. [CrossRef]
48. Brady, G.S.; Clauser, H.R.; Vaccari, J.A. *Materials Handbook*; McGraw-Hill Education: New York, NY, USA, 2002, ISBN 9781119130536.
49. Du, C.; Wang, H.; Hammel, P.C.; Yang, F. $Y_3Fe_5O_{12}$ Spin Pumping for Quantitative Understanding of Pure Spin Transport and Spin Hall Effect in a Broad Range of Materials (Invited). *J. Appl. Phys.* **2015**, *117*, 172603. [CrossRef]
50. Wang, H.L.; Du, C.H.; Pu, Y.; Adur, R.; Hammel, P.C.; Yang, F.Y. Large Spin Pumping from Epitaxial $Y_3Fe_5O_{12}$ Thin Films to Pt and W Layers. *Phys. Rev. B Condens. Matter Mater. Phys.* **2013**, *88*, 100406. [CrossRef]
51. Jin, L.; Zhu, H.; Zhang, D.; Liu, B.; Meng, H.; Tang, X.; Li, M.; Zhong, Z.; Zhang, H. Spin Pumping and Laser Modulated Inverse Spin Hall Effect in Yttrium Iron Garnet/Germanium Heterojunctions. *Appl. Phys. Lett.* **2020**, *116*, 122405. [CrossRef]
52. Dubowik, J.; Graczyk, P.; Krysztofik, A.; Głowiński, H.; Coy, E.; Załęski, K.; Gościańska, I. Non-Negligible Imaginary Part of the Spin-Mixing Conductance and Its Impact on Magnetization Dynamics in Heavy-Metal-Ferromagnet Bilayers. *Phys. Rev. Appl.* **2020**, *13*, 054011. [CrossRef]
53. Bertelli, I.; Simon, B.G.; Yu, T.; Aarts, J.; Bauer, G.E.W.; Blanter, Y.M.; Sar, T. Imaging Spin-Wave Damping Underneath Metals Using Electron Spins in Diamond. *Adv. Quantum Technol.* **2021**, *4*, 2100094. [CrossRef]

54. Souza, A.L.R.; Gamino, M.; Ferreira, A.; de Oliveira, A.B.; Vaz, F.; Bohn, F.; Correa, M.A. Directional Field-Dependence of Magnetoimpedance Effect on Integrated YIG/Pt-Stripline System. *Sensors* **2021**, *21*, 6145. [CrossRef] [PubMed]
55. Bunyaev, S.A.; Serha, R.O.; Musiienko-Shmarova, H.Y.; Kreil, A.J.E.; Frey, P.; Bozhko, D.A.; Vasyuchka, V.I.; Verba, R.V.; Kostylev, M.; Hillebrands, B.; et al. Spin-Wave Relaxation by Eddy Currents in $Y_3Fe_5O_{12}$/Pt Bilayers and a Way to Suppress It. *Phys. Rev. Appl.* **2020**, *14*, 024094. [CrossRef]
56. Flovik, V.; Macià, F.; Kent, A.D.; Wahlström, E. Eddy Current Interactions in a Ferromagnet-Normal Metal Bilayer Structure, and Its Impact on Ferromagnetic Resonance Lineshapes. *J. Appl. Phys.* **2015**, *117*, 143902. [CrossRef]
57. Krysztofik, A.; Głowiński, H.; Kuświk, P.; Ziętek, S.; Coy, L.E.; Rychły, J.N.; Jurga, S.; Stobiecki, T.W.; Dubowik, J. Characterization of Spin Wave Propagation in (111) YIG Thin Films with Large Anisotropy. *J. Phys. D. Appl. Phys.* **2017**, *50*, 235004. [CrossRef]
58. Vaňatka, M.; Szulc, K.; Wojewoda, O.; Dubs, C.; Chumak, A.V.; Krawczyk, M.; Dobrovolskiy, O.V.; Kłos, J.W.; Urbánek, M. Spin-Wave Dispersion Measurement by Variable-Gap Propagating Spin-Wave Spectroscopy. *Phys. Rev. Appl.* **2021**, *16*, 054033. [CrossRef]
59. Sushruth, M.; Grassi, M.; Ait-Oukaci, K.; Stoeffler, D.; Henry, Y.; Lacour, D.; Hehn, M.; Bhaskar, U.; Bailleul, M.; Devolder, T.; et al. Electrical Spectroscopy of Forward Volume Spin Waves in Perpendicularly Magnetized Materials. *Phys. Rev. Res.* **2020**, *2*, 043203. [CrossRef]
60. Kalinikos, B.A.; Slavin, A.N. Theory of Dipole-Exchange Spin Wave Spectrum for Ferromagnetic Films with Mixed Exchange Boundary Conditions. *J. Phys. C Solid State Phys.* **1986**, *19*, 7013–7033. [CrossRef]
61. Bang, W.; Lim, J.; Trossman, J.; Tsai, C.C.; Ketterson, J.B. Propagation of Magnetostatic Spin Waves in an Yttrium Iron Garnet Film for Out-of-Plane Magnetic Fields. *J. Magn. Magn. Mater.* **2018**, *456*, 241–250. [CrossRef]
62. Klingler, S.; Chumak, A.V.; Mewes, T.; Khodadadi, B.; Mewes, C.; Dubs, C.; Surzhenko, O.; Hillebrands, B.; Conca, A. Measurements of the Exchange Stiffness of YIG Films Using Broadband Ferromagnetic Resonance Techniques. *J. Phys. D Appl. Phys.* **2015**, *48*, 015001. [CrossRef]
63. Schwartz, M. *Encyclopedia and Handbook of Materials, Parts, and Finishes*; CRC Press: Boca Raton, FL, USA, 2016; ISBN 9781466567481.
64. Boyes, W. *Instrumentation Reference Book*; Elsevier: Amsterdam, The Netherlands, 2010; ISBN 9780750683081.
65. Mordike, B.B.L.; Ph, D.; Brookes, C.A. The Tensile Properties of Iridium at High Temperatures. *Platin. Met. Rev.* **1960**, *4*, 94–99. [CrossRef]
66. Liang, R.S.; Liu, F.C. Measurement of Thermal Expansion Coefficient of Substrate GGG and Its Epitaxial Layer YIG. *Powder Diffr.* **1999**, *14*, 2–4. [CrossRef]

Supplementary Information

Tuning of Magnetic Damping in $Y_3Fe_5O_{12}$ / Metal Bilayers for Spin-Wave Conduit Termination

Adam Krysztofik[1]*, Nikolai Kuznetsov[2], Huajun Qin[2], Lukáš Flajšman[2], Emerson Coy[3], and Sebastiaan van Dijken[2]

[1] *Institute of Molecular Physics, Polish Academy of Sciences, ul. Smoluchowskiego 17, 60-179 Poznań, Poland*

[2] *NanoSpin, Department of Applied Physics, Aalto University School of Science, P.O. Box 15100, FI-00076 Aalto, Finland*

[3] *NanoBioMedical Centre, Adam Mickiewicz University, ul. Wszechnicy Piastowskiej 3, 61-614 Poznań, Poland*

* adam.krysztofik@ifmpan.poznan.pl

- X-ray reflectometry results
- Gi-XRD measurements of YIG / Ir / GGG (111)
- AFM additional data
- VNA-FMR basic data
- VNA spectroscopy results for YIG / Au / GGG (111)
- Spin-wave packet evolution in a dispersive medium
- Calculation of the effective damping parameter
- Spin wave dispersion relations
- Fourier transform of the magnetic pulse and the spin-wave packet
- Basic material properties of bulk Ir, Pt, Au, YIG and GGG

X-ray reflectometry results

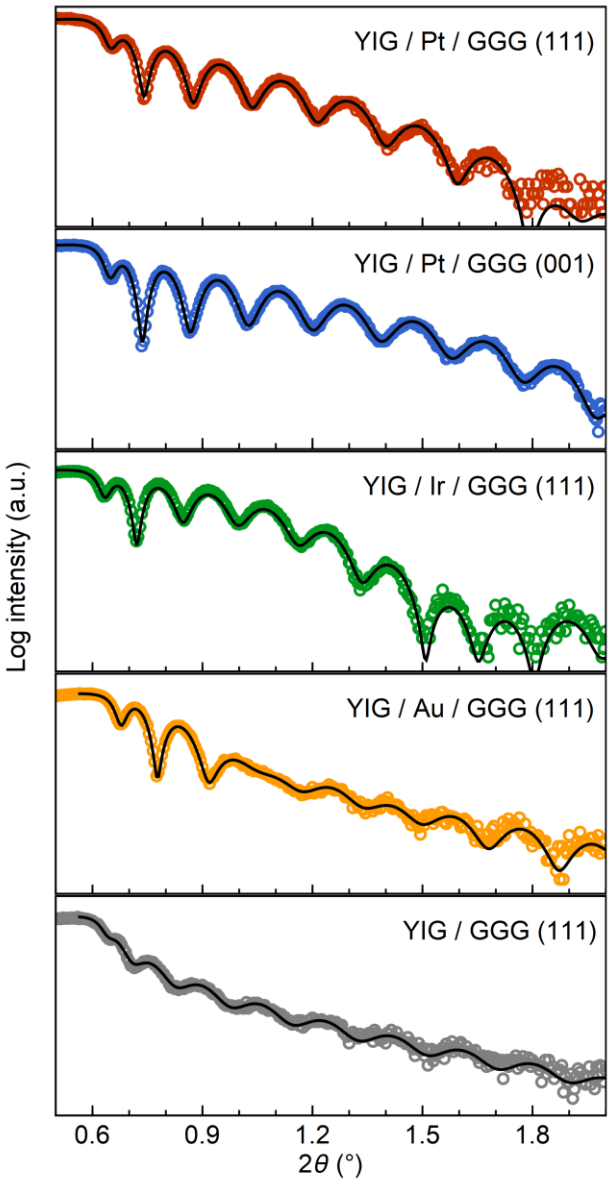

The XRR measurements were performed using an additional vertical slit limiting incident X-ray radiation to 1.5 mm across the metal wedge which corresponds to a change in metal thickness by 0.75 nm. The determined thickness of YIG films ranges between 38.9 and 42.4 nm pointing to good stability of deposition conditions. The roughness of YIG layers grown on metal spacers is increased to 1.0-1.5 nm in comparison to the roughness of the YIG layer grown directly on the GGG substrate (0.7 nm). The determined critical angle of YIG films on top of metal spacers ranges from 0.602° to 0.640°, in congruence with 0.618° for a YIG/GGG reference measurement, and therefore suggests a consistent density of YIG layers.

Gi-XRD measurements of YIG / Ir / GGG (111)

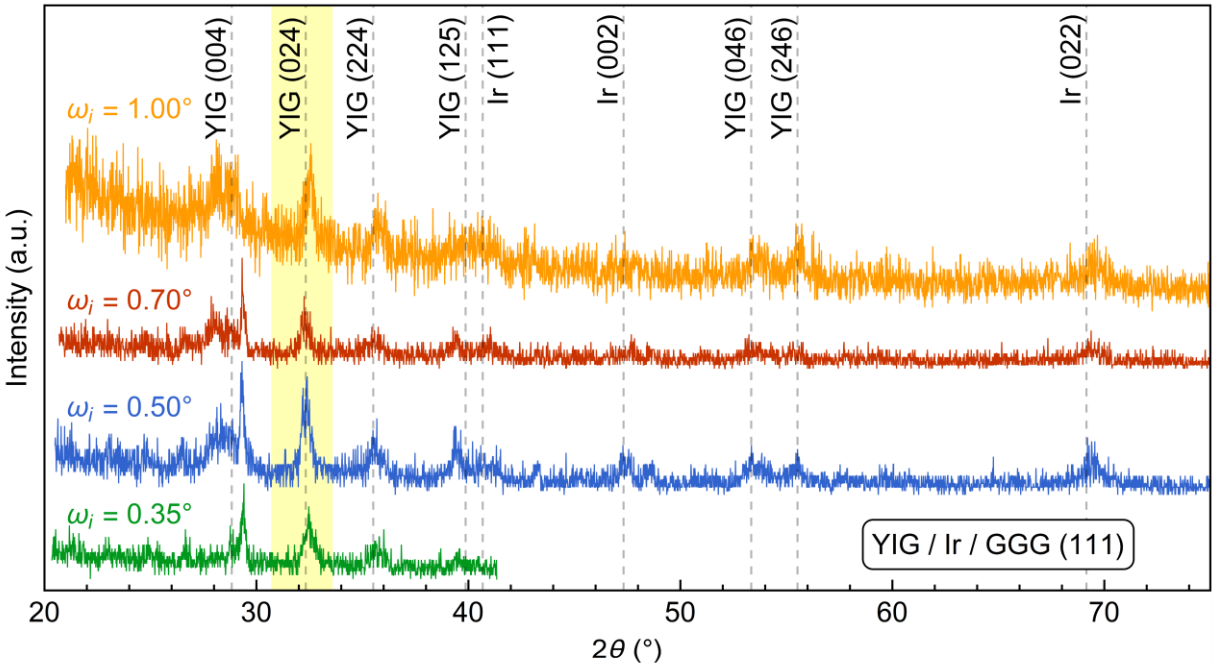

Grazing incident X-ray diffraction for YIG / Ir / GGG (111) sample. The measurements were taken for incident angles ω_i between 0.35-1.00° and show the polycrystalline structure of both films. Dashed lines mark reflection positions for bulk YIG and Ir [42, 45]. Analyzing the width of the highest intensity reflection (024) for YIG with the Scherrer formula, the estimated crystallite size yields 16.9 ± 2.7 nm as averaged from these four scans. The determined lattice parameter of YIG is equal to 1.235 ± 0.004 nm in agreement with the bulk value (1.2375 nm) [42].

AFM additional data

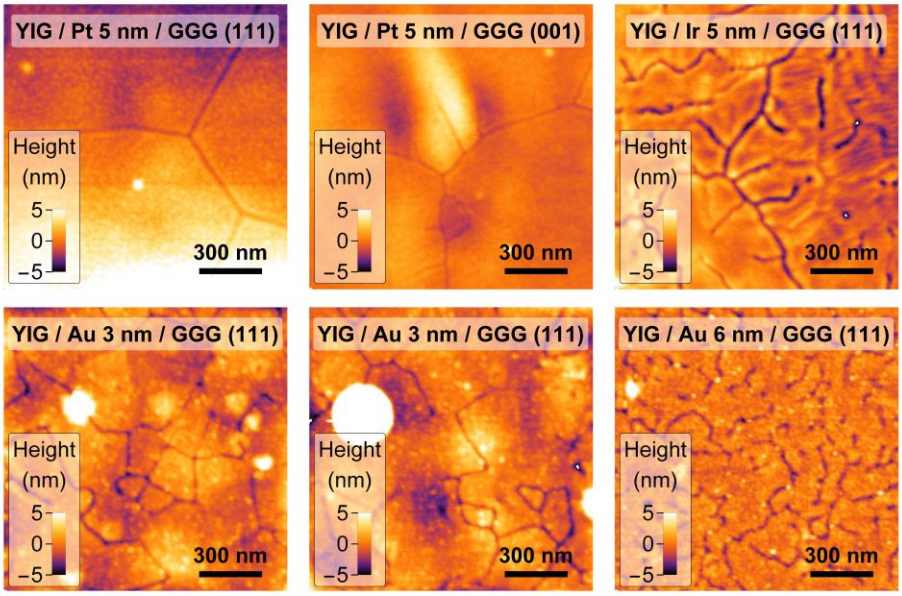

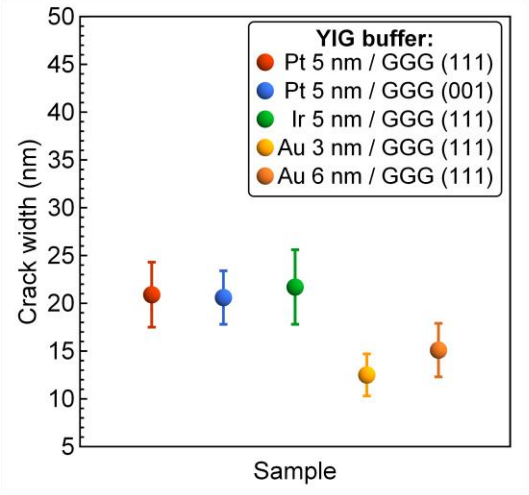

Estimation of crack width based on AFM surface imaging indicating a maximal separation distance between parts of the YIG film. Error bars denote the standard deviation of the mean represented by points. The statistics is based on 30 crack measurements for each sample.

VNA-FMR basic data

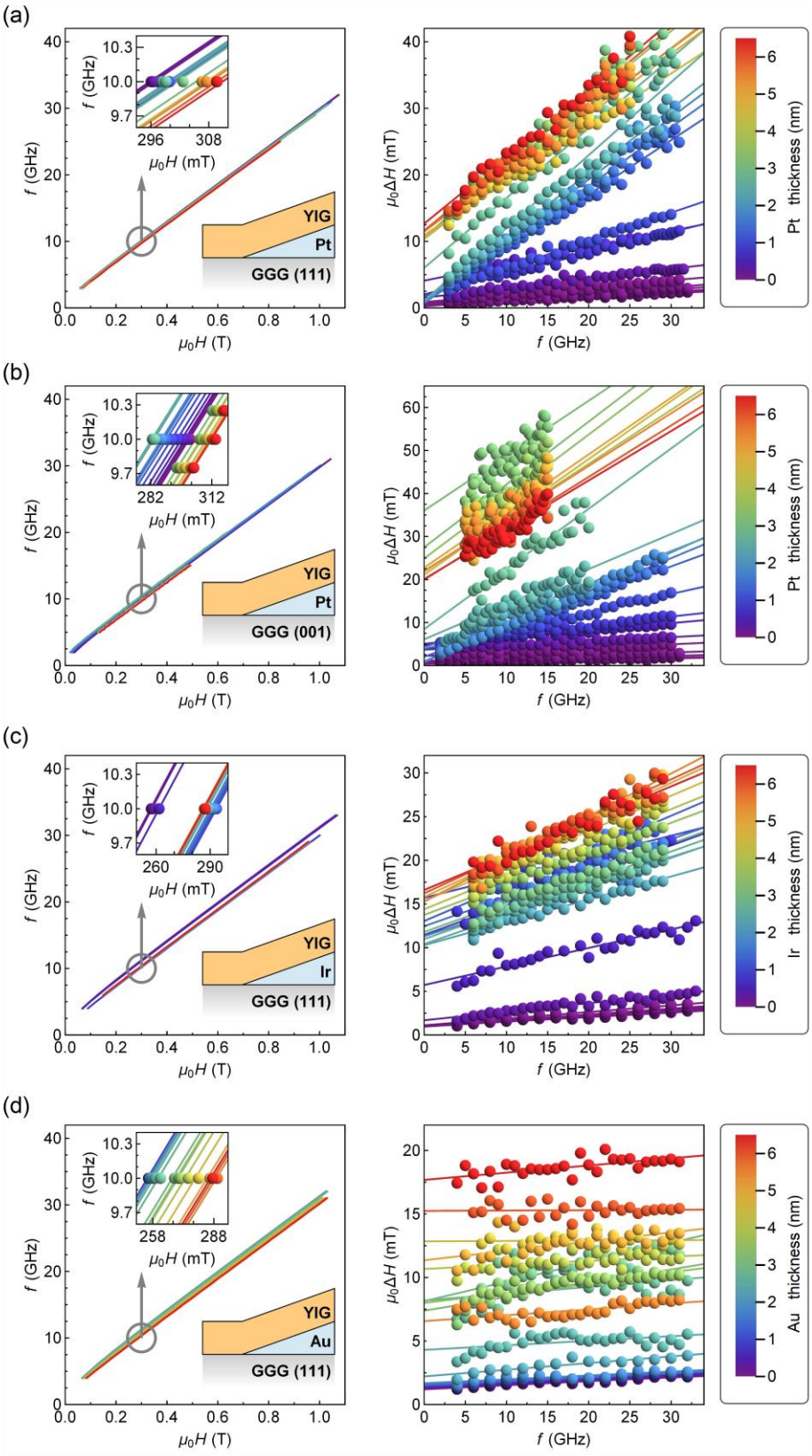

Kittel relation and linewidth dependence on frequency for: (a) YIG/Pt/GGG (111), (b) YIG/Pt/GGG (001), (c) YIG/Ir/GGG (111), and (d) YIG/Au/GGG (111) samples.

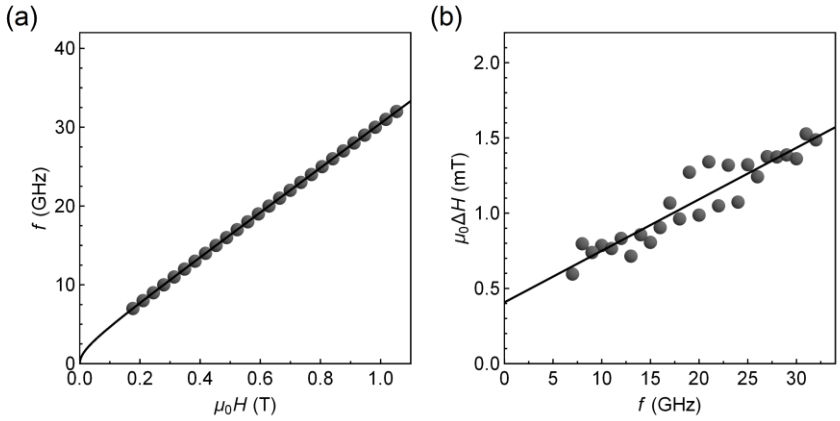

(a) Kittel relation and (b) linewidth dependence on frequency for the epitaxial YIG grown on GGG substrate. The sample was prepared directly in the pulsed laser deposition chamber and have not been in any contact with the magnetron plasma. From the fittings we estimate the effective magnetization M_{eff} =137.5 ± 0.1 kA/m, the Gilbert damping parameter α =(4.8 ± 0.4)·10^{-4}, and the inhomogeneous linewidth broadening $\mu_0 \Delta H_0$ =0.41 ± 0.05 mT.

VNA spectroscopy results for YIG / Au / GGG (111)

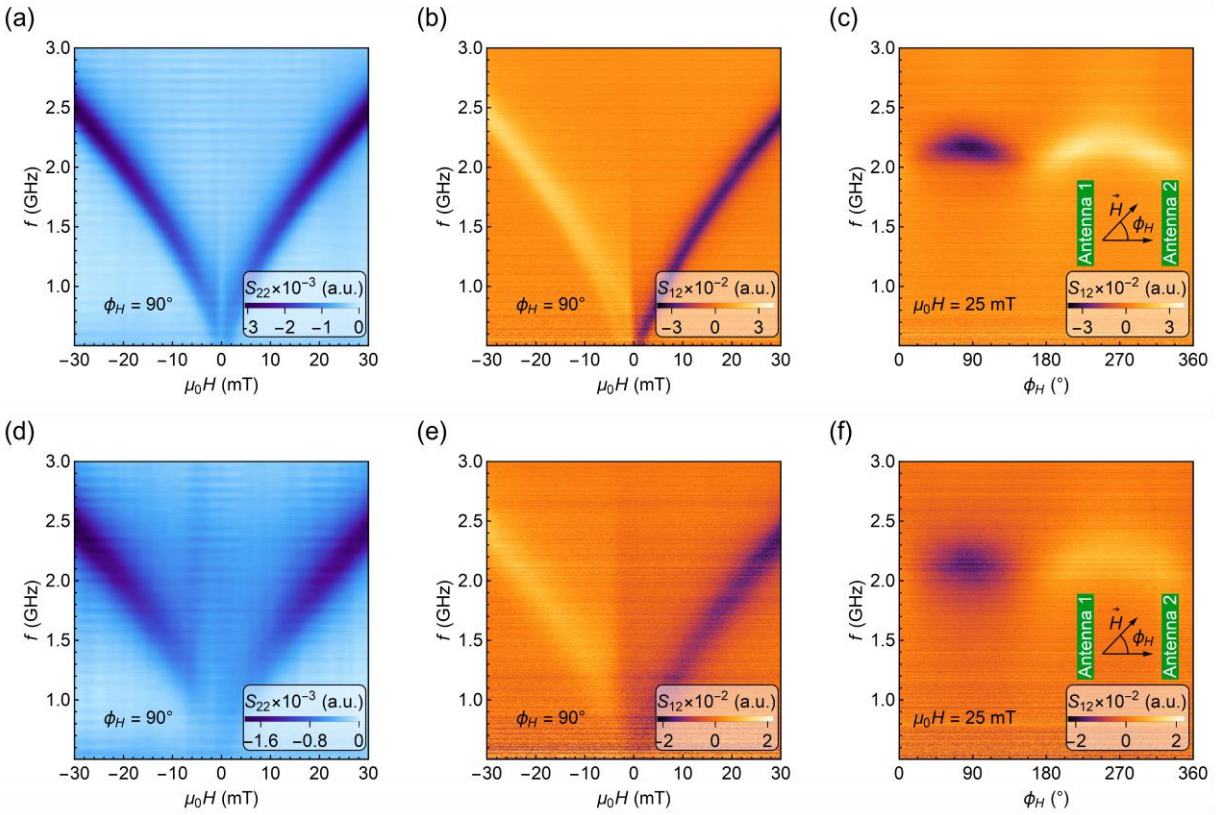

VNA spectroscopy results measured with lithographically patterned antennas for (**a-c**) YIG (40 nm) / Au (3.5 nm) / GGG (111), and (**d-f**) YIG (40 nm) / Au (4 nm) / GGG (111). (**a,d**) Color-coded reflection parameter S_{22} showing the FMR absorption. (**b,e**) Color-coded transmission parameter S_{12} for the magnetic field aligned parallel to the antennas ($\phi_H = 90°$). (**c,f**) Color-coded angular dependence of S_{12} spectrum at $\mu_0 H = 25$ mT. Inset depicts in-plane magnetic field orientation with respect to the antenna geometry. In all figures, the real part of the scattering parameter S_{pq} is plotted.

Spin-wave packet evolution in a dispersive medium

The wavefunction can be calculated using the inverse Fourier transformation:

$$\psi(x,t) \propto \int_{-\infty}^{\infty} \overline{\psi}(k) e^{i(kx-\omega(k)t)} dk, \tag{S1}$$

where $\overline{\psi}(k)$ is derived from

$$\overline{\psi}(k) \propto \int_{-\infty}^{\infty} \psi(x,t=0) e^{-ikx} dx, \tag{S2}$$

and the pulse at time $t = 0$ with carrier wavenumber k_c and the spatial width σ_x has a form:

$$\psi(x,t=0) \propto e^{-\frac{(x-x_0)^2}{4\sigma_x^2}} e^{ik_c x}. \tag{S3}$$

Here, we truncate the dispersion relation to the second-order term $(k-k_c)^2$ in Taylor expansion

$$\omega(k) = \omega(k_c) + (k-k_c)\omega'(k_c) + \frac{1}{2}(k-k_c)^2\omega''(k_c), \tag{S4}$$

and find that the integral in Eq. (S1) yields

$$\psi(x,t) \propto \frac{1}{\sqrt{1+i\omega''(k_c)t/(2\sigma_x^2)}} e^{-\left(\frac{x-x_0-\omega'(k_c)t}{2\sigma(t)}\right)^2} e^{i\phi(x,t)}, \tag{S5}$$

$$\phi(x,t) = k_c x - \omega(k_c)t + \frac{\omega''(k_c)t}{2\omega''^2(k_c)t^2+8\sigma_x^4}(x-x_0-\omega'(k_c)t)^2, \tag{S6}$$

$$\sigma^2(t) = \sigma_x^2 + \left(\frac{\omega''(k_c)}{2\sigma_x}t\right)^2. \tag{S7}$$

The $e^{i\phi(x,t)}$ component of the solution describes only wave oscillations. It is however worth noting that $\omega''(k_c) \neq 0$ in Eq. S6 is responsible for an additional modulation of the oscillations.

By taking the absolute value $|\psi(x,t)|$ we can identify the signal envelope and better read off the temporal evolution of the wave packet:

$$|\psi(x,t)| \propto \sqrt{\frac{\sigma_x}{\sigma(t)} e^{-\frac{1}{2}\left(\frac{x-x_0-\omega'(k_c)t}{\sigma(t)}\right)^2}}. \tag{S8}$$

The exponent in Eq. (S8) shows that the wave packet travels at the group velocity $\omega'(k_c)$ and it broadens in time. Concurrently, the amplitude $\sqrt{\sigma_x/\sigma(t)}$ of the signal decreases. As can be inferred from $\sigma(t)$ (Eq. (S7)), both the pulse broadening and the amplitude drop result from $\omega''(k_c) \neq 0$. Hence, it is important to extend the analysis to account for intrinsic magnetic losses related to the choice of a spin-wave medium.

By introducing a decay term $e^{-\alpha_{\text{eff}}\omega(k)t}$ into Eq. (S1), where α_{eff} is the effective damping parameter and repeating the calculations, we find:

$$|\psi(x,t)| \propto \sqrt{\frac{\sigma_x}{\sqrt{\sigma^2(t)+\alpha_{\text{eff}}\,\omega''(k_c)t}}\,e^{-2\alpha_{\text{eff}}\,\omega(k_c)t}e^{-\frac{1}{2}\left(\frac{x-x_0-\omega'(k_c)t}{\sigma(t)}\right)^2}}. \tag{S9}$$

Hence, we can calculate the decay length of propagating spin-wave packet by numerically solving the following equation:

$$\frac{1}{e} = \sqrt{\frac{\sigma_x}{\sqrt{\sigma^2(\tau)+\alpha_{\text{eff}}\,\omega''(k_c)\tau}}}\,e^{-\alpha_{\text{eff}}\,\omega(k_c)\tau}, \tag{S10}$$

with relaxation time $\tau = L_d/\omega'(k_c)$. The decay length L_d is defined here as the distance at which the amplitude of the wave packet has been reduced by a factor of e.

Calculation of the effective damping parameter

The relation between the relaxation time τ and the spectral width Δω can be found using the Fourier transform of a damped oscillator:

$$\tilde{A}(\omega) = \int_0^\infty A(t)e^{-i\omega t}\,dt, \tag{S11}$$

$$A(t) = e^{-\frac{t}{\tau}}\,e^{i\omega_0 t}. \tag{S12}$$

Calculating integral in Eq. S11, one obtains the real part of $\tilde{A}(\omega)$ as a Lorentz function:

$$\text{Re}\left[\tilde{A}(\omega)\right] = \frac{\frac{1}{\tau}}{\left(\frac{1}{\tau}\right)^2+(\omega-\omega_0)^2}, \tag{S13}$$

so that the relation between τ and Δω is given by:

$$\frac{1}{\tau} = \frac{\Delta\omega}{2}. \tag{S14}$$

Hence, the relaxation term in Eq. S12 can be written in terms of an effective damping parameter α_{eff}:

$$e^{-\frac{t}{\tau}} = e^{-\alpha_{\text{eff}}\omega t}, \tag{S15}$$

by using

$$\alpha_{\text{eff}} = \frac{\Delta\omega}{2\omega}. \tag{S16}$$

As can be seen from Eq. S16, the frequency-swept FMR experiment, in which $\Delta\omega = 2\pi\Delta f$, provides, therefore, direct information on relaxation process and can be used for evaluation of the effective damping straightforwardly. However, in the field-swept ferromagnetic resonance, the FWHM linewidth ΔH is described with the Heinrich formula:

$$\mu_0 \Delta H = \frac{2\alpha}{\gamma}\omega + \mu_0 \Delta H_0, \tag{S17}$$

where α is the intrinsic Gilbert damping parameter, and ΔH_0 is the inhomogeneous linewidth broadening. The required transition to the frequency domain can be well approximated with:

$$\Delta\omega = \frac{\partial\omega}{\partial H}\Delta H. \tag{S18}$$

Combining equations S16-S18, the effective damping parameter now yields:

$$\alpha_{\text{eff}} = \left(\alpha + \frac{\gamma\mu_0\Delta H_0}{2\omega}\right)\frac{1}{\gamma\mu_0}\frac{\partial\omega}{\partial H}. \tag{S19}$$

An explicit form of Eq. S19 can be found calculating the derivative $\frac{\partial\omega}{\partial H}$ from Kittel equations. For an in-plane applied magnetic field H_{IP}, for which

$$\omega = \mu_0\gamma\sqrt{H_{\text{IP}}(H_{\text{IP}} + M_{\text{eff}})}, \tag{S20}$$

and $\omega = 2\pi f$, one obtains:

$$\alpha_{\text{eff}}^{\text{IP}} = \left(\alpha + \frac{\gamma\mu_0\Delta H_0}{4\pi f}\right)\sqrt{1 + \left(\frac{\gamma\mu_0 M_{\text{eff}}}{4\pi f}\right)^2}, \tag{S21}$$

which provides accurate numerical estimates for $f > 1$ GHz. For the out-of-plane applied field H_{OP}, when

$$\omega = \mu_0\gamma(H_{\text{OP}} - M_{\text{eff}}), \tag{S22}$$

one finds:

$$\alpha_{\text{eff}}^{\text{OP}} = \alpha + \frac{\gamma\mu_0\Delta H_0}{4\pi f}. \tag{S23}$$

Both equations S21 and S23 clearly show the relevance of ΔH_0 parameter on magnetization relaxation.

Spin wave dispersion relations

For the calculations presented in Fig. 3 (a-c) the following spin-wave dispersion relations have been used [60, 61]:

- surface spin-waves (SSW), film magnetized in-plane, $\vec{k} \perp \vec{M}$:

$$\omega(k) = \gamma\sqrt{(\mu_0 H + D_{\text{ex}}k^2)(\mu_0 H + D_{\text{ex}}k^2 + \mu_0 M_s) + \left(\frac{1}{2}\mu_0 M_s\right)^2 (1 - e^{-2kd})}, \quad \text{(S24)}$$

- backward volume spin-waves (BVSW), film magnetized in-plane, $\vec{k} \,||\, \vec{M}$:

$$\omega(k) = \gamma\sqrt{(\mu_0 H + D_{\text{ex}}k^2)\left(\mu_0 H + D_{\text{ex}}k^2 + \mu_0 M_s \frac{1-e^{-kd}}{kd}\right)}, \quad \text{(S25)}$$

- forward volume spin-waves (FVSW), film magnetized out-of-plane, $\vec{k} \perp \vec{M}$:

$$\omega(k) = \gamma\sqrt{(\mu_0 H + D_{\text{ex}}k^2 - \mu_0 M_s)\left(\mu_0 H + D_{\text{ex}}k^2 - \mu_0 M_s \frac{1-e^{-kd}}{kd}\right)}, \quad \text{(S26)}$$

where $\omega = 2\pi f$ is the angular frequency, γ is the gyromagnetic ratio, μ_0 is the vacuum permeability, k is the wavenumber, H is the bias magnetic field, M_s is the saturation magnetization, D_{ex} is the exchange stiffness, d is the film thickness. Within Eq. S24-S26, the group velocity $\omega'(k) = \frac{\partial\omega}{\partial k}$ and the second derivative $\omega''(k) = \frac{\partial^2\omega}{\partial k^2}$ have been calculated.

Fourier transform of the magnetic pulse and the spin-wave packet

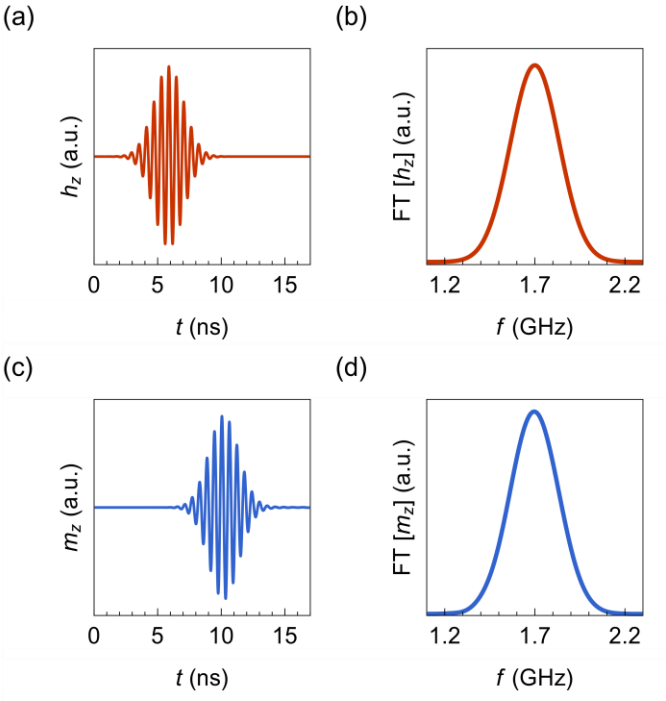

(a) Gaussian-enveloped sinusoidal magnetic pulse (z-component, h_z) used for spin-wave packet excitation and (b) its Fourier transform FT [h_z]. (c) Propagating spin-wave packet (z-component, m_z) and (d) its Fourier transform FT [m_z].

Basic material properties of bulk Ir, Pt, Au, YIG and GGG

Material	Atomic number	Melting point (°C)	Thermal expansion coefficient ($\times 10^{-6}$ K^{-1})	Tensile strength (MPa)	Plasticity
Iridium	77	2450	6.4	500-1000	Brittle
Platinum	78	1770	8.8	117	Ductile
Gold	79	1060	14.2	138	Ductile
YIG	–	1555	9.9-11.4	–	Brittle
GGG	–	1800	8.3-8.7	–	Brittle

Data was taken from Ref. [48, 63-66].

Selected frames from Video S1 and Video S2

Video S1: Total spin-wave packet reflection from the film edge

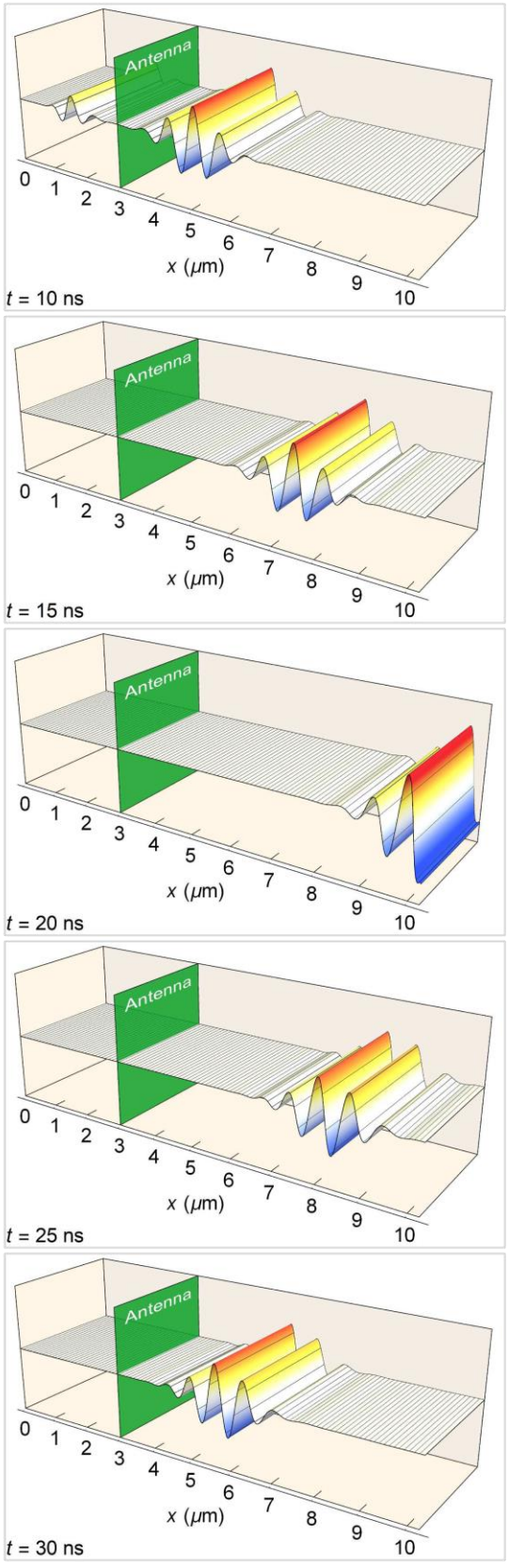

Video S2: Spin-wave packet absorption by the damping unit

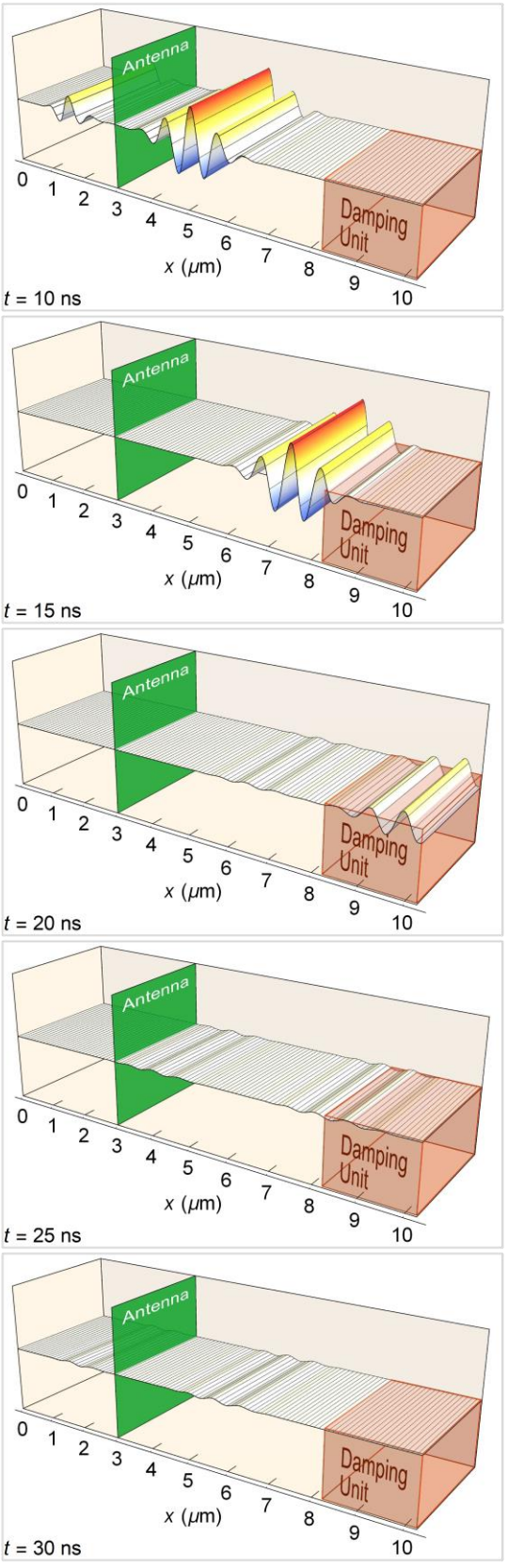

Commentary to the publication *Tuning of Magnetic Damping in $Y_3Fe_5O_{12}$ / Metal Bilayers for Spin-Wave Conduit Termination*

Spin-wave (SW) packet propagation simulations, which are presented in the article, were conducted assuming the thickness of the YIG film equal to $d_{\mathrm{YIG}} = 10$ nm. Simulations were additionally performed for $d_{\mathrm{YIG}} = 50$ nm and the results are attached below considering the same magnetic parameters of YIG and the same investigated geometry. At the external magnetic field of $\mu_0 H = 10$ mT and $d_{\mathrm{YIG}} = 50$ nm, minimal dispersion of SW packet during propagation is observed at the frequency $f = 3.0$ GHz. For those conditions, the SW wavelength is equal to $\lambda = 0.32$ μm and the SW packet spatial width was set to $\sigma_x = 0.3$ μm. It can be seen that for $\alpha_{\mathrm{eff}} = 0$, the SW packet is fully reflected from the right edge so that the reflection coefficient $R = 1$, and the SW packet broadening and the associated amplitude loss are not observed over time (Fig. S1(a)). For an increasing α_{eff} parameter of the damping unit (considered as YIG/metal bilayer), we find that R decreases gradually (Fig. S1(c)). At $\alpha_{\mathrm{eff}} = 0.02$ (also visualized in Fig. S1(b)), the reflection coefficient yields $R = 0.051$, and for $\alpha_{\mathrm{eff}} = 0.03$, $R = 0.035$. Note that for 10-nm-thick YIG as presented in the article, the obtained reflection coefficients are of the same order of magnitude: for $\alpha_{\mathrm{eff}} = 0.02$, $R = 0.086$; and for $\alpha_{\mathrm{eff}} = 0.03$, $R = 0.065$.

To conclude, the dispersionless propagation of the spin-wave packet can be optimized for both 10- and 50-nm-thick YIG. For both cases of YIG thickness, the reflection coefficient R decreases in the same way as α_{eff} of the damping unit increases. Thus, the efficiency of the damping unit does not change when either 10- or 50-nm-thick YIG are considered.

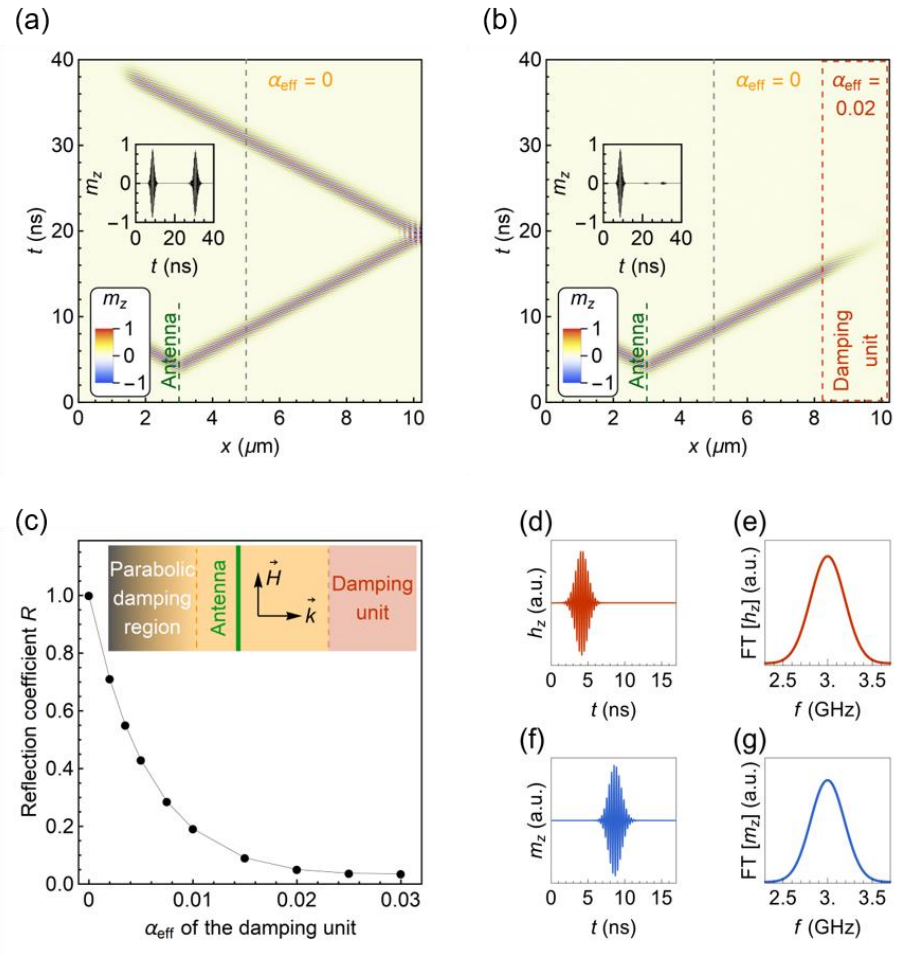

Fig. S1. Micromagnetic simulations of spin-wave packet propagation in 50-nm-thick YIG with $M_s = 140$ kA/m and $D_{ex} = 5.3 \cdot 10^{-17}$ T·m^2. In **a** and **b**, the time evolution of SW packet is shown for a damping unit with $\alpha_{eff} = 0$ and $\alpha_{eff} = 0.02$, respectively. (**c**) Reflection coefficient as a function of the effective damping parameter α_{eff} in the damping unit. The inset illustrates the simulation geometry. (**d**) Gaussian-enveloped sinusoidal magnetic pulse (z-component, h_z) used for spin-wave packet excitation and (**e**) its Fourier transform FT [h_z]. (**f**) Propagating spin-wave packet (z-component, m_z) and (**g**) its Fourier transform FT [m_z].

5 Podsumowanie

W ramach rozprawy doktorskiej zbadano właściwości strukturalne i magnetyczne warstw granatu itrowo-żelazowego ($Y_3Fe_5O_{12}$, YIG) o grubościach kilkudziesięciu nanometrów. Wykorzystując metodę ablacji laserowej, warstwy YIG osadzano na podłożach monokrystalicznych ($Gd_3Ga_5O_{12}$, $Y_3Al_5O_{12}$), amorficznych (SiO_x) oraz polikrystalicznych warstwach metali (Ir, Pt, Au). Główny przedmiot zainteresowań stanowiły badania dynamiki namagnesowania. Pomiary szerokopasmowego rezonansu ferromagnetycznego umożliwiły określenie parametrów opisujących tłumienie precesji namagnesowania – kluczowych wielkości w kontekście projektowania przyszłych urządzeń, których zasada działania opiera się o propagację fal spinowych. W szczególności wykazano, że:

- W osadzanych na podłożu $Gd_3Ga_5O_{12}$ epitaksjalnych warstwach YIG koherentne fale spinowe propagują na odległości sięgające 150-ciu mikrometrów dzięki niskiemu tłumieniu precesji namagnesowania.
- W cienkich warstwach YIG zależność dyspersyjna, jak również prędkość grupowa fal spinowych, w istotnym stopniu zależą od indukowanej wzrostem anizotropii prostopadłej.
- Proces strukturyzowania warstw z wykorzystaniem techniki *lift-off* nie wpływa na własności strukturalne i magnetyczne cienkich warstw YIG.
- Niejednorodność naprężeń epitaksjalnych prowadzi do poszerzenia linii rezonansowej.
- Odmienna wartość współczynnika rozszerzalności termicznej podłoża prowadzi do szeregu defektów strukturalnych w warstwie YIG, a przez to, do wzrostu wartości efektywnego parametru tłumienia magnetyzacji.

- Dwuwarstwy YIG/metal mogą być wykorzystane jako zakończenie falowodów magnonicznych o niskim współczynniku odbicia.

Podsumowując, podłoże granatu gadolinowo-galowego wydaje się pozostawać jedynym, powszechnie dostępnym materiałem umożliwiającym wytworzenie warstw YIG o wysokiej jakości krystalicznej oraz niskim tłumieniu precesji namagnesowania. Zaproponowanie bufora pozwalającego na połączenie warstw granatów z technologiami CMOS wymaga spełnienia rygorystycznych parametrów materiałowych. Badania przedstawione w niniejszej rozprawie wskazują na dwie zasadnicze wielkości: bliski równości współczynnik rozszerzalności termicznej warstwy i podłoża oraz dopasowanie parametru sieciowego na poziomie poniżej 3%.

Bibliografia

1. Krysztofik, A.; Głowiński, H.; Kuświk, P.; Ziętek, S.; Coy, L.E.; Rychły, J.N.; Jurga, S.; Stobiecki, T.W.; Dubowik, J. Characterization of Spin Wave Propagation in (111) YIG Thin Films with Large Anisotropy. *J. Phys. D. Appl. Phys.* **2017**, *50*, 235004, doi:10.1088/1361-6463/aa6df0.

2. Krysztofik, A.; Coy, L.E.; Kuswik, P.; Załęski, K.; Głowinski, H.; Dubowik, J. Ultra-Low Damping in Lift-off Structured Yttrium Iron Garnet Thin Films. *Appl. Phys. Lett.* **2017**, *111*, 192404, doi:10.1063/1.5002004.

3. Krysztofik, A.; Ozoglu, S.; Coy, E. Magnetization Damping in Nanocrystalline Yttrium Iron Garnet Thin Films Grown on Oxidized Silicon. *IEEE Magn. Lett.* **2021**, *12*, 7101605, doi:10.1109/LMAG.2021.3086454.

4. Krysztofik, A.; Özoğlu, S.; McMichael, R.D.; Coy, E. Effect of Strain-Induced Anisotropy on Magnetization Dynamics in $Y_3Fe_5O_{12}$ Films Recrystallized on a Lattice-Mismatched Substrate. *Sci. Rep.* **2021**, *11*, 14011, doi:10.1038/s41598-021-93308-3.

5. Krysztofik, A.; Kuznetsov, N.; Qin, H.; Flajšman, L.; Coy, E.; van Dijken, S. Tuning of Magnetic Damping in $Y_3Fe_5O_{12}$ / Metal Bilayers for Spin-Wave Conduit Termination. *Materials (Basel).* **2022**, *15*, 2814, doi:10.3390/ma15082814.

6. Stancil, D.D.; Prabhakar, A. *Spin Waves. Theory and Applications*; Springer: New York, 2009; ISBN 9780387778648.

7. Coey, J.M.D. *Magnetism and Magnetic Materials*; Cambridge University Press: Cambridge, 2010; ISBN 9780521816144.

8. Geller, S.; Gilleo, M.A. The Crystal Structure and Ferrimagnetism of Yttrium-Iron Garnet, $Y_3Fe_2(FeO_4)_3$. *J. Phys. Chem. Solids* **1957**, *3*, 30–36, doi:10.1016/0022-3697(57)90044-6.

9. Klingler, S.; Chumak, A. V; Mewes, T.; Khodadadi, B.; Mewes, C.; Dubs, C.; Surzhenko, O.; Hillebrands, B.; Conca, A. Measurements of the Exchange Stiffness of YIG Films Using Broadband Ferromagnetic Resonance Techniques. *J. Phys. D. Appl. Phys.* **2015**, *48*, 015001, doi:10.1088/0022-3727/48/1/015001.

10. Qin, H.; Hämäläinen, S.J.; Arjas, K.; Witteveen, J.; Van Dijken, S. Propagating Spin Waves in Nanometer-Thick Yttrium Iron Garnet Films: Dependence on Wave Vector, Magnetic Field Strength, and Angle. *Phys. Rev. B* **2018**, *98*, 224422, doi:10.1103/PhysRevB.98.224422.

11. Dubs, C.; Surzhenko, O.; Thomas, R.; Osten, J.; Schneider, T.; Lenz, K.; Grenzer, J.; Hübner, R.; Wendler, E. Low Damping and Microstructural Perfection of Sub-40nm-Thin Yttrium Iron Garnet Films Grown by Liquid Phase Epitaxy. *Phys. Rev. Mater.* **2020**, *4*, 024416, doi:10.1103/PhysRevMaterials.4.024416.

12. Hauser, C.; Richter, T.; Homonnay, N.; Eisenschmidt, C.; Qaid, M.; Deniz, H.; Hesse, D.; Sawicki, M.; Ebbinghaus, S.G.; Schmidt, G. Yttrium Iron Garnet Thin Films with Very Low Damping Obtained by Recrystallization of Amorphous Material. *Sci. Rep.* **2016**, *6*, 20827, doi:10.1038/srep20827.

13. Ding, J.; Liu, T.; Chang, H.; Wu, M. Sputtering Growth of Low-Damping Yttrium-Iron-Garnet Thin Films. *IEEE Magn. Lett.* **2020**, *11*, 5502305, doi:10.1109/LMAG.2020.2989687.

14. Smit, J.; Beljers, H.G. Ferromagnetic Resonance Absorption in $BaFe_{12}O_{19}$,

a Highly Anisotropic Crystal. *Phillips Res. Reports* **1955**, *10*, 113–130.

15. Baselgia, L.; Warden, M.; Waldner, F.; Hutton, S.L.; Drumheller, J.E.; He, Y.Q.; Wigen, P.E.; Maryko, M. Derivation of the Resonance Frequency from the Free Energy of Ferromagnets. *Phys. Rev. B* **1988**, *38*, 2237–2242, doi:10.1103/PhysRevB.38.2237.

16. *Physics of Magnetic Garnets. Proceedings of the International School of Physics "Enrico Fermi";* Paoletti, A., Ed.; Societa Italiana di Fisica: Italy, 1978;

17. Kittel, C. *Introduction to Solid State Physics, 8th Edition*; 8th Editio.; John Wiley and Sons: Hoboken, 2004;

18. Manuilov, S.A.; Khartsev, S.I.; Grishin, A.M. Pulsed Laser Deposited $Y_3Fe_5O_{12}$ Films: Nature of Magnetic Anisotropy I. *J. Appl. Phys.* **2009**, *106*, 123917, doi:10.1063/1.3446840.

19. Manuilov, S.A.; Grishin, A.M. Pulsed Laser Deposited $Y_3Fe_5O_{12}$ Films: Nature of Magnetic Anisotropy II. *J. Appl. Phys.* **2010**, *108*, 013902, doi:10.1063/1.3446840.

20. Yin, L.F.; Wei, D.H.; Lei, N.; Zhou, L.H.; Tian, C.S.; Dong, G.S.; Jin, X.F.; Guo, L.P.; Jia, Q.J.; Wu, R.Q. Magnetocrystalline Anisotropy in Permalloy Revisited. *Phys. Rev. Lett.* **2006**, *97*, 067203, doi:10.1103/PhysRevLett.97.067203.

21. Li, Y.; Zeng, F.; Zhang, S.S.L.; Shin, H.; Saglam, H.; Karakas, V.; Ozatay, O.; Pearson, J.E.; Heinonen, O.G.; Wu, Y.; et al. Giant Anisotropy of Gilbert Damping in Epitaxial CoFe Films. *Phys. Rev. Lett.* **2019**, *122*, 117203, doi:10.1103/PhysRevLett.122.117203.

22. Mallik, S.; Bedanta, S. Study of Anisotropy, Magnetization Reversal and Damping in Ultrathin Co Films on MgO (001) Substrate. *J. Magn. Magn.*

Mater. **2018**, *446*, 270–275, doi:10.1016/j.jmmm.2017.09.035.

23. Gubbiotti, G.; Carlotti, G.; Hillebrands, B. Spin Waves and Magnetic Anisotropy in Ultrathin (111)-Oriented Cubic Films. *J. Phys. Condens. Matter* **1998**, *10*, 2171–2180, doi:10.1088/0953-8984/10/9/019.

24. Heinrich, B.; Cochran, J.F.; Hasegawa, R. FMR Linebroadening in Metals Due to Two-Magnon Scattering. *J. Appl. Phys.* **1985**, *57*, 3690–3692, doi:10.1063/1.334991.

25. *Ultrathin Magnetic Structures II. Measurement Techniques and Novel Magnetic Properties.*; Heinrich, B., Bland, J.A.C., Eds.; Springer-Verlag: Berlin Heidelberg, 1994; ISBN 3540219560.

26. Kalinikos, B.A.; Slavin, A.N. Theory of Dipole-Exchange Spin Wave Spectrum for Ferromagnetic Films with Mixed Exchange Boundary Conditions. *J. Phys. C Solid State Phys.* **1986**, *19*, 7013–7033, doi:10.1088/0022-3719/19/35/014.

27. Bang, W.; Lim, J.; Trossman, J.; Tsai, C.C.; Ketterson, J.B. Propagation of Magnetostatic Spin Waves in an Yttrium Iron Garnet Film for Out-of-Plane Magnetic Fields. *J. Magn. Magn. Mater.* **2018**, *456*, 241–250, doi:10.1016/j.jmmm.2018.02.030.

28. Kalinikos, B.A.; Kostylev, M.P.; Kozhus, N. V.; Slavin, A.N. The Dipole-Exchange Spin Wave Spectrum for Anisotropic Ferromagnetic Films with Mixed Exchange Boundary Conditions. *J. Phys. Condens. Matter* **1999**, *2*, 9861–9877, doi:10.1088/0953-8984/2/49/012.

29. *Pulsed Laser Deposition of Thin Films*; Eason, R., Ed.; Wiley & Sons: New Jersey, 2007; ISBN 9780471447092.

30. Adachi, H.; Hata, T.; Matsushima, T.; Motohiro, T.; Tominaga, K. *Handbook of Sputter Deposition Technology: Fundamentals and*

Applications for Functional Thin Films, Nano-Materials and MEMS; Wasa, K., Kanno, I., Kotera, H., Eds.; Second Edi.; Elsevier: Amsterdam, 2012; ISBN 9781437734843.

31. Cullity, B.D.; Stock, S.R. *Elements of X-Ray Diffraction*; Third Edit.; Pearson: Harlow, 2014;

32. *X-Ray and Neutron Reflectivity: Principles and Applications*; Daillant, J., Gibaud, A., Eds.; Second Edi.; Springer-Verlag: Berlin Heidelberg, 2009; ISBN 9783540885887.

33. Vignaud, G.; Gibaud, A. REFLEX: A Program for the Analysis of Specular X-Ray and Neutron Reflectivity Data. *J. Appl. Crystallogr.* **2019**, *52*, 201–213, doi:10.1107/S1600576718018186.

34. Pietsch, U.; Holy, V.; Baumbach, T. *High-Resolution X-Ray Scattering: From Thin Films to Lateral Nanostructures*; Second Edi.; Springer-Verlag: New York, 2004; ISBN 9781441923073.

35. Ul-Hamid, A. *A Beginners' Guide to Scanning Electron Microscopy*; First Edit.; Springer: Switzerland, 2018; ISBN 9783319984810.

36. Voigtländer, B. *Atomic Force Microscopy*; Second Edi.; Springer-Verlag: Switzerland, 2019; ISBN 9783030136536.

37. Pacyna, A.W. General Theory of the Signal Induced in a Vibrating Magnetometer. *J. Phys. E.* **1982**, *15*, 663–669, doi:10.1088/0022-3735/15/6/014.

38. Pacyna, A.W.; Ruebenbauer, K. General Theory of a Vibrating Magnetometer with Extended Coils. *J. Phys. E.* **1984**, *17*, 141–154, doi:10.1088/0022-3735/17/2/016.

39. *The SQUID Handbook: Vol. I Fundamentals and Technology of SQUIDs and SQUIDs Systems.*; Clarke, J., Braginski, A.I., Eds.; WILEY-VCH

Verlag GmbH & Co. KGaA: Weinheim, 2004; ISBN 3527402292.

40. Clarke, J.; Braginski, A.I. *The SQUID Handbook: Vol. II Applications of SQUIDs and SQUID Systems.*; Clarke, J., Braginski, A.I., Eds.; WILEY-VCH Verlag GmbH & Co. KGaA: Weinheim, 2006; ISBN 9783527404087.

41. Vansteenkiste, A.; Leliaert, J.; Dvornik, M.; Helsen, M.; Garcia-Sanchez, F.; Van Waeyenberge, B. The Design and Verification of MuMax3. *AIP Adv.* **2014**, *4*, 107133, doi:10.1063/1.4899186.

42. Brown, W.F. *Interscience Tracts on Physics and Astronomy. Vol.18 Micromagnetics*; Marshak, R.E., Ed.; John Wiley and Sons: New York, London, 1963;

43. Jamali, M.; Kwon, J.H.; Seo, S.-M.; Lee, K.-J.; Yang, H. Spin Wave Nonreciprocity for Logic Device Applications. *Sci. Rep.* **2013**, *3*, 1–5, doi:10.1038/srep03160.

44. Chumak, A. V.; Serga, A. a.; Hillebrands, B. Magnon Transistor for All-Magnon Data Processing. *Nat. Commun.* **2014**, *5*, 4700, doi:10.1038/ncomms5700.

45. Vogt, K.; Fradin, F.Y.; Pearson, J.E.; Sebastian, T.; Bader, S.D.; Hillebrands, B.; Hoffmann, A.; Schultheiss, H. Realization of a Spin-Wave Multiplexer. *Nat. Commun.* **2014**, *5*, 1–5, doi:10.1038/ncomms4727.

46. Gertz, F.; Kozhevnikov, A. V.; Filimonov, Y.A.; Nikonov, D.E.; Khitun, A. Magnonic Holographic Memory: From Proposal to Device. *IEEE J. Explor. Solid-State Comput. Devices Circuits* **2015**, *1*, 67–75, doi:10.1109/JXCDC.2015.2461618.

47. Serga, A.; Chumak, A. V; Hillebrands, B, . YIG Magnonics. *J. Phys. D. Appl. Phys.* **2010**, *43*, 264002, doi:10.1088/0022-3727/43/26/264002.

48. Bessonov, V.D.; Mruczkiewicz, M.; Gieniusz, R.; Guzowska, U.; Maziewski, A.; Stognij, A.I.; Krawczyk, M. Magnonic Band Gaps in YIG-Based One-Dimensional Magnonic Crystals: An Array of Grooves versus an Array of Metallic Stripes. *Phys. Rev. B* **2015**, *91*, 104421, doi:10.1103/PhysRevB.91.104421.

49. Kostylev, M.P.; Serga, A.A.; Schneider, T.; Leven, B.; Hillebrands, B. Spin-Wave Logical Gates. *Appl. Phys. Lett.* **2005**, *87*, 153501, doi:10.1063/1.2089147.

50. Lee, J.M.; Jang, C.; Min, B.C.; Lee, S.W.; Lee, K.J.; Chang, J. All-Electrical Measurement of Interfacial Dzyaloshinskii-Moriya Interaction Using Collective Spin-Wave Dynamics. *Nano Lett.* **2016**, *16*, 62–67, doi:10.1021/acs.nanolett.5b02732.

51. Sushruth, M.; Grassi, M.; Ait-Oukaci, K.; Stoeffler, D.; Henry, Y.; Lacour, D.; Hehn, M.; Bhaskar, U.; Bailleul, M.; Devolder, T.; et al. Electrical Spectroscopy of Forward Volume Spin Waves in Perpendicularly Magnetized Materials. *Phys. Rev. Res.* **2020**, *2*, 043203, doi:10.1103/PhysRevResearch.2.043203.

52. Neusser, S.; Duerr, G.; Bauer, H.G.; Tacchi, S.; Madami, M.; Woltersdorf, G.; Gubbiotti, G.; Back, C.H.; Grundler, D. Anisotropic Propagation and Damping of Spin Waves in a Nanopatterned Antidot Lattice. *Phys. Rev. Lett.* **2010**, *105*, 067208, doi:10.1103/PhysRevLett.105.067208.

53. Kwon, J.H.; Mukherjee, S.S.; Deorani, P.; Hayashi, M.; Yang, H. Characterization of Magnetostatic Surface Spin Waves in Magnetic Thin Films: Evaluation for Microelectronic Applications. *Appl. Phys. A* **2013**, *111*, 369–378, doi:10.1007/s00339-012-7542-x.

54. Yu, H.; d'Allivy Kelly, O.; Cros, V.; Bernard, R.; Bortolotti, P.; Anane, A.; Brandl, F.; Huber, R.; Stasinopoulos, I.; Grundler, D. Magnetic Thin-Film

Insulator with Ultra-Low Spin Wave Damping for Coherent Nanomagnonics. *Sci. Rep.* **2015**, *4*, 6848, doi:10.1038/srep06848.

55. Wang, H.L.; Du, C.H.; Pu, Y.; Adur, R.; Hammel, P.C.; Yang, F.Y. Large Spin Pumping from Epitaxial $Y_3Fe_5O_{12}$ Thin Films to Pt and W Layers. *Phys. Rev. B - Condens. Matter Mater. Phys.* **2013**, *88*, 100406(R), doi:10.1103/PhysRevB.88.100406.

56. Chiang, W.-C.; Chern, M.Y.; Lin, J.G.; Huang, C.Y. FMR Studies of $Y_3Fe_5O_{12}/Gd_3Ga_5O_{12}$ (YIG/GGG) Superlattices and YIG Thin Films. *J. Magn. Magn. Mater.* **2002**, *239*, 332–334, doi:10.1016/S0304-8853(01)00655-2.

57. Kehlberger, A.; Richter, K.; Onbasli, M.C.; Jakob, G.; Kim, D.H.; Goto, T.; Ross, C.A.; Götz, G.; Reiss, G.; Kuschel, T.; et al. Enhanced Magneto-Optic Kerr Effect and Magnetic Properties of $CeY_2Fe_5O_{12}$ Epitaxial Thin Films. *Phys. Rev. Appl.* **2015**, *4*, 014008, doi:10.1103/PhysRevApplied.4.014008.

58. Vlaminck, V.; Bailleul, M. Spin-Wave Transduction at the Submicrometer Scale: Experiment and Modeling. *Phys. Rev. B - Condens. Matter Mater. Phys.* **2010**, *81*, 014425, doi:10.1103/PhysRevB.81.014425.

59. Eshbach, J.R.; Damon, R.W. Surface Magnetostatic Modes and Surface Spin Waves. *Phys. Rev.* **1960**, *118*, 1208–1210, doi:10.1103/PhysRev.118.1208.

60. Schwarze, T. Spin Waves in 2D and 3D Magnonic Crystals : From Nanostructured Ferromagnetic Materials to Chiral Helimagnets. *PhD thesis* **2013**.

61. Onbasli, M.C.; Kehlberger, A.; Kim, D.H.; Jakob, G.; Kläui, M.; Chumak, A. V.; Hillebrands, B.; Ross, C.A. Pulsed Laser Deposition of Epitaxial Yttrium Iron Garnet Films with Low Gilbert Damping and Bulk-like

Magnetization. *APL Mater.* **2014**, *2*, 106102, doi:10.1063/1.4896936.

62. Collet, M.; Gladii, O.; Evelt, M.; Bessonov, V.; Soumah, L.; Bortolotti, P.; Demokritov, S.O.; Henry, Y.; Cros, V.; Bailleul, M.; et al. Spin-Wave Propagation in Ultra-Thin YIG Based Waveguides. *Appl. Phys. Lett.* **2017**, *110*, 092408, doi:10.1063/1.4976708.

63. Onbasli, M.C.; Beran, L.; Zahradník, M.; Kucera, M.; Antoš, R.; Mistrík, J.; Dionne, G.F.; Veis, M.; Ross, C.A. Optical and Magneto-Optical Behavior of Cerium Yttrium Iron Garnet Thin Films at Wavelengths of 200-1770 nm. *Sci. Rep.* **2016**, *6*, 23640, doi:10.1038/srep23640.

64. Bonda, A.; Uba, S.; Uba, L. Ultrafast Magneto-Optical and Magnetization-Induced Second Harmonic Generation Techniques for Studies of Magnetic Nanostructures. *Acta Phys. Pol. A* **2012**, *121*, 1225.

65. Dubs, C.; Surzhenko, O.; Linke, R.; Danilewsky, A.; Brückner, U.; Dellith, J. Sub-Micrometer Yttrium Iron Garnet LPE Films with Low Ferromagnetic Resonance Losses. *J. Phys. D. Appl. Phys.* **2017**, *50*, 204005, doi:10.1088/1361-6463/aa6b1c.

66. Perzlmaier, K.; Woltersdorf, G.; Back, C.H. Observation of the Propagation and Interference of Spin Waves in Ferromagnetic Thin Films. *Phys. Rev. B* **2008**, *77*, 054425, doi:10.1103/PhysRevB.77.054425.

67. Maendl, S.; Stasinopoulos, I.; Grundler, D. Spin Waves with Large Decay Length and Few 100 nm Wavelengths in Thin Yttrium Iron Garnet Grown at the Wafer Scale. *Appl. Phys. Lett.* **2017**, *111*, 012403, doi:10.1063/1.4991520.

68. Sadovnikov, A. V.; Davies, C.S.; Kruglyak, V. V.; Romanenko, D. V.; Grishin, S. V.; Beginin, E.N.; Sharaevskii, Y.P.; Nikitov, S.A. Spin Wave Propagation in a Uniformly Biased Curved Magnonic Waveguide. *Phys. Rev. B* **2017**, *96*, 060401, doi:10.1103/PhysRevB.96.060401.

69. Nikitin, A.A.; Ustinov, A.B.; Semenov, A.A.; Chumak, A. V.; Serga, A.A.; Vasyuchka, V.I.; Lahderanta, E.; Kalinikos, B.A.; Hillebrands, B. A Spin-Wave Logic Gate Based on a Width-Modulated Dynamic Magnonic Crystal. *Appl. Phys. Lett.* **2015**, *106*, 102405, doi:10.1063/1.4914506.

70. Hansen, U.H.; Demidov, V.E.; Demokritov, S.O. Dual-Function Phase Shifter for Spin-Wave Logic Applications. *Appl. Phys. Lett.* **2009**, *94*, 252502, doi:10.1063/1.3159628.

71. Fang, Z.; Mitra, A.; Westerman, A.L.; Ali, M.; Ciccarelli, C.; Cespedes, O.; Hickey, B.J.; Ferguson, A.J. Thickness Dependence Study of Current-Driven Ferromagnetic Resonance in $Y_3Fe_5O_{12}$/Heavy Metal Bilayers. *Appl. Phys. Lett.* **2017**, *110*, 092403, doi:10.1063/1.4977490.

72. Yu, H.; Brechet, S.D.; Che, P.; Vetro, F.A.; Collet, M.; Tu, S.; Zhang, Y.G.; Zhang, Y.; Stueckler, T.; Wang, L.; et al. Thermal Spin Torques in Magnetic Insulators. *Phys. Rev. B* **2017**, *95*, 104432, doi:10.1103/PhysRevB.95.104432.

73. Tang, C.; Aldosary, M.; Jiang, Z.; Chang, H.; Madon, B.; Chan, K.; Wu, M.; Garay, J.E.; Shi, J. Exquisite Growth Control and Magnetic Properties of Yttrium Iron Garnet Thin Films. *Appl. Phys. Lett.* **2016**, *108*, 102403, doi:10.1063/1.4943210.

74. Fu, J.; Hua, M.; Wen, X.; Xue, M.; Ding, S.; Wang, M.; Yu, P.; Liu, S.; Han, J.; Fu, J.; et al. Epitaxial Growth of $Y_3Fe_5O_{12}$ Thin Films with Perpendicular Magnetic Anisotropy. *Appl. Phys. Lett.* **2017**, *110*, 202403, doi:10.1063/1.4983783.

75. Yu, H.; d'Allivy Kelly, O.; Cros, V.; Bernard, R.; Bortolotti, P.; Anane, A.; Brandl, F.; Heimbach, F.; Grundler, D. Approaching Soft X-Ray Wavelengths in Nanomagnet-Based Microwave Technology. *Nat. Commun.* **2016**, *7*, 11255, doi:10.1038/pj.2016.37.

76. Gallagher, J.C.; Yang, A.S.; Brangham, J.T.; Esser, B.D.; White, S.P.; Page, M.R.; Meng, K.Y.; Yu, S.; Adur, R.; Ruane, W.; et al. Exceptionally High Magnetization of Stoichiometric $Y_3Fe_5O_{12}$ Epitaxial Films Grown on $Gd_3Ga_5O_{12}$. *Appl. Phys. Lett.* **2016**, *109*, 072401, doi:10.1063/1.4961371.

77. D'Allivy Kelly, O.; Anane, A.; Bernard, R.; Ben Youssef, J.; Hahn, C.; Molpeceres, A.H.; Carrétéro, C.; Jacquet, E.; Deranlot, C.; Bortolotti, P.; et al. Inverse Spin Hall Effect in Nanometer-Thick Yttrium Iron Garnet/Pt System. *Appl. Phys. Lett.* **2013**, *103*, 082408, doi:10.1063/1.4819157.

78. Sokolov, N.S.; Fedorov, V. V.; Korovin, A.M.; Suturin, S.M.; Baranov, D.A.; Gastev, S. V.; Krichevtsov, B.B.; Maksimova, K.Y.; Grunin, A.I.; Bursian, V.E.; et al. Thin Yttrium Iron Garnet Films Grown by Pulsed Laser Deposition: Crystal Structure, Static, and Dynamic Magnetic Properties. *J. Appl. Phys.* **2016**, *119*, 023903, doi:10.1063/1.4939678.

79. Lutsev, L. V.; Korovin, A.M.; Bursian, V.E.; Gastev, S. V.; Fedorov, V. V.; Suturin, S.M.; Sokolov, N.S. Low-Relaxation Spin Waves in Laser-Molecular-Beam Epitaxy Grown Nanosized Yttrium Iron Garnet Films. *Appl. Phys. Lett.* **2016**, *108*, 182402, doi:10.1063/1.4948304.

80. Jermain, C.L.; Aradhya, S. V; Reynolds, N.D.; Buhrman, R.A.; Brangham, J.T.; Page, M.R.; Hammel, P.C.; Yang, F.Y.; Ralph, D.C. Increased Low-Temperature Damping in Yttrium Iron Garnet Thin Films. *Phys. Rev. B* **2017**, *95*, 174411, doi:10.1103/PhysRevB.95.174411.

81. Zhu, N.; Chang, H.; Franson, A.; Liu, T.; Zhang, X.; Johnston-Halperin, E.; Wu, M.; Tang, H.X. Patterned Growth of Crystalline $Y_3Fe_5O_{12}$ Nanostructures with Engineered Magnetic Shape Anisotropy. *Appl. Phys. Lett.* **2017**, *110*, 252401, doi:10.1063/1.4986474.

82. Jungfleisch, M.B.; Zhang, W.; Jiang, W.; Chang, H.; Sklenar, J.; Wu, S.M.; Pearson, J.E.; Bhattacharya, A.; Ketterson, J.B.; Wu, M.; et al. Spin

Waves in Micro-Structured Yttrium Iron Garnet Nanometer-Thick Films. *J. Appl. Phys.* **2015**, *117*, 17D128, doi:10.1063/1.4916027.

83. Okamura, Y.; Ishida, M.; Yamamoto, S. Magnetooptic Rib Waveguides in YIG: An Experiment. *Appl. Opt.* **1984**, *23*, 124, doi:10.1364/AO.23.000124.

84. Lara, A.; Moreno, J.R.; Guslienko, K.Y.; Aliev, F.G. Communication and Information Processing in Magnetic Nanostructures with Edge Spin Waves. *Sci. Rep.* **2017**, 1–12, doi:10.1038/s41598-017-05737-8.

85. Gruszecki, P.; Romero-Vivas, J.; Dadoenkova, Y.S.; Dadoenkova, N.N.; Lyubchanskii, I.L.; Krawczyk, M. Goos-Hänchen Effect and Bending of Spin Wave Beams in Thin Magnetic Films. *Appl. Phys. Lett.* **2014**, *105*, 242406, doi:10.1063/1.4904342.

86. Gruszecki, P.; Dadoenkova, Y.S.; Dadoenkova, N.N.; Lyubchanskii, I.L.; Romero-Vivas, J.; Guslienko, K.Y.; Krawczyk, M. Influence of Magnetic Surface Anisotropy on Spin Wave Reflection from the Edge of Ferromagnetic Film. *Phys. Rev. B* **2015**, *92*, 054427, doi:10.1103/PhysRevB.92.054427.

87. Kanazawa, N.; Goto, T.; Sekiguchi, K.; Granovsky, A.B.; Takagi, H.; Nakamura, Y.; Inoue, M. Spin Wave Absorber Generated by Artificial Surface Anisotropy for Spin Wave Device Network. *AIP Adv.* **2016**, *6*, 095204, doi:10.1063/1.4962664.

88. Koczorowski, W.; Kuświk, P.; Przychodnia, M.; Wiesner, K.; El-Ahmar, S.; Szybowicz, M.; Nowicki, M.; Strupiński, W.; Czajka, R. CMOS-Compatible Fabrication Method of Graphene-Based Micro Devices. *Mater. Sci. Semicond. Process.* **2017**, *67*, 92–97, doi:10.1016/j.mssp.2017.05.021.

89. Sun, Y.; Song, Y.Y.; Chang, H.; Kabatek, M.; Jantz, M.; Schneider, W.; Wu, M.; Schultheiss, H.; Hoffmann, A. Growth and Ferromagnetic

Resonance Properties of Nanometer-Thick Yttrium Iron Garnet Films. *Appl. Phys. Lett.* **2012**, *101*, 152405, doi:10.1063/1.4759039.

90. Manuilov, S.A.; Fors, R.; Khartsev, S.I.; Grishin, A.M. Submicron Y3Fe5O12 Film Magnetostatic Wave Band Pass Filters. *J. Appl. Phys.* **2009**, *105*, 033917, doi:10.1063/1.3075816.

91. Mitra, A.; Cespedes, O.; Ramasse, Q.; Ali, M.; Marmion, S.; Ward, M.; Brydson, R.M.D.; Kinane, C.J.; Cooper, J.F.K.; Langridge, S.; et al. Interfacial Origin of the Magnetisation Suppression of Thin Film Yttrium Iron Garnet. *Sci. Rep.* **2017**, *7*, 11774, doi:10.1038/s41598-017-10281-6.

92. Ziętek, S.; Chęciński, J.; Frankowski, M.; Skowroński, W.; Stobiecki, T. Electric-Field Tunable Spin Waves in PMN-PT/NiFe Heterostructure: Experiment and Micromagnetic Simulations. *J. Magn. Magn. Mater.* **2017**, *428*, 64–69, doi:10.1016/j.jmmm.2016.11.056.

93. Kuświk, P.; Głowiński, H.; Coy, E.; Dubowik, J.; Stobiecki, F. Perpendicularly Magnetized $Co_{20}Fe_{60}B_{20}$ Layer Sandwiched between Au with Low Gilbert Damping. *J. Phys. Condens. Matter* **2017**, *29*, 435803.

94. Glowinski, H.; Goscianska, I.; Krysztofik, A.; Barnas, J.; Cecot, M.; Kuswik, P.; Dubowik, J. Damping in Finemet Films Capped by Platinum. In Proceedings of the 2016 21st International Conference on Microwave, Radar and Wireless Communications (MIKON); IEEE, May 2016; pp. 1–4.

95. Bhoi, B.; Diware, M.S. Preferred-Oriented Polycrystalline $Y_3Fe_5O_{12}$ Films Grown on Quartz with Low Microwave Loss. *J. Am. Ceram. Soc.* **2021**, *104*, 2423–2427, doi:10.1111/jace.17675.

96. Capku, Z.; Deger, C.; Aksu, P.; Yildiz, F. Origin of Perpendicular Magnetic Anisotropy in Yttrium Iron Garnet Thin Films Grown on Si (100). *IEEE Trans. Magn.* **2020**, *56*, 2–7,

doi:10.1109/TMAG.2020.3021646.

97. Che, P.; Zhang, Y.; Liu, C.; Tu, S.; Liao, Z.; Yu, D.; Vetro, F.A.; Ansermet, J.P.; Zhao, W.; Bi, L.; et al. Short-Wavelength Spin Waves in Yttrium Iron Garnet Micro-Channels on Silicon. *IEEE Magn. Lett.* **2016**, *7*, 1–4, doi:10.1109/LMAG.2016.2616105.

98. Coll, M.; Fontcuberta, J.; Althammer, M.; Bibes, M.; Boschker, H.; Calleja, A.; Cheng, G.; Cuoco, M.; Dittmann, R.; Dkhil, B.; et al. Towards Oxide Electronics: A Roadmap. *Appl. Surf. Sci.* **2019**, *482*, 1–93, doi:10.1016/j.apsusc.2019.03.312.

99. Conca, A.; Papaioannou, E.T.; Klingler, S.; Greser, J.; Sebastian, T.; Leven, B.; Lösch, J.; Hillebrands, B. Annealing Influence on the Gilbert Damping Parameter and the Exchange Constant of CoFeB Thin Films. *Appl. Phys. Lett.* **2014**, *104*, 182407, doi:10.1063/1.4875927.

100. Coy, E.; Graczyk, P.; Yate, L.; Załęski, K.; Gapiński, J.; Kuświk, P.; Mielcarek, S.; Stobiecki, F.; Mróz, B.; Ferrater, C.; et al. Second Harmonic Generation Response in Thermally Reconstructed Multiferroic B′-$Gd_2(MoO_4)_3$ Thin Films. *Sci. Rep.* **2017**, *7*, 11800, doi:10.1038/s41598-017-12370-y.

101. Delgado, A.; Guerra, Y.; Padrón-Hernández, E.; Peña-Garcia, R. Combining the Sol Gel Method and Spin Coating to Obtain YIG Films with Low FMR Linewidth on Silicon (100) Substrate. *Mater. Res. Express* **2018**, *5*, 026419, doi:10.1088/2053-1591/aaaff8.

102. Guillemard, C.; Petit-Watelot, S.; Rojas-Sánchez, J.C.; Hohlfeld, J.; Ghanbaja, J.; Bataille, A.; Le Fèvre, P.; Bertran, F.; Andrieu, S. Polycrystalline Co_2Mn-Based Heusler Thin Films with High Spin Polarization and Low Magnetic Damping. *Appl. Phys. Lett.* **2019**, *115*, 172401, doi:10.1063/1.5121614.

103. Hou, J.T.; Liu, L. Strong Coupling between Microwave Photons and Nanomagnet Magnons. *Phys. Rev. Lett.* **2019**, *123*, 107702, doi:10.1103/PhysRevLett.123.107702.

104. Huebl, H.; Zollitsch, C.W.; Lotze, J.; Hocke, F.; Greifenstein, M.; Marx, A.; Gross, R.; Goennenwein, S.T.B. High Cooperativity in Coupled Microwave Resonator Ferrimagnetic Insulator Hybrids. *Phys. Rev. Lett.* **2013**, *111*, 127003, doi:10.1103/PhysRevLett.111.127003.

105. Kang, Y.M.; Wee, S.H.; Baik, S. Il; Min, S.G.; Yu, S.C.; Moon, S.H.; Kim, Y.W.; Yoo, S.I. Magnetic Properties of YIG($Y_3Fe_5O_{12}$) Thin Films Prepared by the Post Annealing of Amorphous Films Deposited by Rf-Magnetron Sputtering. *J. Appl. Phys.* **2005**, *97*, 10A319, doi:10.1063/1.1855460.

106. Kumar, N.; Misra, D.S.; Venkataramani, N.; Prasad, S.; Krishnan, R. Magnetic Properties of Pulsed Laser Ablated YIG Thin Films on Different Substrates. *J. Magn. Magn. Mater.* **2004**, *272–276*, 899–900, doi:10.1016/j.jmmm.2003.12.223.

107. Lachance-Quirion, D.; Wolski, S.P.; Tabuchi, Y.; Kono, S.; Usami, K.; Nakamura, Y. Entanglement-Based Single-Shot Detection of a Single Magnon with a Superconducting Qubit. *Science (80-.).* **2020**, *367*, 425–428, doi:10.1126/science.aaz9236.

108. Li, Y.; Polakovic, T.; Wang, Y.L.; Xu, J.; Lendinez, S.; Zhang, Z.; Ding, J.; Khaire, T.; Saglam, H.; Divan, R.; et al. Strong Coupling between Magnons and Microwave Photons in On-Chip Ferromagnet-Superconductor Thin-Film Devices. *Phys. Rev. Lett.* **2019**, *123*, 107701, doi:10.1103/PhysRevLett.123.107701.

109. Lutsev, L. V.; Dubovoy, V.A.; Stognij, A.I.; Novitskii, N.N.; Mozharov, A.M.; Mukhin, I.S.; Ketsko, V.A. Spin-Wave Filters Based on Thin

$Y_3Fe_5O_{12}$ Films on $Gd_3Ga_5O_{12}$ and Si Substrates for Microwave Applications. *J. Appl. Phys.* **2020**, *127*, 183903, doi:10.1063/5.0007338.

110. McKenzie-Sell, L.; Xie, J.; Lee, C.M.; Robinson, J.W.A.; Ciccarelli, C.; Haigh, J.A. Low-Impedance Superconducting Microwave Resonators for Strong Coupling to Small Magnetic Mode Volumes. *Phys. Rev. B* **2019**, *99*, 140414, doi:10.1103/PhysRevB.99.140414.

111. Mohseni, M.; Kewenig, M.; Verba, R.; Wang, Q.; Schneider, M.; Heinz, B.; Kohl, F.; Dubs, C.; Lägel, B.; Serga, A.A.; et al. Parametric Generation of Propagating Spin Waves in Ultrathin Yttrium Iron Garnet Waveguides. *Phys. Status Solidi - Rapid Res. Lett.* **2020**, *2000011*, doi:10.1002/pssr.202000011.

112. Popova, E.; Keller, N.; Gendron, F.; Thomas, L.; Brianso, M.-C.; Guyot, M.; Tessier, M.; Parkin, S.S.P. Perpendicular Magnetic Anisotropy in Ultrathin Yttrium Iron Garnet Films Prepared by Pulsed Laser Deposition Technique. *J. Vac. Sci. Technol. A Vacuum, Surfaces, Film.* **2001**, *19*, 2567–2570, doi:10.1116/1.1392395.

113. Qin, H.; Holländer, R.B.; Flajšman, L.; Hermann, F.; Dreyer, R.; Woltersdorf, G.; van Dijken, S. Nanoscale Magnonic Fabry-Pérot Resonator for Low-Loss Spin-Wave Manipulation. *Nat. Commun.* **2021**, *12*, 2293, doi:10.1038/s41467-021-22520-6.

114. Sarker, M.S.; Yamahara, H.; Tabata, H. Current-Controlled Magnon Propagation in Pt/$Y_3Fe_5O_{12}$ Heterostructure. *Appl. Phys. Lett.* **2020**, *117*, 152403, doi:10.1063/5.0019024.

115. Saroha, A.; Dixit, T.; Ganapathi, K.L.; Muralidhar, M.; Murakami, M.; Rao, M.S.R. Nanoscale Probing of Magnetic and Electrical Properties of YIG/Si (100) Thin Films Grown by Pulsed Laser Deposition. *IEEE Magn. Lett.* **2016**, *7*, 1949, doi:10.1109/LMAG.2020.2985338.

116. Schmidt, G.; Hauser, C.; Trempler, P.; Paleschke, M.; Papaioannou, E.T. Ultra Thin Films of Yttrium Iron Garnet with Very Low Damping: A Review. *Phys. Status Solidi* **2020**, *257*, 1900644, doi:10.1002/pssb.201900644.

117. Schoen, M.A.W.; Thonig, D.; Schneider, M.L.; Silva, T.J.; Nembach, H.T.; Eriksson, O.; Karis, O.; Shaw, J.M. Ultra-Low Magnetic Damping of a Metallic Ferromagnet. *Nat. Phys.* **2016**, *12*, 839–842, doi:10.1038/nphys3770.

118. Stognij, A.I.; Lutsev, L. V; Bursian, V.E.; Novitskii, N.N. Growth and Spin-Wave Properties of Thin $Y_3Fe_5O_{12}$ Films on Si Substrates. *J. Appl. Phys.* **2015**, *118*, 023905, doi:10.1063/1.4926475.

119. Stognij, A.I.; Novitskii, N.N.; Golikova, O.L.; Bespalov, A. V.; Gieniusz, R.; Maziewski, A.; Stupakiewicz, A.; Smirnova, M.N.; Ketsko, V.A. Growth of $Y_3Fe_5O_{12}$ Films on Si with AlO_x and SiO_2 Buffer Layers by Ion Beam Sputtering. *Inorg. Mater.* **2017**, *53*, 1069–1074, doi:10.1134/S0020168517100156.

120. Tabuchi, Y.; Ishino, S.; Ishikawa, T.; Yamazaki, R.; Usami, K.; Nakamura, Y. Hybridizing Ferromagnetic Magnons and Microwave Photons in the Quantum Limit. *Phys. Rev. Lett.* **2014**, *113*, 083603, doi:10.1103/PhysRevLett.113.083603.

121. Tabuchi, Y.; Ishino, S.; Noguchi, A.; Ishikawa, T.; Yamazaki, R.; Usami, K.; Nakamura, Y. Coherent Coupling between a Ferromagnetic Magnon and a Superconducting Qubit. *Science (80-.).* **2015**, *349*, 405–408, doi:10.1126/science.aaa3693.

122. Träger, N.; Groß, F.; Förster, J.; Baumgaertl, K.; Stoll, H.; Weigand, M.; Schütz, G.; Grundler, D.; Gräfe, J. Single Shot Acquisition of Spatially Resolved Spin Wave Dispersion Relations Using X-Ray Microscopy. *Sci.*

Rep. **2020**, *10*, 18146, doi:10.1038/s41598-020-74785-4.

123. Yamada, K.; Kogiso, K.; Shiota, Y.; Yamamoto, M.; Yamaguchi, A.; Moriyama, T.; Ono, T.; Shima, M. Dependence of Gilbert Damping Constant on Microstructure in Nanocrystalline YIG Coatings Prepared by Co-Precipitation and Spin-Coating on a Si Substrate. *J. Magn. Magn. Mater.* **2020**, *513*, 167253, doi:10.1016/j.jmmm.2020.167253.

124. Yang, Y.; Liu, T.; Bi, L.; Deng, L. Recent Advances in Development of Magnetic Garnet Thin Films for Applications in Spintronics and Photonics. *J. Alloys Compd.* **2021**, *860*, 158235, doi:10.1016/j.jallcom.2020.158235.

125. Zaumseil, P. High-Resolution Characterization of the Forbidden Si 200 and Si 222 Reflections. *J. Appl. Crystallogr.* **2015**, *48*, 528–532, doi:10.1107/S1600576715004732.

126. Zhang, X.; Zou, C.L.; Jiang, L.; Tang, H.X. Strongly Coupled Magnons and Cavity Microwave Photons. *Phys. Rev. Lett.* **2014**, *113*, 156401, doi:10.1103/PhysRevLett.113.156401.

127. Zhao, Y.; Li, Y.; Zhu, S.; Chen, C.; Yao, M.; Zhao, Y.; Hu, Z.; Peng, B.; Liu, M.; Ziyao, Z. Voltage Tunable Low Damping YIG/PMN-PT Multiferroic Heterostructure for Low-Power RF/Microwave Devices. *J. Phys. D Appl. Phys. Phys.* **2021**, *54*, 245002, doi:10.1088/1361-6463/abce7c.

128. Zhao, Y.; Song, Q.; Yang, S.H.; Su, T.; Yuan, W.; Parkin, S.S.P.; Shi, J.; Han, W. Experimental Investigation of Temperature-Dependent Gilbert Damping in Permalloy Thin Films. *Sci. Rep.* **2016**, *6*, 22890, doi:10.1038/srep22890.

129. Jin, L.; Jia, K.; He, Y.; Wang, G.; Zhong, Z.; Zhang, H. Pulsed Laser Deposition Grown Yttrium-Iron-Garnet Thin Films: Effect of Composition and Iron Ion Valences on Microstructure and Magnetic Properties. *Appl.*

Surf. Sci. **2019**, *483*, 947–952, doi:10.1016/j.apsusc.2019.04.050.

130. Mokarian Zanjani, S.; Onbaşlı, M.C. Predicting New Iron Garnet Thin Films with Perpendicular Magnetic Anisotropy. *J. Magn. Magn. Mater.* **2020**, *499*, 166108, doi:10.1016/j.jmmm.2019.166108.

131. Soumah, L.; Beaulieu, N.; Qassym, L.; Carrétéro, C.; Jacquet, E.; Lebourgeois, R.; Ben Youssef, J.; Bortolotti, P.; Cros, V.; Anane, A. Ultra-Low Damping Insulating Magnetic Thin Films Get Perpendicular. *Nat. Commun.* **2018**, *9*, 1–9, doi:10.1038/s41467-018-05732-1.

132. Ciubotariu, O.; Semisalova, A.; Lenz, K.; Albrecht, M. Strain-Induced Perpendicular Magnetic Anisotropy and Gilbert Damping of $Tm_3Fe_5O_{12}$ Thin Films. *Sci. Rep.* **2019**, *9*, 17474, doi:10.1038/s41598-019-53255-6.

133. Ortiz, V.H.; Aldosary, M.; Li, J.; Xu, Y.; Lohmann, M.I.; Sellappan, P.; Kodera, Y.; Garay, J.E.; Shi, J. Systematic Control of Strain-Induced Perpendicular Magnetic Anisotropy in Epitaxial Europium and Terbium Iron Garnet Thin Films. *APL Mater.* **2018**, *6*, 121113, doi:10.1063/1.5078645.

134. Wang, C.T.; Liang, X.F.; Zhang, Y.; Liang, X.; Zhu, Y.P.; Qin, J.; Gao, Y.; Peng, B.; Sun, N.X.; Bi, L. Controlling the Magnetic Anisotropy in Epitaxial $Y_3Fe_5O_{12}$ Films by Manganese Doping. *Phys. Rev. B* **2017**, *96*, 224403, doi:10.1103/PhysRevB.96.224403.

135. Lin, Y.; Jin, L.; Zhang, H.; Zhong, Z.; Yang, Q.; Rao, Y.; Li, M. Bi-YIG Ferrimagnetic Insulator Nanometer Films with Large Perpendicular Magnetic Anisotropy and Narrow Ferromagnetic Resonance Linewidth. *J. Magn. Magn. Mater.* **2020**, *496*, 165886, doi:10.1016/j.jmmm.2019.165886.

136. Jermain, C.L.; Paik, H.; Aradhya, S. V.; Buhrman, R.A.; Schlom, D.G.; Ralph, D.C. Low-Damping Sub-10-nm Thin Films of Lutetium Iron Garnet

Grown by Molecular-Beam Epitaxy. *Appl. Phys. Lett.* **2016**, *109*, 192408, doi:10.1063/1.4967695.

137. Wang, H.; Du, C.; Hammel, P.C.; Yang, F. Strain-Tunable Magnetocrystalline Anisotropy in Epitaxial $Y_3Fe_5O_{12}$ Thin Films. *Phys. Rev. B - Condens. Matter Mater. Phys.* **2014**, *89*, 134404, doi:10.1103/PhysRevB.89.134404.

138. Li, G.; Bai, H.; Su, J.; Zhu, Z.Z.; Zhang, Y.; Cai, J.W. Tunable Perpendicular Magnetic Anisotropy in Epitaxial $Y_3Fe_5O_{12}$ Films. *APL Mater.* **2019**, *7*, 041104, doi:10.1063/1.5090292.

139. Kumar, R.; Samantaray, B.; Hossain, Z. Ferromagnetic Resonance Studies of Strain Tuned Bi:YIG Films. *J. Phys. Condens. Matter* **2019**, *31*, 435802, doi:10.1088/1361-648X/ab2e93.

140. Vysotskii, S.L.; Khivintsev, Y. V.; Kozhevnikov, A. V.; Sakharov, V.K.; Filimonov, Y.A.; Stognii, A.I.; Novitskii, N.N.; Nikitov, S.A. The Influence of Strains on the Ferromagnetic Resonance Spectrum of Submicron Yttrium Iron Garnet Films Obtained by Ion Beam Sputtering. *J. Commun. Technol. Electron.* **2019**, *64*, 1398–1406, doi:10.1134/S1064226919100140.

141. Gurjar, G.; Sharma, V.; Patnaik, S. Control of Magnetization Dynamics by Substrate Orientation in YIG Thin Films. *Mater. Res. Express* **2021**, *8*, 066401, doi:10.1088/2053-1591/ac0311.

142. Guo, H.; Dong, S.; Rack, P.; Budai, J.; Beekman, C.; Gai, Z.; Siemons, W.; Gonzalez, C.; Timilsina, R.; Wong, A.T.; et al. Strain Doping: Reversible Single-Axis Control of a Complex Oxide Lattice via Helium Implantation. *Phys. Rev. Lett.* **2015**, *114*, 256801, doi:10.1103/PhysRevLett.114.256801.

143. Sarker, M.S.; Nakamura, S.; Yamahara, H.; Seki, M.; Tabata, H. Multifrequency Spin-Wave Propagation for Parallel Data Processing Using

Microstructured Yttrium Iron Garnet Thin Films. *IEEE Trans. Magn.* **2021**, 3087812, doi:10.1109/tmag.2021.3087812.

144. Coy, E.; Fina, I.; Załęski, K.; Krysztofik, A.; Yate, L.; Rodriguez, L.; Graczyk, P.; Głowiński, H.; Ferrater, C.; Dubowik, J.; et al. High-Temperature Magnetodielectric $Bi(Fe_{0.5}Mn_{0.5})O_3$ Thin Films with Checkerboard-Ordered Oxygen Vacancies and Low Magnetic Damping. *Phys. Rev. Appl.* **2018**, *10*, 054072, doi:10.1103/PhysRevApplied.10.054072.

145. Li, S.; Zhang, W.; Ding, J.; Pearson, J.E.; Novosad, V.; Hoffmann, A. Epitaxial Patterning of Nanometer-Thick $Y_3Fe_5O_{12}$ Films with Low Magnetic Damping. *Nanoscale* **2016**, *8*, 388–394, doi:10.1039/c5nr06808h.

146. Nakatsuka, A.; Yoshiasa, A.; Yamanaka, T. Cation Distribution and Crystal Chemistry of $Y_3Al_{5-x}Ga_xO_{12}$ ($0 \leq x \leq 5$) Garnet Solid Solutions. *Acta Crystallogr. Sect. B Struct. Sci.* **1999**, *55*, 266–272, doi:10.1107/S0108768198012567.

147. Popova, E.; Deb, M.; Bocher, L.; Gloter, A.; Stéphan, O.; Warot-Fonrose, B.; Berini, B.; Dumont, Y.; Keller, N. Interplay between Epitaxial Strain and Low Dimensionality Effects in a Ferrimagnetic Oxide. *J. Appl. Phys.* **2017**, *121*, 115304, doi:10.1063/1.4978508.

148. Shin, C.S.; Rudenja, S.; Gall, D.; Hellgren, N.; Lee, T.Y.; Petrov, I.; Greene, J.E. Growth, Surface Morphology, and Electrical Resistivity of Fully Strained Substoichiometric Epitaxial TiN_x ($0.67 \leq x < 1.0$) Layers on MgO (001). *J. Appl. Phys.* **2004**, *95*, 356, doi:10.1063/1.1629155.

149. Willmann, H.; Beckers, M.; Birch, J.; Mayrhofer, P.H.; Mitterer, C.; Hultman, L. Epitaxial Growth of Al-Cr-N Thin Films on MgO(111). *Thin Solid Films* **2008**, *517*, 598–602, doi:10.1016/j.tsf.2008.07.003.

150. Zaki, A.M.; Blythe, H.J.; Heald, S.M.; Fox, A.M.; Gehring, G.A. Growth of High Quality Yttrium Iron Garnet Films Using Standard Pulsed Laser Deposition Technique. *J. Magn. Magn. Mater.* **2018**, *453*, 254–257, doi:10.1016/j.jmmm.2017.11.054.

151. Zhou, X.; Cheng, W.; Lin, F.; Ma, X.; Shi, W. Effect of Post-Annealing Temperature on the Microstructure and Magnetic Properties of Ce:YIG Thin Films Deposited on Si Substrates. *Appl. Surf. Sci.* **2006**, *253*, 2108–2112, doi:10.1016/j.apsusc.2006.04.002.

152. Lee, S.; Grudichak, S.; Sklenar, J.; Tsai, C.C.; Jang, M.; Yang, Q.; Zhang, H.; Ketterson, J.B. Ferromagnetic Resonance of a YIG Film in the Low Frequency Regime. *J. Appl. Phys.* **2016**, *120*, 033905, doi:10.1063/1.4956435.

153. Arias, R.; Mills, D.L. Extrinsic Contributions to the Ferromagnetic Resonance Response of Ultrathin Films. *Phys. Rev. B - Condens. Matter Mater. Phys.* **1999**, *60*, 7395–7409, doi:10.1103/PhysRevB.60.7395.

154. McMichael, R.D.; Krivosik, P. Classical Model of Extrinsic Ferromagnetic Resonance Linewidth in Ultrathin Films. *IEEE Trans. Magn.* **2004**, *40*, 2–11, doi:10.1109/TMAG.2003.821564.

155. Belmeguenai, M.; Tuzcuoglu, H.; Gabor, M.S.; Petrisor, T.; Tiusan, C.; Berling, D.; Zighem, F.; Chauveau, T.; Chérif, S.M.; Moch, P. Co_2FeAl Thin Films Grown on MgO Substrates: Correlation between Static, Dynamic, and Structural Properties. *Phys. Rev. B* **2013**, *87*, 184431, doi:10.1103/PhysRevB.87.184431.

156. Lee, H.K.; Barsukov, I.; Swartz, A.G.; Kim, B.; Yang, L.; Hwang, H.Y.; Krivorotov, I.N. Magnetic Anisotropy, Damping, and Interfacial Spin Transport in Pt/LSMO Bilayers. *AIP Adv.* **2016**, *6*, 055212, doi:10.1063/1.4950971.

157. Oliveira, A.B.; Rodríguez-Suárez, R.L.; Correa, M.A.; Bohn, F.; Raza, S.A.; Sommer, R.L.; Chesman, C. Filtering Magnetic Relaxation Mechanisms of YIG(001) Thin Films Using Ferromagnetic Resonance. *J. Magn. Magn. Mater.* **2020**, *507*, 166851, doi:10.1016/j.jmmm.2020.166851.

158. Zakeri, K.; Lindner, J.; Barsukov, I.; Meckenstock, R.; Farle, M.; Von Hörsten, U.; Wende, H.; Keune, W.; Rocker, J.; Kalarickal, S.S.; et al. Spin Dynamics in Ferromagnets: Gilbert Damping and Two-Magnon Scattering. *Phys. Rev. B - Condens. Matter Mater. Phys.* **2007**, *76*, 104416, doi:10.1103/PhysRevB.76.104416.

159. McMichael, R.D.; Twisselmann, D.J.; Kunz, A. Localized Ferromagnetic Resonance in Inhomogeneous Thin Films. *Phys. Rev. Lett.* **2003**, *90*, 227601, doi:10.1103/PhysRevLett.90.227601.

160. McMichael, R.D. A Mean-Field Model of Extrinsic Line Broadening in Ferromagnetic Resonance. *J. Appl. Phys.* **2008**, *103*, 07B114, doi:10.1063/1.2837887.

161. Barman, A.; Gubbiotti, G.; Ladak, S.; Adeyeye, A.O.; Krawczyk, M.; Grafe, J.; Adelmann, C.; Cotofana, S.; Naeemi, A.; Vasyuchka, V.I.; et al. The 2021 Magnonics Roadmap. *J. Phys. Condens. Matter* **2021**, *33*, 413001, doi:10.1088/1361-648X/abec1a.

162. Mahmoud, A.; Ciubotaru, F.; Vanderveken, F.; Chumak, A. V.; Hamdioui, S.; Adelmann, C.; Cotofana, S. Introduction to Spin Wave Computing. *J. Appl. Phys.* **2020**, *128*, 161101, doi:10.1063/5.0019328.

163. Barman, A.; Mondal, S.; Sahoo, S.; De, A. Magnetization Dynamics of Nanoscale Magnetic Materials: A Perspective. *J. Appl. Phys.* **2020**, *128*, 170901, doi:10.1063/5.0023993.

164. Sheng, L.; Chen, J.; Wang, H.; Yu, H. Magnonics Based on Thin-Film Iron

Garnets. *J. Phys. Soc. Japan* **2021**, *90*, 081005, doi:10.7566/jpsj.90.081005.

165. Kruglyak, V. V. Chiral Magnonic Resonators: Rediscovering the Basic Magnetic Chirality in Magnonics. *Appl. Phys. Lett.* **2021**, *119*, 200502, doi:10.1063/5.0068820.

166. Pirro, P.; Vasyuchka, V.I.; Serga, A.A.; Hillebrands, B. Advances in Coherent Magnonics. *Nat. Rev. Mater.* **2021**, *6*, 1114–1135, doi:10.1038/s41578-021-00332-w.

167. Ding, J.; Liu, C.; Zhang, Y.; Erugu, U.; Quan, Z.; Yu, R.; Mccollum, E.; Mo, S.; Yang, S.; Ding, H.; et al. Nanometer-Thick Yttrium Iron Garnet Films with Perpendicular Anisotropy and Low Damping. *Phys. Rev. Appl.* **2020**, *14*, 014017, doi:10.1103/PhysRevApplied.14.014017.

168. Holzmann, C.; Ullrich, A.; Ciubotariu, O.T.; Albrecht, M. Stress-Induced Magnetic Properties of Gadolinium Iron Garnet Nanoscale-Thin Films: Implications for Spintronic Devices. *ACS Appl. Nano Mater.* **2022**, *5*, 1023–1033, doi:10.1021/acsanm.1c03687.

169. Wu, G.; Wang, D.; Verma, N.; Rao, R.; Cheng, Y.; Guo, S.; Cao, G.; Watanabe, K.; Taniguchi, T.; Lau, C.N.; et al. Enhancing Perpendicular Magnetic Anisotropy in Garnet Ferrimagnet by Interfacing with Few-Layer WTe2. *Nano Lett.* **2022**, *22*, 1115–1121, doi:10.1021/acs.nanolett.1c04237.

170. Böttcher, T.; Ruhwedel, M.; Levchenko, K.O.; Wang, Q.; Chumak, H.L.; Popov, M.A.; Zavislyak, I. V.; Dubs, C.; Surzhenko, O.; Hillebrands, B.; et al. Fast Long-Wavelength Exchange Spin Waves in Partially Compensated Ga:YIG. *Appl. Phys. Lett.* **2022**, *120*, 102401, doi:10.1063/5.0082724.

171. Zhang, Y.; Yang, Q.; Liu, X.; Zhang, D.; Rao, Y.; Zhang, H. Comparison of the Magnetic Properties of Bismuth Substituted Thulium Iron Garnet

and Yttrium Iron Garnet Films. *AIP Adv.* **2021**, *11*, 065113, doi:10.1063/5.0050340.

172. Syvorotka, I.I.; Sugak, D.; Yakhnevych, U.; Buryy, O.; Włodarczyk, D.; Pieniążek, A.; Zhydachevskyy, Y.; Levintant-Zayonts, N.; Savytskyy, H.; Bonchyk, O.; et al. Investigation of the Interface of $Y_3Fe_5O_{12}/Gd_3Ga_5O_{12}$ Structure Obtained by the Liquid Phase Epitaxy. *Cryst. Res. Technol.* **2022**, 2100180, doi:10.1002/crat.202100180.

173. Rao, Y.; Zhang, D.; Jin, L.; Zhong, Z.; Yang, Q.; Li, M.; Li, J.; Yang, Y.; Wang, G.; Gan, G.; et al. Magnetic Properties of a $Y_3Fe_5O_{12}/(TmBi)_3(FeGa)_5O_{12}$ Heterostructure Related to Strain-Induced Magnetic Anisotropy. *J. Magn. Magn. Mater.* **2020**, *497*, 165817, doi:10.1016/j.jmmm.2019.165817.

174. Wu, Y.; Yang, Q.; Zhang, D.; Zhang, Y.; Rao, Y.; Wen, Q.; Syvorotka, I.I.; Zhang, H. The Submicron Garnet Film with Perpendicular Magnetic Anisotropy Prepared by Liquid Phase Epitaxy Method. *J. Magn. Magn. Mater.* **2020**, *506*, 166689, doi:10.1016/j.jmmm.2020.166689.

175. Capku, Z.; Yildiz, F. Spin Wave Modes Observation in YIG Thin Films with Perpendicular. *J. Magn. Magn. Mater.* **2021**, *538*, 168290, doi:10.1016/j.jmmm.2021.168290.

176. Kim, H.; Jung, H.; Yang, J.; Jo, Y.; Yoo, J.; Park, A.M.; Jeong, J.; Kim, K. Deposition of Crystalline GdIG Samples Using Metal Organic Decomposition Method. *Magnetochemistry* **2022**, *8*, 28.

177. Krichevsky, D.M.; Xia, S.; Mandrik, M.P.; Ignatyeva, D.O.; Bi, L.; Belotelov, V.I. Silicon-Based All-Dielectric Metasurface on an Iron Garnet Film for Efficient Magneto-Optical Light Modulation in near Ir Range. *Nanomaterials* **2021**, *11*, 2926, doi:10.3390/nano11112926.

178. Hashimoto, R.; Itaya, T.; Uchida, H.; Funaki, Y.; Fukuchi, S. Properties of

Magnetic Garnet Films for Flexible Magneto-Optical Indicators Fabricated by Spin-Coating Method. *Materials (Basel).* **2022**, *15*, 1241, doi:10.3390/ma15031241.

179. Wei, Z.; Yan, W.; Qin, J.; Deng, L.; Bi, L. Dysprosium Substituted Ce:YIG Thin Films for Temperature Insensitive Integrated Optical Isolator Applications. *Materials (Basel).* **2022**, *15*, 1691, doi:10.3390/ma15051691.

180. Kanazawa, N.; Goto, T.; Sekiguchi, K.; Granovsky, A.B.; Ross, C.A.; Takagi, H.; Nakamura, Y.; Inoue, M. Demonstration of a Robust Magnonic Spin Wave Interferometer. *Sci. Rep.* **2016**, *6*, 30268, doi:10.1038/srep30268.

181. Venkat, G.; Fangohr, H.; Prabhakar, A. Absorbing Boundary Layers for Spin Wave Micromagnetics. *J. Magn. Magn. Mater.* **2018**, *450*, 34–39, doi:10.1016/j.jmmm.2017.06.057.

182. Obaidulla, S.M.; Giri, P.K. Surface Roughening and Scaling Behavior of Vacuum-Deposited SnCl2Pc Organic Thin Films on Different Substrates. *Appl. Phys. Lett.* **2015**, *107*, 221910, doi:10.1063/1.4936937.

183. Nakatsuka, A.; Yoshiasa, A.; Takeno, S. Site Preference of Cations and Structural Variation in $Y_3Fe_{5-x}Ga_xO_{12}$ ($0 \leq x \leq 5$) Solid Solutions with Garnet Structure. *Acta Crystallogr. Sect. B* **1995**, *51*, 737–745, doi:10.1107/S0108768194014813.

184. Gołębiewski, M.; Gruszecki, P.; Krawczyk, M.; Serebryannikov, A.E. Spin-Wave Talbot Effect in a Thin Ferromagnetic Film. *Phys. Rev. B* **2020**, *102*, 134402, doi:10.1103/PhysRevB.102.134402.

185. Martyshkin, A.A.; Beginin, E.N.; Sadovnikov, A. V. Spin Waves Transport in 3D Magnonic Waveguides. *AIP Adv.* **2021**, *11*, 035024, doi:10.1063/9.0000185.

186. Álvarez-Prado, L.M. Control of Dynamics in Weak PMA Magnets. *Magnetochemistry* **2021**, *7*, 43, doi:10.3390/magnetochemistry7030043.

187. Yao, X.; Wang, Z.; Deng, M.; Li, Z.X.; Zhang, Z.; Cao, Y.; Yan, P. Magnetic Skyrmion Generation by Reflective Spin Wave Focusing. *Front. Phys.* **2021**, *9*, 729967, doi:10.3389/fphy.2021.729967.

188. Stückler, T.; Liu, C.; Yu, H.; Heimbach, F.; Chen, J.; Hu, J.; Tu, S.; Alam, M.S.; Zhang, J.; Zhang, Y.; et al. Spin Wave Propagation Detected over 100 μm in Half-Metallic Heusler Alloy Co_2MnSi. *J. Magn. Magn. Mater.* **2018**, *450*, 13–17, doi:10.1016/j.jmmm.2017.09.074.

189. Lake, S.R.; Divinskiy, B.; Schmidt, G.; Demokritov, S.O.; Demidov, V.E. Efficient Geometrical Control of Spin Waves in Microscopic YIG Waveguides. *Appl. Phys. Lett.* **2021**, *119*, 182401, doi:10.1063/5.0071757.

190. Krysztofik, A.; Özoglu, S.; Coy, E. Magnetization Damping in Nanocrystalline Yttrium Iron Garnet Thin Films Grown on Oxidized Silicon. *IEEE Magn. Lett.* **2021**, *12*, 7101605, doi:10.1109/LMAG.2021.3086454.

191. Wyckoff, R.W.. *Crystal Structures*; Second edi.; NY, USA: New York, 1963;

192. Li, Z.; Zhang, X.; Zhang, D.; Liu, B.; Meng, H.; Xu, J.; Zhong, Z.; Tang, X.; Zhang, H.; Jin, L. Magnetization Dynamics in the YIG / Au / YIG Magnon Valve. *APL Mater.* **2022**, *10*, 021101, doi:10.1063/5.0081104.

193. Jin, L.; Zhang, D.; Zhang, H.; Yang, Q.; Tang, X.; Zhong, Z.; Xiao, J.Q. Tuning of the Spin Pumping in Yttrium Iron Garnet/Au Bilayer System by Fast Thermal Treatment. *J. Appl. Phys.* **2014**, *115*, 17C511, doi:10.1063/1.4864046.

194. Brady, G.S.; Clauser, H.R.; Vaccari, J.A. *Materials Handbook*; McGraw-

Hill Education: New York, 2002; ISBN 9781119130536.

195. Du, C.; Wang, H.; Hammel, P.C.; Yang, F. Y3Fe5O12 Spin Pumping for Quantitative Understanding of Pure Spin Transport and Spin Hall Effect in a Broad Range of Materials (Invited). *J. Appl. Phys.* **2015**, *117*, 172603, doi:10.1063/1.4913813.

196. Jin, L.; Zhu, H.; Zhang, D.; Liu, B.; Meng, H.; Tang, X.; Li, M.; Zhong, Z.; Zhang, H. Spin Pumping and Laser Modulated Inverse Spin Hall Effect in Yttrium Iron Garnet/Germanium Heterojunctions. *Appl. Phys. Lett.* **2020**, *116*, 122405, doi:10.1063/1.5141400.

197. Dubowik, J.; Graczyk, P.; Krysztofik, A.; Głowiński, H.; Coy, E.; Załęski, K.; Gościańska, I. Non-Negligible Imaginary Part of the Spin-Mixing Conductance and Its Impact on Magnetization Dynamics in Heavy-Metal-Ferromagnet Bilayers. *Phys. Rev. Appl.* **2020**, *13*, 054011, doi:10.1103/PhysRevApplied.13.054011.

198. Bertelli, I.; Simon, B.G.; Yu, T.; Aarts, J.; Bauer, G.E.W.; Blanter, Y.M.; Sar, T. Imaging Spin-Wave Damping Underneath Metals Using Electron Spins in Diamond. *Adv. Quantum Technol.* **2021**, *4*, 2100094, doi:10.1002/qute.202100094.

199. Souza, A.L.R.; Gamino, M.; Ferreira, A.; de Oliveira, A.B.; Vaz, F.; Bohn, F.; Correa, M.A. Directional Field-Dependence of Magnetoimpedance Effect on Integrated YIG/Pt-Stripline System. *Sensors* **2021**, *21*, 6145, doi:10.3390/s21186145.

200. Bunyaev, S.A.; Serha, R.O.; Musiienko-Shmarova, H.Y.; Kreil, A.J.E.; Frey, P.; Bozhko, D.A.; Vasyuchka, V.I.; Verba, R. V.; Kostylev, M.; Hillebrands, B.; et al. Spin-Wave Relaxation by Eddy Currents in $Y_3Fe_5O_{12}$/Pt Bilayers and a Way to Suppress It. *Phys. Rev. Appl.* **2020**, *14*, 024094, doi:10.1103/PhysRevApplied.14.024094.

201. Flovik, V.; Macià, F.; Kent, A.D.; Wahlström, E. Eddy Current Interactions in a Ferromagnet-Normal Metal Bilayer Structure, and Its Impact on Ferromagnetic Resonance Lineshapes. *J. Appl. Phys.* **2015**, *117*, 143902, doi:10.1063/1.4917285.

202. Vaňatka, M.; Szulc, K.; Wojewoda, O.; Dubs, C.; Chumak, A. V.; Krawczyk, M.; Dobrovolskiy, O. V.; Kłos, J.W.; Urbánek, M. Spin-Wave Dispersion Measurement by Variable-Gap Propagating Spin-Wave Spectroscopy. *Phys. Rev. Appl.* **2021**, *16*, 054033, doi:10.1103/PhysRevApplied.16.054033.

203. Schwartz, M. *Encyclopedia and Handbook of Materials, Parts, and Finishes*; CRC Press: Boca Raton, FL, USA, 2016; ISBN 9781466567481.

204. Boyes, W. *Instrumentation Reference Book*; Elsevier: Amsterdam, 2010; ISBN 9780750683081.

205. Mordike, B.B.L.; Ph, D.; Brookes, C.A. The Tensile Properties of Iridium at High Temperatures. *Platin. Met. Rev.* **1960**, *4*, 94–99, doi:10.1016/0043-1648(60)90239-8.

206. Liang, R.S.; Liu, F.C. Measurement of Thermal Expansion Coefficient of Substrate GGG and Its Epitaxial Layer YIG. *Powder Diffr.* **1999**, *14*, 2–4, doi:10.1017/S0885715600010216.

Oświadczenia współautorów

W tej części pracy załączone są oświadczenia określające indywidualny wkład współautorów w powstanie artykułów będących podstawą ninejszej rozprawy.

Prof. UAM dr hab. Emerson Coy

NanoBioMedical Centre
Adam Mickiewicz University
Wszechnicy Piastowskiej 3
61-614 Poznań, Poland

A declaration

Hereby I declare my contribution to the following articles:

1. *Characterization of spin wave propagation in (111) YIG thin films with large anisotropy*
   A. Krysztofik, H. Głowiński, P. Kuświk, S. Ziętek, **L.E. Coy**, J.N. Rychły, S. Jurga, T.W. Stobiecki, J. Dubowik
   Journal of Physics D: Applied Physics **50**, 235004 (2017)
   DOI: 10.1088/1361-6463/aa6df0

In this publication, I have performed high-resolution X-ray diffraction measurements. I was also involved in the discussion concerning obtained results and manuscript revision.

2. *Ultra-low damping in lift-off structured yttrium iron garnet thin films*
   A. Krysztofik, **L. E. Coy**, P. Kuświk, K. Załęski, H. Głowiński, J. Dubowik
   Applied Physics Letters **111**, 192404 (2017)
   DOI: 10.1063/1.5002004

In this publication, I have performed high-resolution X-ray diffraction and atomic force microscopy measurements. I was also involved in the discussion concerning obtained results and manuscript revision.

3. *Magnetization damping in nanocrystalline yttrium iron garnet thin films grown on oxidized silicon*
   A. Krysztofik, S. Özoğlu, **E. Coy**
   IEEE Magnetics Letters **12**, 7101605 (2021)
   DOI: 10.1109/LMAG.2021.3086454

In this publication, I have supervised atomic force microscopy measurements. I was also involved in the discussion concerning obtained results and manuscript revision.

4. *Effect of strain-induced anisotropy on magnetization dynamics in $Y_3Fe_5O_{12}$ films recrystallized on a lattice-mismatched substrate*
   A. Krysztofik, S. Özoğlu, R.D. McMichael, **E. Coy**
   Scientific Reports **11**, 14011 (2021)
   DOI: 10.1038/s41598-021-93308-3

In this publication, I have supervised high-resolution X-ray diffraction, X-ray reflectivity, and atomic force microscopy measurements. I was also involved in the discussion concerning obtained results and manuscript revision.

5. *Tuning of Magnetic Damping in $Y_3Fe_5O_{12}$ / metal bilayers for spin-wave conduit termination*
   A. Krysztofik, N. Kuznetsov, H. Qin, L. Flajšman, **E. Coy**, S. van Dijken
   Materials **15**, 2814 (2022)
   DOI: 10.3390/ma15082814

In this publication, I have performed high-resolution X-ray diffraction and atomic force microscopy measurements. I was also involved in the discussion concerning obtained results and manuscript evaluation.

13.05.2022 .....

Date Signature

Prof. dr hab. Janusz Dubowik

Institute of Molecular Physics
Polish Academy of Sciences
Smoluchowskiego 17
60-179 Poznań, Poland

A declaration

Hereby I declare my contribution to the following articles:

1. *Characterization of spin wave propagation in (111) YIG thin films with large anisotropy*
   A. Krysztofik, H. Głowiński, P. Kuświk, S. Ziętek, L.E. Coy, J.N. Rychły, S. Jurga, T.W. Stobiecki, **J. Dubowik**
   Journal of Physics D: Applied Physics **50**, 235004 (2017)
   DOI: 10.1088/1361-6463/aa6df0

In this publication, I was involved in the discussion concerning obtained results, manuscript revision and its evaluation.

2. *Ultra-low damping in lift-off structured yttrium iron garnet thin films*
   A. Krysztofik, L. E. Coy, P. Kuświk, K. Załęski, H. Głowiński, **J. Dubowik**
   Applied Physics Letters **111**, 192404 (2017)
   DOI: 10.1063/1.5002004

In this publication, I was involved in the discussion concerning obtained results, manuscript revision and its evaluation.

17.05.2022 .....

Date Signature

Dr. Lukáš Flajšman

NanoSpin
Department of Applied Physics
Aalto University School of Science
FI-00076 Aalto, Finland

A declaration

Hereby I declare my contribution to the following article:

1. *Tuning of Magnetic Damping in $Y_3Fe_5O_{12}$ / metal bilayers for spin-wave conduit termination*
   A. Krysztofik, N. Kuznetsov, H. Qin, **L. Flajšman**, E. Coy, S. van Dijken
   Materials **15**, 2814 (2022)
   DOI: 10.3390/ma15082814

In this publication, I have performed SNS-MOKE measurements. I was also involved in the discussion concerning obtained results and manuscript evaluation.

19. 05. 2022 ……

Date Signature

dr Hubert Głowiński

Institute of Molecular Physics
Polish Academy of Sciences
Smoluchowskiego 17
60-179 Poznań, Poland

A declaration

Hereby I declare my contribution to the following articles:

1. *Characterization of spin wave propagation in (111) YIG thin films with large anisotropy*
   A. Krysztofik, **H. Głowiński**, P. Kuświk, S. Ziętek, L.E. Coy, J.N. Rychły, S. Jurga, T.W. Stobiecki, J. Dubowik
   Journal of Physics D: Applied Physics **50**, 235004 (2017)
   DOI: 10.1088/1361-6463/aa6df0

In this publication, I was involved in the discussion concerning obtained results, manuscript evaluation and correspondence with the journal.

2. *Ultra-low damping in lift-off structured yttrium iron garnet thin films*
   A. Krysztofik, L. E. Coy, P. Kuświk, K. Załęski, **H. Głowiński**, J. Dubowik
   Applied Physics Letters **111**, 192404 (2017)
   DOI: 10.1063/1.5002004

In this publication, I was involved in the discussion concerning obtained results, manuscript evaluation and correspondence with the journal.

13.5.2022 ..... Hubert Głowiński

Date Signature

Adam Krysztofik

Institute of Molecular Physics
Polish Academy of Sciences
Smoluchowskiego 17
60-179 Poznań, Poland

A declaration

Hereby I declare my contribution to the following articles:

1. *Characterization of spin wave propagation in (111) YIG thin films with large anisotropy*
   A. Krysztofik, H. Głowiński, P. Kuświk, S. Ziętek, L.E. Coy, J.N. Rychły, S. Jurga, T.W. Stobiecki, J. Dubowik
   Journal of Physics D: Applied Physics **50**, 235004 (2017)
   DOI: 10.1088/1361-6463/aa6df0

In this publication, I have written the original draft, analyzed the experimental and theoretical results, performed literature analysis and PLD depositions, carried out: the VNA-FMR, VSM, angle-resolved FMR, spin-wave spectroscopy measurements, results visualization and part of simulations in *Comsol Multiphysics*. I have also prepared a response to reviewer questions and comments.

2. *Ultra-low damping in lift-off structured yttrium iron garnet thin films*
   A. Krysztofik, L. E. Coy, P. Kuświk, K. Załęski, H. Głowiński, J. Dubowik
   Applied Physics Letters **111**, 192404 (2017)
   DOI: 10.1063/1.5002004

In this publication, I have written the original draft, analyzed the experimental and theoretical results, performed literature analysis and PLD depositions, carried out: the VNA-FMR, angle-resolved FMR measurements, and results visualization. I have also prepared a response to reviewer questions and comments.

3. *Magnetization damping in nanocrystalline yttrium iron garnet thin films grown on oxidized silicon*
   A. Krysztofik, S. Özoğlu, E. Coy
   IEEE Magnetics Letters **12**, 7101605 (2021)
   DOI: 10.1109/LMAG.2021.3086454

In this publication, I have written the original draft, analyzed the experimental results, performed literature analysis and PLD depositions, carried out: the XRD, SEM, VSM, VNA-FMR measurements, and results visualization. I have also prepared a response to reviewer questions and comments and conducted correspondence with the journal.

4. *Effect of strain-induced anisotropy on magnetization dynamics in $Y_3Fe_5O_{12}$ films recrystallized on a lattice-mismatched substrate*
   A. Krysztofik, S. Özoğlu, R.D. McMichael, E. Coy
   Scientific Reports **11**, 14011 (2021)
   DOI: 10.1038/s41598-021-93308-3

In this publication, I have written the original draft, analyzed the experimental and theoretical results, performed literature analysis and PLD depositions, carried out: the VSM, VNA-FMR, angle-resolved FMR measurements, theoretical calculations, and results visualization. I have also prepared a response to reviewer questions and comments and conducted correspondence with the journal.

5. *Tuning of Magnetic Damping in $Y_3Fe_5O_{12}$ / metal bilayers for spin-wave conduit termination*
   A. Krysztofik, N. Kuznetsov, H. Qin, L. Flajšman, E. Coy, S. van Dijken
   Materials **15**, 2814 (2022)
   DOI: 10.3390/ma15082814

In this publication, I have written the original draft, analyzed the experimental and theoretical results, performed literature analysis and PLD depositions, carried out: the XRD, XRR, GIXRD, SEM, VNA-FMR, theoretical calculations, micromagnetic simulations, results visualization and part of spin-wave spectroscopy measurements. I have also prepared a response to reviewer questions and comments and conducted correspondence with the journal.

……13.05.2022…… Adam Krysztofik ……

Date Signature

dr hab. Piotr Kuświk, prof. IFM PAN

Institute of Molecular Physics
Polish Academy of Sciences
Smoluchowskiego 17
60-179 Poznań, Poland

Declaration

I hereby declare my contribution to the following articles:

1. *Characterization of spin wave propagation in (111) YIG thin films with large anisotropy*
   A. Krysztofik, H. Głowiński, **P. Kuświk**, S. Ziętek, L.E. Coy, J.N. Rychły, S. Jurga, T.W. Stobiecki, J. Dubowik
   Journal of Physics D: Applied Physics **50**, 235004 (2017)
   DOI: 10.1088/1361-6463/aa6df0

In this publication, I have fabricated coplanar waveguides using maskless photolithography technique. I was also involved in the discussion concerning obtained results and manuscript evaluation.

2. *Ultra-low damping in lift-off structured yttrium iron garnet thin films*
   A. Krysztofik, L. E. Coy, **P. Kuświk**, K. Załęski, H. Głowiński, J. Dubowik
   Applied Physics Letters **111**, 192404 (2017)
   DOI: 10.1063/1.5002004

In this publication, I have performed maskless photolithography for patterning of YIG films. I was also involved in the discussion concerning obtained results and manuscript evaluation.

23.05.2022 Piotr .....

Date Signature

Nikolai Kuznetsov

NanoSpin
Department of Applied Physics
Aalto University School of Science
FI-00076 Aalto, Finland

A declaration

Hereby I declare my contribution to the following article:

1. *Tuning of Magnetic Damping in $Y_3Fe_5O_{12}$ / metal bilayers for spin-wave conduit termination*
   A. Krysztofik, **N. Kuznetsov**, H. Qin, L. Flajšman, E. Coy, S. van Dijken
   Materials **15**, 2814 (2022)
   DOI: 10.3390/ma15082814

In this publication, I have conducted VNA spectroscopy measurements. I was also involved in the discussion concerning obtained results and manuscript evaluation.

13.05.2022 .....

Date Signature

Dr. Robert D. McMichael

National Institute of Standards
and Technology
Gaithersburg, MD 20899, USA

A declaration

Hereby I declare my contribution to the following article:

1. *Effect of strain-induced anisotropy on magnetization dynamics in $Y_3Fe_5O_{12}$ films recrystallized on a lattice-mismatched substrate*
   A. Krysztofik, S. Özoğlu, **R.D. McMichael**, E. Coy
   Scientific Reports **11**, 14011 (2021)
   DOI: 10.1038/s41598-021-93308-3

In this publication, I have contributed to the development of the FMR linewidth model, discussion and interpretation of the obtained results, and manuscript evaluation.

May 13, 2022 R.D.McM

Date Signature

Sevgi Özoğlu

Faculty of Physics
Adam Mickiewicz University
Sciences
Uniwersytetu Poznanskiego 2
61-614 Poznań, Poland

Department of Physics, Graduate
School of Natural and Applied

Hakkari University
30000 Hakkari, Turkey

A declaration

Hereby I declare my contribution to the following articles:

1. *Magnetization damping in nanocrystalline yttrium iron garnet thin films grown on oxidized silicon*
   A. Krysztofik, **S. Özoğlu**, E. Coy
   IEEE Magnetics Letters **12**, 7101605 (2021)
   DOI: 10.1109/LMAG.2021.3086454

In this publication, I have carried out atomic force microscopy measurements under the supervision of Dr. Emerson Coy. I was also involved in the discussion concerning obtained results.

2. *Effect of strain-induced anisotropy on magnetization dynamics in $Y_3Fe_5O_{12}$ films recrystallized on a lattice-mismatched substrate*
   A. Krysztofik, **S. Özoğlu**, R.D. McMichael, E. Coy
   Scientific Reports **11**, 14011 (2021)
   DOI: 10.1038/s41598-021-93308-3

In this publication, I have carried out atomic force microscopy, X-ray diffraction, and X-ray reflectivity measurements under the supervision of Dr. Emerson Coy. I was also involved in the discussion concerning obtained results.

13.05.2022 .....

Date Signature

Dr. Huajun Qin

NanoSpin
Department of Applied Physics
Aalto University School of Science
FI-00076 Aalto, Finland

A declaration

Hereby I declare my contribution to the following article:

1. *Tuning of Magnetic Damping in $Y_3Fe_5O_{12}$ / metal bilayers for spin-wave conduit termination*
   A. Krysztofik, N. Kuznetsov, **H. Qin**, L. Flajšman, E. Coy, S. van Dijken
   Materials **15**, 2814 (2022)
   DOI: 10.3390/ma15082814

In this publication, I have designed and fabricated microwave antennas using optical lithography and magnetron sputtering. I was also involved in the discussion concerning obtained results and manuscript writing.

.....

Date 2022.05.14 Signature *Huajun Qin*

dr Justyna Rychły-Gruszecka

Faculty of Physics
Adam Mickiewicz University
Umultowska 85
61-614 Poznań, Poland

Institute of Molecular Physics
Polish Academy of Sciences
Smoluchowskiego 17
60-179 Poznań, Poland

A declaration

Hereby I declare my contribution to the following article:

1. *Characterization of spin wave propagation in (111) YIG thin films with large anisotropy*
   A. Krysztofik, H. Głowiński, P. Kuświk, S. Ziętek, L.E. Coy, **J.N. Rychły**, S. Jurga, T.W. Stobiecki, J. Dubowik
   Journal of Physics D: Applied Physics **50**, 235004 (2017)
   DOI: 10.1088/1361-6463/aa6df0

In this publication, I have performed electromagnetic simulations in *Comsol Multiphysics*. I was also involved in the discussion concerning obtained results and manuscript evaluation.

16.05.2022..... Rychły-Gruszecka.....

Date Signature

Prof. dr hab. Tomasz Stobiecki Kraków, 16. 05. 2022

AGH University of Science and Technology
Faculty of Computer Science, Electronics and Telecommunications
Institute of Electronics
al. Mickiewicza 30,
30-059 Kraków, Poland
stobieck@agh.edu.pl

A declaration

Hereby I declare my contribution to the following article:

1. *Characterization of spin wave propagation in (111) YIG thin films with large anisotropy*
   A. Krysztofik, H. Głowiński, P. Kuświk, S. Ziętek, L.E. Coy, J.N. Rychły, S. Jurga, **T.W. Stobiecki**, J. Dubowik
   Journal of Physics D: Applied Physics **50**, 235004 (2017)
   DOI: 10.1088/1361-6463/aa6df0

In this publication, I was involved in the discussion concerning obtained results, manuscript evaluation and managing the experimental study.

Prof. Sebastiaan van Dijken

NanoSpin Group
Department of Applied Physics
Aalto University School of Science
FI-00076 Aalto, Finland

A declaration

Hereby I declare my contribution to the following article:

1. *Tuning of Magnetic Damping in $Y_3Fe_5O_{12}$ / metal bilayers for spin-wave conduit termination*
   A. Krysztofik, N. Kuznetsov, H. Qin, L. Flajšman, E. Coy, **S. van Dijken**
   Materials **15**, 2814 (2022)
   DOI: 10.3390/ma15082814

In this publication, I have supervised the work, contributed to the discussion concerning obtained results, manuscript evaluation and its revision.

16.5.2022

Date

Signature

dr Karol Załęski

NanoBioMedical Centre
Adam Mickiewicz University
Wszechnicy Piastowskiej 3
61-614 Poznań, Poland

A declaration

Hereby I declare my contribution to the following article:

1. *Ultra-low damping in lift-off structured yttrium iron garnet thin films*
   A. Krysztofik, L. E. Coy, P. Kuświk, **K. Załęski**, H. Głowiński, J. Dubowik
   Applied Physics Letters **111**, 192404 (2017)
   DOI: 10.1063/1.5002004

In this publication, I have performed SQUID measurements. I was also involved in the discussion concerning obtained results and manuscript evaluation.

25.05.2022 .....

Date Signature

dr Sławomir Ziętek

Department of Electronics
AGH University of Science and Technology
Al. Mickiewicza 30
30-059 Kraków, Poland

A declaration

Hereby I declare my contribution to the following article:

1. *Characterization of spin wave propagation in (111) YIG thin films with large anisotropy*
   A. Krysztofik, H. Głowiński, P. Kuświk, **S. Ziętek**, L.E. Coy, J.N. Rychły, S. Jurga, T.W. Stobiecki, J. Dubowik
   Journal of Physics D: Applied Physics **50**, 235004 (2017)
   DOI: 10.1088/1361-6463/aa6df0

In this publication, I was involved in the discussion concerning obtained results and manuscript evaluation.

17.05.2022 Sławomi Ziętek

Date Signature